OPTIMUM DESIGN AND DEVELOPMENT OF SEGMENTED MIRROR TELESCOPE OPTICS AND PHASING SYSTEM

A Thesis
Submitted for the Degree of
Doctor of Philosophy (Technology)

Submitted by
Annu Jacob

Department of Applied Optics & Photonics
University College of Technology
University of Calcutta

October 2020

To my Family,

Friends and Teachers...

List of Publications

1. **Refereed Journal Articles**

    (a) **Creating a large aspheric primary mirror using spherical segments** - ***Annu Jacob***, *Padmakar Parihar, Melvin K. James*, Experimental Astronomy,vol. 50, issue. 01, 51-71,07, 2020, DOI: 10.1007/s10686-020-09663-y.[1]

2. **Refereed Conference Proceedings**

    (a) **A co-phasing technique for segmented mirror telescopes** - ***Annu Jacob***, *Padmakar Parihar*, Proc.SPIE 9654G,15 June 2015, doi:10.1117/12.2181778.[2]

    (b) **Modeling the segmented primary for a 10-meter-class telescope** - *Vineeth Valsan, S. Sriram,* ***Annu Jacob****, J. P. Lancelot, G. C. Anupama*, Proc.SPIE 96540C, 15 June 2015, doi:10.1117/12.2181743.[3]

    (c) **Prototype segmented mirror telescope: a pathfinder of India's Large Optical-NIR telescope project** - *Padmakar Singh S. Parihar, Prasanna Deshmukh,****Annu Jacob****, Varun Kumar, Abhishek Goudar, S. Sriram, S. Nagabhusan, Amit Kumar Sahgal, K. V. Govinda, D.S. Sandeep, P.M.M. Kemkar, G.C. Anupama*, Proc.SPIE 107001A, 6 July 2018, doi.org/10.1117/12.2313079.[4]

    (d) **Aligning and phasing segmented mirror telescope with the pyramid sensor** - ***Annu Jacob***, *Padmakar Parihar, Sindhu Divakaran, Melvin K. James, Varun Kumar*, Proc.SPIE 107001G, 6 July 2018, doi.org/10.1117/12.2313096.[5]

    (e) **Study on creating an aspheric primary mirror of a large telescope using spherical mirror segments** - ***Annu Jacob***, *Pad-*

---

[1] Presented in Chapter 3

[2] Presented in Chapter 4

[3] Presented in Chapter 3

[4] Presented in Chapter 2

[5] Presented in Chapter 5

makar Parihar, Melvin K. James, Proc.SPIE 11207, 3 October 2019, doi.org/10.1117/12.2530932.[6]

---

[6] Presented in Chapter 3

Presentations

1. **A co-phasing technique for segmented mirror telescopes** - ***Annu Jacob***, *Padmakar Parihar*, International Conference on Optics and Photonics, Kolkata, India, June 2015 **Oral presentation**
2. **Phasing techniques** - ***Annu Jacob***, *Padmakar Parihar*, TMT science and instrumentation workshop, organized by Department of Earth& Space Science IIST, Trivandrum, India, June 2015 **Oral presentation**
3. **Optics for prototype segmented mirror telescope** - ***Annu Jacob***, *Padmakar Parihar,Sriram.S, J.P.Lancelot*, 34th meeting of Astronomical society of India, Jammu Kashmir, India, May 2016 **Poster presentation**
4. **Pyramid sensor for aligning and phasing segmented mirror telescope-** ***Annu Jacob***, *Padmakar Parihar,Sindhu Divakaran*, 35th meeting of Astronomical society of India,Jaipur, India, March 2017 **Poster presentation**
5. **Optical Design and Analysis of PSMT** - ***Annu Jacob***, *Padmakar Parihar,Febins Francis*, TMT Science Forum, Mysuru, India, November 2017 **Poster presentation**
6. **Aligning and phasing segmented mirror telescope with the pyramid sensor-** ***Annu Jacob***, *Padmakar Parihar,Sindhu Divakaran, Melvin. K.James, Varun Kumar*, SPIE conference on Astronomical Telescopes+ Instrumentation, Austin, USA, June 2018 **Oral presentation**
7. **Study on creating aspheric primary mirror of a large telescope using spherical mirror segments-** ***Annu Jacob***, *Padmakar Parihar, Melvin.K.James*, International Conference on Applications in Optics and Photonics in Lisbon, Portugal, June 2019 **Oral presentation**

Abstract

Astronomy today is in the path of constructing large telescopes. Due to several manufacturing and maintenance difficulties, large telescopes of more than 8 m are predominantly segmented. To fulfill the need for its growing astronomical community, India is also aspiring to create a 10 m class Optical-NIR observing facility within the country. A telescope of this size requires huge investment along with hundreds of scientists, engineers, and technicians working together about a decade to realize it. Therefore, before embarking on such a challenging mega-project, the segmented mirror technology, which is not yet standardized, needs to be demonstrated. Considering this, it has been proposed to develop a 1 m class Prototype Segmented Mirror Telescope (PSMT). The PSMT is expected to be a perfect test-bed for the primary mirror control and alignment and the phasing system.

As a part of the thesis work, we have come up with a cost-effective, optimum design of the optics for the PSMT. The PSMT optics, which uses spherical primary and oblate ellipsoid secondary, is unique in design and simple in construction. We have designed telescope optics considering the segmented primary mirror, and have also carried out a detailed analysis for the sensitivity, tolerance, and the error estimation. In the next step, we also designed the optics for the proposed 10 m class telescope named National Large Optical Telescope (NLOT). Since NLOT will be a large segmented mirror telescope, an extensive study has been carried to understand the effect of segment size, miss-alignment (tip-tilt,de-center, and clocking), phasing error, segment to segment ROC variations, figure error as well as inter-segment gaps. In this process, we developed many generic tools and techniques which makes segmentation related study simpler. For the 10 m class telescope, we have also explored the possibility of using spherical mirror segments in place of aspheric ones, which are quite difficult to manufacture.

A segmented telescope can provide diffraction limited design performance only if their mirror segments are aligned and phased. So, the second part of this thesis is dedicated to developing phasing techniques. We have carried out an extensive study and laboratory experimentation on two different phasing schemes. The first phasing scheme is based on Shack-Hartmann working in the physical optics domain, whereas the other is based on the pyramid sensor. The basic principle of these two phasing schemes are explored, and simulations have been carried out to check their performances. We also attempted to undertake laboratory experimentation on the above phasing techniques. The results of the simulation and the experimentation have been presented and discussed.

Contents

List of Figures

List of Tables

Chapter 1

Introduction

1.1 Large Telescopes

Astronomy is one of the oldest sciences. It is an integral and inspiring part of the scientific development since antiquity. In recorded history, many civilizations have been methodically observing celestial bodies. This helped in organizing their day to day actives and also in navigation. During renaissance time in the 16th century, Galileo's first refractive telescope pushed this field's scientific potential further. With the use of the telescope, observational astronomy got out of the limitation of the naked eye. From then onward, astronomers are always in favor of building larger and larger telescopes.

Although space-based telescopes such as HST, Kepler, Spitzer, Herschel, etc., have immensely enriched our understanding and many space-based programs also lined up, the importance of the ground-based astronomy is remaining unchallenged. Nearly over half a century, the world's largest optical telescopes were of the size of 3-5 meters. The 5 m Hale telescope developed in the 1940s is considered one of the perfect machines that revolutionized optical astronomy. Then after a number of advancements happened in the telescope technology, like the use of computer-controlled hardware, building large altitude-azimuth (alt-az) mounts, advances in mirror casting, and computer-controlled mirror polishing and the use of a segmented mirror. These advancements finally resulted in the development of many large telescopes of the size of 8-10 meters, such as Keck, VLT, Subaru, Gemini, HET, etc. Since 1990, these large optical telescopes have served the community and given birth to many astronomical discoveries. After 20-30 years of using the large optical telescopes, the necessity to build even larger telescopes has only increased, and we are witnessing the development of 25-40 m size extremely large telescopes such as GMT, TMT, and E-ELT.

There are many reasons behind the ambition of building large astronomical telescopes. Nonetheless, these can be summarized into two points, namely resolution and light collecting capacity. Telescope resolution can be divided into two types, Seeing-limited and Diffraction-limited. Seeing limited telescopes are the ones that have a fixed resolution given by equation λ/r_o. Where r_o is the fried parameter indicating 'seeing' or the atmosphere condition of the place. In a seeing limited telescope, the observing time required to reach an SNR(signal to noise ratio) is dependent on $1/D^2$, where D is the aperture diameter of the primary mirror. Diffraction limited telescopes are the ones whose resolution is not limited by the atmosphere. In this case, the resolution is depended on λ/D. Large ground-based telescopes operating in a diffraction-limited regime are only possible due to the advent of adaptive optics, which correct the atmospheric aberrations. In background-limited adaptive optics observations, the SNR and the telescope's sensitivity (time to reach required SNR) vary as $1/D^4$[12].

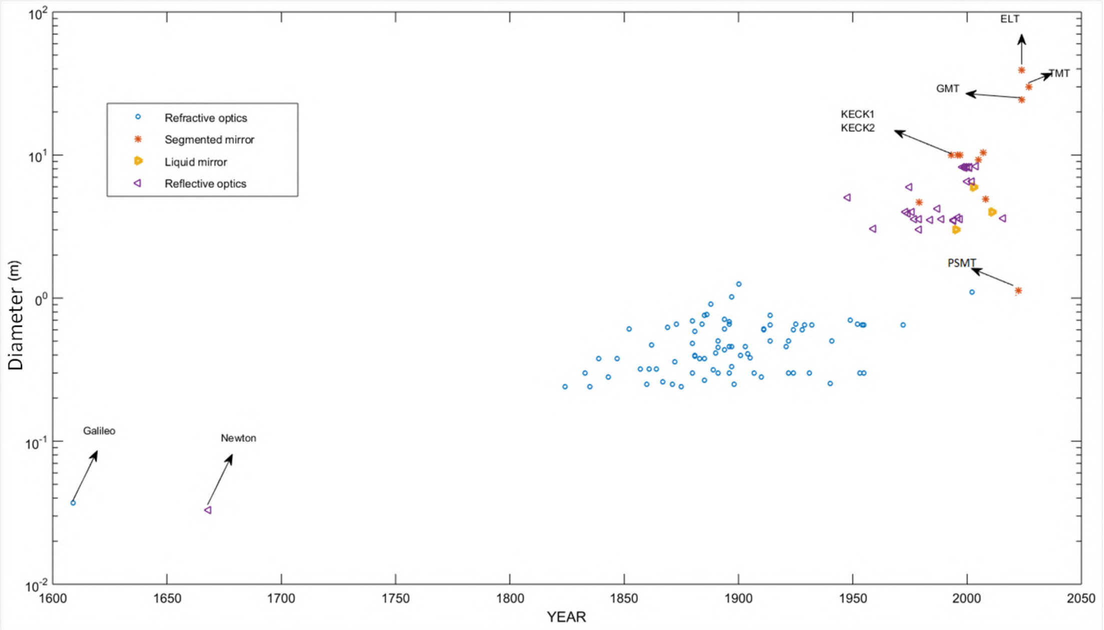

Figure 1.1: Plot showing evolution of optical telescope's size since Galileo's time.

Figure 1.1 shows the evolution in the telescope size since Galileo, who is considered to be the first to use optical telescope for astronomical observations. Sudden jumps in the telescope size can be easily linked with some technological innovation.

1.1.1 Problem in Constructing Large Telescope Made of Monolithic Primary Mirror

The largest size telescope made of single monolithic primary is 8.4 m. There-after construction and operation of large telescopes having monolithic primary larger than 10 m found to be almost impractical. There are several problems associated with building a large telescope made of a single monolith mirror, and few of them are listed below:

1. Casting a high-quality mirror blank of 8 m or large is a big challenging task.
2. There is a greater risk of possible damage of the blank or the mirror during manufacturing, transportation, assembly, or maintenance.
3. The tools required for the grinding, polishing, and final figuring of the mirrors are usually very large as the mirror size increases.
4. Gravitational deflection suffered by the optic is proportional to D^4, where D is the diameter. To avoid this deflection, a monolithic mirror has to be very thick or else need to be actively corrected.
5. The vacuum chamber sizes increase as the mirror size increase. This in-effect makes them very expensive
6. Astronomical observatory sites usually situated in remote places. Shipping a significantly larger mirror to these remote locations is very impractical.
7. Thermal surface deformations will be large as the size of the mirror increases.
8. The Activate and/or Passive mirror support system will get complex as the mirror's size increases. This also will cause additional surface deformations.

Small mirror segments come as a natural solution to the problems associated with the manufacture and operation of these large monolithic mirror telescope.

Segmented mirrors can be stated as an array of small mirrors distributed to act as a single monolithic mirror.

1.1.2 Segmented Mirror Telescopes

In Syracuse's history, Archimedes, around 212BC, used an array of mirrors to focus sun's rays in the roman ships to burn them. Maybe this can be stated as the first recorded use of segmented optics. Historically, telescope made of a segmented mirror was developed by Horn d'Arturo of Italy [13]in 1932 and Pierre Connes of France in 1970 [14]. However, both telescopes were very primitive in quality and hardly be used for any meaningful science observations. Very serious effort to make segmented telescope started with MMT project which uses 7 mirrors each of 1.8 m size and each having its own secondary. A complex technique [17] combined the beam. In that sense, MMT was not a true segmented mirror. However, a true breakthrough happened in segmented mirror technology, when Keck telescopes were design and built-in 1980-90 [18]. Keck optics has been designed around RC (Ritchy Chretien), and it uses 36 segmented mirrors, each 1.8 m in size. After the Keck-1 telescope's success, a second telescope named Keck-2 was constructed near the Keck-1. It was completed in 1996. Keck telescope is later replicated under the GTC project in Spain. However, despite having new technology, the off-axis mirror segments are always difficult to manufacture and, hence, costly, increasing the telescope's budget. To resolve this problem, the attempt started to use a spherical primary mirror so that each mirror segment will be identical, and spherical mirrors are very easy to fabricate. The substantial spherical aberration introduced by the spherical mirror is corrected by the use of few reflecting optics located close to the prime focus [34],[35]. The HET and SALT telescopes use this technology and provided to the world two cheapest telescopes [36].

Presently all of the large up-coming telescopes are segmented. GMT or the Giant Magellan telescope is one member of the next generation segmented telescope. GMT will use seven honeycomb mirrors, each of 8.4 m as segments, forming a single optical surface of 24.5 m. GMT is a work of an international collaboration of leading universities and scientific institutions. Another upcoming segmented telescope with great scientific value is TMT or Thirty-meter telescope. This is also an international venture with five countries, namely India, China, Japan, USA, and Canada. TMT will have a Ritchey Chretien design with hyperbolic primary and secondary. The Primary will be made of 492 segments. E-ELT or European Extremely large telescope is another segmented mirror telescope that is on construction. It is a project by the European southern observatory. E-ELT will have primary consisting of 984 segments. The optics design consist of an anastigmat with three powered mirrors and two fold flats. All these existing or upcoming segmented telescopes need active control of the primary mirror and other optical elements to make them work like a monolithic to achieve the resolution and the light collecting capacity the telescope was designed for.

For making a large telescope using segmented mirrors, one must understand different technological challenges associated with it. A few of them are listed below.

1. Segmented mirror telescope requires a large number of the segment and associated subsystems such as actuator and the edge sensors. This escalation in the number of subsystems makes the telescope functions very complex.

2. The segments can be made either symmetrical (spherical) or asymmetric (aspheric) depending on the optics design. Nevertheless, owing to better performance, usually, segments are made as aspheric. In such cases, the off-axis sections of the parent figure of revolution are not circularly symmetric. Making these off-axis segments then becomes complex and expensive.

3. While going ahead with a segmented mirror telescope, there can be a problem with alignment and phasing of each mirror segment. So that the telescope can act like a monolithic mirror. Without this, a segmented mirror telescope cannot achieve the expected resolution and sensitivity of that of a telescope made of equivalent sized monolithic mirror. Segmented mirror telescopes also require a sophisticated primary mirror control system.

4. The gaps and edges of the segments cause diffraction and thermal background effects in the image plane

Despite having its complexities, the concept of segmented mirror telescopes has spread worldwide. Almost all of the future large telescopes are developed around this technology.

1.2 Optical Telescopes in India

India's path towards large telescopes has not been a linear one. When many 2-5 meter class telescopes served the world astronomical communities, India's largest optical telescopes were not bigger than half a meter. During 1970s it was Vainu Bappu who became instrumental in building and installing many large telescopes in India. The 2.34 m Vainu Bappu telescope, entirely designed and built in India during the 1980s was considered the largest telescope in Asia. After over more than three decades, no serious effort was made to install a large telescope. Whereas during the same period, the world moved towards the commissioning of many 8-10 m class telescopes. Indian optical astronomical community could not keep pace with world trends and solely rely on the 2 m class telescopes. At present, the largest telescope in India is 3.6 m Devesthal optical telescope (DOT), which has been recently commissioned by ARIES Nainital. India is also one of the partners of the 30m TMT project. Having access to one of the world largest telescope, the Indian community is expected to contribute to frontiers in astronomical research prominently. However, there would be a large gap between 3.6 m DOT and 30 m TMT telescope, which need to be filled by either getting access to existing 10m telescopes or building our own 10 m class telescope.

1.3 National Large Optical Telescope Project

Recognizing the need for a large telescope, long back in 1990s, the Indian Institute of Astrophysics (IIA) proposed to install a 6.5 m telescope somewhere in the Himalayan region. To identify suitable sites for a large Optical-NIR observatory, IIA started surveying Himalayan and trans-Himalayan regions. Using available topographical maps, weather data, and satellite imagery, six potential sites all more than 4000 m above from mean sea level were identified. Based on a preliminary survey conducted at six places, Digpa-ratsa Ri, Hanle (mount Saraswati), was chosen for further detailed studies. Hanle is a high-altitude, arid and cold place. This place is far from any artificial light pollution, having low atmospheric aerosols, not much affected by monsoon, and has got clear sky all through the year. This place provides an excellent opportunity for developing astronomical facilities at a variety of Electromagnetic wave frequencies. Finally, Hanle was identified as the best site for establishing the Indian Astronomical Observatory (IAO), which now hosts the 2 m HCT and the gamma-ray array telescope called HAGAR. More than a decade long observing experience with 2 m size telescope, it has been found that Hanle region has the required characteristics of a good astronomical site and could be a natural candidate site for any future large aperture Indian optical-infrared telescope. After a long pause, in 2007, a group of astronomers from IIA resurrected the project to install a modern, state-of-the-art 10 m class telescope working in optical and NIR regions. A committee was formed to explore the sites and look at the telescope's technical aspects and come up with a construction proposal and the road-map. Initially, this project was named Indian Large Optical Telescope project, which later renamed to National Large Optical Telescope project (NLOT). When NLOT related activities were in peak, India joined the TMT consortium. The group working for the NLOT got involved with this new but significant initiative, and work related to building a 10 m class telescope again subsided. After streamlining TMT related works, the focus has been again brought back to NLOT. In 2015, the director of IIA constituted a new working group with a mandate to prepare a detailed project report for NLOT and carry out a pilot study on segmented mirror telescope technology. So far NLOT related activities were confined to IIA. To make it truly national, a one-day meeting to discuss various aspects of the 10 m telescope with the broader Indian community was held on February 18, 2019. About 100 astronomers representing different institutions participated in the meeting, endorsed the plan to get 10 m size telescope, and agreed to participate in the design, and the development works actively.

The NLOT is expected to be a 10-12 m size, fully steerable Optical-NIR telescope, developed around segmented mirror technology. The plan is that many TMT subsystems that form the primary mirror, such as mirror segments, supports, actuators, edge sensors, etc. would be used with minor changes. However, the telescope's mechanical structure, mount and drives, secondary and tertiary assemblies, science instruments, controls, etc. will be different from TMT and require to be designed and developed indigenously. A team of engineers is working on conceptualizing the whole telescope and many of its subsystems (see Figure 1.2). Whereas, optical design and analysis of the 10 m telescope have been carried under the present thesis works. Any private firm can not provide a large telescope of this size, and it is usually a joined endeavor of industry and research institutions. Therefore, the participation of private industries in realizing 10 m Indian telescope is going to be crucial. Since segmented mirror technology has complexities, before embarking on any large telescope making project, which requires huge investment, one needs to get acquainted with the technology. Considering this, it has been decided to explore the critical subsystem by conducting studies, simulations, and laboratory experimentation. Furthermore, to get complete hands-on segmented mirror technology, a project to develop a 1 m class Prototype Segmented Mirror Telescope has also been initiated at IIA.

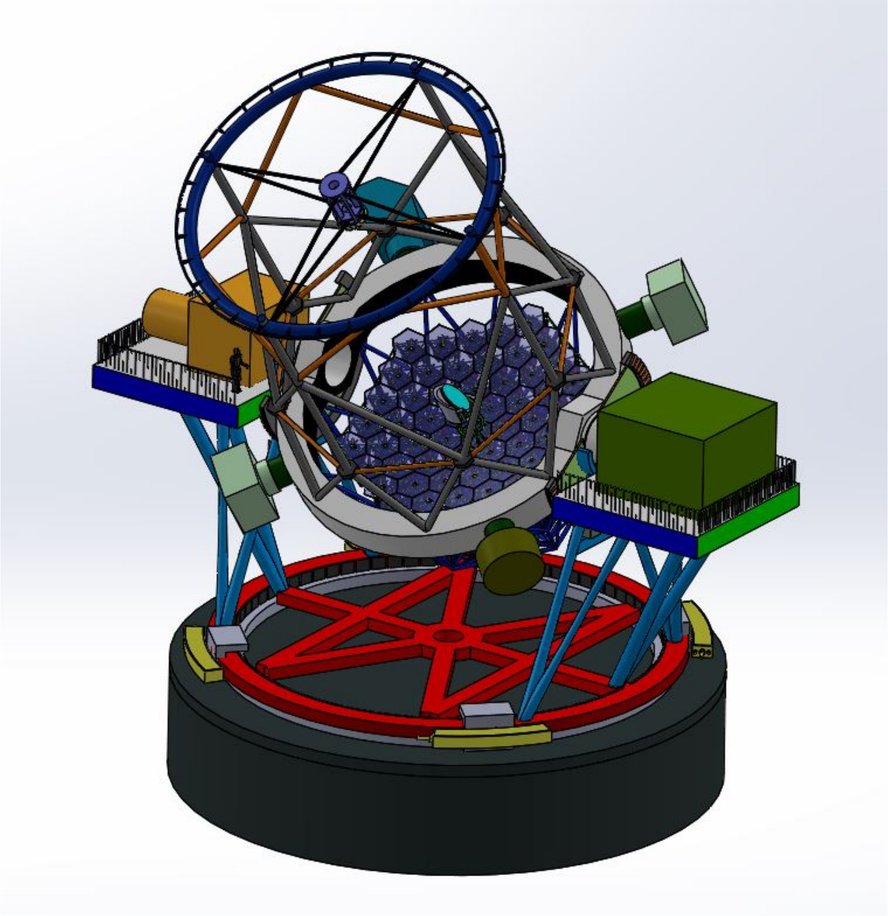

Figure 1.2: Conceptual design of the 10 m class National Large Optical telescope

1.4 Prototype Segmented Mirror Telescope

Prototype Segmented mirror telescope is primarily conceived as a technology demonstrator and an exploratory experiment to develop a large segmented mirror telescope in India. Furthermore, it can also be used to carry out a few specific sciences linked with variability study of transients, doing either or both of photometry and spectroscopy. The proposal is to develop a segmented mirror prototype telescope of about a meter, having all kinds of subsystems, which is expected in a larger telescope. To reduce the cost of the prototype, various measures have been undertaken, and one of them is to use spherical optics for primary segemnts rather than a spheroid parabola/hyperbola.

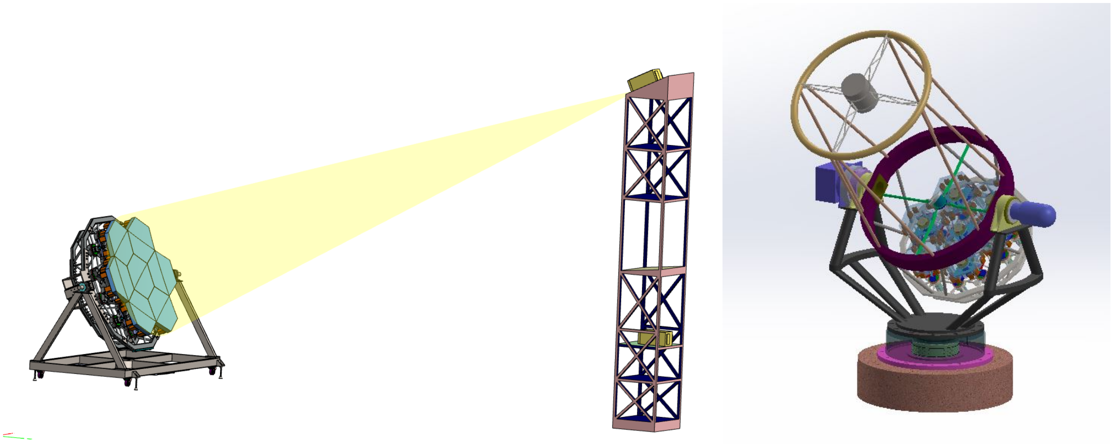

Figure 1.3: 3D model of the PSMT phase-I which is a laboratory test-bed (left) and the PSMT phase-II, a full-fledged segmented mirror telescope (right).

PSMT will have seven hexagonal mirrors making a spherical primary, and an aspheric secondary with two Nasymth focus, having an effective aperture of 1.3 m. Segments will be supported by simple mirror support assembly, driven by indigenously developed voice coil based actuator. The telescope will have an Alt-Az mount and field rotator system with a direct driving motor system. In-house developed inductive edge sensor is planed to be used to measure inter-segment relative displacement to great accuracy. The telescope mirror control, actuators, sensor are developed under different projects in the India TMT coordination center (ITCC) laboratory of IIA. The entire development activities is divided into two phases. In the first phase, a seven segment laboratory testbed will be developed. Whereas, in the second phase, the full-fledged telescope will be realized.The phase-

I laboratory test bed is created to understand the complexities linked with the primary mirror(PM) control (M1CS). The testbed will use the same seven-segment primary mirror, which will later be used for the Phase-II. To understand the effect of the variable gravity on the mirror control, the PM will be mounted on a motorized mount, allowing it to swing in the elevation direction. A Shack-Hartmann based alignment and phasing device mounted on the tower will be placed near the PM's ROC. The performance of the M1CS will be judged based on the optical feedback by SH at two different pointing orientations (35deg and 0deg with respect to the horizon). By using the feedback from the edge sensor, one can evaluate M1CS performance over variable gravity by rotating PM from zenith to horizon. After the successful technology demonstration, the final telescope is planned to be installed in Hanle, Ladakh, India, where it can be used for a few dedicated science cases.

1.5 The Building Blocks of a Segmented Primary Mirror

Though segmentation solves many problems associated with large monolithic primaries, it also brings its complexities into the system. For the segmented telescope to work, several subsystems should be well designed, precisely manufactured and tested, and deployed in the final telescope system. In general, any mirror segments will be subjected to six degrees of freedom, three out of the plane, namely piston, tip and tilt, and three in-plane, X, Y translation, and the clocking. The out-of-plane motion piston, tip, and tilt are usually more sensitive to image quality than the in-plane degrees of freedom; hence, they need to be corrected actively with actuators the edge sensors. A closed-loop primary mirror controller that takes input from the edge sensor generates command for the actuator using a control matrix. Any change in the primary mirror's shape due to segment motion is precisely measured by the edge sensor and corrected by the controller through actuators. This way shape of the segmented primary mirror is maintained against variable gravity, temperature, and external disturbances such as the wind. The mirror segments are placed on a specifically designed segment support system. The support system of all large telescopes are also fitted with a warping harness, which either corrects the figure error leftover after manufacturing the segment and/or correct any error induced later by the support system itself due to change in the temperature as well as the gravity. On top of these control loops, most of the large segmented telescopes are also equipped with an additional adaptive optics loop that corrects the wave-front errors introduced by the earth's atmosphere.

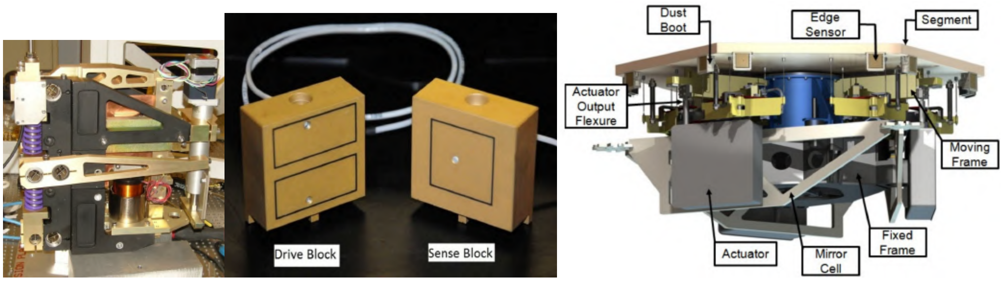

Figure 1.4: TMT SSA[27]

Even though the active control system with the help of actuators and edge sensors, can maintain the overall shape of the primary mirror, it would require a reference position. The edge sensor's reference position will be the perfectly aligned and phased segmented primary mirror, giving a minimal wave-front error and facilitating diffraction-limited performance. The system used for this purpose of reference identification is called the Alignment and Phasing (APS) device, and it is one of the vital instruments for any segmented mirror telescope. Upon successful correction of the segment positioning, the APS gives a lookup table to actuator -edge sensor loop to freeze and maintain the segment position.

1.6 Alignment and Phasing of Segmented Mirror Telescopes

The major factors to be considered by APS to make a segmented telescope act like a monolithic mirror telescope are Co-aligning, co-focusing, and co-phasing.

Co-aligning is merely the stacking of all images formed by individual mirror segments to achieve maximum intensity. Co-focusing deals with making the spot size produced by each mirror of the same size. This can be achieved by figuring the mirror segments at the manufacturing stage and later tuning the segment

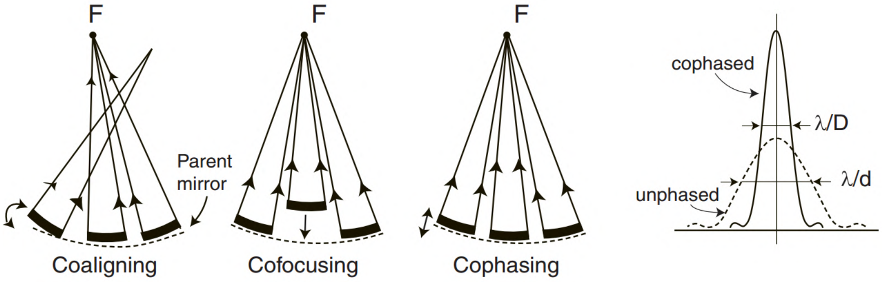

Figure 1.5: Co-aligning, co-focusing, and co-phasing a segmented system (left). The PSF of a segmented system where the mirror segments are out of phased or in-phase (right). The width of the PSF is λ/d in the first case, where d is the diameter of the mirror segment, and it is λ/D in the second case, where D is the diameter of the full primary mirror[63].

support assembly. When these two factors are met, the telescope acts as a large light collector. However, it will still not give the image quality produced by a single mirror of the same total size. This is because the light from each segment reaches the image plane with a phase difference between them introduced by the piston effect. The piston effect is introduced by the phase discontinuity between edges of the adjacent segments. In the presence of large piston error, the PSF of the telescope is the incoherent sum of the individual PSFs of the segments. This lowers the image quality, affects the telescope's resolution, and results in speckles in the image background[63]. Optical phasing of segmented mirrors is done using a phasing sensor which uses a comparatively bright star to produce an image. Co-phasing is one of the core interest of this thesis. A number of co-phasing techniques are proposed/developed; however, except the one used in Keck Telescope, no other techniques have been demonstrated with the real telescope. Depending on the techniques used, the recovery of the phase can be made directly in the Image plane, pupil plane, or intermediate planes. These different techniques are briefly explained in the subsequent section. piston (p) as shown in the differential piston

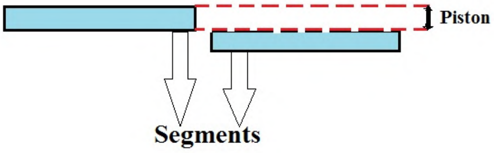

Figure 1.6: Segments showing piston error.

generated by the postional difference between two optical surfaces p=p1-p2 . In terms of wavefront

$\phi_1 = 2pi/\lambda * p1$

$\phi_2 = 2pi/\lambda * p2$

piston $\Delta\phi = \phi_1 - \phi_2$

1.7 Review of Phasing Techniques

1.7.1 Image and Intermediate plane Techniques

1.7.1.1 Phase Retrieval

In this technique, the phase is derived from a single focal plane image of a point source. The point spread function (PSF) contains information about the wavefront error induced by any imaging device such as a telescope. Through an inversion technique, it is possible to retrieve the wavefront phase information from the image[1]. As for as the requirement of hardware is a concern, this technique is found to be simple, and any existing detectors installed in the telescope can be used to grab the image of a point source such as a star. However, the difficulty is associated with the substantial computational requirement to retrieve the phase back. This is because the PSF of an optical system (intensity distribution) is linked to the pupil plane phases in a highly non-linear way. Furthermore, since an image is a distribution of intensity, it does not preserve the sign component of the complex phase distribution, leading to sign ambiguity in the retrieved phase.

1.7.1.2 Phase Diversity

The technique of phase diversity is nothing but some improvement over the phase retrieval technique. Here the phase is extracted with the help of two images. One in the focal plane and another one with a known added aberration, usually a defocus[2]. This technique is also easy to implement but at the expense of considerable computation power. The advantage of this technique is that it can be applied not only to point source but also to extended objects. This technique is also sensitive to the atmospheric seeing; however, it shows promising results for high contrast imaging systems such as extreme AO.

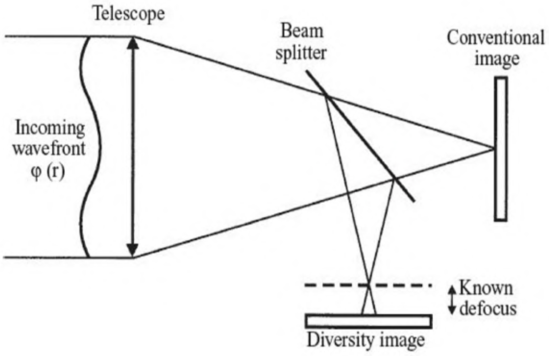

Figure 1.7: Principle of the phase diversity

1.7.1.3 Curvature Sensor

The curvature sensor was proposed by Roddier et al.in 1988 [5] to directly measure local curvature of the wavefront rather than tilt from the intensity distribution in the images obtained just before and after the focal plane. This is an intermediate plane technique. The intra focal image will be brighter in the regions with positive curvature and darker in regions with negative curvature, whereas intensity distribution in the extra focal images would be just the opposite. The phase information can be extracted from the intensity distribution. The relation between intensity distribution of the images to the wavefront is given by

$$\frac{(I_2 - I_1)}{(I_2 + I_1)} = \frac{f(f-l)}{l}\left[\Delta^2 z(\vec{u}) - \frac{\partial}{\partial u} z(\vec{u})\delta_c\right]_{u=f(\vec{r})/l} \tag{1.1}$$

Where $\Delta^2 z(\vec{u})$ is the Laplacian of the wavefront z and δ_c is a liner impulse distribution around the pupil edge weighted by the wavefront radial tilt $\frac{\partial z}{\partial u}$. I_1 and I_2 are the intensities associated with intra and extra focal images. [5]

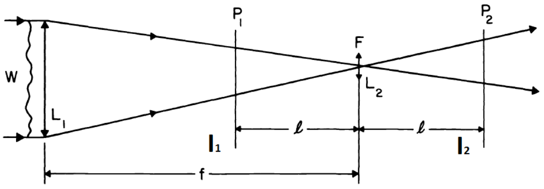

Figure 1.8: Principle of curvature Sensor, I_1 and I_2 are the intensity distribution at intra-focal plane P_1 and extra focal plane P_2.

The curvature sensor described above is based on geometrical optics and works only for the continuous wavefront. However, once the wavefront is broken, as the case with the segmented mirror is subjected to piston errors, we need to consider this technique's physical optics behavior. To execute the technique in the case of segmented telescope, the scale of diffraction effects (associated with primary mirror segments) in the image plane should be small compared to the diameter d of a segment mapped onto the image plane. Also, the diffraction effects associated with the segments should predominate over those associated with the atmosphere.

1.7.2 Pupil Plane Techniques

1.7.2.1 Modified Shack Hartmann phasing sensor

This technique is based on the physical optics realization of the Shack Hartmann sensor. In this technique, microlenses are arranged on the reimaged pupil plane such that they straddle the inter-segment gap of two segment edges. The diffraction limited images of the point source such as star are formed by these lenses on the detector plane. The shape of the image or rather point spread function changes as the piston error between two mirror segments vary [62]. The phase information is extracted by comparing theoretically simulated images with the observed one. The detailed exploration of this technique is one of the objectives of the current thesis, and the work carried out in this regard is given in chapter 4.

1.7.2.2 Pyramid Sensor

The pyramid sensor is another pupil plane wavefront sensor used to measure piston and other low order aberrations. In the case of the pyramids sensor, optical devices such as telescope form an image of the point source at the pyramid's tip. The four faces of the pyramid sample light from four quadrants of the PSF and deflected it in slightly different directions so that by use of a reimaging lens, four pupil images can be created on the detector plane. If the incident light is subjected to any aberrations, then four pupil images will no longer be having identical intensity distribution. The relative point-to-point intensity differences in these four pupil images can be used to derive local gradient in the wavefront.[74] Pyramid sensor is another tool that we have explored in detail to be used as a phasing device; details are given in chapter 5.

1.7.2.3 The Lateral Shearing Interferometer

Another wavefront sensor used to measure piston and other low-order aberration can is based on Lateral Shearing Interferometer(LSI). The LSI's basic principle is that an aberrated wavefront is split into two parts, one of the beams is laterally shifted (sheared) to a small amount and then after combined to form an interference pattern [51]. The mathematical formulation of the LSI as a wavefront sensor can be briefly presented as:

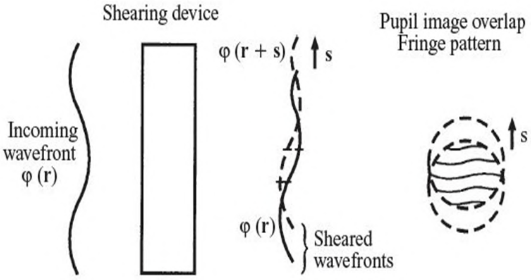

Figure 1.9: Principle of lateral shearing interferometer

$$I(r) = \frac{1}{2}[exp[(i\phi(r)] + exp[(i\phi(r+s)]]^2 \tag{1.2}$$

where s is the displacement in lateral direction, $\phi(r)$ is phase and $I(r)$ is intensity.

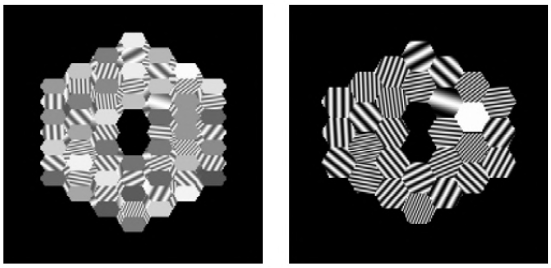

Figure 1.10: Simulated shearing interferograms corresponding to segment tip/tilt errors for the Keck Telescope: (left) half-segment shear, and (right) full-segment shear; both in the vertical direction [51]

.

Likewise, classical Shack-Hartmann wavefront sensor, LSI, is a local wavefront slope detector. The distribution of the slopes within the overlapping area is derived in only one direction. However, to sense the wavefront fully, slopes in two mutually orthogonal directions are required. That means LSI needs two sets of the shearing

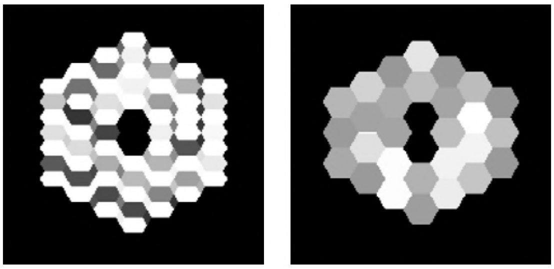

Figure 1.11: Simulated shearing interferograms corresponding to segment piston errors for the Keck Telescope: (left) half-segment shear, and (right) full-segment shear; both in the vertical direction [51]

.

mechanism and detectors, which makes the system a little complex. The LSI has a variable gain and a large dynamic range. In a segmented telescope, LSI is not sensitive to the global piston; it is sensitive to the global tilt component. For the Keck telescope, the Simulated fringe pattern of the tip, tilt and piston errors are shown in the figure 1.10 and 1.11. For the HET telescope, LSI was initially planned to be used as a precision segment alignment tool; however, due to many technical difficulties, it was replaced by a more stable Shack Hartmann based alignment device[6].

1.7.2.4 Mach-Zehnder Interferometer

Mach-Zehnder Interferometer (MZI) is another optical interference-based device that can be used to precisely measure phase error in any segmented mirror telescope [7]. Unlike SH based technique, which requires very precise registration between inter-segment region and lenslet array, MZI can use the entire pupil and hence best suited for large telescopes made of a hundred-thousand of segments. In the MZI, the telescope's beam is split into the interferometer's two arms and focused at the intermediate plane, as shown in Figure 1.12. A pinhole placed at the intermediate focal plane of one arm acts as a spatial filter. All the high-frequency structure corresponds to edges, and the inter-segment gap is removed from this beam and can be regarded as a reference wavefront. In comparison, the beam in another arm carries information about the piston as well as tilts errors. These two beams are finally recombined to form two complementary interference patterns recorded by two imaging detectors. The phase and tilts errors of the segmented are extracted by analyzing these two interferograms. The ZDI appears to be an excellent device to measure segment piston and tilt errors simultaneously; however, its optics' alignment is critical. Furthermore, system performance is found to be quite sensitive to the choice of the pinhole size and atmospheric seeing.

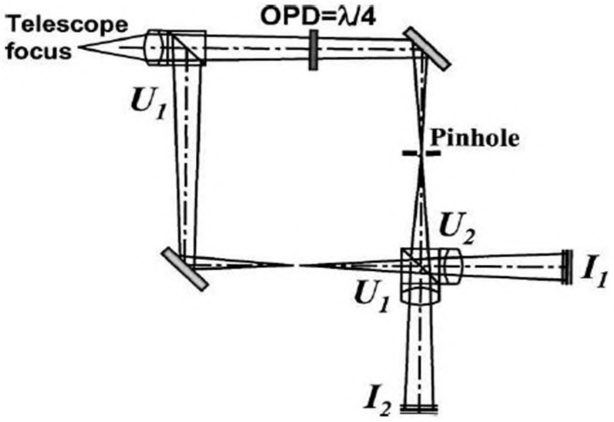

Figure 1.12: The schematic showing Mach-Zernder Interferometer setup to measure segment piston and tilt errors

1.8 Scope of The Thesis

Many projects are initiated by different groups/countries to build large telescopes, including the one proposed in India. The proposed large 10 m class telescope NLOT is at a very early phase of the planning conceptualizing and optomechanical designing. For any telescope larger than 4 m, it appears that segment mirror technology has become a natural choice. NLOT is also planned to be developed using segmented mirror technology (SMT) . Though SMT is not new and many telescopes have already built using a segmented primary mirror, the SMT technology has not yet standardized. Many technological challenges need to be dealt with extensive R &D activities. Under this thesis, attempt has been made first to design the optimized optics of two segmented mirror telescopes. Then, extensive analysis has been carried out to explore the effect of the segmentation on the overall telescope performance. Since many analyses can not be carried out using available conventional techniques, as part of thesis work we have also developed many tools and techniques and some of them indeed innovative in approach. Before embarking on building a large 10m size NLOT telescope, a pilot study on segmented mirror technology has been initiated at IIA. Under this activity, a small prototype segmented mirror telescope (PSMT) is being developed. The design of the PSMT optics using a spherical primary mirror with very few auxiliary optics was the top level design requirement. After exploring many possible design options available, we finally ended up with our own design that meets the requirement and makes the system cost-effective and straightforward.

Any segmented mirror telescope will deliver the best performance, which will match to its equivalent monolithic mirror telescope, when all the mirror segments are aligned, co-focused, and phased. As discussed in the section 1.6, co-aligning and co-focusing are relatively straight forward tasks and usually sensed by using the classical Sack-Hartmann device. Whereas, co-phasing the mirror segments to the accuracy of one-tenth of lambda or better is indeed a difficult task. The phasing task becomes further challenging when the telescope has many segments, which is the case with HET/SALT, TMT, and the E-ELT telescopes. Additionally, in a realized segmented mirror telescope, variable environmental conditions and atmospheric seeing make co-phasing exercise far more difficult than one can find in the stable laboratory condition. At present only twin Keck telescopes are phased and provide close to diffraction limited performance, whereas all other working segmented mirror telescopes such as HET, SALT, GTC, and LAMOST are only aligned and co-focused. Except for GTC, these later telescopes performance is supposed to be seeing limited, and hence co-phasing of their mirror segments are not required. Since the diffraction limited performance is also aimed for the NLOT, phasing its mirror segments becomes essential. There are many phasing techniques either just proposed or already developed and few them have been already briefly described in the section1.7 These techniques not only differ from each other in term of basic working principal but they have also got different precision, capture range, stability as well as instrumentation complexities. After going through an extensive survey of the literature, we decided to deeply explore two phasing techniques as a part of the thesis work. The first one is the technique developed for the Keck telescope and another one based on the pyramid sensor.

1.9 Outline of The Thesis

There are a total of six chapters in the thesis. The first chapter is the introduction, which provides an overview of the large segmented mirror telescope, its importance, and India's plan to build a 10 m class optical-NIR telescope. The basic building blocks of the SMT's and criticalities in phasing the mirror segments are also explained briefly. The second and third chapters describe our effort to design telescope optics for the PSMT and NLOT telescopes and results of the extensive analysis carried out to explore the segmentation effect. The fourth and fifth chapters are exclusively dedicated to phasing related studies and experimentation. The phasing technique developed for the Keck telescope is explored, simulated, and experimented in the laboratory. Whereas, as in the fifth chapter, we present our work on using a pyramid sensor primarily for measuring the piston error as well as other low order aberrations such as tip-tilt and the defocus. The last chapter provides a conclusion of work carried out under the present thesis and scope for further studies and exploration, which can be undertaken in the near future.

Chapter 2

The PSMT Optics

2.1 Introduction

The largest size telescope indigenously built in India is 2.3 m Vainu Bappu Telescope (VBT). VBT was built in the 80s, then after India has not made any optical telescope on its own. In between telescope technology has evolved considerably in all the aspects. In the Indian astronomical community, there is a proposal to develop a 10 m class National large optical telescope (NLOT), which will be developed around segmented mirror technology. A telescope of 8-10 m size can not be simply acquired from any telescope manufacture, and it is always a joint work of research institutions and several industries. Where the design, analysis, integration, installation and testing activities are handled by proposing organization and the manufacturing of various telescope parts as per design is carried out by private industries.

Once segments are aligned and phased in any segmented mirror telescope, then after keeping the alignment intact over weeks and months, using a precision actuator, edge sensor, and primary mirror controller in variable gravity and environment condition is a big challenge. Except for Keck telescopes, all other segmented telescopes developed so far, such as HET, SALT, GTC, and LAMOST, have gravely suffered over the years after their commissioning to deliver intended performances. Building a large telescope requires a huge amount of investment, and a large number of highly skilled people comprising of scientists, engineers, and technicians have to work almost over a decade to realize it. Therefore, before embarking on any large segmented mirror telescope project, it becomes essential to understand the segmented mirror technology complexities. One way to get acquainted with technology is by conducting some kind of laboratory experimentation on the SMT, as carried out by many groups [3] [4] [48]. Another option can be developing a small prototype segmented mirror telescope itself. Considering many advantages over laboratory experimentation, it is proposed to develop a small 1.2-1.5 m prototype segmented mirror prototype telescope (PSMT) at IIA Bangalore. The PSMT will have all kinds of subsystems that one can expect in any large telescope made of segmented mirrors. The PSMT can also be considered a step forward toward building the NLOT. Under the current thesis, we have attempted to develop an optimum design of the PSMT optics that meets the requirement and is also very cost-effective.

2.2 The Design Requirements of the PSMT Optics

The primary aim behind developing the PSMT is to demonstrate the technology required to build a large segmented mirror telescope. So we need a segmented primary with a minimum number of segments that can be used to test the control system. In the hexagonal configuration, minimum one ring with 7 segments including the central one would require to make a segmented primary. To facilitate 12 edge sensors and three actuators on the segment's backside, the minimum size of the segment should be about 500 mm. This will make an effective aperture of the PSMT about 1.3m. The most preferred optical design for any telescope is RC, which requires an aspheric hyperbolic primary mirror. However, manufacturing off-axis mirror segments of aspheric primary are challenging and require very specialized processes such as stress mirror polishing (SMP) or highly complex CNC polishing machines [30]. This makes the off-axis mirror segment very costly. Whereas, segments of the spherical primary mirror are identical and can be manufactured using conventional tools. The spherical mirror segments will reduce the manufacturing cost and complexity but will increase the toll on aberration correction. For the PSMT, we have decided to have the primary mirror as spherical.

In order to reduce the wind-induced structural stability issues, the D-space i.e., distance between primary and secondary mirrors, should be kept minimum, preferably less than two times the diameter of the primary [8]. The secondary size is another constraint that should be chosen considering the Alignment and Phasing system, which is an integral part of any segment telescope for its operation. We have planned to have Keck type phasing system, which requires light from the primary mirror to be sampled from the inter-segment region. Therefore, this requirement leads to a design constraint that the secondary mirror's size should be smaller than the central segment's size. Though the primary objective of PSMT is a technology demonstration, however, 1 m size telescope installed at a good site can also be utilized to undertake a few dedicated science observations. The PSMT is intended to be used for both spectroscopic observations of the point source and photometry of the extended fields. Having a decent image quality over a relatively large field will be advantageous to meet the science related requirements. Few important top-level design requirement for the PSMT optics is given in the Table 2.2

Table 2.1: Table showing the top level requirements of the PSMT optics

	Parameters	**Values**
1	Effective Aperture	1.0-1.5m
2	Telescope F/n	F/8-F/12
3	Primary mirror optics	Spherical
4	Segment shape	Regular hexagonal
5	Plate Scale	0.010-0.015 arc-sec/μm
6	Field of view	10 arc-minutes or more
7	On-axis image quality	<0.5”
8	Off-axis image quality (10 arc-minutes)	<1.3 arc-sec
9	Focus	Dual Nasmyth
10	D-space	less than 2 times of the telescope aperture
11	Back focal length	600-900 mm after primary mirror

2.3 Review on Telescope Optics Design

The most preferred optical design for any moderate to large telescope is Ritchey Chretien(RC). In RC design, both primary and secondary mirrors are hyperbolic in shape. If the primary is made of monolithic mirror, then there exist 360 degree rotational symmetry, and conventional grinding polishing techniques can handle manufacturing of a large hyperbolic mirror. Subaru, Gemini, and VLT telescopes are few examples of large telescopes made of a monolithic primary mirror with the RC design. However, in the segmented primary, except the central segment, each mirror segment acts like an off-axis mirror, i.e., no more rotational symmetry. Making off-axis mirrors segment with different asphericity requires a complex manufacturing process and the tool, like the Stress Mirror Polishing (SMP) technique [30]. The twin Keck and GTC are only segmented mirror telescopes that use RC optics.

One of the solutions to overcome difficulties of making off-axis mirror segments is to use spherical primary in place of hyperbolic. All the mirror segments of spherical primary mirrors are identical in shape and have the same radius of curvature. Making such a mirror segment is easy and can be done using conventional mirror grinding/polishing techniques. The fabrication process becomes faster due to the use of a full-size polishing tool, which rapidly removes the material. Few large segmented mirror telescope-like HET, SALT, and LAMOST use spherical mirror segments. Since spherical mirrors are subjected to extremely large spherical aberration, therefore, for acceptable image quality, it requires some aberration correcting mechanism. Both HET and SALT telescopes use few reflecting optics located close to the prime focus, named as a SAC (Spherical Aberration Corrector) [34] [35]. The most significant limitation of this design is that it has only a prime focus, which is not suitable for many science programs where large instruments weighing up to several tons are required. Such bulky instruments are usually placed in Cassegrain and/or Nasmyth focus. There are few efforts made to explore alternate designs which not only uses a spherical primary mirror but provide an option to have Nasmyth/Cassegrain focus[37] [38] [39] .

Other options to correct spherical aberration is the use of full-aperture refrac-

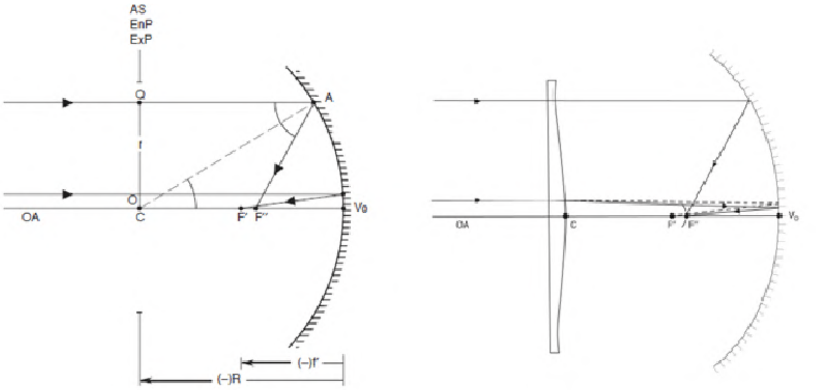

Figure 2.1: Spherical aberration in spherical mirror(left) and use of Schmidt correcting plate (right).

tive correcting plate/lenses. The one very popular design is Schmidt optics, in which a correcting plate is placed at the ROC of the primary mirror (see Figure 2.1). The Schmidt telescope's optical design is well known to provide excellent images over a large field of view and widely used in small telescopes. However, it simply can not be scaled-up in a large telescope because it is highly impractical to hold a large refractive Schmidt correcting lens that will deform by its own weight. Another full aperture correcting optics proposed by Maksutov in 1944 uses a negative meniscus lens. This optical design, which has got many variants, also suffers from Schmidt telescope's same problem. Instead of using refractive correcting optics that can not be made larger, it is possible to use a reflective Schmidt corrector plate. The 5 m class LAMOST telescope is developed with this approach [48]. This design's primary limitations are that it leads to a telescope configuration that is not fully steerable and the size of the telescope pupil becomes variable. To overcome gravity induced distortion found in Schmidt and Maksutov, several designs are proposed in which sub-aperture correcting lenses are placed immediately after the secondary mirror. Field-Maksutov, Klevtsov, Celestron HDEdge, and New-Wise are a few examples of optics design based on the sub-aperture correction. Telescope based on sub-aperture correction is not very popular, and the main reason appears that the fabrication and alignment tolerances are significantly more stringent. For the PSMT, we explored many design options in which a spherical primary mirror can be used, and finally, we ended up with our design. The next section describes our effort carried out in this regard.

2.4 The Design Options

As briefly discussed in the previous section, there are many ways to handle telescope optics design with spherical primary. Few of these designs are found to be suitable for smaller telescopes, whereas others are found to be best suited for large aperture telescopes. Considering our top-level design requirement for the PSMT, which is about a meter size telescope, we first explored all potential optical designs. While working on optical design, we considered the primary mirror is monolithic and also circular. Then after telescope optics has been designed in the Zemax and on and off-axis image qualities characterized in terms of RMS spot radius and encircled energies are derived. Though we explored many design options, results related to only five design options are presented here. The optical layout of the these designs are given in the Figure 2.2, whereas, Table 2.2 provides the summary of the image qualities. A brief description of these designs are given below:

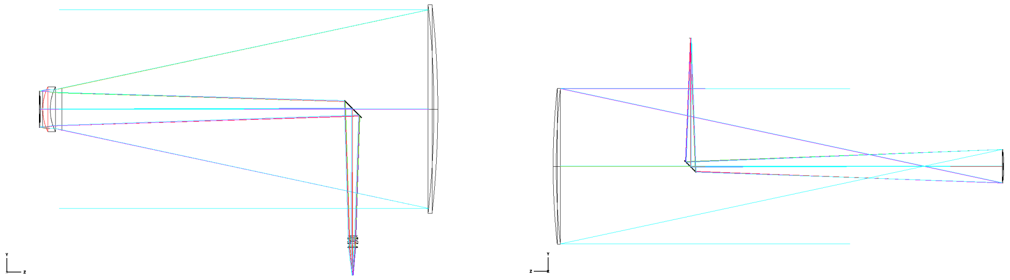

(a) Modified field Maksutov design **(b)** Gregorian Design

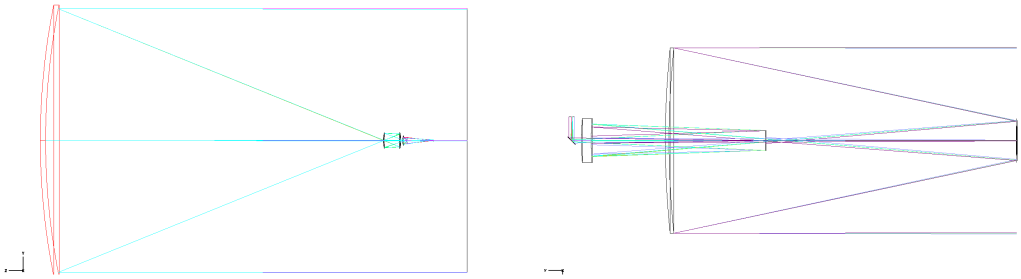

(c) SALT Design **(d)** Four mirror Design

Figure 2.2: Optical layout for various design options

2.4.1 Modified Field Maksutov

The Maksutov is one of the popular designs for a small telescope in which a spherical mirror is used as primary. Likewise, Schmidt design a full-size negative lens is placed at the entrance pupil of the telescope. There are many variant designs of the Maksutov, and one of the designs uses a sub-aperture correcting lens just after the secondary mirror.[9] We tried to explore this design for the PSMT and our optical layout is shown in the Figure 2.2 (a). A positive meniscus lens is placed in front of spherical secondary mirror, which corrects spherical aberration and coma, but introducing chromatic aberration on the wavelength range we require. This needs to be corrected out further with added corrector lenses kept just before the focus. The best on-axis image quality (D50 and D80), which we could achieve for this design are 1.86“ and 2.88“, which is not at all acceptable for the PSMT. The off-axis image quality degrades further. Due to the F-number constraint of the primary and secondary, the system inherently has limitations on the aberration correction. The advantage of this design is that all the components are spherical and hence easy to manufacture. However, there are a number of problems with the modified Maksutov design. The meniscus lens is found to quite large (about 300mm) and very sensitive to alignment error. The large size lens is also subjected to gravity-induced deformations. The radius of curvature of the lens is found to very sensitive as it corrects the most of the aberrations. After noticing all these problems at the beginning of the design, we did not attempt to optimize the design further.

2.4.2 The Gregorian Design

The classical Gregorian telescope optics uses parabolic primary and ellipsoid secondary. Both secondary and primary are concave, and the secondary is placed after the primary's focal plane. Secondary being concave, manufacturing, and testing becomes easier. In our case, the primary mirror is spherical; therefore, instead of ellipsoidal, a hyperbolic secondary with conic constant -3.2724 is used. There are two focal planes in a Gregorian design, the primary forms the first one, and it lies in between the primary and the secondary. This intermediate focal plane is very suitable for either a field stop and/or small corrective optics to achieve a large aberration-free field. Just two mirror Gregorian designs without any corrective lens give almost acceptable on-axis image quality (see the Table2.2), which is acceptable for the PSMT as a technology demonstrator. The major disadvantage of this design is that the separation between primary and secondary is vast it requires 3.8 m tube length. The large tube/truss lead to gravity-induced flexure as well as the problem of wind induces disturbances. Also, the off-axis image quality degrades much faster than any other design explored.

2.4.3 Scaled down SALT Design

HET and SALT are two large telescopes built around the spherical primary mirror. The huge spherical aberration induced by the primary mirror is corrected by using four element all reflective mirror systems placed near the prime focus.[35] We have explored the possibility of using the optical design of the SALT to one-meter size PSMT telescope. We used a similar configuration as SALT, scaled-down all the parameters for 11 m SALT to 1.3 m PSMT, after Zemax is used to optimize the design further. The SALT design gives excellent performance and provides diffraction limited performances for both on and off-axis. The image quality of the PSMT-SALT design is much better than the SALT telescope design itself, which appears degraded primarily due to large aperture primary. Although SALT design offers the best image quality, we have not considered this design for the PSMT. The primary reason are: (1) elements of SAC are found to be very sensitive to alignment error, (2) one of the mirrors which is high order aspheric, turns out very small and hence manufacturing of this mirror which is indeed a challenge and (3) keeping multiple instruments at the prime focus along with de-rotator and focus/tip/tilt mechanism was complicated.

2.4.4 Four Mirror Design

One of the very promising designs which we explored is the four mirror design. The optical layout is shown in the Figure 2.2(d). In this design, primary, secondary, and one more mirror M1 are all spherical and very easy to manufacture. Whereas, the fourth mirror (M2) is 6th order aspheric. This design is a modification of 4 mirror anastigmatic designs proposed by [10],[11]. It provides excellent image quality all over the field up 10 arc-minutes and meets most of the design requirements. Despite providing very excellent image quality over large field of view, we did not select four mirror design because of following reasons. We found that M2 is extremely alignment sensitive from the tolerance analyses and may require an active lookup table-based gravity-induced flexure compensation mechanism. Secondly, it provides only Cassegrain focus and hence requires a large hole on the central mirror, making the central mirror fragile. We also found that the four mirror design creates vignetting, which becomes severe after four arc-minute radii.

Table 2.2: Summery of the imaging performances of different optical designs considered for the PSMT in arcsec diameter of Encircled energy.

Design Option	On axis		20“		40“		60“		120“		240“	
	50%	80%	50%	80%	50%	80%	50%	80%	50%	80%	50%	80%
Modified Maksutov	1.86	2.88	1.86	2.91	1.86	2.93	1.89	2.99	2.03	3.22	2.54	4.00
Gregorian design	0.99	1.36	0.96	1.52	1.10	1.92	1.40	2.43	2.50	4.07	4.85	7.49
Scaled down SALT	0.12	0.21	0.12	0.21	0.12	0.21	0.12	0.21	0.12	0.22	0.12	0.24
Four mirror design	0.10	0.20	0.10	0.20	0.10	0.20	0.10	0.20	0.10	0.20	0.10	0.20
PSMT two mirror	0.36	0.51	0.41	0.71	0.62	1.02	0.88	1.39	1.70	2.57	3.36	4.93

2.5 The PSMT Optics with Two Mirror Design

We explored many optical designs for the PSMT in which primary can be made of a spherical mirror. Not all but few potential designs options are briefly described in the previous section. After preliminary design studies, because of one or other reasons, we did not pursue them further. We searched for simple RC kinds of two mirror design, which primarily correct the spherical aberration for the on-axis imaging so that the telescope can be used at least for the technology demonstration. In our exploration, we found that if we use an oblate ellipsoid secondary along with a spherical primary mirror, then it provides near diffraction-limited image quality for the on-axis. This optical configuration is like a modified inverse of Dall-Kirkham in which primary is elliptical, and secondary is spherical. After getting acceptable on-axis image quality, we chose this design is a baseline design for the PSMT and carried out extensive design optimization and analysis work. The design optimization has been first carried out considering the primary mirror as a monolithic, and then after keeping all the other design parameters the same, the primary mirror is replaced by the segmented mirror.

2.5.1 The PSMT Optics Design With Monolithic Primary

The first round of the optics design optimization has been carried out considering primary is a monolithic mirror. The primary is derived considering each segment is regular hexagonal in the shape and length of its all six sides are the same and equal to 250 mm. Such a hexagonal segment can be created by cutting sides of a 500 mm roundel shape spherical mirror. We need a minimum of seven identical segments to create a segmented primary in which one segment will be placed at the center, and six will be in the first ring. All the gaps between mirror segments are uniform and considered to be 5 mm. The six segments in the periphery need to be tilted and pistoned so that all seven segments form a large spherical primary mirror of an effective aperture of 1333 mm. While designing the PSMT optics with a monolithic primary, we have considered its aperture 1333 mm. The figure.2.3 shows the segmentation projection view from top, which in turn used to get the design Entrance pupil diameter for the monolithic telescope.

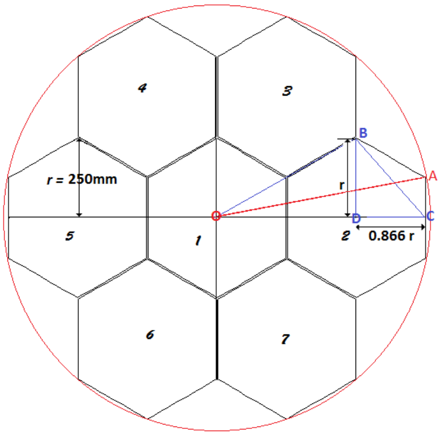

Figure 2.3: The segmentation procedure to find the total monolithic aperture size (OA= 666.348 mm, the selected physical radius of the monolithic telescope, including a 5 mm inter-segment gap).

The initial size of the secondary is chosen, keeping the phasing related requirement into consideration. We need to have a secondary that should cast a shadow smaller than one segment and leaves about 10 mm intersegment region. This requirement leads to the constraint on the secondary's size, not allowed to be larger than 300-350 mm. Since PSMT is a small segmented telescope, so there is not much scope to accommodate Cassegrain focus. Therefore we decided to have two Nasmyth focus, one for the science instrument and another to host Alignment and Phasing Device. The dual Nasmyth focus requires a flat tertiary mirror mounted on the rotating platform. Considering the telescope's opto-mechanical arrangement and the instrument, we wanted to have back length of the telescope (the distance from the edge of the primary mirror) somewhere 600-900 mm.

The distance between primary and the secondary (D-space) is primarily decided by focal lengths and hence radius of the curvature(ROC) of the primary as well as the secondary. In the two-mirror system, the D-space is one of the important parameters which govern various primary aberrations of the telescope. The larger D-space and hence tube length, on the one hand, helps to reduce the optical aberration of the telescope; however, on the other hand, it introduces higher tube flexure due to gravity as well as the problem of increased wind shake. Therefore, before initiating the Zemax based design optimization, we analytically explored efftct of ROC, and tube length on image quality. For this, we used aberration formula given by Wilson for the two mirror telescopes[44]. From this analytical study, we finally decided to have initial values for the D-space of 2400 mm, primary and secondary focal lengths 3100 mm and 850 mm, respectively.

In our two-mirror design the secondary mirror is convex and oblate ellipsoidal in shape. Again using the prescription given by the Wilson[44], we compute the possible conic constant for the PSMT secondary mirror.

$$(b_{s2})_{SP} = \frac{f'}{L}\Big(\frac{m2}{m2+1}\Big)^3 - \Big(\frac{m2-1}{m2+1}\Big)^2 \tag{2.1}$$

$$f' = D1 * Fno = 1333 * 10.7 = 14263.1mm = 14.2m \tag{2.2}$$

$$f1 = 3175mm \tag{2.3}$$

and

$$m2 = \frac{f'}{f1'} = \frac{14263.1}{-3175} = -4.4923 \tag{2.4}$$

$$L = f' - m2d1 = 14263.1 - 4.4923 * 2483 = 3108.6819mm \tag{2.5}$$

$$(b_{s2})_{SP} = \frac{14263.1}{3108.6819}\Big(\frac{-4.4923}{-4.4923+1}\Big)^3 - \Big(\frac{-4.4923-1}{-4.4923+1}\Big)^2 = 7.292 \tag{2.6}$$

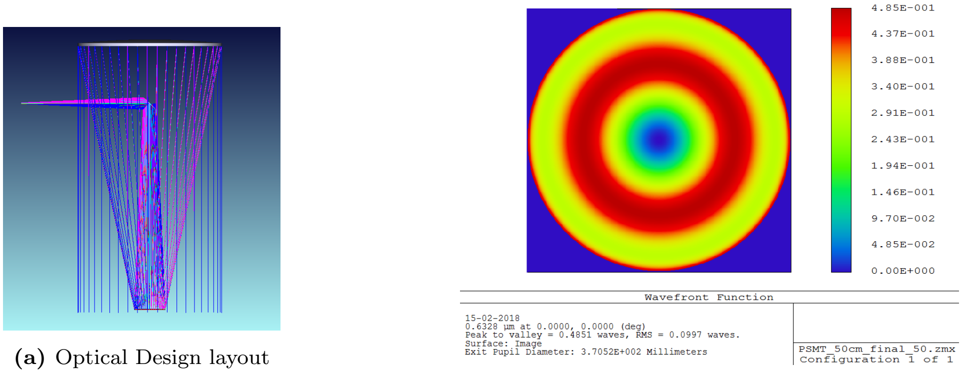

```
15-02-2018
0.6328 µm at 0.0000, 0.0000 (deg)
Peak to valley = 0.4851 waves, RMS = 0.0997 waves.
Surface: Image
Exit Pupil Diameter: 3.7052E+002 Millimeters
PSMT_50cm_final_50.zmx
Configuration 1 of 1
```

(a) Optical Design layout

(b) On-axis wavefront

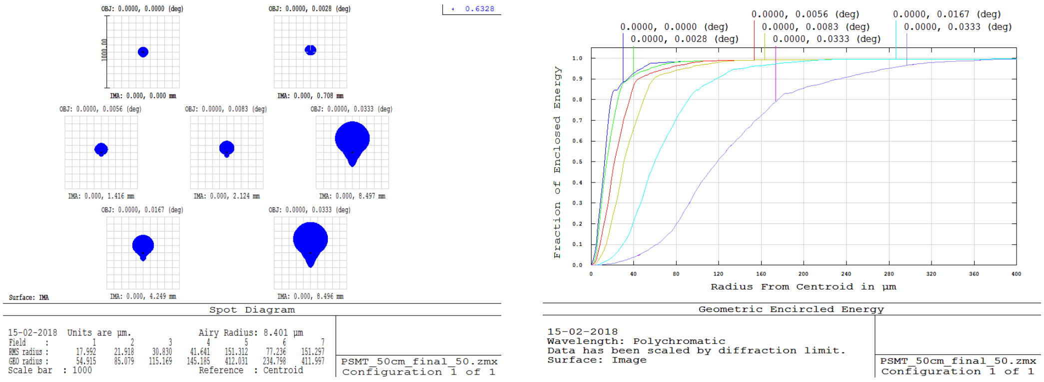

```
15-02-2018  Units are µm.              Airy Radius: 8.401 µm
Field      :       1        2        3        4        5        6        7
RMS radius :  17.992   21.918   30.830   41.641  151.312   77.236  151.297
GEO radius :  54.915   85.079  115.169  145.185  412.031  234.798  411.997
Scale bar  : 1000                   Reference  : Centroid
PSMT_50cm_final_50.zmx
Configuration 1 of 1
```

```
15-02-2018
Wavelength: Polychromatic
Data has been scaled by diffraction limit.
Surface: Image
PSMT_50cm_final_50.zmx
Configuration 1 of 1
```

(c) The spot diagrams for different fields

(d) Encircled Energy plot

Figure 2.4: The optical design of the PSMT with monolithic primary mirror.

Table 2.3: PSMT Monolithic Design values summery

Parameter	Values
Diameter of Entrance pupil	1333mm.
Primary ROC	6350.71mm
Primary F no	2.38
Secondary ROC	1777.385mm
Secondary size	300
Secondary sag	6.429
Secondary F No	F/4.58
Secondary Conic	7.518724
Tertiary Size	216 (major axis)
Plate scale	0.014 arcsec/μm
D-Space	2484mm
Distance between primary and Tertiary	675mm
The back-focal length (Distance between edge of primary to the focal plane)	635mm

Once having all the required initial parameters, we have carried out the design optimization using the sequential mode of the Zemax. The design optimization was carried for the on-axis and various off-axis fields hence weights were given accordingly. The spot diagrams and EE plots show that the on-axis image quality can be as good as 0.35 arcsec (D50), and 90% can reside within an arcsec. Figure 2.4b show the on-axis pupil wavefront at the focus. For the on-axis, the ellipsoid secondary has reduced spherical aberration to the extent of Lambda/10 RMS wavefront error, which is very good and usually targeted by any research-grade optical telescope. However, when we move out, the off-axis image quality degrades rapidly. The image quality up to 60 arcsec FoV appears to be sub arcsec and comparable to the local seeing. Beyond one arc-minute FoV, the telescope image quality degrades to the extent that it may not be so useful for any science observation. Since the two mirror optics meets the image quality requirement of the PSMT as narrow-field telescope. Therefore, we accepted this design and moved to the next level in which further design optimization has been carried out, considering primary as a segmented mirror.

2.6 The Segmented Design

While carrying out design optimization, we kept all other telescope design parameters the same as the monolithic design optimization process described in the previous section. The only change we have done is that the monolithic primary mirror, which is also circular in aperture, is replaced with the segments primarily made of seven identical mirror segments. The gaps between segments are kept 5 mm, which also includes the beveling of the segment edges. The XY tilt and the piston (sag) required to create a segmented primary is given in Table 2.4.We calculate each segment's center using the approach that all the segments look regular hexagons in the projection when we look from the top. This is a usual practice in almost all the segment telescope design. In a real optical segment system, this will create an elongation in the segments as we go to the outer rings, but in the case of PSMT, as it is a small one-ring telescope, we can potentially ignore this elongation.

Once a segmented primary mirror is created, then design optimization can be carried out in many ways. For example, we can use sequential system, non-sequential system and sequential-non sequential Mixed mode system. In all these design modes, we can make use of a user-defined aperture (UDA) file used by

Table 2.4: calculated Sag, X position, Y position, Tilt about X,Y axis

Segment No	Sag in mm	X position in mm	Y position in mm	X tilt in degree	Y tilt in degree
1	0	0	0	0	0
2	15.123013	219.0063509	0	0	3.9595881
3	15.123013	438.0127019	-252.8867514	-3.4284206	1.9786118
4	15.123013	-438.0127019	-252.8867514	-3.4284206	-1.9786118
5	15.123013	-219.0063509	0	0	-3.9595881
6	15.123013	-438.0127019	252.8867514	3.4284206	-1.9786118
7	15.123013	438.0127019	252.8867514	3.4284206	1.9786118

ZEMAX. ZEMAX considers a UDA aperture as a surface projected from the aperture's vertex tangent plane into the optical base surface. As PSMT has a spherical primary, the UDA file can be created in both local and global coordinate systems. If it is created in a global coordinate system, users have to enter the radius and conic constant and other surface defining quantities to get the desired segment shape. Creating the segment UDA file in the global coordinate system is more convenient when designing aspheric or complex primary segments. For the spherical primary, the design can be better created in the local coordinate system using the same segment UDA file for all the segments. Additional information needed is the segment, X, Y, Z position and rotation about X, Y, and Z axes. If the segments are subjected to any manufacturing error, then mirror deformation for each segment can also be given in Zernike coefficients. We have briefly explained these approaches here; however, some more details may be found in the Appendix A.2.2.

2.6.0.1 PSMT Design with the Segmented Primary

Once the segmented primary mirror is created using the procedure described in the previous section then after all other telescope design parameters are taken from the monolithic design as given in the Table 2.3 and used as starting values for the design. Few parameters, such as ROC of the primary, ROC of secondary, and its conic constant, back focal length, are kept constant during the optimization run. Whereas the Dspace (secondary focus) is used as a compensator. In the segmented primary design we get additional parameters such as segment tilt and

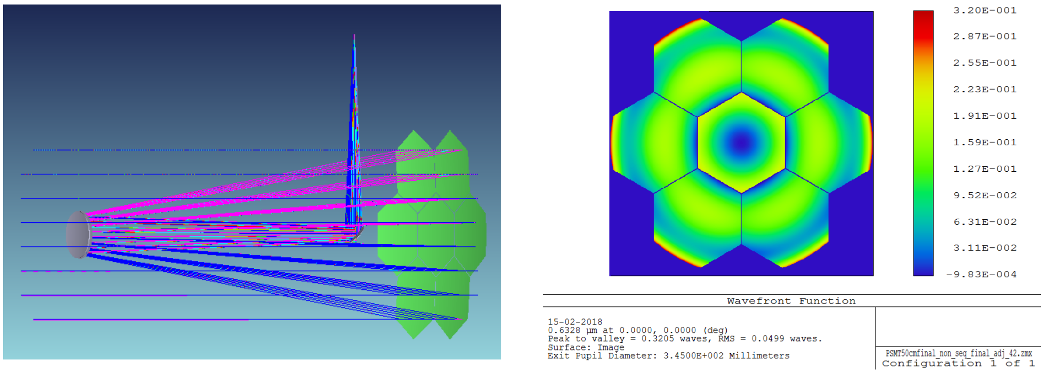

```
15-02-2018
0.6328 µm at 0.0000, 0.0000 (deg)
Peak to valley = 0.3205 waves, RMS = 0.0499 waves.
Surface: Image
Exit Pupil Diameter: 3.4500E+002 Millimeters
```

(a) Segmented Design layout

(b) Segmented wavefront

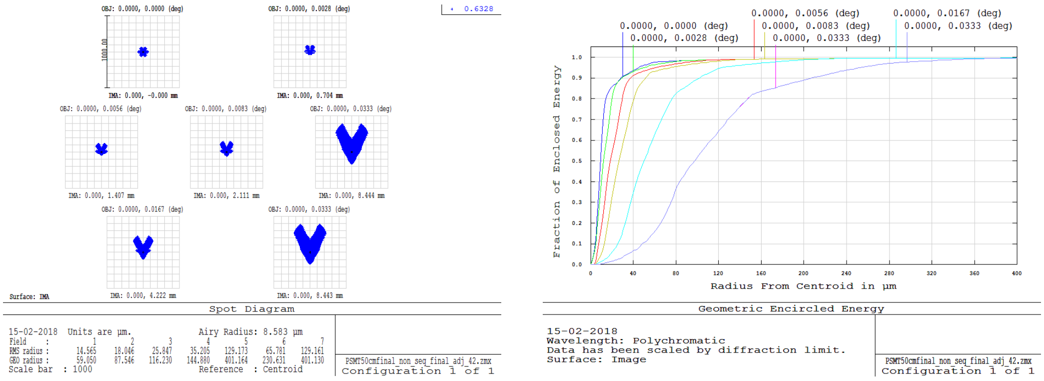

```
15-02-2018  Units are µm.                Airy Radius: 8.583 µm
Field      :       1        2        3        4        5        6        7
RMS radius :  14.565   18.046   25.847   35.205  129.173   65.781  129.161
GEO radius :  59.050   87.546  116.230  144.880  401.164  230.631  401.130
Scale bar  : 1000                         Reference  : Centroid
```

```
15-02-2018
Wavelength: Polychromatic
Data has been scaled by diffraction limit.
Surface: Image
```

(c) Segmented spot diagram

(d) Segmented Encircled Energy

Figure 2.5: Design with Segmented Primary(in Sequential non-sequential mixed mode)

Table 2.5: The Image quality difference in encircled energy(EE) between monolithic and segmented telescope given as arcsec diameter.

Percentage of GEE	On axis diameter	20" diameter	40" diameter	60" diameter	120" diameter	240" diameter
50% Monolithic	0.356	0.413	0.616	0.883	1.700	3.360
50% Segmented	0.264	0.343	0.528	0.749	1.420	2.750
68% Monolithic	0.441	0.571	0.826	1.150	2.150	4.240
68% Segmented	0.329	0.488	0.721	0.993	1.830	3.580
80% Monolithic	0.515	0.707	1.020	1.390	2.570	4.920
80% Segmented	0.426	0.568	0.851	1.160	2.190	4.200
90% Monolithic	0.990	1.050	1.300	1.650	3.280	6.560
90% Segmented	0.809	0.851	1.060	1.460	2.890	5.900

the piston for the optimization. The optimization can be done for the wavefront or RMS spot size. As a first step, we run the local optimization and then run the global optimization. Figure 2.5 shows the optical layout, spot diagrams, EE plot as well as on-axis wavefront at the focal plane. When comparing performances of the segmented design over monolithic one (see Table 2.5), we can find appreciable improvement in the image quality of the segmented telescope. The on-axis image quality improves from $0.35''$ to $0.26''$ and off-axis image of one arc-minutes FoV changes from $0.88''$ to $0.74''$. Similarly, the on-axis pupil RMS wavefront error, which is 0.0997 wave in monolithic, becomes almost half (0.0499 waves) . The improvement of the image quality of the segmented mirror over monolithic can be explained in two ways. The first reason is that the marginal rays (rays from the edge of the aperture) that contribute a significant fraction in the spherical aberration get cut down by segmented primary whose overall shape is hexagonal. Another reason seems to be the flexibility of segmented primary to individually tilt and piston all the mirror segments. This feature allows for correcting some of the aberrations, making the spherical primary behave like a slightly aspheric primary mirror.

2.7 Exploring Various Optimization Options

Even after achieving the required image quality with segmented primary mirror optimized with the sequential-non sequential mixed-mode, we decided to explore all possible optimization methods and compare the results. These options are summarised in the Table 2.6. For the comparison, the design with monolithic primary optimized in sequential mode is also given as the first option. Other six options are generated based on design modes (sequential or mixed), Pupil integration methods (Gaussian or rectangular), and segment piston and tip/tilt are fixed or variable. Options two and four really are not a segmented mirror in the true sense, but the monolithic primary mirror is virtually divided into segmented using the UDA. This design optimization option is different from the monolithic in the sense that it makes the primary mirror a seven hexagonal segmented shape as a whole, and the effect of the gap is also taken into account.

Zemax optical design software, which works on the ray-tracing principle, uses two different pupil integration methods, the Gaussian quadrature and the rectangular array. The Gaussian quadrature numerical method calculates integrals as a weighted sum at just a few carefully chosen points. Using any one of the above pupil integration methods, the optimization can be carried out using very few rays and hence saving computation time, which is very much needed for a complex de-

Table 2.6: Different optimization options explored for the PSMT optics design.

Optimization Technique No	Sequential mode	Mixed mode	Segmented Primary	Pupil Int Gaussian Quadrature	Pupil Int Rectangular Array	Segment P,T,T
1	✓			✓		
2	✓		✓	✓		
3		✓	✓	✓		
4	✓		✓		✓	
5		✓	✓		✓	
6		✓	✓		✓	✓
7		✓	✓	✓	✓	✓

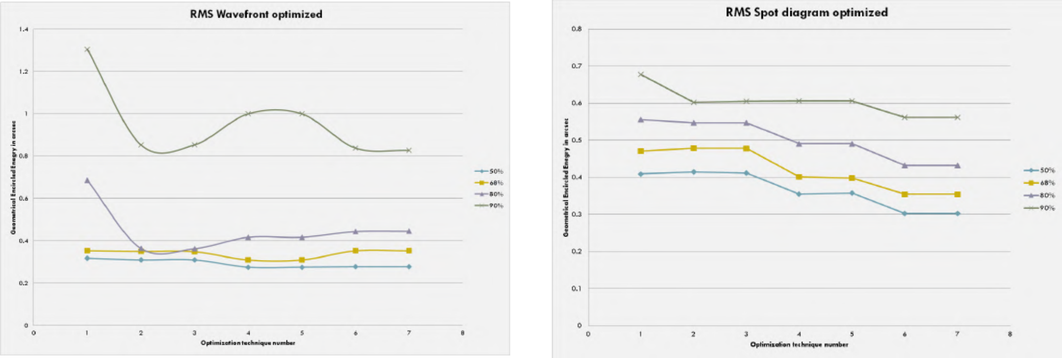

(a) Wavefront optimization plots

(b) RMS spot optimization plots

Figure 2.6: On axis image quality of the PSMT with various optimization options

sign optimization task such as telescope with the segmented primary. The results of the image qualities (D50, D68, D80 and D90) obtained for all seven options are shown in Figure2.6. The optimization has been carried out for the RMS wavefront error as well as the RMS spot radius. In the wavefront optimization, the energy concentration to the core of the PSF is more prominent than the wings and that's why D90 is much larger than D50 and/or D80. Due to this reason, wavefront optimization is preferred while carrying out design optimization for high-resolution observational requirements. In optimizing for RMS spot size, we can see a gradual improvement in the image quality from the Monolithic primary mirror to the segmented one with tip/tilt and piston variable. In both cases, it has been noticed that the pupil integration method the Rectangular array is the best approach for the segmented primary mirror.

2.8 Tolerance Analysis and Error Budget

Once the telescope design has been completed, then after the next task is to identify the sensitive parameters in the design, find the tolerances, and estimate the error budget, predicting how the system will perform when it is realized. We have developed few tools on the python - Zemax dynamic data exchange(DDE) platform to carry out the tolerance and error analysis in a generic way.

2.8.1 Tolerance Analysis

Since PSMT is designed as a seeing limited telescope, suppose to be installed at Hanle where median seeing is about 1.2 arc-sec; therefore, for the tolerance analysis, on-axis system performance for D80 (diameter of the 80% of Geometrical EE) is allowed to degrade up to 1 arc-sec. The tolerance parameters can be classified into two groups, manufacturing and alignment. Some of the important design parameters which we have considered for the tolerance study are given below.

2.8.1.1 Manufacturing related tolerances

Telescope optics, which mainly comprises primary, secondary and tertiary mirrors, requires many months and years of effort to manufacture them. Even though great care is taken while manufacturing the telescope optics, they are subjected to errors of different kinds. Prior to use, it is good to understand the effect of these errors and, if possible, reduce the manufacturing error and/or look for some compensator. For the PSMT tolerating study, the following parameters linked with the optic's manufacturing have been considered.

1. Primary surface irregularity
2. Primary Segments radius of curvature, global and local
3. Secondary surface irregularity
4. Secondary Radius of curvature - manufacturing
5. Secondary conic constant

6. Tertiary surface error in fringes (tertiary is a plane mirror)
7. Tertiary surface irregularity

2.8.1.2 Alignment related tolerances

Even if optics are manufactured precisely, when installed in mechanical support/mount, they go through some kind of miss-alignment, which is usually static in nature. However, due to variable gravity and the temperature, telescope optics goes through dynamic miss-alignment. The effect of both static and dynamic alignment error on telescope performance need to be also explored and corrected. The alignment error which we have considered in our tolerance study are:

1. Primary segments X, Y tilt
2. Primary segment piston
3. Secondary X,Y tilt
4. Secondary X,Y de-center
5. Tertiary X,Y tilt
6. Tertiary X,Y de-center
7. Focus and de-space change

Tolerance analysis of a monolithic telescope using a ray-tracing software like ZEMAX is a well-established procedure. However, when it comes to segmented design, then it is a bit unexplored field. The tolerance parameters in ZEMAX are defied in the tolerance data editor. We can choose Normal statistical distribution or truncated Gaussian distribution for the design parameters subjected to the tolerance study. The figure error is introduced to the system with the Python-based segmentation code through Python-Zemax DDE. Unlike the monolithic mirror, the segment, if not made from the same batch of the material, can have different CTE. Therefore in our analysis, we have also kept CTE difference, reflecting in ROC changes as one tolerance parameter. The segment CTE variation induced radius of curvature changes is calculated with the thermal deformation equation's help. The tolerance analysis in the Zemax is based on Montecarlo simulations, in which random distribution of each parameter's values is generated within the given tolerance range. While carrying out tolerance analysis, one can provide one or more compensators that try to nullify the various errors. While tolerancing, the compensator acts like a variable. Most often, in telescope design analysis, the focus is taken as a compensator.

Other than surface figure error, all other parameters are set within in allowable error limit, and the Montecarlo runs are carried out. At the end of the Montecarlo run, we identified the sensitive parameters and tightened them if required, and then repeated the process until system performance is reached. If the system is within the allowable degradation, then the range is selected as tolerance for that parameter. The tolerance for the primary figure is carried out at last. Once the tolerance analysis gets completed, we come up with a tolerance sensitivity table that ranks all the parameters in terms of their sensitivity. The worst offender (the parameter that contributes highest in the performance degradation) is ranked first, then after the next offender, and so on. The table 2.7 gives the sensitivity of the parameters considered in the PSMT tolerancing study. From the table, the figure error of the primary is the most sensitive parameter and contributes the highest in image degradation. Segment tilt and ROC errors occupy second and third place in the sensitivity table. After that, the next ranks are somewhere linked with secondary focus or alignment errors. As expected, the least sensitive parameters are linked with the tertiary alignment.

2.8.2 The Error Budget

Once the tolerance study is completed, we have a reasonably good idea about how these parameters will vary over the analysis range. The next task is estimating the possible image degradation (error) the telescope will have when it is realized. The steps are pointed out below,

- Generate a set of ZEMAX files providing the error within the parameter range decided by tolerance analysis. The error is estimated for the only parameter, keeping all other parameters as per optimized design.

Table 2.7: Tolerance and Sensitivity ranking

Ranking	Error	Value
1	Primary surface irregularity	$\lambda/20$ rms
2	X,Y tilt of Primary segments	± 0.1 arcsec
3	Segment roc	± 0.1mm
4	Defocus	±0.01
5	Segment support	20 Zernikes fitted
6	Y de-center of secondary	±0.1mm
7	X de-center of secondary	± 0.1mm
8	Secondary X tilt	±18 arcsec
9	Secondary Y tilt	± 18arsec
10	Secondary fabrication	$\lambda/20$ rms
11	Blank CTE variation of Segments	±0.05PPM/Degree C
12	Tertiary fabrication	±0.8 fringes
13	Secondary Roc	± 4mm
14	Primary Global roc	± 6mm
15	tertiary conic	±0.001
16	Piston of Segments	± 25nm
17	Y Tilt of tertiary	±12 arcmin
18	y De-center of tertiary	0.2mm
19	X De-center of tertiary	0.2mm
20	X de-center of tertiary	-0.2mm
21	Y De-center of tertiary	-0.2mm
22	X tilt of tertiary	±12 arcmin

- Retrieving Geometrical encircled energies(GEE) (50,68,80,90 %) from each file and convert it into arcsec using the plate scale.

- Find EE for the best and worst cases, and then after computing the EE difference with respect to the ideal case using the quadrature subtraction formula ($E_{error}=\sqrt{E_{total}^2 - E_{ideal}^2}$). These are the extreme errors caused by any parameters which vary over the tolerance range.

- Since the Montecarlo simulation parameters are created as a normal distribution over the tolerance range; the worst performance case scenario may be the most pessimistic combination of all the errors. Therefore, while deriving the realistic error, the mean value of the best and worst performance is computed and set it as the error value to be used in the error budget for that particular parameter.

Since the error needs to be estimated for many parameters following the above procedure, which is very labor-intensive, a python-based tool has been developed.

The errors are estimated for all possible EE, however in the tables 2.8 to 2.10, we give only D 50%, and D 80%, which are two widely used quantity to judge the image quality of the telescope. The D50 is equivalent to the full width at half maxima (FWHM) used by astronomers. In the primary mirror, the main contributor is figuring errors(Surface and support). Segment to segment small ROC error can be compensated by differently tilting and pistoning individual segments. However, in this process, we introduce a phase error which may not be crucial for the seeing limited PSMT telescope. For the secondary mirror, it is primarily an alignment error that causes image degradation. If we qudraturly add up all the error, including the basic design error, then D50 turns out to be 0.3 arc-sec and D80 0.97 arc-sec. We can conclude that the expected image quality for the on-axis is well within the design requirement.

Table 2.8: Primary Error Budget

Sl.NO	Source of Error	D-50 (arcsec)	D-80 (arcsec)
1	Primary surface figure error (31.64 to 33.3nm)	0.26	0.46
2	Segment ROC (Segment to segment difference)± 0.1mm	0.14	0.32
3	Segment alignment± 0.1arcsec	0.24	0.38
4	Segment piston ± 25nm	4.55E-6	3.36E-6
5	Primary global ROC ± 6mm	0.014	0.021
6	Segment support with 20 zernikes fitted	0.14	0.25
7	Segment CTE variation of ±0.05PPM/°C	0.07	0.18

One of the unexpected result which we found from our error analysis is that the surface irregularity (figuring error) of the primary mirror segment is the most dominant term and superseded to all other errors. In the case of the PSMT, we have no mechanism (such as warping harness), which can be used to compensate for the figuring error, except opting for very precise optics, which will escalate the cost of the project. Considering this, we decided to carry out an in-depth exploration of the effects on the image quality due to segment figuring error.

Table 2.9: Secondary & Tertiary Error Budget

Sl.NO	Source of Error	D-50 (arcsec)	D-80 (arcsec)
1	Secondary collimation De-centre ± 100micron, tilt± 18arcsec	0.13	0.22
2	Primary Secondary Separation of ± 10 micron	0.17	0.29
3	Secondary ROC(±4mm manufacturing)	0.021	0.047
4	Secondary Conic accuracy ± 0.001	0.004	0.006
5	Tertiary Collimation , De-Centre ± 200micron, tilt=± 12arcmin	9E-10	23E-9
6	Secondary Fabrication figuring error of $\lambda/20$ rms	0.11	0.18
7	Tertiary Fringe(ROC error)±0.8 fringes	0.06	0.18

Table 2.10: Full Telescope error budget

Sl.NO	Source of Error	D-50 (arcsec)	D-80 (arcsec)
1	Telescope optical design (design error)	0.266	0.45
2	Primary Mirror(including all)	0.41	0.74
3	Secondary and tertiary (manufacturing + collimation)	0.25	0.44
4	Focus of 10 micron	0.046	0.095

2.9 Exploring Effect of Segment figuring Error

From the tolerance analysis, we noticed that the primary mirror segment's figure error is one of the most sensitive parameters. Also, while investigating other segmented mirror telescopes such as TMT, we found that a huge allowance has been given to segment figure error [19]. This prompted us to explore the effect of the segment figuring error on the overall telescope performance in detail.

The figuring error present in the segment can be created using the Zernike polynomial, which can mimic figuring error spatially distributed over a wide frequency range. In the beginning, we used a random distribution of Zernike coefficients to represent figure error, which lead to the need for extremely high precision optics to achieve acceptable image quality. We soon realized that the Zernike coefficient's random selection does not represent the real mirror's figuring error. We need to use the weighted Zernike coefficients, where the weight should be derived by using metrological data of the fabricated mirrors. Using the data from our in-house mirror segment manufacturing effort for the PSMT and looking at other telescope mirror data, we came up with a weighing scheme that mimics the real figuring error. Figure 2.7 shows a distribution of the seven set of weighted Zernike coefficients used.

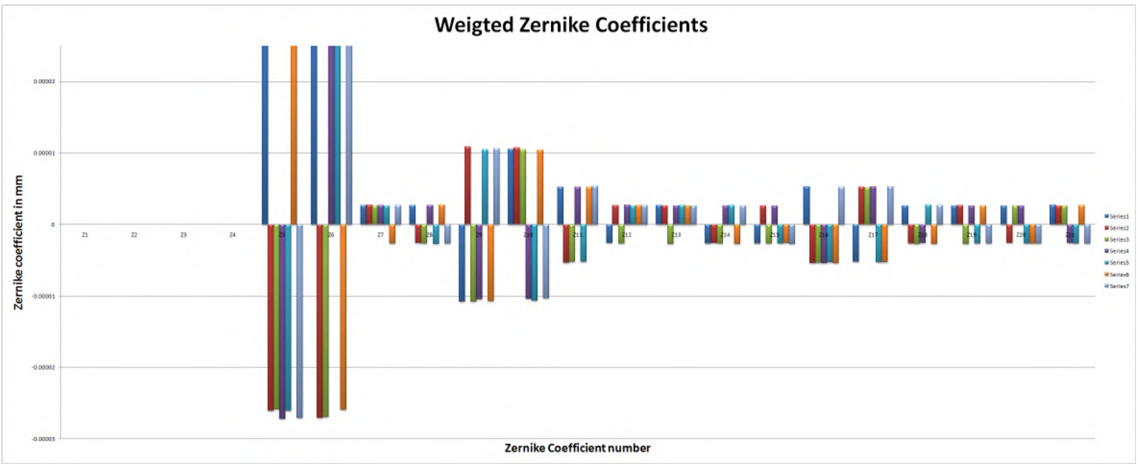

Figure 2.7: Distribution of weighted Zernike coefficients used to generate figuring error.

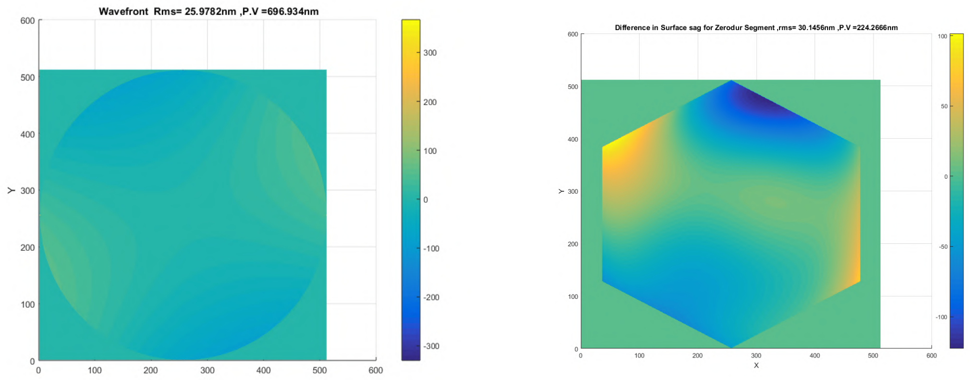

(a) Monolithic PSMT surface deformation for Zernike normalization radius of 666.5mm , rms=25.07nm

(b) Surface deformation over one segment for Non-weighted Zernike coefficients (top view), rms=31 nm

Figure 2.8: Creating figuring error in the circular primary and the hexagonal segment.

For the comparison, we first used primary as a monolithic mirror of 1333 mm diameter and then after figuring errors characterized by $\lambda/20$ - $\lambda/19$ (31.64-33.3 nm), RMS is injected into the surface of the primary mirror. In practical terms, the weighted Zernike coefficient values are scaled up in a way that it should provide required figuring errors. Then after when we estimated the image quality, we found that figuring error has degraded the image quality by 0.1“ (D50) and 0.107“ (D80). After that, the same procedure is applied to the segmented primary mirror i.e., figuring error of the same amount is injected to each hexagonal mirror segment. From the error estimation, we got that contribution of figuring error in the segmented case has increased almost three times (0.1" to 0.32"). This finding puzzles us, and a possible explanation seems to be a manifestation of low spatial frequency errors in each segments into an increased contribution by the mid spatial frequency of figuring errors when we consider the full aperture.

2.9.0.1 Analysis Using Aperture Edge Smoothing Function

When we carried out figuring analysis on segmented primary with weighted Zernike, we observed a noticeable difference in the figure's appearance at the segment's edges that form the primary mirror. We found that even though we specify the orientation of figure error and placement of the segments, a phase jump is seen between the segment edges, which would create an effect like a piston error. To overcome this problem, the need for edge smoothing was realized.

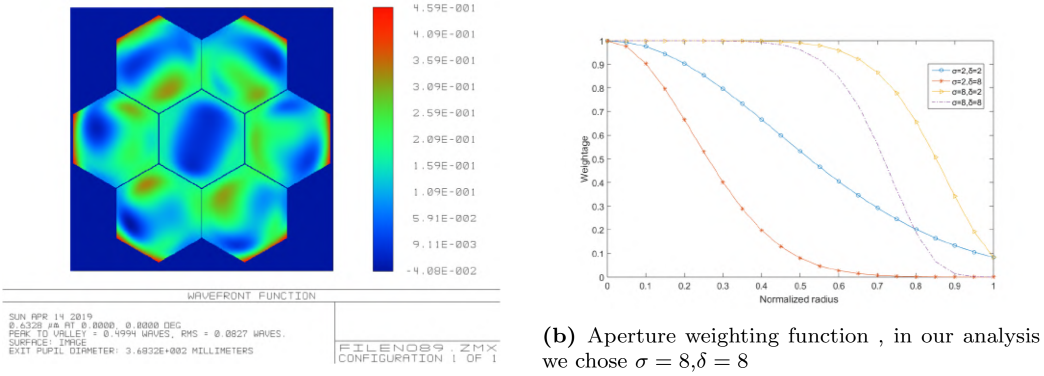

```
SUN APR 14 2019
0.6328 µm AT 0.0000, 0.0000 DEG
PEAK TO VALLEY = 0.4994 WAVES, RMS = 0.0827 WAVES.
SURFACE: IMAGE
EXIT PUPIL DIAMETER: 3.6832E+002 MILLIMETERS
```

(a) Segmented telescope wavefront

(b) Aperture weighting function , in our analysis we chose $\sigma = 8$,$\delta = 8$

Figure 2.9: Analysis with weighted Zernike with edge smoothing approach

The formula is given in the equation 2.7 can be used to create an aperture weighing function.

$$weightage = \left(\exp - \left((r^{\sigma}) \frac{(\frac{4}{pi}) + 0.14r^2}{1 + 0.14r^2} \right)^{\delta} \right) \tag{2.7}$$

By controlling σ and δ in the equation, we can create the required smoothing of the figure error at the edge of the segment. The figure2.9b shows the plot of aperture smoothing function for different combination of the σ and δ. For our analysis, we have used $\sigma = 8$ and $\delta = 8$, which provide a smooth edge and remove any discontinuity that may arise in the inter-segment regions. The image quality of the PSMT substantially improves after edge smoothing. The D50, which was earlier 0.32“ becomes 0.26“ The D80 also improves accordingly.

Table 2.11: Primary Mirror figure Error Budget

Sl.NO	Source of Error	D-50 (arcsec)	D-80 (arcsec)
1	Monolithic primary with Normalization radius of 666.5mm with weighted Zernikes	0.1	0.107
2	Segmented primary with Normalization radius of 250mm with weighted Zernikes	0.32	0.56
3	Segmented primary with Normalization radius of 250mm with weighted Zernikes Segment edge smoothing	0.26	0.46

2.10 Thermal Analysis of the PSMT Optics

Even after manufacturing telescope optics very precisely, telescope optics goes through gravity and temperature-induced deformations and miss-alignments during the operation. As for the telescope optics in concern, the temperature can directly affect the figure of the mirrors when it is subjected to variable temperature. Whereas mechanical stress injected to the mirror through its support due to temperature change can indirectly affect the figure of the mirror and hence the image quality. Thermal analysis of the material used for making the telescope mirror is one of the critical step. For the large segmented telescopes like TMT and ELT, thermal analysis is conducted in a very detailed manner by considering heat flows through conduction, convection, and radiation, resulting in changes in the global mirror temperature and can also create temperature gradients. Low CTE material such as Zerodur and Ultra-Low Expansion (ULE) is the most preferred glass-ceramic material for the telescope optics. However, these are very costly material, and PSMT is a small one-meter class experimental telescope; therefore, we explored the possibility of using the least expensive glass such as Schott Supremax. Therefore, before choosing the material to be used to make PSMT primary mirror segments, and secondary we have conducted a study to understand the effect of the mirror material on telescope performance. For this study, we have used two glass material, Zerodur, and the Supremax, and their mechanical properties are given in Table.2.12

Table 2.12: Mirror materiel parameters

Parameter	Supremax	Zerodur
Elastic Modules (N/m^2)	6.4x 10^{10}	9.3x 10^{10}
Poisson's Ratio	0.2	0.243
Shear Modulus (N/m^2)	3x 10^{10}	3.67 x10^{10}
Mass Density (kg/m^3)	2200	2530
Coefficient of thermal expansion (m/K)	3.25x10^{-6}	-2x10^{-8}
Thermal Conductivity (W/(m-K))	1.2	1.63
Specific heat (J/(kg-K)	830	830

2.10.1 Thermal Analysis of the Primary Mirror

The thermal study has been carried out using the COMSOL Multiphysics software. Since all the PSMT mirror segments are identical, therefore to save the computation time, thermal analysis is carried out for a single mirror, and the same result is used for the segmented primary made of seven segments. The hexagonal mirror segment of 250 side length, thickness 50 mm, and the ROC of 6350.72 mm is meshed and analyzed for 3, 5, and 30°C temperature changes. The temperature change leads to surface deformation captured at every node point on the mirror surface. The surface deformation is decomposed into Zernike coefficients, and the first 21 coefficients are shown in Figure 2.10.

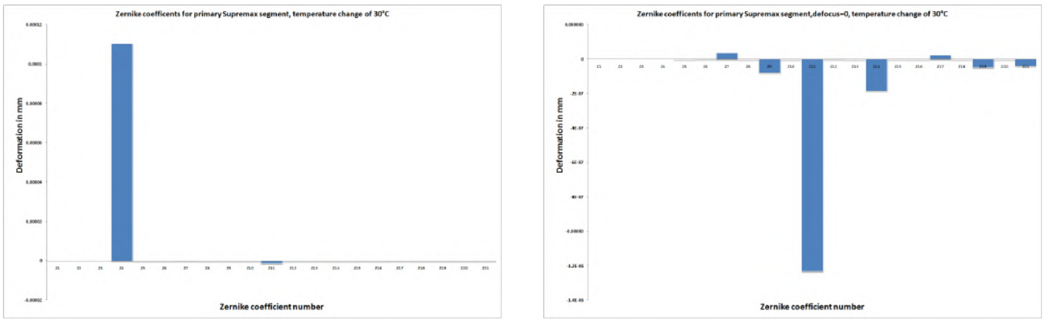

(a) Zernike coefficients for supermax for 30^{0}C temperature change

(b) Zernike coefficients for supremax for 30^0 C temperature change, with defocus=0

Figure 2.10: First 21 Zernike coefficients of the thermal deformation of the primary mirror made of the Supremax material The change in the temperature is 30^{0}C .

From the Zernike coefficients, which represent the thermal deformation, we found that in both Supermax and the Zerodur, the deformation is primarily dominated by the defocus, which is linked with the change in the ROC of the primary mirror. The second term which contributes to the deformation is spherical aberration. These two are low order radial terms. Then after, all other Zernike coefficients are insignificant. From our analysis, we find that the change in segment surface sag RMS and PV after Piston, tip, tilt (P, T, T)removal is 149.84 nm and 380.60 nm for the Supremax . Whereas, it is 0.9268 nm and 2.34 nm for the Zerodur. If we correct defocus, then deformation reduces substantially, and RMS and PV become 2.59 nm and 4.29 nm for the Supremax. Once defocus is corrected for the Zerodur, surface deformation RMS and PV is 0.018 nm and 0.03 nm, in ZEMAX optical system with primary and secondary this makes the system to reach back to its ideal state.

(a) Degrdation in the Wavefornt **(b)** Spot diagram

(c) Optimized Wavefornt **(d)** Optimized Spot diagram

Figure 2.11: Wavefront and spot diagram for the telescope made of Supremax and subjected to 30^0C temperature change.

2.10.2 The Final Material Chosen for the PSMT Primary Mirrors

Supremax deform linearly with respect to temperature were as the rate of deformation is less in Zerodur. The cost of Zerodur is way too much in comparison to that of Supremax. Our study found that the thermal effect predominantly introduces a defocus error caused by ROC change of the primary mirror. The change in ROC of the primary due to thermal effect can be compensated by tilting outer

(a) Degradation in the Wavefornt **(b)** Spot diagram

(c) Optimized Wavefornt **(d)** Optimized Spot diagram

Figure 2.12: Wavefront and spot diagram for the telescope made of Zerodur and subjected to 30^0C temperature change.

mirror segments and pistoning the central segment.

In the case of Zerodur, this compensation can be avoided as even for 30^0C change; the deformation is very less and within the acceptable range. Although the large defocus error of Spremax can be compensated fully, we decided to use Zerodur material for the PSMT. The reason behind this selection are: (1) any small difference in the CTE of the segment made of Supermax will create differential ROC error which will be difficult to compensate (2) There will be additional over-head to primary mirror controller to correct the temperature effect by giving required tip/tilt, and piston (3) any temperature gradient present within the primary mirror segments will lead to additional differential ROC error.

2.11 PSMT Widefield with the FOSC Instrument

The PSMT optics is designed primarily for technology demonstration, to provide acceptable image quality over about one arc-minutes FoV. Though few sciences is also possible with a telescope having a narrow field, however, a general-purpose telescope requires at least 10 arcminutes clear FoV with decent image quality. From a science perspective, a one-meter class telescope is a fairly good size and can be very effectively used for verities of astronomical research. Therefore, we explored PSMT optics design to get a larger field with few refractive optics. Since only one Nasmyth focus of the PSMT is available for the science instrument, we choose a multi-tasking instrument that can be used for both spectroscopy and imaging. The one such device which is widely used by many mid to large size telescopes is Faint Object Spectrograph and Camera (FOSC) ([20], [21] ,[22]). Since this device uses a re-imaging optics comprising a collimator and the camera, we decided to design the FOSC optics so that it can also correct the PSMT off-axis field aberration and provide acceptable image quality over at least 10 arcminutes FoV. So the device proposed for the PSMT serve a dual purpose. It corrects off-axis aberration present in the two mirror PSMT optics design and provides a usable wide field. Furthermore, it works as a very valuable science instrument. The top-level design requirements for the PSMT FOSC device is given in the next section.

2.11.1 Design Requirements

1. Up to 10 arc-minutes un-vignetted field of view available for the photometry and spectroscopy.

2. The 50% encircled energy should be to be within 1.2 arcsec, over entire FoV and the spectral window. This requirement is generated considering the median seeing of IAO Hanle is about 1.2“.

3. Spectral coverage of 4000-9000 A^0 .

4. The spectral resolution 1500 - 3000 over the designed spectral band. The resolution is chosen considering the low-resolution spectroscopy requirement of many science cases.

5. The design to be optimized for a 4096x4096 (15-micron pixel pitch) CCD chip.

6. The maximum optical track length should be less than a meter.

7. The instrument to be operable at 4500 meter altitude and in temperature variation of -25 to 30^0C.

8. The collimated beam diameter to be between 50 - 60 mm.
9. The slits, filters, and grisms to be housed on a rotating wheel.
10. Having a provision for in-site calibration unit.

2.11.2 Optical Design and System Performance

There are a number of FOSC developed for various size range telescopes. However, almost for all these FOSC devices, the telescope designs offer very well on and off-axis image qualities, and therefore, designing FOSC optics becomes easy. However, in the PSMT telescope, the off-axis aberration is very severe, so the optics design of its FOSC becomes challenging. In the first attempt, we decided to have a simple design using all spherical lenses. Likewise, PSMT, the FOSC optical design, has also been carried by using ZEMAX ray-tracing software. Following the conventional design methodology usually opted in any FOSC device, the system has collimating and camera units. The filters and/or dispersive elements can be placed in the collimated beam. The dispersive element, such as grism, is usually placed in the collimated beam so that astigmatism caused by the dispersing element itself can be minimized. The refractive collimator has got three singlet lenses. It receives an F/11 beam from the telescope and collimates the beam and forms a pupil at 90 mm from the collimator's last element. The pupil's size is about 25 mm and provides enough space to introduce grism and filter wheels. The focal length of the three-element collimator is 207 mm. The collimated beam then passes through the three-element camera unit. The camera acts like a focal reducer and converts the F/11 telescope beam to an F/9 beam. The focal length of the three-element camera is 187.5 mm. The optical layout of the FOSC is shown in Figure 2.13.

Both collimator and camera together correct off-axis aberrations and improves the system performance over a wide field. Figure 2.14 and table2.14 provide plot of the the D50 and D80 with and without corrector against wavelength. The plot and table show that a very simple six-element optics made of all-spherical singlet lenses remarkably improve off-axis image quality while keeping on-axis performance almost the same. The D80 of 10 arcmin FoV without corrector, which

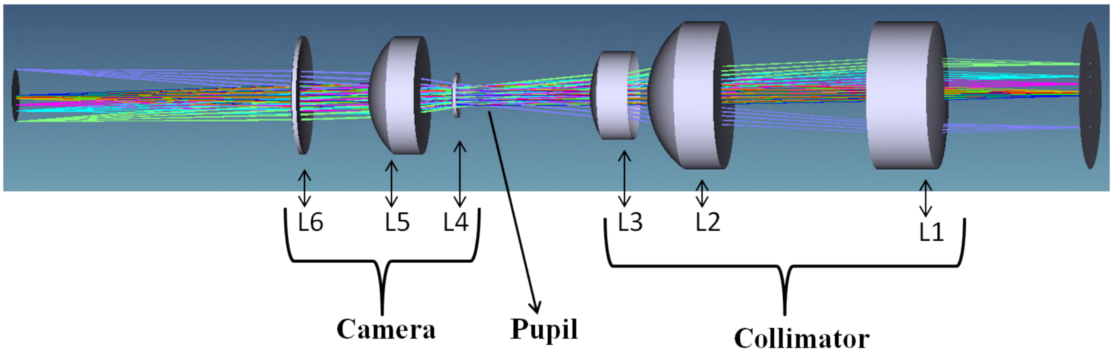

Figure 2.13: Optical layout of the FOSC which also act like a wide field corrector.

Table 2.13: Details of FOSC optics

Element	Notion	Martial	Aperture Diameter (mm)
Collimator :1st Lens	L1	N-FK51	60
Collimator :2nd lens	L2	ULTRAN20	50
Collimator :3rd Lens	L3	KZFSN5	40
Grism	Grism	SFL6	25
Camera :1st Lens	L4	SF19	40
Camera :2nd Lens	L5	LITHOTEC-CAF2	60
Camera :3rd Lens	L6	SK51	70

is around 11 arcsec, has become 2.4 arcsec or better. This is around five times improvement compared to the uncorrected system. Figure 2.15a and2.15b gives the polychromatic spot diagram and Encircled Energy of the FOSC for different fields.

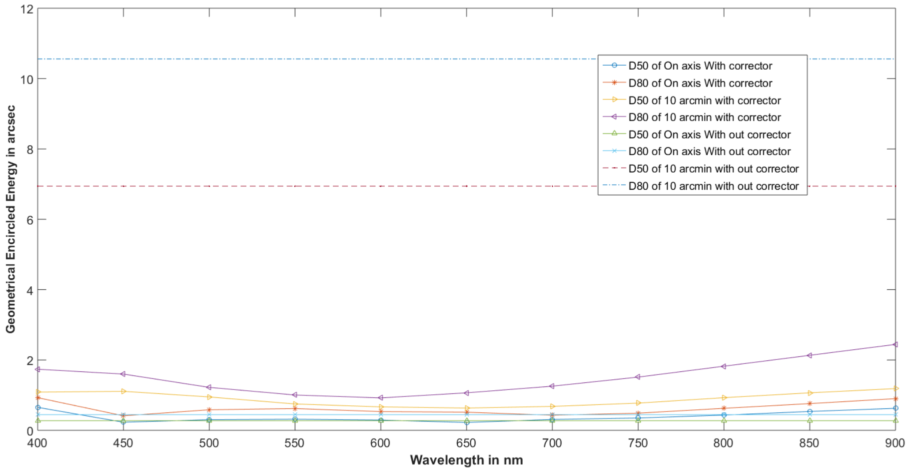

Figure 2.14: Plot of geometrical Encircled Energy against with and without corrector

Table 2.14: Performance of PSMT with corrector(WC) and without corrector(WOC), all values are for EE in arcsec diameter.

Wavelength(nm)	D50, $0'$ WOC	D80, $0'$ WOC	D50, $10'$ WOC	D80, $10'$ WOC
400-900	0.276	0.445	6.942	10.558
	D50, $0'$ WC	D80, $0'$ WC	D50, $10'$ WC	D80, $10'$ WC
400	0.654	0.929	1.087	1.738
450	0.231	0.413	1.110	1.600
500	0.303	0.585	0.950	1.221
550	0.317	0.619	0.750	1.005
600	0.292	0.533	0.667	0.922
650	0.224	0.516	0.633	1.067
700	0.310	0.430	0.681	1.256
750	0.351	0.489	0.774	1.514
800	0.434	0.626	0.929	1.824
850	0.537	0.760	1.067	2.133
900	0.626	0.901	1.187	2.400

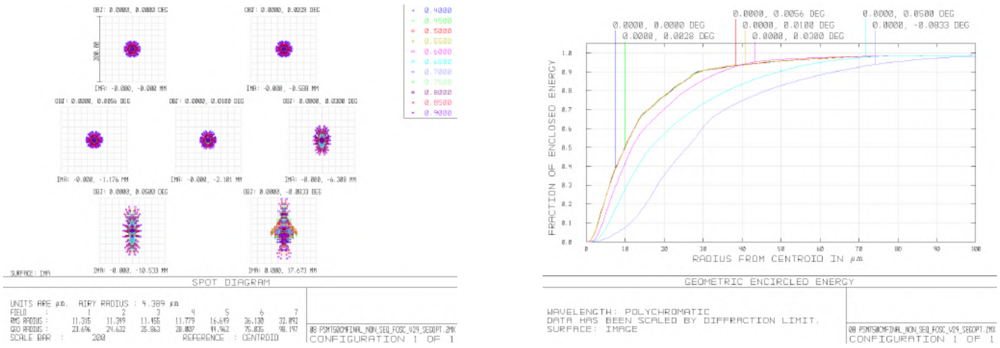

(a) Spot diagram **(b)** Geometrical encircled energy

Figure 2.15: System performance after the introduction of wide filed corrector.

2.11.3 Future Possible Improvements in the FOSC

The FOSC design is not yet finalized, and it is still under work in progress. The design which is presented in the previous section can be further optimized and improved. We can envisage many ways to improve the current FOSC design so that its performance can meet the design goal. To reduce the cost of our initial design, we have decided to stick with air-spaced singlets. The use of singlet lenses has introduced chromatic aberration, which can be eliminated by using achromatic doublets. Another problem we noticed with the current design is that it is subjected to strong filed curvature, predominantly seen when a dispersive element grism is introduced. The field curvature problem can be solved by incorporating a filed flatterer element in the camera design. Another possible option is the use of aspheric elements in the design, which can further reduce the spherical aberration.

Chapter 3

The NLOT Optics

3.1 Introduction

The growing astronomical community in India requires world-class observing facilities so that Indian astronomers can also effectively contribute to front-end research happening to unfold mysteries of the universe. Recently one major step that has been taken toward fulfilling this requirement is that India decided to join as a partner in the Thirty Meter Telescope(TMT) project[90]. The TMT which will be be one of the world's most powerful ground-based optical and near-infrared telescope, it is being developed in collaboration with CalTech (University of California) Canada, Japan, China, and India. Participation in the TMT project has allowed the Indian community to get acquainted with segmented mirror technology and effectively contribute to building the world's second-largest telescope. Indian in-kind contribution to the TMT is primarily on the segmented primary. Almost all the vital components which form the TMT primary mirror are being manufactured in India. However, despite becoming one of the partners to the TMT project, the Indian community still requires a 10 m class telescope because India's largest telescope is a 3.6 m DOT telescope. Hence, there would be a large gap between 3 m to 30 m. In the era of 30-40 m size telescopes, the 10m class telescope becomes feeder, and in the absence of such mid-size telescope in India, many science programs can not be effectively executed in the TMT. Another compelling reason for building a 10 m class telescope in India is that Indian participation in the TMT is only 10%, which would not be enough to cater to the diverse needs of the large community.

The proposed National Large Optical-NIR Telescope (NLOT) is expected to be a 10-12 m size, fully steerable telescope, developed around segmented mirror technology. The plan is that we will make use of most of the TMT subsystems such as mirror segments, supports, actuators, edge sensors, etc., which forms segmented primary mirror with very little or no modifications. However, the telescope's mechanical structure, mount, and drives, secondary and tertiary assemblies, science instruments etc, will differ from the TMT and require to be designed indigenously. Many optics design options are available; however, the telescope optics is primarily dictated by the science requirements. Since Ritchey-Chretien(RC) optics with just two mirrors provide diffraction limited performance over a sufficiently large field and decent image quality over the extended field up to 20 arc-minutes; therefore, it has become one of the first choices of many general-purpose large telescopes such as VLT, Subaru, Gemini, Keck, TMT, etc. However, as an exploratory exercise, it is always good to explore possible design options and then finally choose the one which is best suited for the community's science requirement.

India's proposed 10 m class telescope will be built around segmented mirror technology. Like a telescope made of the monolithic primary mirror, the segmented telescope's performance would also depend on many factors. However, the segmented primary would be subjected to many additional error sources, which may play a critical role in deciding the telescope performance. More specifically, when a telescope aims to provide diffraction-limited image quality, one needs to understand the effect of segment surface figure, miss alignment (tip-tilt, XY decenter or shear, and clocking), phasing error, segment to segment ROC variations, and inter-segment gaps as well as the size of the segment itself.

In this chapter, we present our work carried out toward the optimum design of the proposed 10 m class optical near-infrared telescope and the results of the detailed analysis. As one of the design options, we also attempted to mimic an aspheric hyperbolic primary mirror of an RC telescope by using spherical mirror segments. The related work is presented at the end of the chapter.

3.2 The Requirements and Design Constraints

The optical specification of any new telescope is primarily governed by the scientific requirements and the site parameters. Like many large telescopes of the world, NLOT is also expected to be a general-purpose telescope, and hence it needs to meet the diverse observing requirements of the community. With the use of multi-conjugate AO, diffraction limited imaging is possible over a relatively wide field. Hence, telescope optics design should provide diffraction limited performance up to 5-10 arc-minutes. The 10 m Indian telescope is supposed to be installed at IAO Hanle, an extremely dry and cold place, and best suited for near-infrared observations. Many exciting science programs require observation in NIR, and therefore, telescope optics design should work effectively up to 25-30 micron wavelength. The extreme adaptive optics add a venue to directly image faint objects coupled with a bright source such as an extra-solar planet with high contrast imaging. The high contrast imaging requires the meticulous design of the basic telescope optics, and great care is needed to manufacture high-quality optics. The science instruments are equally or more important than the telescope itself. For varieties of scientific interest, many instruments are simultaneously mounted on the telescope. Some of these multitasking instruments can weigh up to 10-20 tones. Therefore, telescope design should support many focal stations that can host small to large instruments, almost instantly available to the observer. The high-level requirement generated for proposed 10 m telescope by Indian astronomers are summarized in the Table 3.1. We have taken this as a design input while working for the NLOT optics.

3.3 Design Options for the NLOT optics

There are many segmented mirror telescopes of 10 m size, and larger that are either already completed or in various phases of design and construction. Therefore, before choosing one design as a baseline design for the NLOT, which will undergo through detailed study, we first explored few potential design options such as Keck[18], E-ELT [23], Chinese LOT [24],[25] and HET/SALT,[36],[34],[35]. Except for E-ELT, all other telescopes are nearly 10m size. While working on the E-ELT

Table 3.1: Requirements for NLOT

SN	Parameters	Values
1	Effective Aperture of the primary mirror	$\geq 10\,\mathrm{m}$
2	Preferred optics design	Ritchey- Chretien
3	Image quality	≥ 5 arcmin (diffraction limited) ≥ 20 arcmin (seeing limited)
4	Wavelength range	1) 0.3 - 30 μm 2)High throughput in both the optical and IR regions
5	Optimized Secondary	Minimal secondary obstruction and thermal emission.
6	Plate Scale	0.7 - 1.4 arcsec/mm
7	F ratio	F15-40
8	Optical performance	Telescope optics should not degrade site seeing by more than 10% It will have AO correction from the beginning
9	Instrument ports	1)Possibility of hosting 3-4 large instruments in Nasmyth and Cassegrain focus. 2)Provision for 4-6 small instruments on bent cassegrain focus.
10	Mount	1) Alt-Azimuth 2)Fully steerable 3)Excellent pointing and tracking with active focus correction.

kind of design option developed for 40 m class telescope, we have scaled-down all the optical parameters that decide the telescope optics.

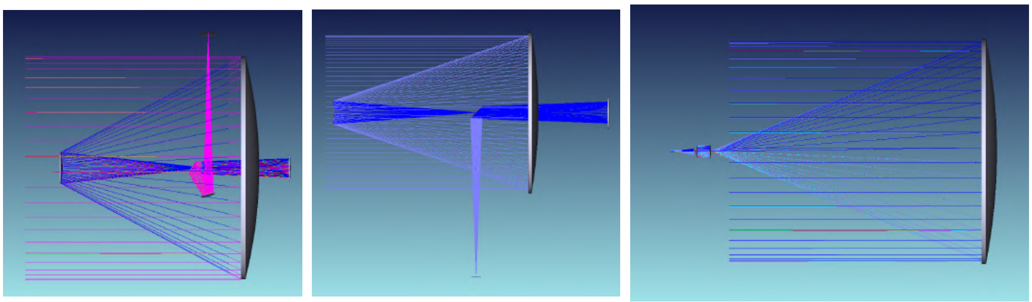
(a) ELT **(b)** CLOT **(c)** SALT

Figure 3.1: Layout of Modified Design options for NLOT.

The ELT (The European Large telescope)[23] optics is a five mirror design consisting of an elliptical primary (M1), Hyperbolic secondary (M2), and a 6th order aspheric tertiary (M3). The fourth (M4) and fifth (M5) mirror a flat mirror. The M4 is an adaptive mirror that will correct both high (due to atmosphere) and low spatial frequencies (due to wind, gravity, and thermal loading) wavefront errors. The basic telescope optics design gives diffraction limited field of view up to 20 arcmin, then after the image quality degrades. The problem associated with this design is that it requires a fast ellipsoidal primary mirror (f/0.93). Another issue with the design is with the 6th order aspheric mirror (M3) of about 1.5 m, which has very tight mechanical tolerance. The larger fields suffer from vignetting and contrast reduction problem due to various mirrors and hence not found to be suitable for very wide-field imaging. Due to all these reasons, we did not select the E-ELT design for further perusal.

The Chinese Large Optical Telescope(CLOT) [24][25] has primary as an ellipsoid, secondary is hyperbolic with sixth-order asphericity, and the tertiary is an ellipsoid with both 6th and 8th order asphericity. The Quaternary is a plane mirror creating the Nasymth focal point. The design needs two higher-order aspheric of a size more than 1.5 m. The 4th mirror, M4, allows the light from the secondary to go to the tertiary, but it creates vignetting due to the central hole. Also, the design has tight tolerances on secondary and tertiary mirrors. Due to these complexities, we decided not to go with this design. Another design that we explored is the South African Large Telescope (SALT) design, which uses a Spherical Primary and four-element reflective spherical aberration corrector [36],[34],[35]. Even though it does not have a Nasmyth focus, having only Cassegrain focus, we were keen to explore this design as the primary being spherical. The design gives D80% for the on-axis and ten arcmins, 0.035 and 0.203 arc-sec, respectively. The design was discarded due to the multi-element corrector's vignetting, the absence of a Nasymth focus, and non-sufficient image quality correction. The optical layout all design options are given in Figure 3.1.

Next, we explored the Keck type Ritchey-Chretien (RC) design [18]. RC is the most preferred design for the very small to the large aperture telescopes like the TMT. The RC telescopes provide a wide field of view, free from most optical aberrations that otherwise any two-mirror telescope suffers. Compared to any other optical configuration, the RC has a very short optical tube assembly and compact design for a given focal length. After going through extensive exploration of optical design options, we realized that the Keck type RC design with an option to have multiple focal planes is the best possible choice for the NLOT and meets most of the scientific requirements. In the Keck telescope, the primary's focal ratio is 1.75. It has two different secondaries, which cater to the wide field for the optical, and least thermal emission for the NIR observation. For the NLOT, we explored the possibility of using fast primary with F-ratio as small as 1.25. The results of RC design options with different primary and telescope F numbers are summarized in Table 3.2. All the RC design options are analyzed for the working wavelengths 0.3 - 30μm. The shorter system focal length option results in a smaller plate scale and facilitates a small detector to capture large FoV. However, having a short system focal length increases the secondary size, which in turn creates issues of the thermal emissions in NIR observations. The RC design's on-axis performance is best compared to E-ELT and CLOT design; however, it degrades more rapidly than other designs when the FoV is increased. Whereas, Modified ELT and CLOT provide excellent off-axis performance indeed till 10arc-min or larger FoV. These two designs, which are almost similar in optical configuration, may be best suited for the telescope equipped with a ground-layer adaptive optics system, aiming for large field surveys. We finally chose the baseline design for the NLOT with a primary of 35 m radius of curvature, and the system F number 15, which provides optimum performances and meets most of the design requirements.

3.4 NLOT Monolithic Optics Design

Likewise the PSMT, the NLOT design, is first carried out considering primary is made of a monolithic mirror. The effective aperture of the NLOT is going be slightly larger than 10 m. The segmented primary which is non-circular and the outer diameter is about 11.3 m (refer the Figure 3.3), therefore for the monolithic design we considered 11.6 m is the diameter of the primary mirror. The radius of the curvature of the primary mirror is chosen to be about 35 m and hence the Fno of the primary mirror turns out to be F 1.5. Then after by using ZEMAX we once again optimized the design and derived the optical parameters of the telescope which is given in Table 3.3.

Figure 3.2 shows the radial variation of the spot sizes. As telescope optics has got only mirrors system, hence there is no chromatic aberration. The plate scale of the telescope is 1.4 arcsec/mm. In the Table 3.4 we gives the Geometric encircled

Table 3.2: RC design options summary

Parameter	Opt:1	Opt:2	Opt:3	Opt:4	Opt:5
Primary F-ratio (Final F ratio)	1.25(F15)	1.5(F15)	1.75(F15)	1.75(25)	1.75(40)
Primary-ROC (m)	25	30	35	35	35
Primary F-ratio	1.25	1.5	1.75	1.75	1.75
ROC of the secondary (m)	2.853	4.012	5.103	2.907	1.766
Focal plane ROC (m)	1.379	1.886	2.333	1.350	0.835
Diameter of primary (m)	10	10	10	10	10
Diameter of secondary (m)	1.116	1.286	1.382	0.793	0.503
Primary conic	-1.0016	-1.0026	-1.0039	-1.0039	-1.0039
Secondary conic	-1.4169	-1.5645	-1.6423	-1.3865	-1.2830
WFNO	15	15	15	25	40
Effective Focal Length (m)	150	150	150	250	400
Plate scale (arcsec/mm):	1.3751	1.3751	1.3751	0.825	0.5156
FOV(in m) :	0.87	0.87	0.87	1.442	2.24
Primary Secondary distance (m)	11.11	13.19	15.24	16.15	16.66
Secondary tertiary distance (m)	8.953	10.55	12.32	12.32	12.32
Back focal length (m)	6.739	7.5	7	7	7
50% GEE Onaxis	0.0140	0.0140	0.0140	0.014	0.014
50% DEE Onaxis	0.0149	0.0143	0.0141	0.014	0.014
80% GEE Onaxis	0.0240	0.0240	0.024	0.024	0.024
80% DEE Onaxis	0.034	0.0240	0.024	0.024	0.024
50% GEE 20arcmin	0.377	0.327	0.305	-	-
50% DEE 20arcmin	0.341	0.314	0.293	-	-
80% GEE 20arcmin	0.473	0.409	0.382	-	-
80% DEE 20arcmin	0.418	0.385	0.363	-	-

energy (GEE) which is basically an integration of intensity produced by the rays on the focal plane and the diffraction encircled energy(DEE), which is the energy concentration considering the diffraction effect. For monolithic primary mirror, the energy distribution and intensity distribution seem to vary almost in the same way.

The RC design gives diffraction-limited performance, i.e., about 0.026 arcsec for around 5 arcmin diameter at 632.8 nm wavelength. Then the performance

Table 3.3: Optical design parameters of the NLOT considering primary as a monolithic mirror

Parameter	Value
Segment side length (mm)	720
ROC of primary (m)	35
Primary F/no	1.5
ROC of secondary (m)	4.57
Focal plane ROC is (m)	2.05
Diameter of primary (m)	11.6
Diameter of secondary (m)	1.4
Primary conic	-1.00360800
Secondary conic	-1.65949326
Working F/no	12.6
Effective Focal Length (m)	147
Plate scale (arcsec/mm):	1.4
20 arc-minute FOV (m) :	0.86
Primary-Secondary distance (m)	15.49
Secondary-tertiary distance (m)	10.14
Back focal length (m)	6.78

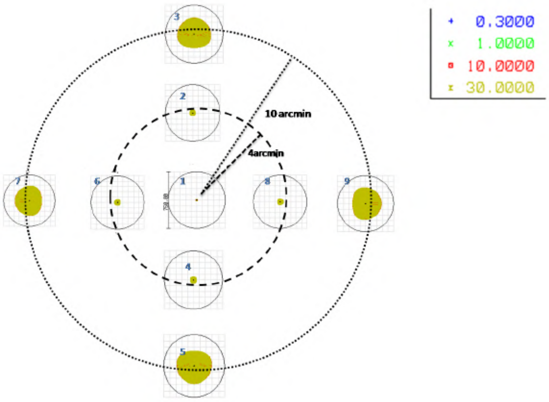

Figure 3.2: The radial variation of the spot profile for monolithic design with 0, 4, 10 arcmin field radius. The circle around spots are 1 arcsec in diameter

degrades. The telescope optics provides acceptable performance to fairly large filed i.e. upto 20 arc-minutes. Once the optimum design is achieved using monolithic primary, then after we moved on to design the telescope considering the primary made of segmented mirrors.

3.5 The Segmentation Tool

We have already seen that making large primary mirror of the telescope is possible through segmentation. When converting from a monolithic to the segmented surface, radial petal-shaped segments are the ideal structure for dense segmentation.[92]. We can also use patterns like annular, triangular hexagonal, etc. In a flat mirror, a regular pattern can only be made out of regular polygons (e.g., hexagons). However, telescope mirrors are usually curved surfaces, this will requires irregular polygons to fill the aperture densely with a uniform gap. These irregular polygons are made such that on the projection from the top, they appear to be regular polygons. Different segments shaped like hexagonal or petal have their own advantages and disadvantages, specific to the fabrication techniques. When we consider manufacturing complexities and polishing, hexagonal segments are a better choice as they are close to typically circular shaped mirror blanks compared to four or three-sided polygons. For an aspheric primary, considering circular symmetry for a telescope primary made with N hexagonal segments, there are N/6 different segment shapes. They are arranged in six sectors. Hexagonal segments are easier to support against gravity; also, position actuators (three per Segment) can easily be attached, due to their symmetry. The advantages of hexagonal segments have made this the segmentation pattern of choice for the most current and planned segmented-mirror telescopes. [12] [91]. The details of various approaches into segmentation studies are given in Appendix A. Here we briefly explain the Python-based segmentation tool, developed in a generic, scalable approach. The tool can be used to generate various data for doing the segmentation studies of any telescope made of the hexagonal segmented primary mirror with any aperture size, inter-segment gap, conic constant, and asphericity. The tool has the option to do segmentation with a regular or elongated hexagon with the option of producing a master sector and avoiding any hexagons user may choose. The tool has got also a feature to analyze the effect of the piston, tip, tilt, XY displacement or shear, Segment to segment Radius of curvature(ROC) error, clocking etc. The tool is equipped with creating an equivalent spherical segment of an aspheric with ROC, either analogs to a spherometer provided ROC or with a Best-fit ROC. It can also create surface deformation using standard Zernike polynomial. Using this tool, combined with the ZEMAX, the NLOT optics is designed and analyzed.

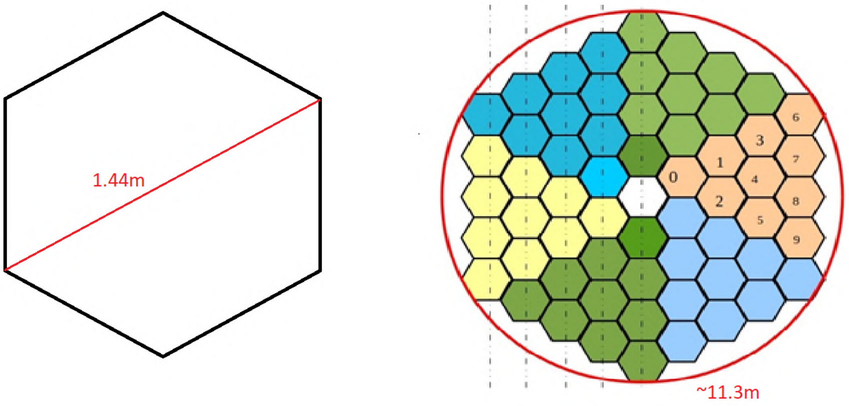

Figure 3.3: The 1.44 m size hexagonal segment (left) as well as 4 ring segmented primary mirror (right). The segmented primary is made of six repeating sectors and each sector comprises ten different type of off-axis aspheric mirror segments.

3.6 NLOT Segmented Optics Design

The tools and techniques which we have developed during the design and analysis of the PSMT optics has been used for the NLOT also. However, since NLOT is a large research grade telescope, therefore, much more effort has gone in doing analysis on the segmentation effect. The NLOT optics is RC and it uses a hyperbolic primary and secondary along with a plane tertiary mirror. So the segmentation of primary has been introduced with UDA (user-defined aperture) files in the global coordinate system, as explained in section A.2.2. The segment size has been chosen as 1440 mm corner to corner, which of the same size as used in the TMT and E-ELT telescopes. The inter-segment gap has been kept as 5 mm. The design uses primary mirror made of 61 segments, including the center one, segments are arranged in four rings, distributed over six sectors. Each sector has got 10 different type off-axis hyperbolic mirror segments subjected to different asphericity (see the Figure 3.3). The segment asphericity increases from the centre to outward. The optical parameters of secondary tertiary are kept the same as the monolithic one. The plate scale of the telescope is 1.4 arcsec/mm. The system is further optimized to change the primary segment positions, keeping other mirror optical parameters like the radius of curvature and conic constant same.

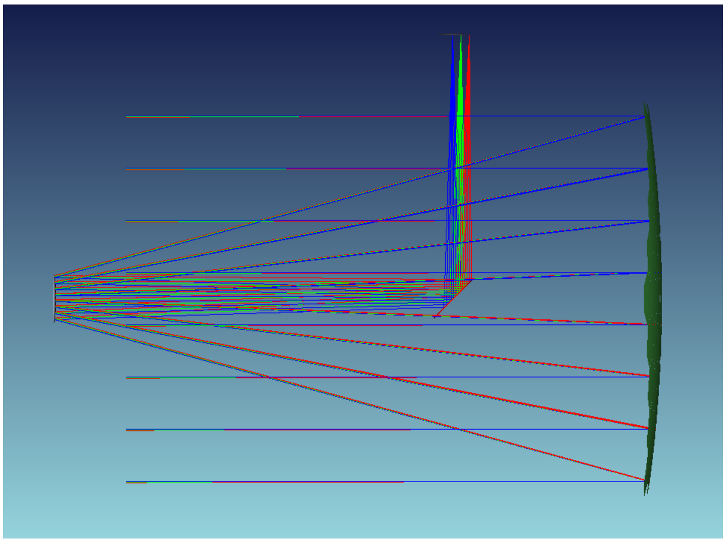

(a) Layout

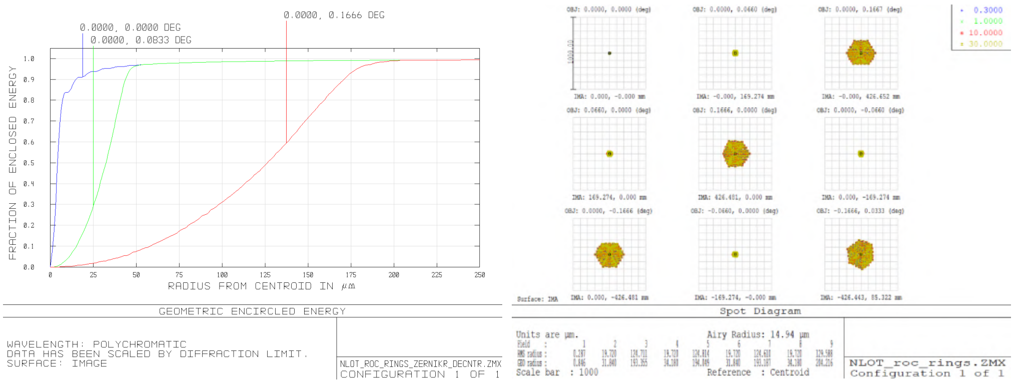

(b) Encircled Enegry plot (c) On and off-axis spot diagram

Figure 3.4: The NLOT optics design with the segmented primary mirror

The Figure 3.4 shows optical layout of the NLOT with the segmented primary as well as plots related to the geometrical encircled energy and the spot diagrams. Whereas, in the Table 3.4 we provide image qualities for both monolithic and the segmented primary. When we compare the segmented design performances with monolithic, then we can find slightly better performance in GEE and DEE for the segmented primary. This performance improvement is due to reduced total system aberrations, especially from the elimination of rays from the aperture edges, thereby improvement to the total energy distribution as in Table 3.4. In the RC optics, off-axis aberrations like coma and astigmatism becomes prominent. However, despite the degradation seen in the off-axis image quality, the telescope optics provides diffraction limited performance up to 5 arc-minuets, which is probably sufficient for many AO assisted science programs.

Table 3.4: The image quality of the NLOT RC optics with the monolithic and segmented primary

Percentage of G-EE	Onaxis diameter	10 arcmin diameter	20 arcmin diameter
Monolithic 50%	0.012	0.102	0.401
Segmented 50%	0.011	0.091	0.356
Monolithic 68%	0.015	0.118	0.465
Segmented 68%	0.015	0.105	0.412
Monolithic 80%	0.020	0.127	0.505
Segmented 80%	0.019	0.114	0.449
Monolithic 90%	0.042	0.136	0.544
Segmented 90%	0.041	0.123	0.482
Percentage of D-EE			
Monolithic 50%	0.011	0.094	0.397
Segmented 50%	0.012	0.083	0.35
Monolithic 68%	0.015	0.111	0.456
Segmented 68%	0.017	0.098	0.404
Monolithic 80%	0.019	0.125	0.492
Segmented 80%	0.023	0.114	0.437
Monolithic 90%	0.043	0.148	0.533
Segmented 90%	0.062	0.143	0.481

3.7 Exploring Segmentation Related Effects

Making large telescopes is possible with segmented primary mirrors, where a mosaic of smaller mirrors create the large equivalent monolithic primary. Due to mechanical constraints, these large telescope's primary mirrors are fast mirrors having smaller and smaller Fno s. Also, these mirrors are aspheric to compensate for large aberrations otherwise present in the system. These two factors add up to give off-axis segments having large aspheric departures[12]. If we consider the mirror segments are a rigid body (that is not the real case, they are thin and hence flexible), they are subjected to six degrees of freedom (DOF) and get miss-aligned in any of these six DOF. Therefore, it becomes essential to study the effect of changes in the segment's rigid body positions on overall telescope performance. The various rigid body positional errors like piston, tip, tilt clocking, etc., affect segmented mirror telescope's optical performance. These errors become more critical as we increase the segmentation and asphericity of the segments. Our analysis used Zernike polynomials (Noll coefficients) to introduce Piston, tip, tilt, and figure errors into the segments. Whereas, the clocking of the segments has been done by physically rotating the segment about its local reference frame. We introduce these errors so that for ± X error, the error is given into the segments as a normal distribution with zero mean and standard deviation as ± X/2, having the maximum error not exceeding ± X. The mathematical formulation for various segmentation related errors has been listed by Feenix Y.et.al in 2004[26]. Their study mostly focuses on the effect of these errors in the Strehl ratio. However, in our analysis, along with the Strehl ratio, we also obtained the spot diagram, wave-front, PSF, and encircled energy distribution. In addition to exploring the effect of rigid body errors, we also studied the effect of surface figuring error in the telescope's optical performance.

3.7.1 The Piston Error

In a segmented telescope, the presence of the piston error introduces phase discontinuity between the segments. The phase error finally affects the diffraction pattern of the telescope and hence limits its spatial resolution. To achieve diffraction limited performance in any segmented mirror telescope, the piston error must be reduced to 1/20 of λ or even as small as possible [62].

For a given Zernike coefficient α, associated with the piston term of any segment, the corresponding generated wave-front error can be given as $2\pi\alpha$. If σ_p is the standard deviation of the wavefront error at the mirror surface in the unit of waves, then the Strehl ratio S for any segment telescope can be given as [28]

$$S = 1 + (N-1)\exp^{-{\sigma_p}^2}/N \tag{3.1}$$

From the above analytical formula, one can get a feel of how the Strehl ratio of the segmented mirror telescope will get affected by the piston error. However, to explore the effect of the piston error on overall image quality (on the PSF), we used ZEMAX based design of the segmented mirror telescope and injected random piston, distributed as a normal distribution of error. The piston errors introduced varies from $\pm\,25\,\mathrm{nm}$ to $\pm\,1000\,\mathrm{nm}$. The results are presented as PSF, spot diagrams, Strehl ratio and encircled energy for various piston errors in the figures 3.5 to 3.9. Figure 3.6a shows the ideal diffraction-limited PSF in the logarithmic scale, which has got a Strehl ratio of one. Over almost two lambda piston errors, the geometrical aberration effect is expected to be primarily defocus is almost negligible. The degradation in image quality is mainly due to the diffraction effect and hence falls under the physical optics realm.

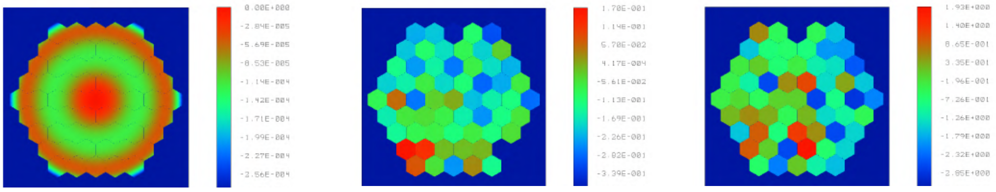

(a) Ideal telescope **(b)** ± 100 nm **(c)** ± 1000 nm

Figure 3.5: Telescope wavefront for the Piston error

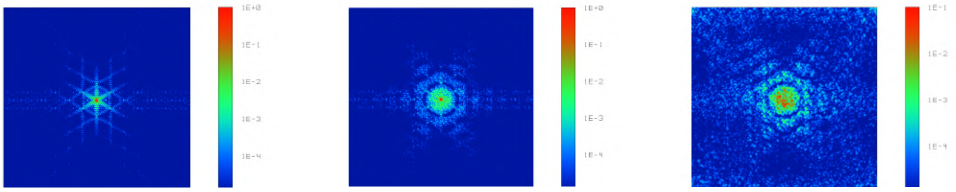

(a) Ideal telescope **(b)** ± 100 nm **(c)** ± 1000 nm

Figure 3.6: Logarithmic PSF for the Piston error

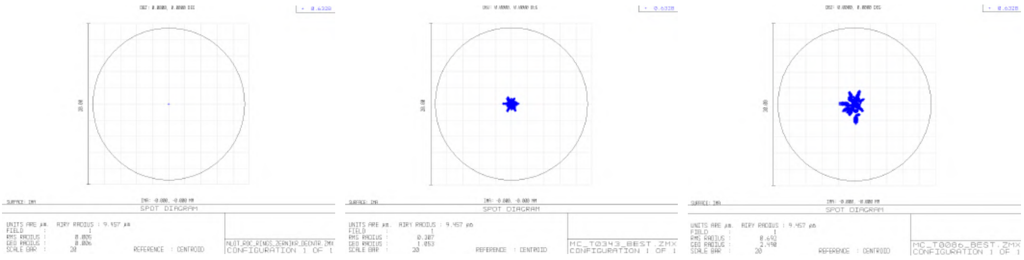

(a) Ideal telescope **(b)** ± 100 nm **(c)** ± 1000 nm

Figure 3.7: Spot diagram for the Piston error

For a ± 25 nm piston error, the Strehl ratio is dropped from 1 to 0.9362. As piston error approaches ± 100 nm, the Strehl drops to 0.7109. The PSF in Figure 3.6b can be seen to have some spread in the core energy. For ± 1000 nm, piston error, as one can see in figure 3.6c, the core of the PSF splits, and many speckles created in the focal plane reducing the resolution and intensity contrast of the telescope. The Strehl ratio also dropped by a huge amount, and it becomes almost 1/20th of the ideal diffraction-limited PSF. The Strehl ratio derived from the ZEMAX simulation is compared with the theoretical model as per equation 3.1

in the figure 3.8. There is a close agreement between the two Strehl ratio, and through this work, we happened to validate the much-publicized equation 3.1. The spot diagrams generated considering geometrical optics are shown in figure 3.7. Not much variation can be seen in the spot diagram, and the image quality falls well within the diffraction limit, even for ± 1000 nm piston error.

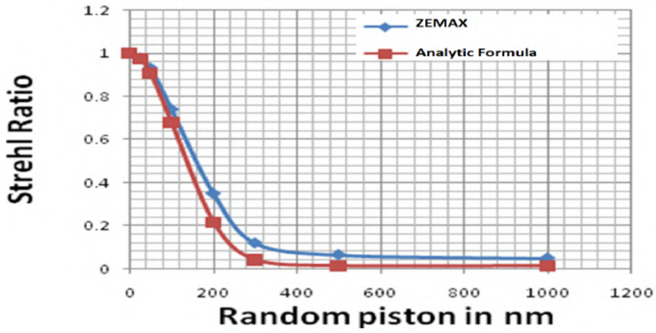

Figure 3.8: Strehl ratio variation for the Piston error

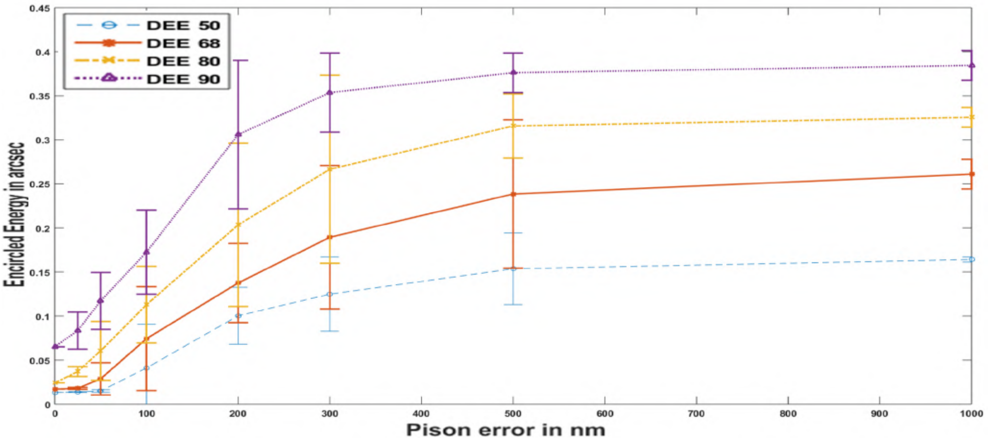

(a) Diffraction Encircled Energy

Figure 3.9: Variation in the Encircled Energy due to the piston error

The figure 3.9a shows variation in the diffraction encircled energy 50% ,68%, 80% and 90% against piston error. The variation is very least between 0 - 50 nm, then after EE increases very steeply between 50 - 300 nm. Once the piston error becomes larger than half a wavelength, then, as expected, the saturation effect arises, and no further change happens in the DEE. This happens due to the fact that light reflected from the segments starts getting added incoherently. At this stage, the diffraction limited resolution of the telescope would be decided by the single segment's size, not by the full primary mirror. We conclude this from our ZEMAX based simulation studies on the piston error. We could extract much valuable information about the image quality, which otherwise would not have been noticed.

3.7.2 The Tip /Tilt Error

The tip, tilt errors are introduced simultaneously with Zernike Coefficients Z2 and Z3. First, we generate the distribution of Zernike coefficients corresponding to the tip/tilt error in the range of ± 0.005 to ± 0.05 arc-sec, which give rise to the wave-front errors ± 8.73 nm to ± 87.3 nm. Then after a set of these distributions are used to inject tip/tilt error in the segmented telescope.

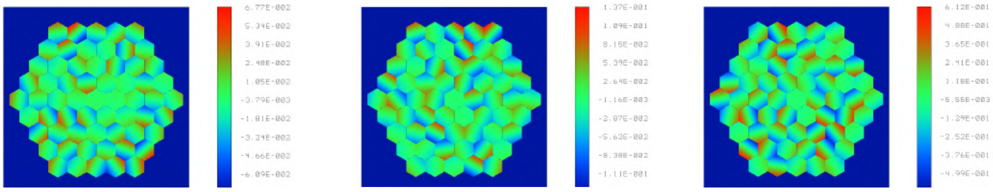

(a) ± 0.005 arcsec **(b)** ± 0.01 arcsec **(c)** ± 0.05 arcsec

Figure 3.10: Wavefront for the tip/tilt error

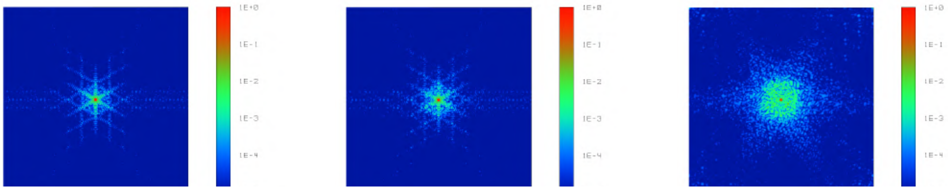

(a) ± 0.005 arcsec **(b)** ± 0.01 arcsec **(c)** ± 0.05 arcsec

Figure 3.11: Logarithmic PSF for tip/tilt error

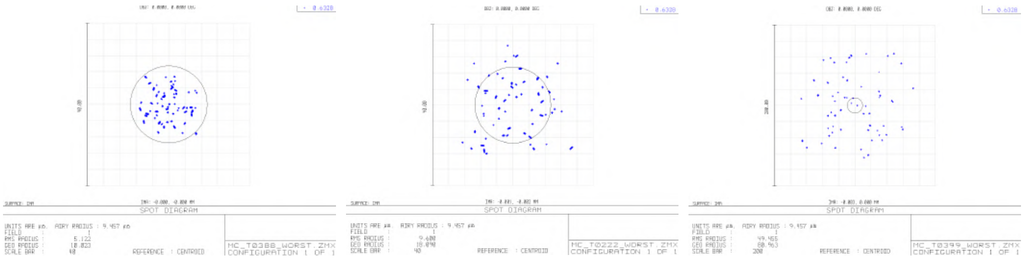

(a) ± 0.005 arcsec **(b)** ± 0.01 arcsec **(c)** ± 0.05 arcsec

Figure 3.12: Spot diagram for tip/tilt error

Figure 3.10 shows the pupil wave-fronts after the injection of tip/tilt errors of different amplitudes. Whereas, figure 3.11 shows the PSF on logarithmic scale. We can notice that the shape of the PSF core is more or less intact, but there are noticeable changes in the PSF wings. The Strehl changes to 0.9882 in the case of ± 0.005 arcsec tip/tilt error, and about 0.3383 when the error is ± 0.05 arc-sec. The degradation in the Strehl ratio is more severe than it is caused by the piston error when both are subjected to similar RMS wave-front error. We can also see systematically distributed speckles in the logarithmic PSF as we increase the tilt error to a limit of ± 0.05 arcsec.

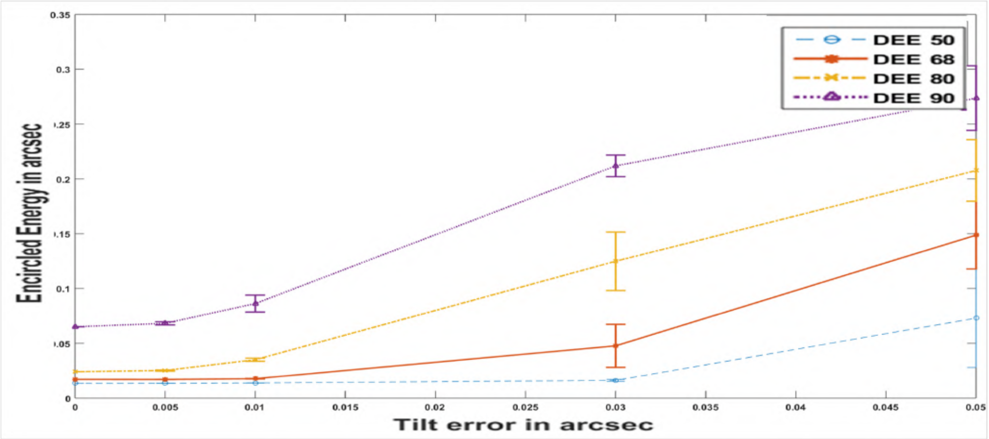

(a) Diffraction Encircled Energy

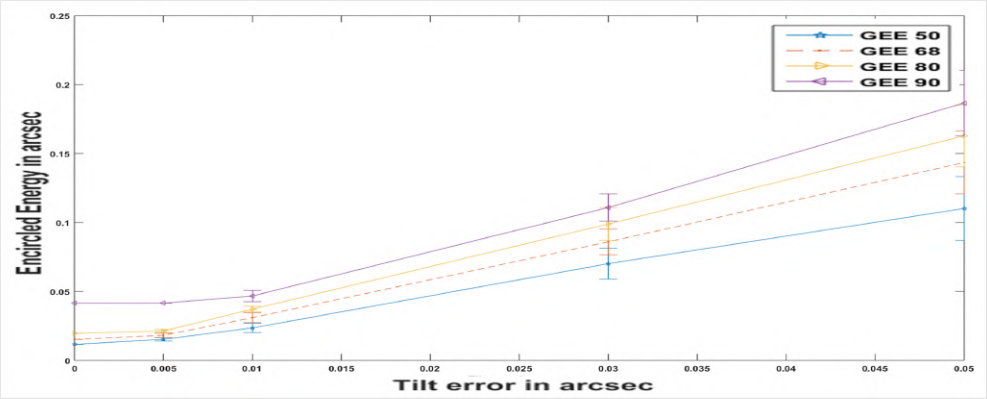

(b) Geometrical Encircled Energy

Figure 3.13: Plot of encircled energy against tip/ tilt errors.

The Figure 3.13a and 3.13b, shows variation in the diffraction and geometrical encircled energy against tip/tilt errors. In the case of DEE, up to 0.01 arc-sec tip/tilt error telescope seems to be working within the diffraction limited regime. After there are steep changes, energy gets re-distributed from the core to the outer part of the PSF. The tip/tilt changes affect telescope image qualities in two ways. First, like piston error, it creates phase discontinuities around segment edges, which lead to change in the diffraction pattern. Whereas, due to geometrical optics, the rays reflected from different segments subjected to tip/tilt error, get spread on the focal plane and, hence degrade the image quality almost linearly.

From this study, it is clear that a 10 m class segmented mirror telescope aiming to achieve diffraction limited performance has to first measure the tip/tilt with an accuracy of 0.01 arc-sec or better and then after correct it using the precision actuators. This is quite a high demand for any segment alignment tool considering the practical situation like variable seeing, wind-induced disturbances, the aberration of alignment optics, and limited centroiding accuracy. The telescopes like KECK/SALT can achieve alignment accuracy of about 0.05 arc-sec [18],[101], which is barely enough to get the best telescope performance in very good seeing condition. We conclude that the tilt effect is indeed one of the very prominent source of error. It needs to be dealt with great care in any segmented mirror telescope, irrespective of working seeing or diffraction-limited domain.

3.7.3 The Clocking Error

In a segmented telescope that uses aspheric mirrors, creating an aspheric profile requires off-axis segments getting strongly aspheric as we move from center to outer segment rings also when the primary gets optically fast. These off-axis aspheric segments placed in the segment support system can be subjected to rotational error or clocking errors, causing severe aberrations. The mathematical description of these errors is given by Feenix Y.et.al in 2004[26]. Our investigation introduced this in-plane rotation of a segment about its center while keeping segment origin fixed (see Appendix A.1.5 for the more detailed description). We present the results of± 1, ± 10,± 100, and± 288 arcsec clocking errors. This entire analysis was achieved with the help of the python-based segmentation tool.

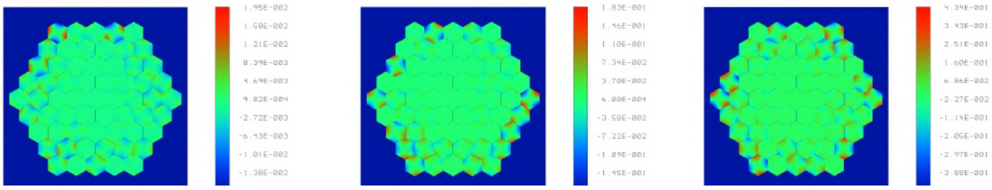

(a) ± 10 arcsec **(b)** ± 100 arcsec **(c)** ± 288 arcsec

Figure 3.14: Telescope wavefront for Clocking error

Figure 3.14 shows three sets of wavefronts subjected to different clocking errors. It is observed that clocking affects the off-axis segment wave-front more severely,

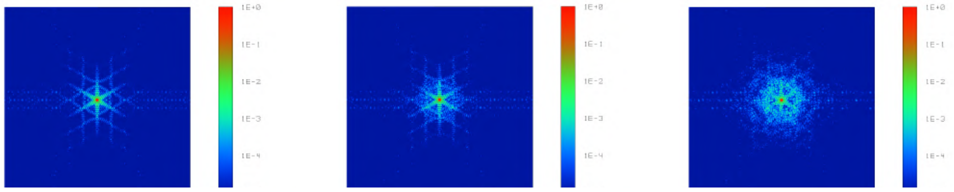

(a) ± 10 arcsec **(b)** ± 100 arcsec **(c)** ± 288 arcsec

Figure 3.15: Logarithmic Scale PSF for Clocking error

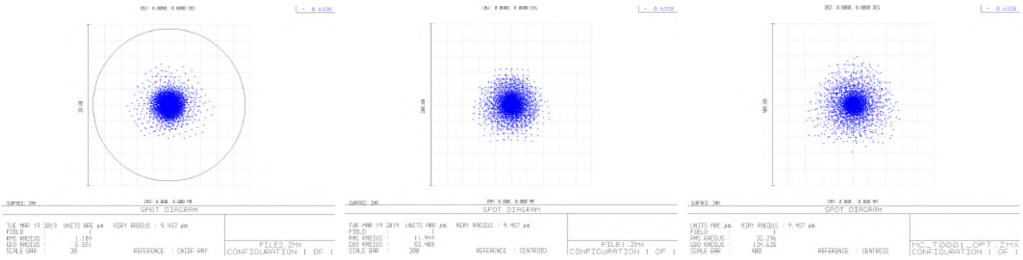

(a) ± 10 arcsec **(b)** ± 100 arcsec **(c)** ± 288 arcsec

Figure 3.16: Spot diagram for Clocking error

where the asphericity is prominent. The large segmented telescope which uses small Fno can be subjected to large asphericity and hence the problem of enhanced clocking error.

Figure 3.15 shows the PSF in the logarithmic scale. As one can find, the large clocking errors cause energy leakage from the core into the wings. It creates speckles distributed over a large area, specifically on the wings. Nevertheless, unlike piston or tip and tilt, the PSF wing pattern created by clocking, as seen in Figure 3.15c has got less background contamination. Similarly, the Strehl ratio's degradation due to clocking error is least, 0.9998 to 0.8624 as we increase clocking error from ±10 arc-sec to ± 228 arc-sec. The spot diagrams in the 3.16 indicate a radial spread in the ray distribution when the clocking error increase. Clocking error induces mainly astigmatism, dominated by off-axis segments who have higher asphericity. That is, the marginal rays coming from the off-axis segments are more affected, causing spread in wings rather than in the core of the PSF. Figure 3.17b shows geometrical EE plotted against the clocking error. From the plot, it appears that clocking error linearly affects the geometrical EE. Whereas, Figure 3.17a gives the diffraction encircled energy(DEE) distribution for clocking error. There is not much change in the 50% 68% DEE, indicating that clocking has less effect on the energy at the core of PSF. Whereas D80 and D90 start to slowly increase after 100 arc-sec clock errors, showing the error primarily affect the wings of the

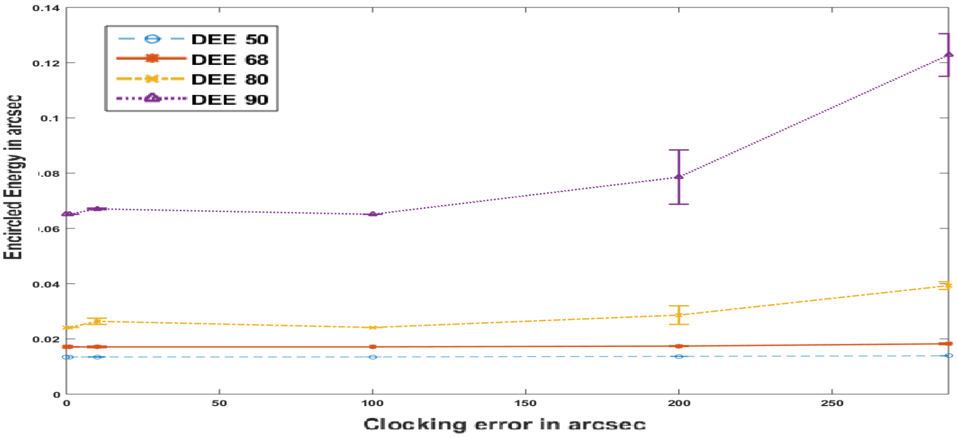

(a) Diffraction Encircled Energy

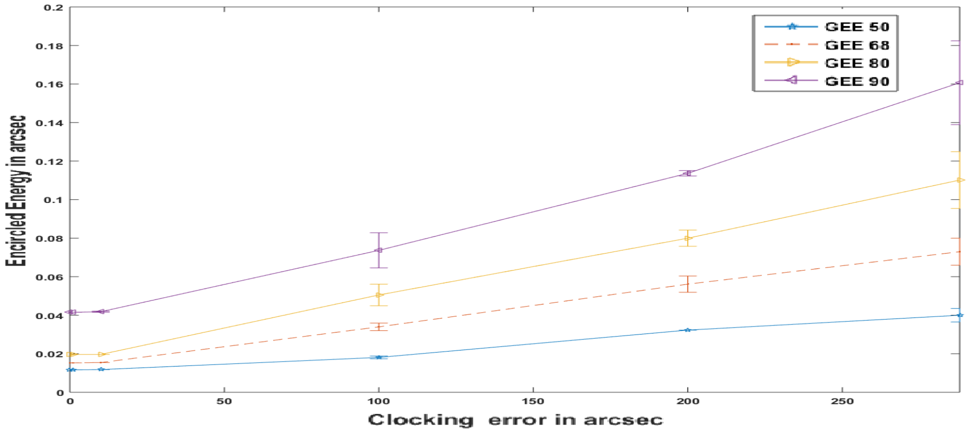

(b) Geometrical Encircled Energy

Figure 3.17: Encircled energy distribution for Clocking analysis

PSF. In the TMT documents, the values assigned for the residual clocking error are around 1.4 nm RMS after AO. In contrast, the total assembled segment figure error is given a large value of around 20 nm[93]. From our analysis, we observed that even for 100 arc-sec clocking error, the total telescope surface sag variation is only around 8 nm RMS. From this analysis, we find that clocking error is also one of the important wave-front error sources. It needs to be carefully considered, especially when the telescope has to deliver the diffraction limited performance.

3.7.4 Effect of the Segment Size and Inter-segment Gap

The segment size and other NLOT design parameters were chosen, considering India's involvement in Thirty-meter telescope [27] and the possibility of reusing the existing technology and manufacturing techniques. Still, we wanted to explore the effect of Segment size and Gap in the diffraction pattern and the focal plane energy distributions. The amount of energy in a diffraction pattern and the angular scale distribution of the pattern can be stated to depend on two things- the linear scales (l) over which the diffraction happens and the wavelength (λ) under consideration. Such that the diffracted energy spread over an angular scale of λ/l [12]. This linear scale can be considered as segment edges, inter-segment gaps, spiders, etc. While studying the effects of Gap and the size of the segments, we have not considered the spider or any other sources causing the diffraction effect.

Using our python-based segmentation code as given in section A, we create different telescope primary of fixed total aperture, first by varying segment size keeping the inter-segment gap the same. Then in the next step, we vary the segment gap, keeping the size of the segment the same. The analysis has been carried out for two different wavelengths 632.8 nm, and another for 1000 nm. The 632.8 nm is the system wavelength we used for various other analyses, whereas 1000 nm is included because the telescope is supposed to perform in the near-infrared band too.

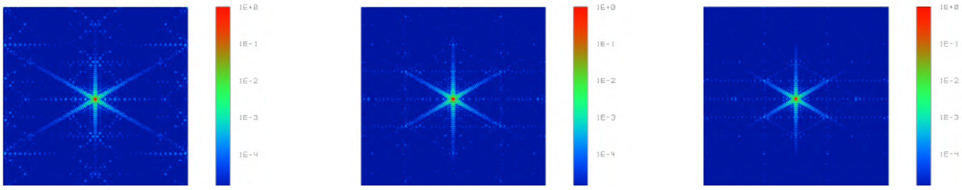

(a) 100 mm side **(b)** 200 mm side **(c)** 300 mm side

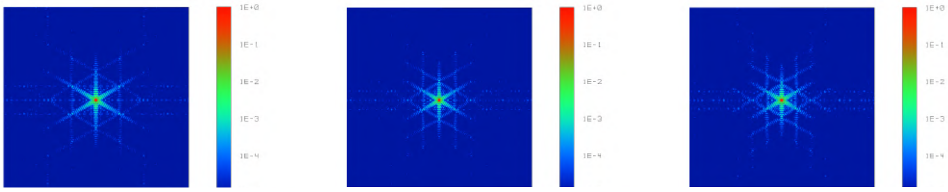

(d) 400 mm side **(e)** 600 mm side **(f)** 660 mm side

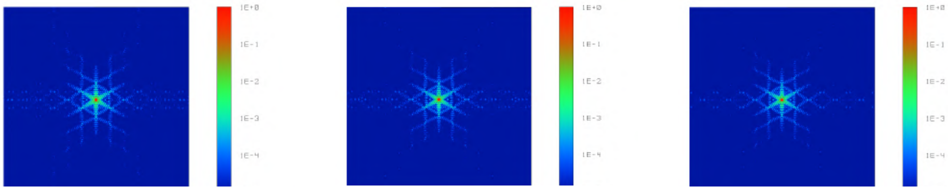

(g) 690 mm side **(h)** 720 mm side **(i)** 750 mm side

Figure 3.18: Logarithmic Scale PSF of telescope for Segment edge length variation and 5 mm inter-segment gap

We observed that the effects of Segment size and Gap are not affecting in geometrical encircled energy or the Spot diagram, indicating that segmentation's main effect is in the wave optics domain. So we decided to use PSF and Diffraction

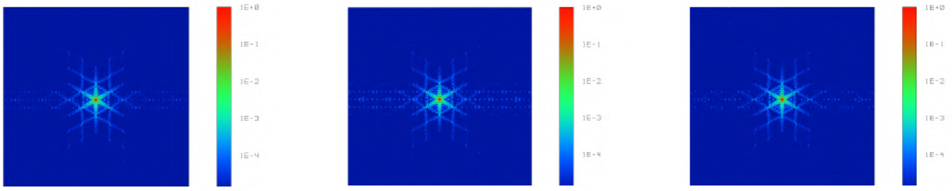

(a) 1 mm gap **(b)** 3 mm gap **(c)** 5 mm gap

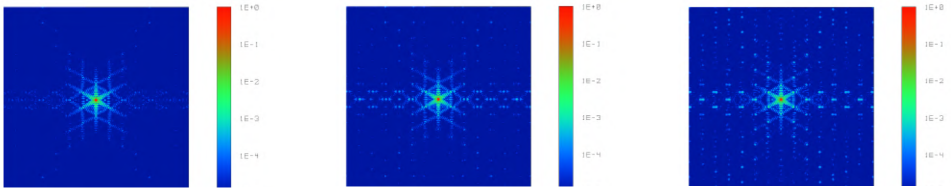

(d) 10 mm gap **(e)** 20 mm gap **(f)** 50 mm gap

Figure 3.19: Logarithmic Scale PSF of telescope with hexagonal segment of 720 mm side and varying inter-segment gap

encircled energy for our analysis. Segment size and Gap have affected the PSF's shape, even though the Strehl ratio remains the same. In figure 3.18 and figure 3.19 we have given the effect of segment size and gap on logarithmic scale PSF for 632.8 nm wavelength. The figure 3.18 gives the change in PSF with variation of segment edge length from 100 mm to 750 mm. As the segment's size increases, the PSF gets more symmetric, and the effects of wings reduce in size, achieving better image contrast by reducing background contamination. So it is advisable to go with larger segment sizes. In figure 3.19, we can see as the gap increases, there are speckle patterns produced in the background, and it gets prominence even with a few mm gap. So a small gap is ideal. After this, the same analysis with varying segments and the inter-segment gap was carried out for 1000 nm. We obtained Geometrical and Diffraction encircled distribution for 50%, 68%, 80%, 90% of the encircled energy. We observed there is not much change in Geometrical encircled energy(GEE) distribution in both 632.8 nm, and 1000 nm. However, there was a prominent change in the Diffraction encircled energy(DEE).

Figure 3.20 and figure 3.21 indicates that changing the Size or Gap of the telescope segments does not affect much in the 50%, 68% of the total DEE. The effect of Gap and size is not exactly linear, but in both the wavelengths, we can see from Figure 3.20a and Figure 3.20b as the size of the segment increase, the energy distribution improves as the effect of wings reduce. The segment size of 750 mm, which is the maximum size we analyzed, shows the best performance. Compared to 750 mm, we can see 720 mm is also an acceptable candidate. Being

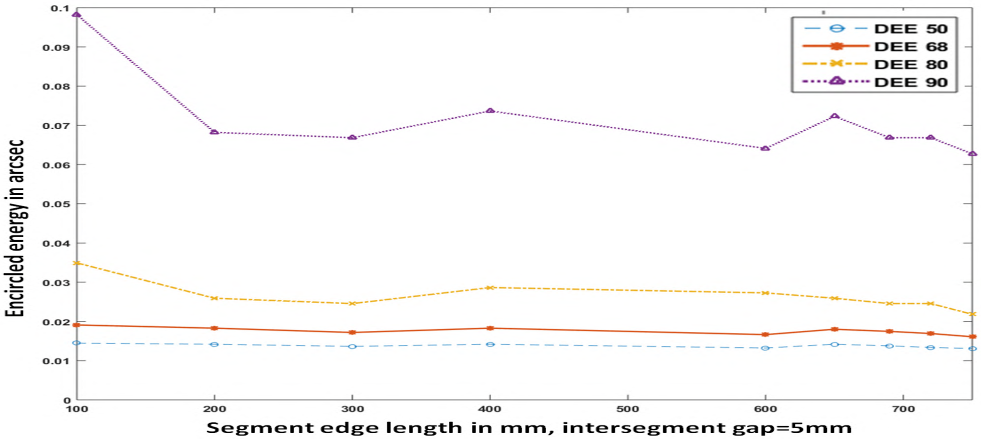

(a) λ=632.8 nm

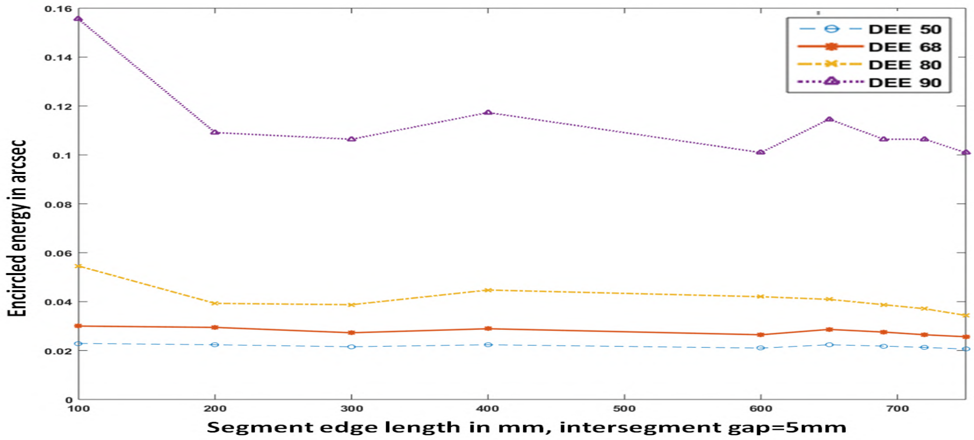

(b) λ=1000 nm

Figure 3.20: Diffraction Encircled Energy for Segment size change, inter-segment gap of 5 mm

the same size as the TMT segment, considering ease of manufacturing, we can go for 720 mm segment. When we consider the effect of the Gap, the same tread in the 50%, 68% can be observed as in the case of segment size change. As the gap increases, the energy distribution gets poor. Creating more and more wing effect and background contamination. From the plots 3.21a and 3.21b a gap size within 10 mm, ideally in the range of 3 - 5 mm is preferable for a 10 m class telescope.

3.7.5 The Shearing error

In a segmented telescope, the segments are placed in a Segment support Assembly (SSA), which should ideally arrest the segment's position such that each segment occupies its ideal position. However, in practical situations achieving this ideal rigid body position is difficult. The segments will have some transitional in-plane errors that can be stated as X Y displacement or shearing error. After segmenta-

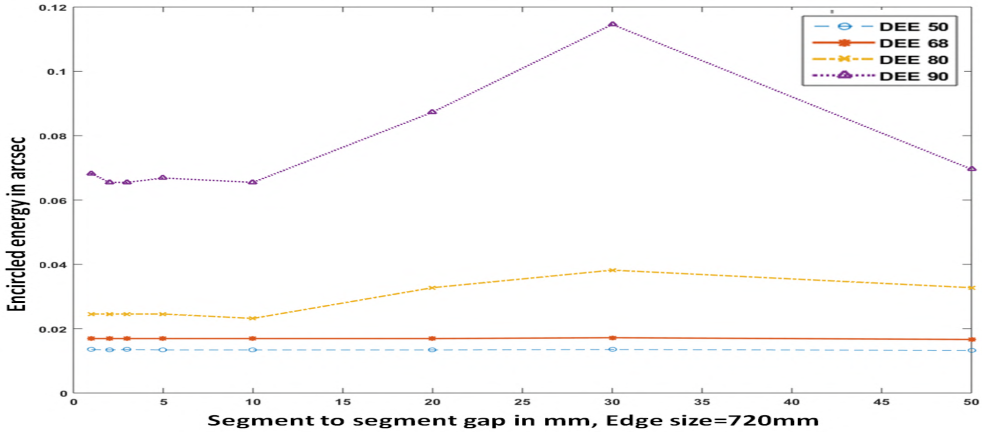

(a) λ=632.8 nm

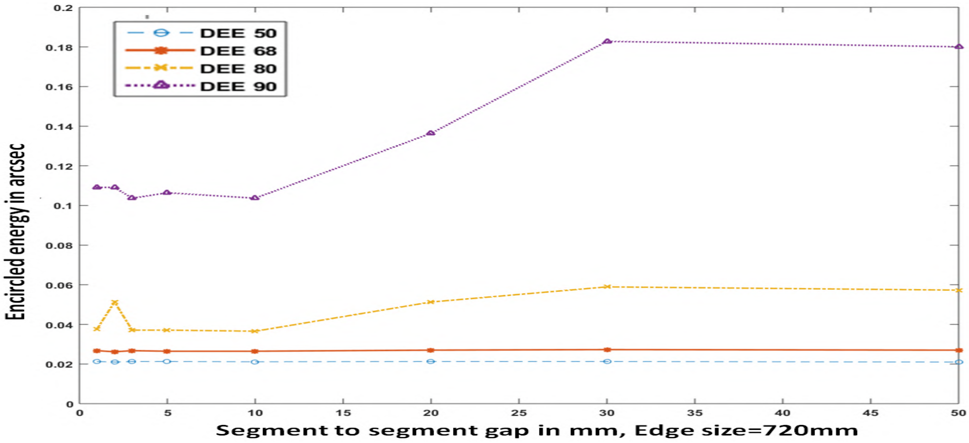

(b) λ=1000 nm

Figure 3.21: Plot shoiwng variation in the encircled energy due change in the inter segment gap. The segment size is chosen to be 720 mm

tion, we give a random transitional error simultaneously in both the X and Y axis for each segment in the ZEMAX optical design. Then the system is optimized with the correction of Piston, tip, and tilt errors.

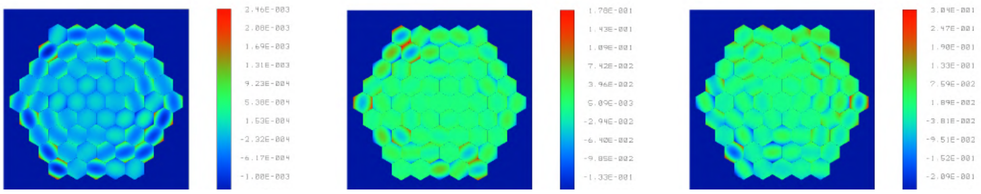

(a) ± 0.001 mm **(b)** ± 1 mm **(c)** ± 2 mm

Figure 3.22: Telescope wavefront subjected to the X-Y shear

The figure 3.22 shows the wave-fronts for three iterations for ± 0.001 mm, ± 1 mm and ± 2 mm. The transitional errors manifest as mostly defocus and astigmatism. Due to strong defocus, transnational errors can show prominence in both the on-axis and off-axis segments. The logarithmic PSFs given in figure

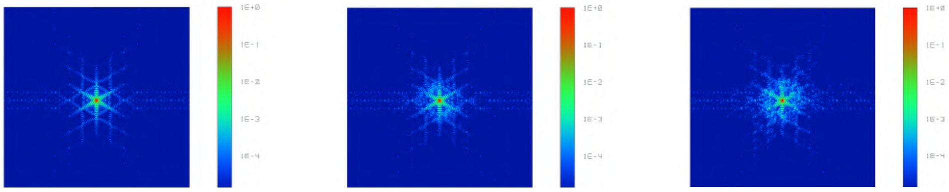

(a) ±0.001 mm **(b)** for ±1 mm **(c)** ±2 mm

Figure 3.23: Logarithmic PSF due different amount of X-Y shear

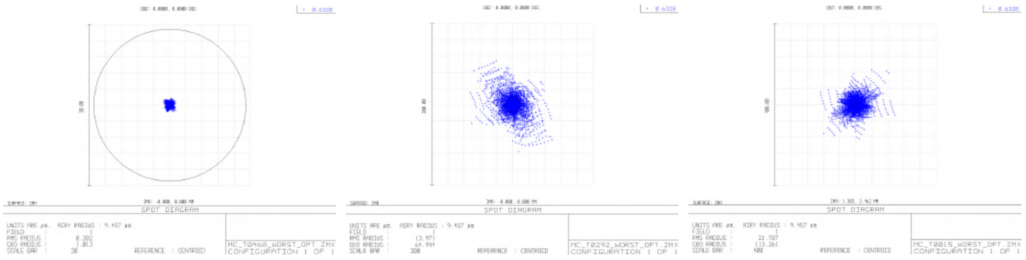

(a) ±0.001 mm **(b)** ±1 mm **(c)** ±2 mm

Figure 3.24: Spot diagrams showing effect of the Shear in the X-Y.

3.23 show that transitional errors keep the core of the PSF intact, also causing the minimum wing effect compared to other aberrations. The Strehl ratio also drops only about 0.9460, even for ±2 mm X Y displacement. The spot diagrams in figure 3.24 show that transitional errors cause the total ray distribution to spread out as we increase the error.

The Figure 3.25a gives the total energy distribution in the focal plane. It indicates that the transitional errors affect mostly the 90% DEE distribution. Indicating the wing effect created by mostly defocus and astigmatism errors. The GEE or the energy by the ray distribution pattern in 3.25b shows that the effect of transitional errors is linear across the ray distribution. So, in Geometrical encircled energy the degradation is steeper for higher percentile of energy. From our analysis we observed that XY translation errors to be considered stringently for telescopes aiming for diffraction limited performance. But they have less severity compared to piston or tip-tilt.

3.7.6 The Effect of the Radius of Curvature Variation

One of the main requirements in any segmented telescope is that all the segments work together to mimic a monolithic, to achieve that, there should be continuity of edge surfaces location between the segments. One of the essential requirements for

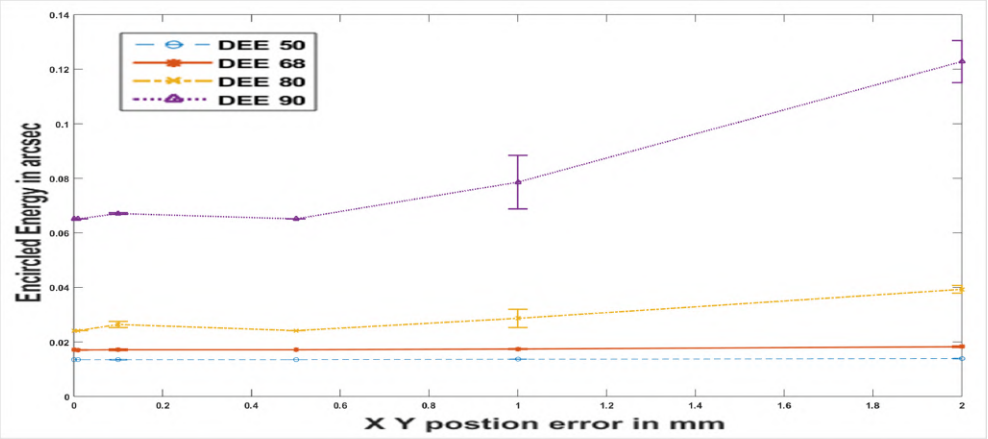

(a) Diffraction Encircled Energy

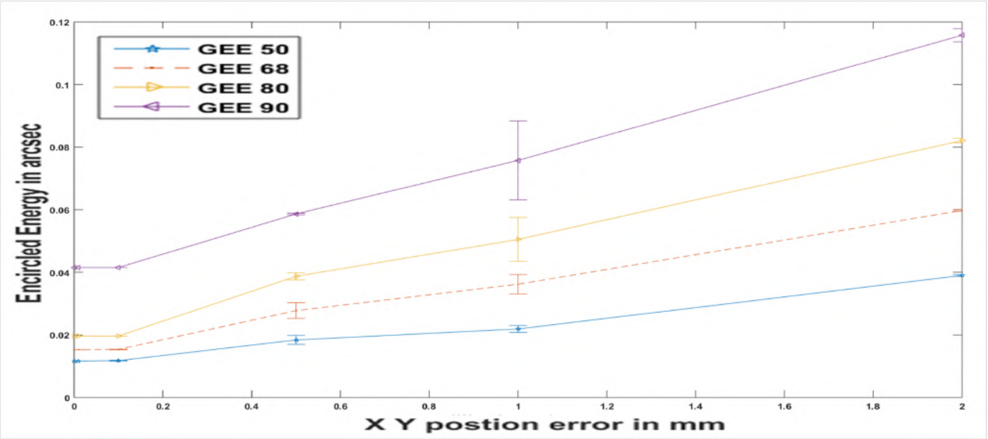

(b) Geometrical Encircled Energy

Figure 3.25: Plot showing changes in the Encircled Energy due to the Shear in the X-Y

this is the segment to segment radius of curvatures remains the same. However, as each segment is manufactured separately in a segmented telescope, this is a troublesome task to achieve, resulting in an error in the local radius of curvatures of each segment. We tried to find the effect of this error on the segmented telescope's performance.

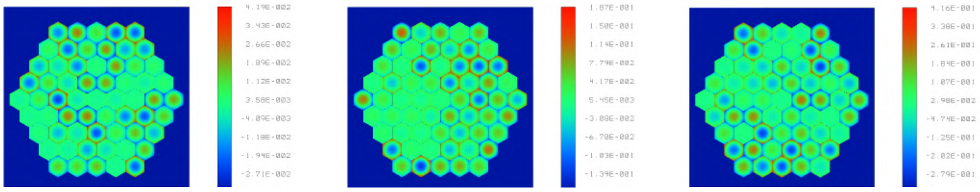

(a) ± 0.1 mm error **(b)** ± 0.5 mm error **(c)** ± 1 mm error

Figure 3.26: Wavefront for Segment to segment ROC variation

From the wave-front maps in Figure 3.26, we can observe that the effect of the ROC error is mostly defocus localized to each segment. We observed that the next dominant aberration is spherical aberration. The defocus aberration coefficient is

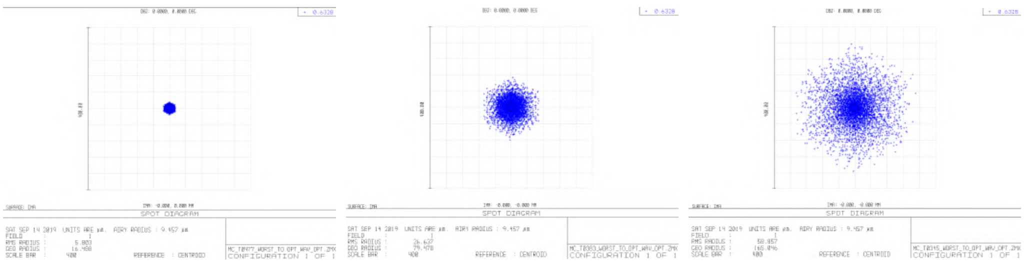
(a) ± 0.1 mm error **(b)** ± 0.5 mm error **(c)** ± 1 mm error

Figure 3.27: Spot diagram for Segment to segment ROC variation (all spot diagrams are to the same scale)

about ten times bigger than the value of the spherical aberration coefficient. Figure 3.27 indicates that the spot diagrams get spread out symmetrically as the ROC error increases, indicating a radial re-distribution in the total ray energy in the focal plane.

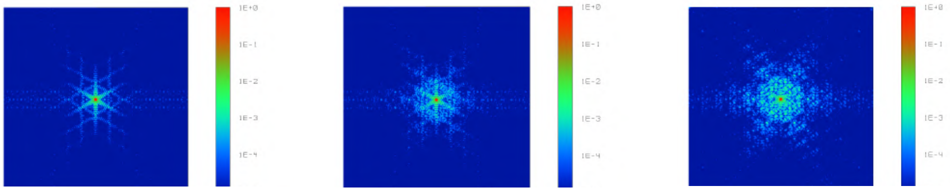

(a) ± 0.1 mm error **(b)** ± 0.5 mm error **(c)** ± 1 mm error

Figure 3.28: Logarithmic PSF for Segment to segment ROC variation

The logarithmic scale PSF in Figure 3.28 indicates that energy at the core of the PSF is more or less sustained with a Strehl ratio drop of 0.9975 for ± 0.1 mm ROC error to 0.7746 ± 1 mm ROC error. However, in the logarithmic scale, we see speckles introduced in the PSF as the error increases. Nevertheless, the symmetry of the PSF is maintained. In the case of a Seeing limited telescope, we observed this error could be corrected to a limit by differential piston and tip, tilt of the telescope segments at the expense of the PSF degradation. In this case, the telescope only achieves a light collecting system's behavior, capable of just summing up the intensity. In a diffraction limited telescope intended for high-resolution imaging, the ROC variation error is corrected with warping harness. However, being circular symmetric aberrations, defocus, and spherical is one of the most difficult aberrations to correct with warping harness due to difficulties in the distribution of force to achieve the required bending.

Figure 3.29a indicated that ROC error mainly causes the energy distribution in the outer rings of the PSF. Also, as the error increases, the range over the

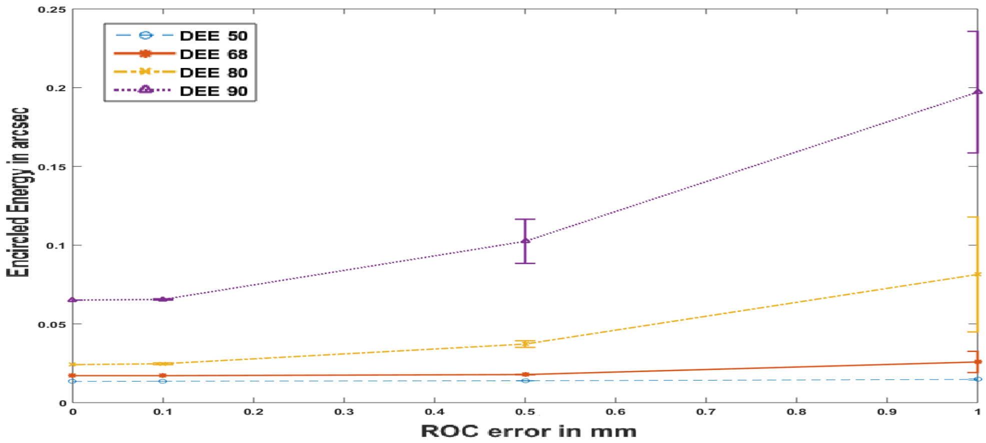

(a) Diffraction Encircled Energy

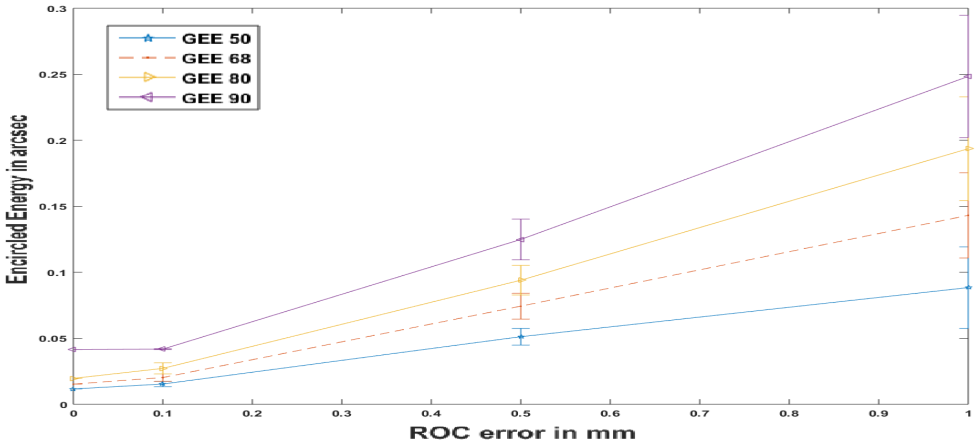

(b) Geometrical Encircled Energy

Figure 3.29: Plot showing variation in the Encircled Energy due to error in the segment ROC

maximum and minimum distribution happens increases as indicated by the error bars. Figure 3.29b indicates that the ray distribution pattern is liner for all the percentile of ray distribution in the focal plane as given by geometrical encircled energy. This error is also a critical error that can cause substantial degradation to both diffraction and geometrical encircled energy. So we suggest that ROC error has to be well corrected for both seeing limited an diffraction limited telescope.

3.7.7 The Segment Figuring Error

In any segmented telescope, a significant portion of the error budget goes to primary mirror segment related errors. Out of which figure error is one of the most important error which is assigned a substantial error budget. For an example in the KECK telescope's the 80% for the whole primary mirror is 0.32 arc-sec, in which 0.242 arc-sec is assigned to segment figuring, which include polishing and support related errors[18]. In the large telescope-like the TMT, the maximum allowable surface RMS deformation is 15-20 nm RMS, as we could collect from different published literature [103],[40],[93]. The tight figure error requirement indicates that this is an important source of error which need to be addressed carefully. Figure error in a segment mainly depends on the manufacturing procedure. Usually polishing with a full-size tool (size of the tool greater than 80% of the segment radius), mounted on very precisely designed segment support system, removing any figuring through Ion beam and finally in-site correction of the figuring error through warping harness, can provide the required high quality optical surface figure. In a telescope like TMT, to achieve the intended performance more than just surface RMS deviation, a segment is needed to possess excellent polished edges and inside surface having minimum to null ripples [102]. Considering all these points, we tried to study the effect of the segment figure in the NLOT which aims to deliver diffraction limited performance over relatively large field. The procedure adopted here is the same as carried for the for the PSMT telescope, described in details in the chapter 2 section 2.9. The tool developed for this purpose uses weightage Zernike (WZ) to simulate figuring error present in the segment and also provide smoothed edges (WZES) as explained in the section 2.9.0.1. For this analysis, we generate random RMS figure error on the segment surface with a mean value of $\lambda/19.5$, $\lambda/39$, and $\lambda/78$ and hence create three different sets of distribution. Such that the randomness in variation of the total RMS value of λ/aN figure error coefficient lies between $\lambda/a(N+0.5)$ to $\lambda/a(N-0.5)$ with N=19.5,and a=1,2,4 for three iterations respectively. All the analyses are done at 632.8 nm wavelength.

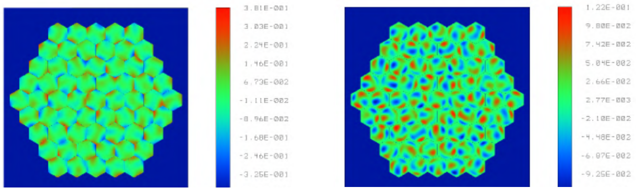

(a) **(b)**

Figure 3.30: Telescope Wavefront Map, (a) WZ, (b)WZES, Applied mean surface figure error of $\lambda/19.5$ nm

Figure 3.30 gives the telescope wave-front for the two different methods used to inject the figure error. In figure 3.30b, we can see the effect of edge smoothing

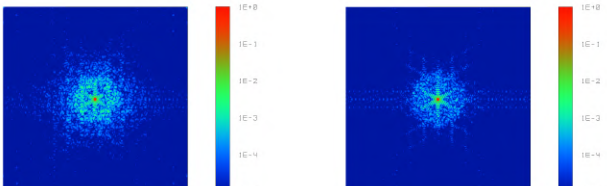

(a) **(b)**

Figure 3.31: Logarithmic Scale PSF, (a)WZ,(b)WZES, Applied mean surface figure error of $\lambda/19.5\,\text{nm}$

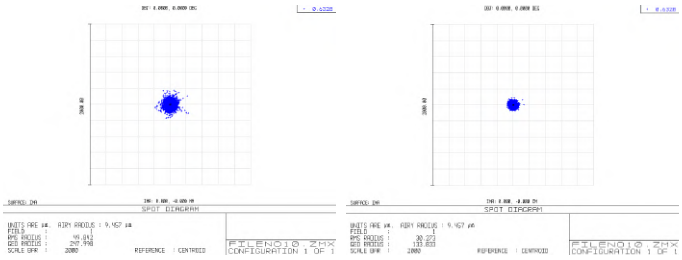

(a) **(b)**

Figure 3.32: Spot diagrams for (a) weightage Zernike and (b) weightage Zernike with smoothed edge. In both cases the mean surface figure error is $\lambda/20\,\text{nm}$

in the wave-front. It not only reduces the total RMS wave-front error but also makes the wave-front continuous across the segment edges. The Figure 3.31 gives the Logarithmic scale PSF. As we translate from the Figure 3.31a to Figure 3.31b we can see the suppression in the speckles such that more energy concentrate in shorter encircled area. The Spot diagrams in Figure 3.32 gives that as we progress through the approaches, the spread of the ray pattern reduces, indicating an improvement in the Geometrical encircled energy.

Figure 3.33 gives the encircled energy variation, when figuring error is injected through only weightage Zernikes (WZ). We observed that the effect of the figure error is more prominent in the higher percentage of the DEE indicating the wing effect. The 50% and 68% energies are less affected by figure error, indicating that even in the presence of substantial figure error, the energy at the core of the PSF holds. Likewise the piston error, there is a shift of energy from the core to the wings, i.e., causing degradation in 80% and 90% encircled energy. The Figure 3.33a indicate how the figure error is different from a piston error, as in Figure 3.9a. Unlike piston figure error also affects GEE ads given by figure 3.33b.

In Figure 3.34, we have used weighted Zernike coefficients with further aperture edge smoothing(WZES). The Figure 3.34a and 3.34b shows that there is a sub-

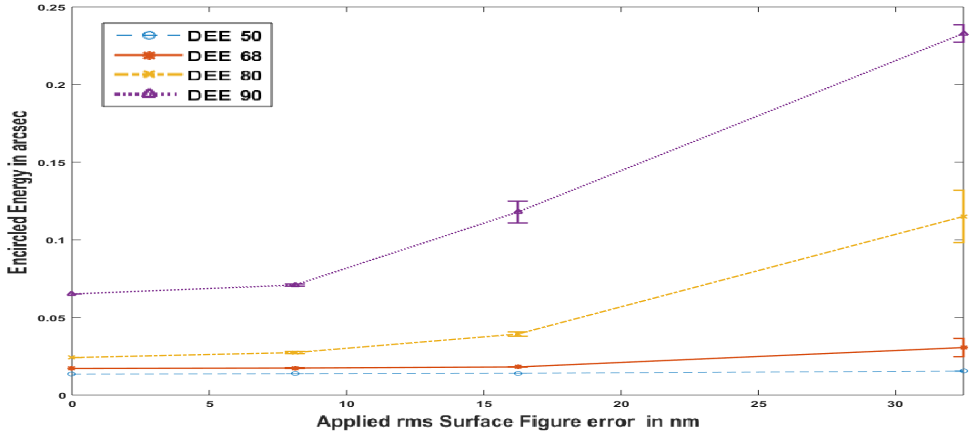

(a) Diffraction Encircled Energy

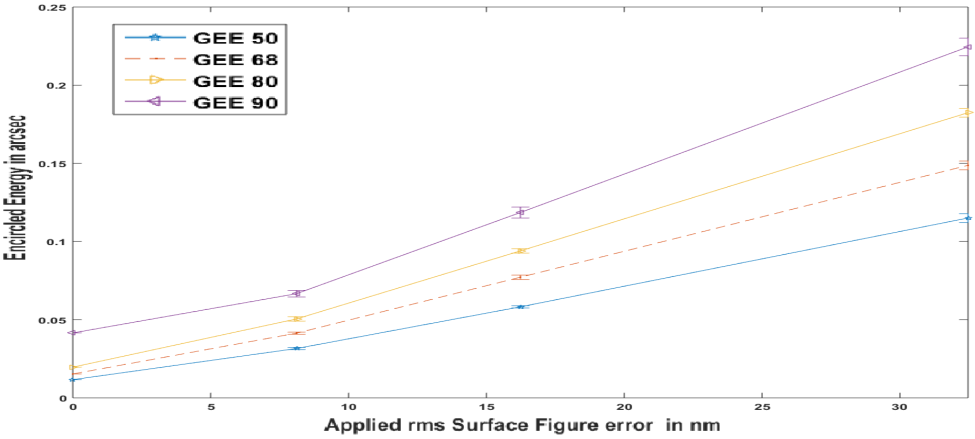

(b) Geometrical Encircled Energy

Figure 3.33: Plot showing effect of the figuring error generated using the weightage Zernike on the encircled energy.

stantial improvement of about two times in the system compared to the weighted Zernike approach. This improvement can be attributed to the reduction in the error produced by each segment edge. However, the most noticeable improvement is in DEE at the 80% and 90% energy. In addition to improving the performance, edge smoothing also serves another purpose. In segmented telescopes, phasing techniques usually minimize the piston error by measuring edge displacement. For the system in which segments are not manufactured with smooth edges, phasing error can not be fully corrected for the entire segment and hence degrades the image quality for the diffraction limited telescope. We can conclude that the figure error can be a severe problem to the telescope working either in the diffraction or seeing limited domain. Deeper understanding of the effect of the figuring error is very important and more extensive study is required to simulate the realistic figuring error using weightage Zernike with the smoothed segment edge and with

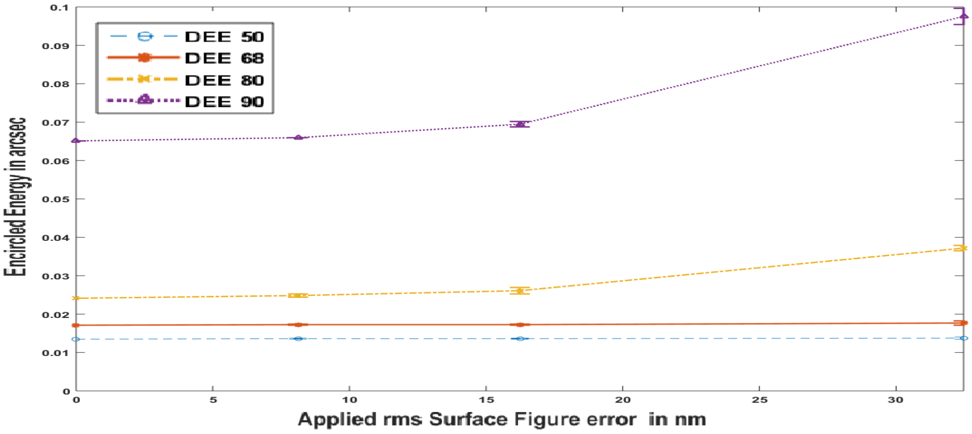

(a) Diffraction Encircled Energy

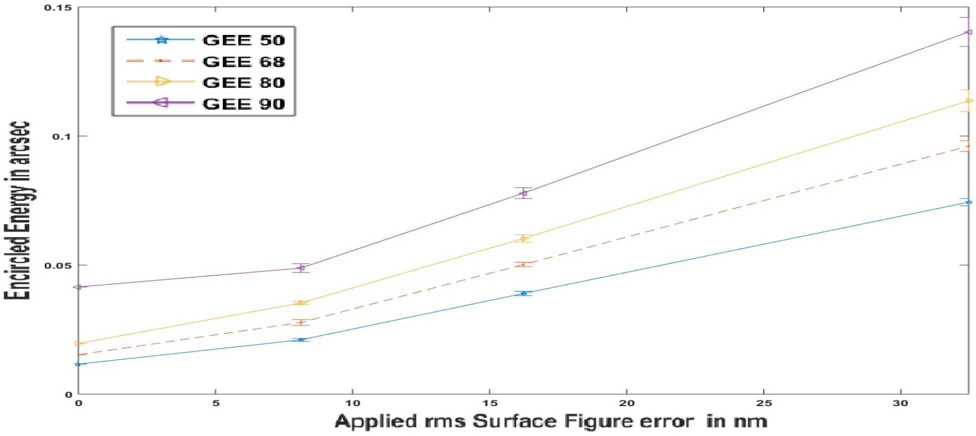

(b) Geometrical Encircled Energy

Figure 3.34: Plot showing effect of the figuring error which also include the edge smoothing on the encircled energy.

reduced surface ripples.

3.8 Tolerance and Error Budget

The top level requirements as given in Table 3.1 formed the basis for the NLOT optics design. Once telescope optics is designed and optical specification is known then next step is to explore the sensitivity of different design parameters which characterized the telescope. The realistic tolerance and hence error estimation is another very important task while designing and building any new telescope. The precise error estimation which can later be used to compare with realized telescope performances, requires knowledge of not only optical tolerance but also needs input from mechanical, thermal as well as wind analysis. As the NLOT design is still under development and not much is know from mechanical front therefore, we have assumed many tolerance values. While making such assumption we explored the literature and whenever possible tried to get the tolerance values from many already realized large telescope such as Keck, SALT, VLT and Gemini. For the NLOT we have opted the same techniques and approaches as we established during the analysis of PSMT, as in section 2.8.

NLOT being a diffraction limited system, will have AO assisted observation, the RMS wave-front error is the ideal tolerance criteria for the telescope. However, in our analysis, we divided the approach into two parts, depending on the error's sensitivity to the tolerance criteria. One being the errors associated with segmented primary alone, which are elaborated in section 3.7, which are considered with RMS wave-front error and for the rest of the system tolerances is derived from the RMS spot radius . Such that all together system performance degrades by a multiple of the initial system performance. The analysis are carried out, and results are presented at 632.8 nm wavelength. The tolerances can be divided into two broader classes, the manufacturing and the operational or the alignment. The operational tolerances are usually non-compensatory at the design level and some of them can corrected by using active correction mechanism. One of the best example of this is use of hexapod based drive for the secondary mirror which maintain its alignment in variable gravity and thermal condition. Whereas, many manufacturing tolerances can be compensatory and hence may be corrected to a limit at the design stage by choosing right kind of compensators. Below we list few important tolerance parameters, which should be at list taken in to consideration:

3.8.0.1 Manufacturing Tolerances

- Primary surface irregularity
- Primary Segments radius of curvature, global and local
- Primary Segment X Y translation
- Primary Segment Clocking
- Secondary surface irregularity
- Secondary Radius of curvature - manufacturing

- Secondary conic constant
- Tertiary surface error in fringes (tertiary is a plane mirror)
- Tertiary surface irregularity

3.8.0.2 Alignment related Tolerances

- Primary segments X, Y tilt
- Primary segment piston
- Secondary X,Y tilt
- Secondary X,Y de-center
- Tertiary X,Y tilt
- Tertiary X,Y de-center
- Focus and de-space change

Tolerances are found with the ZEMAX tolerance analysis scheme. Montecarlo simulations are run with each segment-related error like figure error, and the worst error file is saved for the next error to be added. For other errors other than primary segment related errors, the tolerances are found using the usual established ZEMAX tolerances analysis approach. We present the tolerance analysis for on-axis with telescope facing zenith for three times performance degradation form the ideal diffraction-limited system. This will place the system performance still within the vicinity a near diffraction limited system. The analysis is done with Primary-Secondary Despace, Focus and Primary segment piston, tip, and tilt (PTT) as compensation for segment positional errors.

The sensitivity of the errors with the corresponding tolerances are given in Table 3.5. From this table it is clear that the most sensitive parameter is the figure of primary mirror segment. Without use of AO if we like to achieve diffraction limited performance then mirror segments should be made with exceptionally high optical quality. Then next sensitive parameter is again linked with the optical figure i.e. figuring error of the secondary mirror. After that segment tip/tilt and

ROC errors appears to be very sensitive. The 6-10 ranks are associated with the secondary alignment and the focus error. As expected the alignment errors of the tertiary mirror which is a flat mirror used to just fold the telescope beam to Nasmyth focus, have got the least sensitivity.

Table 3.5: Telescope tolerance

Ranking	Parameter	Nominal value	Tolerance
1	Primary Segment Surface Figure	-	RMS: $\lambda/78$ PV: $\lambda/15.6$
2	Secondary Surface Figure error	-	RMS: $\lambda/50$ PV: $\lambda/10$
3	Primary Segment Tip, Tilt	-	± 0.005 arcsec
4	Primary Segment to segment ROC variation	35000 mm	± 0.05 mm
5	Tertiary Fringe	-	±2
6	tilt in y of the secondary	-	± 0.001 degree
7	tilt in x of the secondary	-	± 0.001 degree
8	De-center x of the secondary	-	±0.03 mm
9	De-center y of the secondary	-	±0.03 mm
10	Distance between the primary and secondary	15.5 m	±0.0025 mm
11	Radius of curvature of the secondary	4.57 m	±15 mm
12	Radius of curvature of the primary	35000 mm	±150 mm
13	Focus Distance	6.8 m	±0.15 mm
14	Primary Segment X-Y translation	-	±0.1 mm
15	Primary Segment Clocking	-	±10 arcsec
16	Tertiary decenter in y	-	(±0.2 mm)
17	Tertiary tilt in y	-	(±0.01 mm)
18	conic secondary	-1.6594932	(±0.001)
19	Conic primary	-1.00360800	((±0.0001)
20	Primary Piston	-	((±50 nm)
21	Tertiary tilt in x	-	((±0.01 mm)
22	Tertiary decenter in x	-	(±0.2 mm)

3.8.1 Error Budget

The last task in the tolerance analysis is generating an error budget break up table. In order to do this one require an image quality performance indicator, such as PSSN, or Central Intensity Ratio (CIR) [104], or Encircled Energy(EE) .

In a very large segmented telescope like the TMT and the E-ELT, the PSSN is found to be the most suitable performance indicator, Whereas, NLOT is a 10 m class telescope like KECK or SALT, which uses encircled energy as a image quality indicator/metric, therefore, we have also used it to create our error budget. We have presented the encircled energy breakup for two EE contours, one at half intensity contour (EE50%) and other one for (EE 80%). The Table 3.6 provide the break up of the error budget.

Table 3.6: Error Budget

Sl.NO	Source of Error	D-50 (arcsec)	D-80 (arcsec)
1	Primary Figure ($\lambda/78$)	0.01700	0.02900
2	Secondary Figure	0.00931	0.01480
3	Primary tip&tilt (±0.005arcsec)	0.00800	0.00830
4	Primary ROC(±0.05 mm)	0.00454	0.00769
5	Tertiary fringe number (±2)	0.00600	0.00610
6	secondary tilt in y(±0.001)	0.00430	0.00531
7	secondary tilt in x (±0.001)	0.003864	0.00531
8	secondary decenter in x(±0.03)	0.003194	0.00532
9	secondary decenter in y (±0.03)	0.003414	0.00532
10	Primary secondary distance(±0.0025mm)	0.0050	0.00510
11	Secondary RoC(±15mm)	0.00317	0.00531
12	Primary RoC(±150mm)	0.00110	0.00556
13	Focus distance (±0.15mm)	0.00333	0.00400
14	Primary X Y position (±0.1mm)	0.00181	0.00190
15	Primary clocking (±10 arcsecmm)	0.00182	0.00132
16	Tertiary decenter in y (±0.2mm)	0.00400	0.00532
17	Tertiary tilt in y (±0.01mm)	0.00400	0.00532
18	conic secondary(±0.001)	0.00100	0.00120
19	Conic primary(±0.0001)	0.00040	0.00060
20a	Primary Piston (±50nm) (Variation in DEE)	0.00309	0.02810
20b	Primary Piston (±50nm) (Variation in GEE)	0.00010	0.00020
21	Tertiary tilt in x (±0.01mm)	0.00010	0.00020
22	Tertiary decenter in x (±0.2mm)	0.00010	0.00020

The errors can be summed in a quadrature addition, assuming all the errors follow a normal distribution. The primary figure is the most dominant term, followed by secondary figure and primary tip and tilt. The primary segment figure requirement of RMS $\lambda/78$ in surface seems to be too tight because we try to maintain the diffraction limited performance in the design itself. In real telescope systems adaptive optics (AO) and warping harness helps in mitigating this tight requirement. As our earlier analyses indicated, primary segment to segment ROC also seems to be another major contributor to the error even with a tight tolerance of ±0.05 mm. As this is an RC telescope, the secondary alignments and figure also play a crucial role in the overall telescope performance. The piston error of primary do contribute to the overall energy budget as per DEE values, but it is not a major contributor when we consider the intensity distribution budget or GEE. Tertiary alignments seem minimum contributor to the error budget. The total system degradation with these errors are D50 = 0.0254 arc-sec and D80 = 0.0478 arc-sec, which is within three times ideal performance. The ideal system performance for on-axis is D50 = 0.011 arc-sec and D80 = 0.018 arc-sec. The total system performance including design errors are D50 = 0.0279 arc-sec and D80 = 0.051 arc-sec. All the values are given in arc-sec diameter. The total FWHM (D50) system performance is still within the diffraction limit of the system, which is about 0.026 arc-sec.

3.9 Mimicking Aspheric Profile with Spherical Segments

One of the challenge linked with segmented mirror technology is the complexities associated with the manufacturing of aspheric off-axis mirror segments. Despite many new mirror fabrication techniques invented during the last three decades [30] [31] [32] [33] , off-axis mirrors are difficult to manufacture and hence very expensive, which increases the overall budget of any new telescope. To solve this problem, an effort started to use the spherical primary mirror so that each mirror segment will be identical and spherical mirror segments are easier to fabricate. In one of the approaches, the substantial spherical aberration introduced by a spherical mirror is corrected by using a few reflecting optics located close to the prime focus [34] [35]. The HET and SALT telescopes used this method and provided the world with two of the cheapest telescopes in that technology [36] . The HET(Hobby- Eberly telescope)/SALT (The South African large telescope) optical design, which has got only a prime focus, may not be suitable for many science programs where large instruments weighing up to several tons are required. Such bulky instruments are usually placed in Cassegrain and/or Nasmyth focus. There are a few efforts made to explore alternate designs which not only uses a spherical primary mirror but provides an option to have Nasmyth/Cassegrain focus[37] [38] [39] . All these designs use 2-3 additional reflective aspheric mirrors to correct spherical aberration introduced by the spherical primary mirror. These design approaches possess their on manufacturing challenges. So taking advantage of the segmented mirror that can be individually placed in any desired fashion, we can attempt to develop a simple two or three mirror RC kind of design using spherical mirror segments, by taking advantage of the fact that individual parts in a segmented mirror design can be placed in any desired fashion.

Making aspheric primary's made of off-axis mirror segments, of astronomical telescopes, is still a challenge. We have conducted a study in which we explored the possibility of mimicking an aspheric hyperbolic primary mirror by using smaller spherical mirror segments. For this, we have designed a 12 m size RC telescope with the parameters as given in Table 3.3 and conducted three analyses such as replacing the aspheric segments with spherical segment with specific ROC. The way we calculate this segment-specific ROC for the second approach and the third approach is given in section.A.1.3 and section.A.1.4 of Appendix respectively. We also conducted studies with changing segment size and F ratio of the primary. We found that none of these methods provided acceptable image quality unless we incorporate the warping harness in the segment support. The use of the warping harness remarkably reduced the wave-front error and delivered a decent image quality over a large field of view.

3.9.0.1 Segments with Fixed Radius of Curvature

In this analysis, all the segments were assigned the same radius of curvature (ROC) as vertex ROC of the ideal aspheric hyperbolic segment. Piston Tip and Tilt (PTT) of each segment are allowed to change in the course of optimization while keeping the ROC fixed.Before optimization, the wavefront error was found to be quite large. With PTT optimization, the wavefront error reduces substantially.

As expected, the smallest segment (220 mm) gave the lowest wavefront error of seven waves at a system wavelength of 632.8 nm. The optimized wavefront of the primary mirror is shown in Figure 3.35.

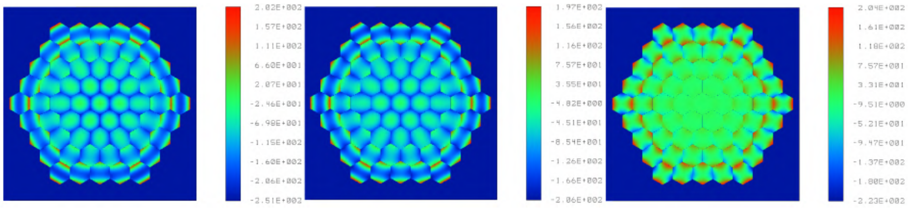

(a) (b) (c)

Figure 3.35: The wave-front maps (in waves) of the full telescope for (a) Fixed ROC , (b) Local ROC and (c) Best fit ROC , Segment size of 720 mm, with PTT optimization

3.9.0.2 Segments with Local Radius of Curvature

Here, the aspheric segment's Local ROC is calculated according to equations given in section A.1.3 of the appendix. Local ROC is equivalent to ROC given by a spherometer. One set of optimized wavefront is shown in Figure 3.35. When we increase the segmentation (by using smaller segment size), then the mismatch between the shape of the aspheric and spherical segments reduces, reducing root mean square (RMS) and peak to valley (PV) wavefront errors. The minimum wavefront error obtained after optimization is 5.5 waves for a 220 mm segment system. The other performance parameters, like spot radius and encircled energy still suffer from huge aberrations introduced due to the replacement of aspheric segments. Even though Compared to the fixed ROC method, there is some improvement; wavefront error is still substantial and unacceptable.

3.9.0.3 Segment with Best-fit Radius of Curvature

In the third method, we used the segments with the best-fit ROC derived for each aspheric segment using the calculations given in section A.1.4 of appendix to replace the aspheric segment, and the system is PTT optimized. The minimum wavefront obtained after optimization is about 4.5 waves for the telescope with a primary mirror made of 220 mm segments. In comparison to the previous two methods, there is a marginal improvement RMS wavefront error. One can find a substantial improvement in the inner part of the primary mirror (see Figure 3.35(c)) where the wavefront error is small and also smooth. The rapid increase in the wavefront error is seen outwards, which is the region where asphericity is very dominant. The spherical mirror fails to mimic aspheric mirror segments despite varying PTT and ROC. The 4.5 wave is a large wavefront error, and the telescope of this kind would not suffice any scientific objectives.

3.9.0.4 Effect of the Segment Size

Our study has not attempted to simulate the performance of very small (below 220 mm) or large (above 720 mm) mirror segments because of one or other reasons they are found to be not adequate for any segment mirror telescope.

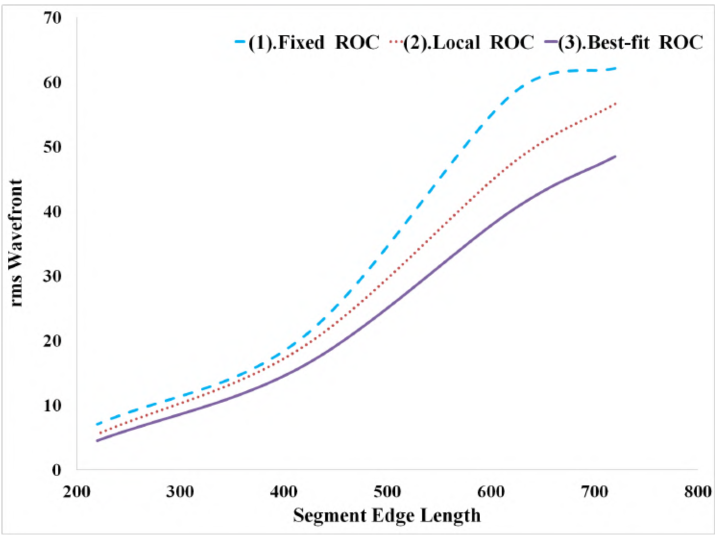

Figure 3.36: Effect of segment size on the optimized rms wave-front error (waves).

In Figure 3.36 we plotted the wavefront errors against segment size as expected; the wavefront error increases as we increase the segment size. The change is slower till 420 mm, after which one can notice a steep increase in the wavefront error. Among all the three options, the best fit ROC gives the lowest wavefront error. However, it requires varying ROC among segments, which can be as large as 3% to the ideal center segment's nominal vertex ROC (35000 mm). This may pose manufacturing difficulty while producing mirror segments using conventional manufacturing techniques. Compared to the best fit method, the variation in the ROC is less in the Local ROC method; however, the wavefront error is a bit larger.

In the Local and best fit method With respect to the nominal ROC of the central mirror, the outermost segment can have a ROC as large as 700 mm. As expected, the best fit ROC method gives the least wavefront error, whereas the fixed ROC has shown little poor performance. We also found in our study that , despite using the smallest segment of 220 mm size, the wavefront error couldn't be brought down to less than 4 waves. Opting very small mirror segments would require a large number of mirror segments to fill the aperture of the primary mirror. This, intern would require active components such as warping harness, actuator, and edge sensors in huge numbers. The use of a smaller mirror segment will not only take control of the primary mirror complex, but it would also not be economical.

3.9.0.5 Effect of the Primary F ratio

From the wavefront error, it is clear that the asphericity effect is predominant in the outer segments and varying PTT, and the segment ROC cannot correct it. The one solution to overcome this problem is using a thin mirror along with a simple warping harness that can correct the residual error. Another option is to increase the F ratio of the primary mirror; this analysis results are shown in Figure 3.37. The wavefront error reduces substantially with the F no. The RMS wavefront error of seven waves for the F/2 system becomes two waves when we go for F/3 primary system made with 420mm segments. A telescope with F/4 primary or larger may not be feasible. However, it may be possible to make use of F/3 primary in a real telescope. Figure 3.38 shows the wavefront error for the primary with F/2 and F/3. From this wavefront plot, outer segments are subjected to large astigmatism type aberrations, which can be corrected by adding a warping harness.

F ratio larger than 3 may not be feasible in practice, due to increased primary-secondary separation which will lead to many problems such as the requirement of the large enclosure, increased wind shake, gravity-induced truss flexure, etc.

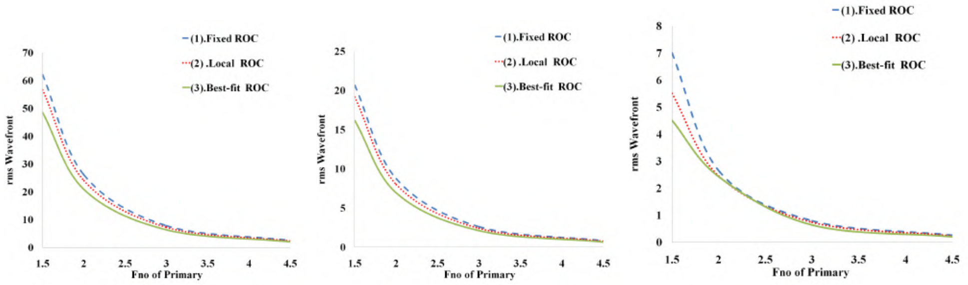

(a) (b) (c)

Figure 3.37: Variation of the optimized rms wave-front (waves) against the F number of the telescope's primary mirror. The three plots are for the telescope made with (a) 720 mm, (b) 420 mm and (c) 220 mm mirror segments respectively.

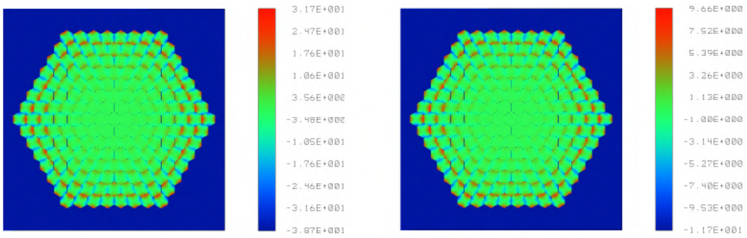

(a) (b)

Figure 3.38: The RMS wave-front(waves) for the system with (a) F/2, (b) F/3. The segment size chosen for the primary is 420 mm and PTT optimization has been carried on the best fit option.

3.9.1 Correcting the figure of the Mirror using Warping Harness

3.9.1.1 Warping Harness

Using force and moment actuators, any thin and large mirror can be warped so that the figuring error introduced during manufacturing and/or due to the effect of variable gravity/temperature on the segment support can be fully/partially corrected. This add-on device, which accomplishes the controlled changes in the figure of the mirror, is called warping harness, and it has become one of the essential features in all segmented mirror telescopes such as Keck, TMT, and E-ELT [18] [40] [41] [42]. The warping harness designed for these segmented mirror telescopes primarily uses moment actuators, which applies discrete pre-calibrated moment at the wiffle tree joints/pivots. The applied moment alters the distribution of the forces exerted to the back of the mirror segment, which creates predictable changes in the mirror surface. For example, the TMT mirror segments are supported at 27 points with the help of nine small and three large wifle tree triangles and have got 12 flexible pivots. There are 21-moment actuators (two-moment actuators working orthogonal at nine pivots and single moment actuators at the remaining three pivots), which can apply $\pm 100\,\mathrm{N}$ push-pull force to 27 support points and can warp TMT mirror segment to few tens of micron P-V. The bending moment is measured in real-time through strain gauges with an accuracy of 0.1%. The relation between the force exerted to each support point, and changes in the optical figure can be expressed in the matrix equation. In most cases, the Singular Value Decomposition (SVD) is used to solve the inversion problem. The low spatial frequency modes that arise, either due to support or mirror manufacturing defect, can effectively be corrected by opting modal approach, in which the optical figure is represented by a set of orthogonal bending modes (SVD or Zernike). The high spatial frequency modes are ignored, as they contribute very little to total wavefront error and require large number actuators as well as very strong forces.[43] [46] [45]. From FEA simulation as well as experimentation with the realized warping harness, it has been found that most of low order optical aberrations can be corrected with very high precision, except rotational symmetric modes such as focus and spherical aberrations. FEA analysis shows that aberration related to astigmatism can be corrected to the extent of 98% or better [40]. However, in practice, correction related accuracy may be primarily limited by the figure/warp measurement error required for the calibration as well as error associated with the generation of force/moment [46] [45], [47].

3.9.1.2 Simulation of Warping of Segments using Zernike Polynomial

The decomposed Zernike aberration coefficients till 17 terms for the extreme segment after PTT optimization in waves has been given in the Table 3.7. Warping harness is not incorporated into the system yet. If we ignore the residual piston term, then one can notice that defocus and astigmatism are the largest contributors to the wavefront error. In contrast, coma, trefoil, and spherical aberrations contribute marginally. Next, the effect of the warping harness is simulated by correcting lower order Zernike polynomial. Once we incorporate warping har-

Table 3.7: Values of decomposed Zernike coefficients in the wave unit for the outermost segment. The Zernike fitting has been carried out after the optimization using best fit and fixed ROC methods, at 632.8 nm wavelength

Zernike-Term	Coefficient (Best fit ROC)	Coefficient (Fixed ROC)	Zernike Equation	Related aberration
Z 1	2.5697	118.0306	1	Piston
Z 2	-2.6916	0.7973	$4^{\frac{1}{2}}(p)\cos(A)$	X-tilt
Z 3	-1.4893	0.6515	$4^{\frac{1}{2}}(p)\sin(A)$	Y-Tilt
Z 4	1.6936	68.3466	$3^{\frac{1}{2}}(2p^2-1)$	Defocus
Z 5	82.3999	84.2538	$6^{\frac{1}{2}}(p^2)\sin(2A)$	Oblique astigmatism
Z 6	-47.5339	-48.7514	$6^{\frac{1}{2}}(p^2)\cos(2A)$	Vertical Astigmatism
Z 7	-6.7450	-6.7825	$8^{\frac{1}{2}}(3p^3-2p)\sin(A)$	Vertical Coma
Z 8	-3.8958	-3.9116	$8^{\frac{1}{2}}(3p^3-2p)\cos(A)$	Horizontal Coma
Z 9	0.0001	-0.0005	$8^{\frac{1}{2}}(p^3)\sin(3A)$	Vertical Trefoil
Z 10	-0.1788	-0.2538	$8^{\frac{1}{2}}(p^3)\cos(3A)$	Horizontal Trefoil
Z 11	0.1626	0.1560	$5^{\frac{1}{2}}(6p^4-6p^2+1)$	Primary Spherical
Z 12	0.0117	0.0155	$10^{\frac{1}{2}}(4p^4-3p^2)\cos(2A)$	Vertical Sec-Astigmatism
Z 13	-0.0203	-0.0268	$10^{\frac{1}{2}}(4p^4-3p^2\sin(2A)$	Oblique Sec-Astigmatism
Z 14	0.0042	0.0032	$10^{\frac{1}{2}}(p^4)\cos(4A)$	Vertical Quadrafoil
Z 15	0.0074	0.0057	$10^{\frac{1}{2}}(p^4)\sin(4A)$	Oblique Quadrafiol
Z 16	0.0009	0.0010	$12^{\frac{1}{2}}(10p^5-12p^3+3p)\cos(A)$	Sec-Coma Horizontal
Z 17	0.0016	0.0018	$12^{\frac{1}{2}}(10p^5-12p^3+3p)\sin(A)$	Sec-Coma Vertical

ness, the primary mirror optimized with the best fit ROC and the fixed ROC give similar image qualities. The amount of maximum warping required is almost similar in both. In the fixed ROC method, all mirror segments will have identical ROC and hence would be much easier to manufacture as well as interchangeable during the long operational life of the telescope. However, fixed ROC would leave large defocus term, which is a bit hard to correct by any warping harness. This problem will be solved with the best fit method; however, it would require many polishing tools while manufacturing the segments. In our study, we have found that if only lower-order aberrations represented till Zernike term 10 can be corrected by warping harness, it can provide telescope image quality that may be good enough for the seeing limited observation. However, when Zernike term 11 (spherical aberration) can also be corrected by warping harness, the telescope can deliver diffraction-limited image quality. Our analysis indicates that the force/warp require to correct the wavefront error associated with mirror segments will be much larger (about 100 microns PV (Peak to valley) changes on the sag) than the extreme force/warp generated by warping harness designed for the TMT and the E-ELT telescopes [41] [42] . FEA analysis, as well as experimentation, has shown that maximum deformation on the segment surface in terms of P-V by TMT warping harness can be as large as 21 microns. Considering deformation is elastic as well as linear, five times more warping forces are required in comparison to the TMT. Warping or stressing mirror by such a large amount is something not impossible. The Stress Mirror Polishing technique used to manufacturing the aspheric mirror segment introduces a warp on the mirror surface of the magnitude of nearly 100-200 microns [49] [32] PV. Despite the large warp required by SMP, analysis has shown that stress injected into the mirror segment is much lower than the yield stress of the material used. From our analysis, we have seen that astigmatism is the most dominant term, and it can be easily corrected by applying a relatively lesser amount of force [43] [46] [45]. Furthermore, since all these lower-order terms with very high amplitudes are well characterized, it can be divided into two parts i.e., large and the small amplitudes. The large amplitude may be treated as a static component and can be corrected with a simple passive warping element. Whereas, smaller amplitude parts may be dynamically corrected with the help of an active warping harness. Another possibility is changing the mirror aspect ratio (diameter to thickness ratio) in a way that it becomes more flexible, but at the same time not create any gravity and/or control-related problems. For example, LAMOST active mirror is 1.1 m in diameter and 25 mm in thickness. By using 34 force actuators, the mirror segment can be deformed by few tens of microns [48] [50]. During our analysis, The overall figure of the segmented primary created using best fit and fixed ROC methods are further optimized using a virtual warping harness represented by Zernike terms. Since 720 mm is considered the preferred segment size for many upcoming segmented mirror telescopes such as TMT, E-ELT, MSE, Chinese 12 m telescope CLOT, and the proposed Indian 12 m class telescope, we decided to carry out our warping harness related studies with the same size. An additional reason for choosing 720 mm is that the warping harness works more effectively in larger mirror segments. We consider the de-

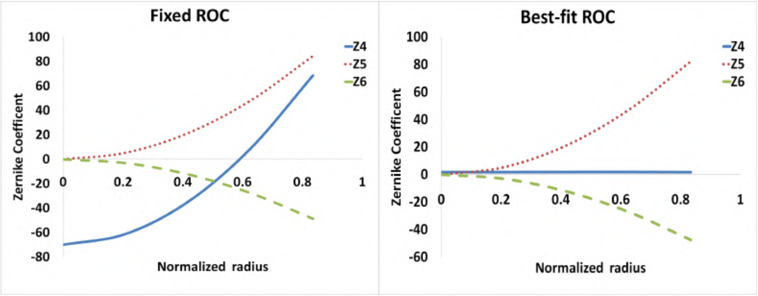

(a) (b)

Figure 3.39: The variation of Zernike coefficients (given in the unit of waves) against normalized radius for the fixed and best-fit ROC methods, of wavefront.

formation effect on the figure of the mirror. We have not attempted to consider issues linked with the mechanical aspects of warping harness, such as bending moment/force, elastic flexibility, and stress.

3.9.1.3 Radial Variation of Low Order Zernike Terms

Asphericity increases radially as we move away from the center to the edge of the primary. From seminal works of [18], one can derive the radial variation of the Zernike coefficients. In Figure 3.39, we have plotted the most dominant terms of the virtual warping harness i.e. the defocus (Z4) and astigmatism (Z5 & Z6) against the normalized radius of the primary mirror. As expected, in the case of the best fit ROC method, the defocus term is pretty small and almost remains invariant over the entire primary mirror. Whereas for the fixed ROC, defocus varies from nearly -70 wave to +70 wave and becomes zero close to 0.6 radii (indicating an optimum ROC for the entire telescope is used as fixed value). On the other hand, the term related to astigmatism varies almost exponentially in both the cases and becomes fairly large to the outermost segments.As we have learned from warping harness related studies that symmetric rotational terms such as defocus and spherical aberration are difficult to correct; therefore, the best-fit method may be preferable.

3.9.2 Wavefront Error and the Image Quality

After we incorporated the virtual warping harness to the PTT optimized telescope,the wavefront is progressively corrected with the Zernike. The RMS value

Table 3.8: RMS wavefront error in waves after correcting Zernike for Fixed and best fit ROC analysis.

Zernike terms	1-3	1-4	1-6	1-8	1-10	1-11	1-13	1-15	1-17
Fixed ROC									
(whole primary)	61.24	47.69	4.73	0.1597	0.1518	0.0058	0.0004	0.0004	0.0002
(outermost segment)	99.94	78.42	6.46	0.1746	0.1523	0.0092	0.0005	0.0005	0.0003
Best fit ROC									
(whole primary)	48.62	47.61	4.66	0.1558	0.1490	0.0055	0.0004	0.0004	0.0001
(outermost segment)	79.36	77.25	6.27	0.165	0.1481	0.0084	0.0005	0.0005	0.0003

of the wavefront error after correcting a set of Zernike terms in the spherical mirror is given in the Table 3.8. The first three terms are a residual piston, tip, and tilt, which can be corrected without a warping harness, whereas the fourth term is defocus and requires a warping harness. Suppose we consider the best fit ROC method. In that case, a substantial improvement over wavefront error seems to happen after the exclusion of astigmatism, which reduced RMS error by almost ten times from 47.61 waves to 4.66 waves. However, even at this stage,telescope image quality is nowhere close to the acceptable range. When we incorporate coma (Zernike terms 7 and 8) in the fitting, then telescope RMS error reduces to $\frac{\lambda}{6.5}$. With added trefoil (Zernike term 9 and 10), RMS error reduces to $\frac{\lambda}{6.6}$, making the telescope to be used for seeing limited observations. After that if we correct the primary spherical aberration (term Z11), then the image quality remarkably improves, and wavefront error reduces to $\frac{\lambda}{188}$, that is diffraction-limited performance. We observed the same trend of performance improvement, also in the case of fixed ROC, as seen in Table 3.8.

In Table 3.9, we present the results of our image quality analysis carried for both optimization methods and the image quality expected from an ideal RC telescope made of the monolithic primary mirror. From Table 3.9 it is clear that both best fit and fixed ROC methods give almost similar on and off-axis image

Table 3.9: Image quality in arcsec of the ideal RC telescope and the optimized segmented mirror telescope

	Fixed ROC			Best Fit ROC		
	RMS Spot Size	EE50	EE80	RMS Spot size	EE50	EE80
PTT & Z4-Z10 Optimization						
On Axis	0.590	0.349	0.768	0.581	0.339	0.743
20 arc-minutes	0.690	0.497	0.810	0.677	0.488	0.799
PTT & Z4-Z11 Optimization						
On Axis	0.0200	0.0155	0.0368	0.0193	0.0152	0.0364
20 arc-minutes	0.349	0.347	0.441	0.348	0.345	0.437
Ideal RC						
On Axis	0.001	0.011	0.019			
20 arc-minutes	0.353	0.354	0.446			

qualities. In the case of RC and Z4-Z11 optimized telescopes, off-axis image quality degrades as the field of view increases. Whereas Z4-Z10 optimized telescope provides almost the same image quality all over the field of view.

3.9.2.1 Figure of the Optimized Segmented Primary Mirror

We have created a map of the surface difference between an ideal hyperbola used to form RC primary and the primary mirror formed using spherical mirror segments after PTT optimization and Zernike warping (see Figure 3.40). The RMS difference between these surfaces is just a few nanometers, which indicates that we could indeed mimic a hyperboloid needed for the RC design in both best fit and fixed ROC methods.

It appears from our study that with the help of wrapping harness which is capable of correcting low order aberrations, the residual wavefront error after PTT optimization can be almost fully corrected and the telescope can provide as good an image quality as one can expect from any telescope made of an aspherical primary mirror. However, one of the practical problems one needs to consider is whether the mirror segment can withstand the large warping force needed to correct defocus and astigmatism, which can have Zernike coefficients as large as 35 - 40 μm.

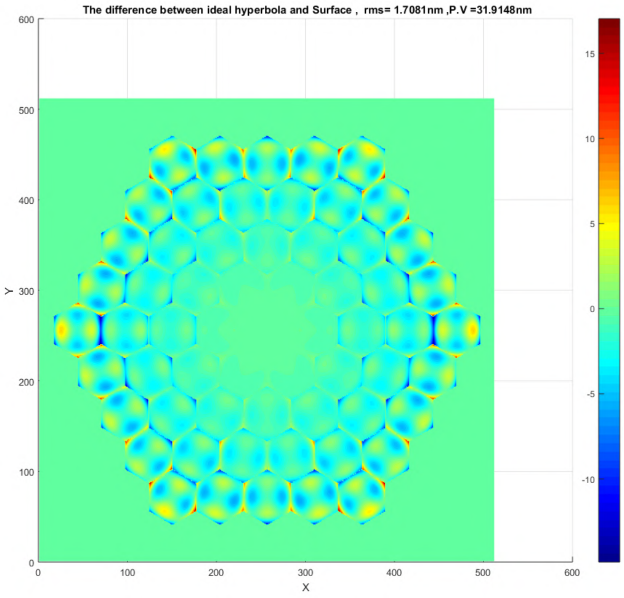

(a) (b)

Figure 3.40: The surface difference map between an ideal hyperbola and the primary mirror created using Fixed roc method with PTT and Z4-Z11 optimization (units in nm).

Chapter 4

Phasing: KECK Type Phasing Scheme

4.1 Introduction

Co-aligning, co-focusing, co-phasing are the three major steps to make a segmented telescope act like a monolithic mirror telescope. KECK telescopes are one of the pioneering examples of segmented mirror telescopes[18],[29]. KECK's primary mirror consists of 36 hexagonal segments that fit together to form a monolithic equivalent optical surface of about 10 m diameter and the side length of each hexagonal segment is 0.9 m. The hexagons create 84 inter-segment gaps. Two capacitive displacement sensors are kept in every inter-segment gap. This edge-sensor and actuator along with the telescope active control system (ACS), keep the mirror segments in the desired position. However, there is no global reference for ACS to keep the mirrors in position. Once the mirror is optically aligned and phased, correcting all tip, tilt, and piston errors, with the alignment and phasing system(APS), the APS provides this data in the form of a look up table for the ACS to freeze the mirrors [62]. Co-aligning, co-focusing, co-phasing are explained below.

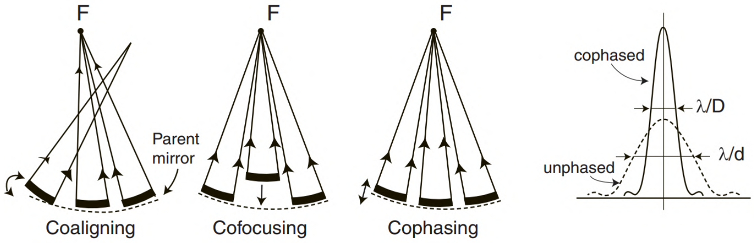

Figure 4.1: Co-aligning, co-focusing, and co-phasing a segmented system (left). The PSF of a segmented system where the mirror segments are out of phased or in-phase (right). The width of the PSF is λ/d in the first case, where d is the diameter of the mirror segment, and it is λ/D in the second case, where D is the diameter of the full primary mirror[63].

[63]Co-aligning is merely stacking all images one over the other to get the maximum intensity [68], this is done by locating which spot of observed star corresponds to which mirror. Co-focusing is making the spot size produced by each mirror of the same size. This is done by sensing and correcting surface deviations in the mirror. We have developed a technique using Shack–Hartmann wavefront sensing in the MATLAB software platform for the co-focusing. The details of which can be found in Appendix B. Once the surface error is sensed, co-focusing can be achieved by figuring the mirror using a warping harness or at the manufacturing stage itself. When co-aligning and co-focusing are done, the telescope acts as a large light collector. Still, it will not give the image quality equivalent of a single monolithic mirror of the same total diameter. The reason is that the light from each segment is reaching the image plane with a phase difference between them introduced by the piston effect [64]. The piston effect is introduced by the phase discontinuity between edges of the adjacent segments. Piston causes the telescope PSF to be the incoherent sum of the PSFs of the individual segments [65]. This reduces the optical quality, affects the resolution of the telescope, and introduces speckles in the image background. Due to these reasons, the RMS phase errors in the segmented telescopes must be made as small as possible. This chapter addresses the KECK type, i.e., Shack-Hartmann(SH) based phasing scheme.

4.2 Co-Phasing

In a segmented mirror telescope, phasing or co-phasing is the detection and correction of phase discontinuity between segment edges. There are a number of different co phasing techniques which can be employed to achieve this task. They are described in brief in Chapter 1 section 1.6 [69]. In this chapter we consider Shack-Hartmann based Phasing system which is used in KECK telescopes co-phasing system[67, 68, 29]. The principle can be divided into narrow and broadband depending on the width of wavelength band used, analogously on the temporal coherence length of the system. From the working principle and algorithm of KECK phasing [66] the theoretical background is derived. A MATLAB based Phasing code is developed in house. The system principle is simulated numerically and analyzed. The simulation results are compared with ZEMAX conceptual design. Preliminary laboratory experiment is designed in ZEMAX and is conducted. Narrow-band principle was successfully validated in laboratory, broadband needs further modifications. We will present the results of MATLAB simulation and experimentation on this chapter.

4.3 Keck Type Phasing Scheme

The piston discontinuity or Piston error is the up down displacement of one segment edge with respect to the nearby segment. This introduces a phase discontinuity between two segments. The principle of operation of the Shack-Hartmann or KECK based phasing is as follows, the light passes through a circular aperture kept straddling between the inter-segment gaps. This light pattern has the shape of two D shaped beams kept close.

The light is then focused to a point through a diffraction limited optical system. The shape of point spread function (PSF) of the system changes with respect to the piston error between the two segment edges. This is because light from the two D patterns (see figure 4.2) coherently adding up at the focus. This process is dependent on the term we call as 'coherence length' given by $\lambda^2/2\Delta\lambda$ of the system, where λ is the central wavelength of the optical band width and $\Delta\lambda$ is the

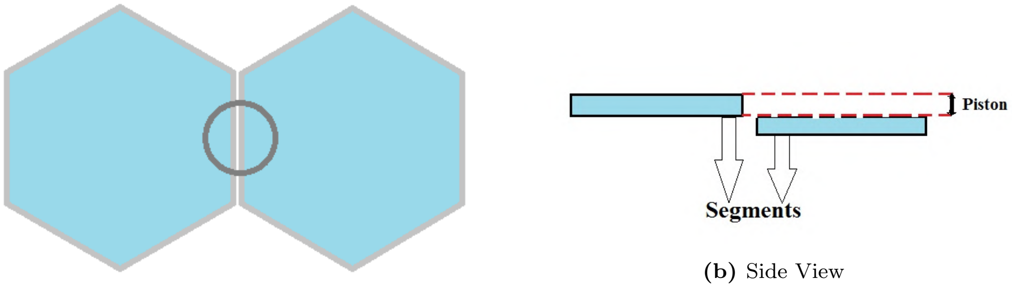

(b) Side View

(a) Top View (aperture shown)

Figure 4.2: Intersegment Gap and aperture showing piston error.

band width. This change in the intensity distribution in PSF can be measured and the segments can be arranged such that piston effect is minimum and we get a piston error minimized, continues optical surface.

4.4 Narrowband

The narrowband uses a small wavelength band or, ideally speaking, a monochromatic beam. That means system will have a very large coherence length, which makes the PSF changes due to piston error cyclic of π for an extensive range of piston. The cycle is from 0 to π or 0 to $\lambda/2$, in phase. Practically, narrowband co-phasing is done after broadband co-phasing. This 2π, ambiguity can be reduced by measurement with more than one narrowband filter for the same piston error[71],[70].

4.4.1 Mathematical Derivation of Narrowband Technique

The light is taken to be monochromatic, with wavelength of λ, implying the coherence length of the light calculated by the expression$\frac{\lambda^2}{2\Delta\lambda}$ is infinity. In an optical system, the image plane's complex amplitude is given by the Fourier transform of the aperture function described by Chanan et.al[62]. So the intensity(I) distribution of PSF can be derived as,

$$\hat{f}(\vec{\omega}, k\delta) = \frac{1}{\pi a^2} \int_0^{2\pi} \int_0^a A(\rho, \theta) e^{\iota k \vec{\omega} \cdot \vec{\rho}} \rho d\rho d\theta \tag{4.1}$$

$$= \frac{1}{\pi a^2}\left[\int_0^{\pi}\int_0^{a} e^{\iota k\delta} e^{\iota k\vec{\omega}.\vec{\rho}} \rho d\rho d\theta + \int_{\pi}^{2\pi}\int_0^{a} e^{-\iota k\delta} e^{\iota k\vec{\omega}.\vec{\rho}} \rho d\rho d\theta\right]$$

So $\hat{f}(\vec{\omega}, k\delta) = \frac{2}{\pi a^2}\int_0^{\pi}\int_0^{a}\cos(k\delta + k\vec{\omega}.\vec{\rho})\ \rho d\rho d\theta$

$$= cos(k\delta)\frac{2}{\pi a^2}\int_0^{\pi}\int_0^{a} cos(k\vec{\omega}.\vec{\rho})\rho d\rho d\theta - sin(k\delta)\frac{2}{\pi a^2}\int_0^{\pi}\int_0^{a} cos(k\vec{\omega}.\vec{\rho})\rho d\rho d\theta$$

$$I(\vec{\omega}, k\delta) = abs(\hat{f}(\vec{\omega}, k\delta))^2$$

Where k=$2\pi/\lambda$, δ is the piston error. Upon derivation we see that Fourier amplitude can be represented as a linear combination of the in-phase (k$\delta = 0$) and maximally out-of-phase (k$\delta = \pi/2$) amplitudes, So intensity distribution is,

$$I(\vec{\omega}, k\delta) = [|cos(k\delta)\hat{f}(\vec{\omega}, 0) + sin(k\delta)\hat{f}(\vec{\omega}, \frac{\pi}{2})|]^2 \tag{4.2}$$

4.4.2 Generation of Images for Narrowband Technique

The narrow band images are monochromatic PSF's of lenslet apertures generated as a Far field Fraunhofer diffraction pattern. KECK telescope uses a lenslet array with a cross wire across each lenslet straddling intersegment gap for pupil registration. On projection to telescope it produce an aperture of size 10 cm with a 20 mm wide strip in the middle [67]. The strip is to cover the irregular edge diffraction effect from the beveled telescope segment edge. In our simulation for a monochromatic wavelength, we use aperture with a diameter of the circle to strip ratio of 10:2 size. The Fourier transform of the aperture is taken after adding a opposite-polarity equal-magnitude phase to two segment edges covered by the aperture. Square of the absolute value of the Fourier transform gives the intensity. We also generated noisy images, mainly with background noise, object noise, thermal noise, and readout noise. So the total noise is $\rho = \sqrt{(\rho b^2 + \rho s^2 + \rho t^2 + \rho r^2)}$ Where' ρ' is the total noise 'ρb' is the background noise 'ρs' source noise 'ρt' is the thermal noise 'ρr' is the readout noise '$SNR = S/\rho$' where S is the signal. The object and background noise is of Poisson distribution in nature. Furthermore, other noises can be considered Gaussian with zero mean and changing variance for each pixel. This will depend on the nature of the CCD. So for analysis purposes, we have added Gaussian and random Poisson noise into the theoretical image. Equal variance of 0.01 is given for all pixels of Gaussian noise image profiles. The figure 4.3 gives a simulated aperture. The figure 4.4 and 4.5 gives the simulated narrow band images and their contour plots respectively.

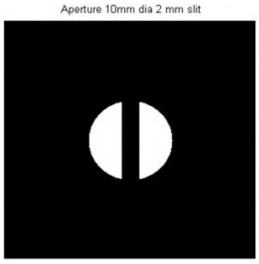

Figure 4.3: Simulated Aperture

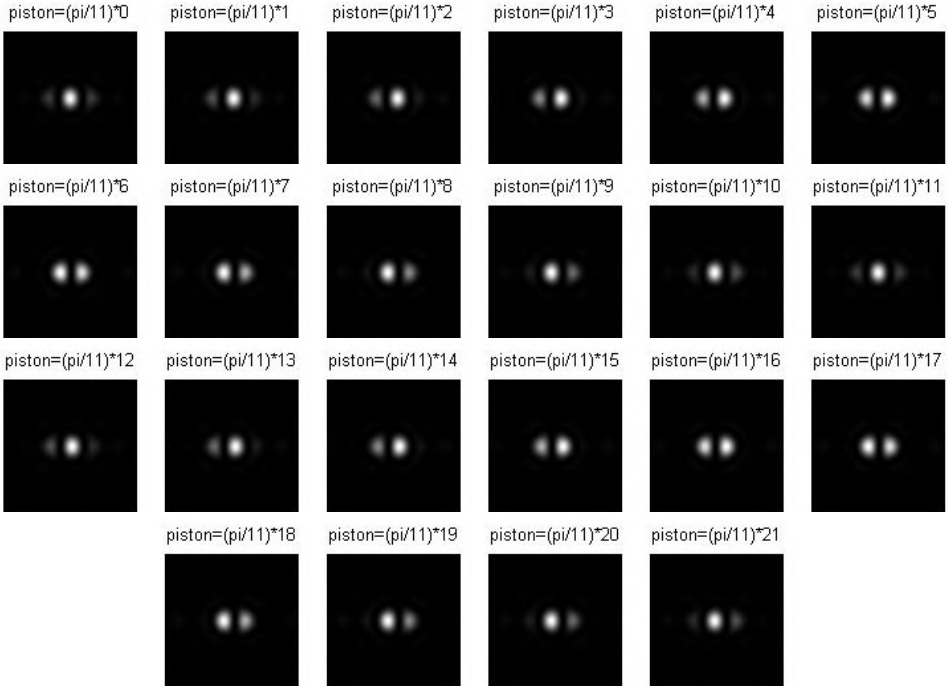

Figure 4.4: Narrowband templates

4.4.3 Generation of Narrowband Correlation Curve

Narrow band correlation curve is generated by correlating an unknown piston monochromatic PSF image with temples of a cycle of simulated monochromatic PSF of 0 to Nπ phase error, with the same number of pixels in size. The Narrow

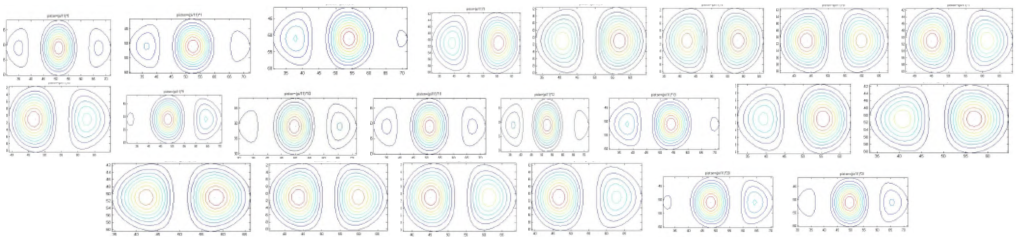

Figure 4.5: Contour plots of narrowband templates

band correlation curve show sinusoidal cyclicity that repeats in a phase cycle of π, or $\lambda/2$ in phase. Once mirrors are co-phased with in the order of λ, this technique does the fine-tuning of reducing that piston error up to small fractions of $\lambda/2$. In an ideal case, this can be corrected up to zero piston. In Keck, narrowband co-phasing is done after broadband co-phasing.

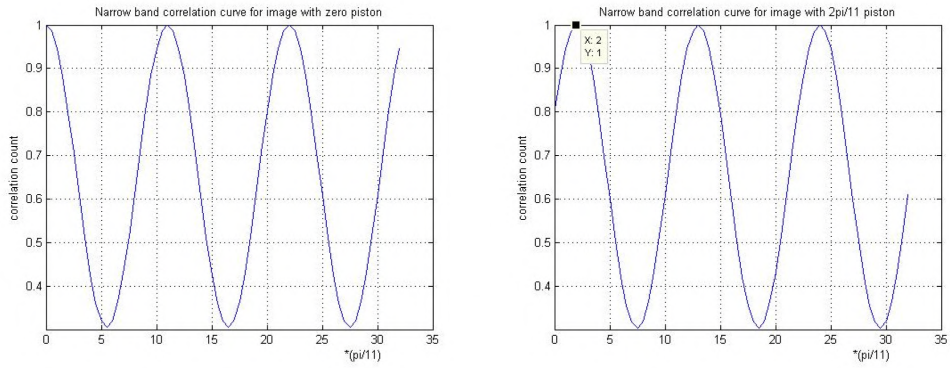

(a) X =Zero piston

(b) X=$2\pi/11$

Figure 4.6: Correlation of a 'X' piston error image with all narrow band images with phases varying from 0 to 3π

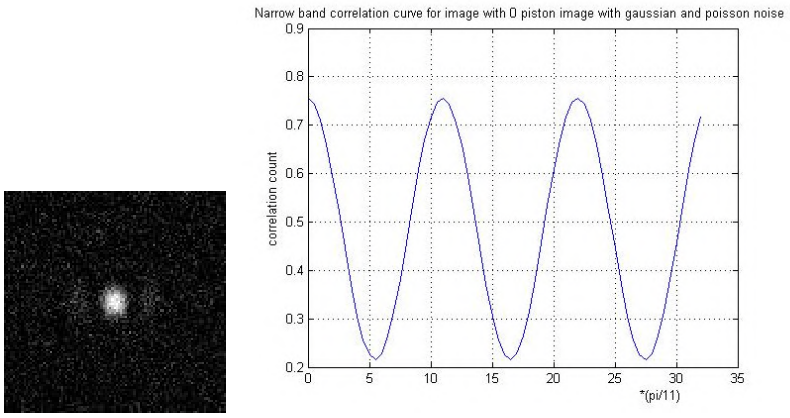

Figure 4.7: Noisy image and, Narrowband Correlation curve of zero piston narrow band images with noise to all theoretical narrow band images with phases varying from 0 to 3π.

The figure 4.6a and 4.6b gives the narrowband correlation plots in two scenarios. In the correlation curves, the least correlated image also has a considerable correlation count. This creates a DC shift which is ignored in narrow band curve but eliminated in broad band curve. For the noisy image and correlation count shown in figure 4.7, There is a drop in the dynamic range of the correlation plot, which can be expected in a practical case. The Gaussian noise added to each pixel is of equal variance, so the plot is still uniform, whereas in the real case, there will be a intensity scattering in the plot. Due to the more considerable coherence length of a monochromatic wavelength λ as per equation $\lambda^2/2\Delta\lambda$, the diffraction pattern with periodicity as a function of phase difference is cyclic over a large piston range. This can be seen in the figures 4.6 and 4.7. This makes an unambiguous finding of the piston greater than $\lambda/4$ on the surface very difficult. Say we use a near-infrared wavelength of 891 nm, then the maximum capture range in practice is around ±100 nm instead of ±223 nm when we avoid the non-linear region of the sinusoidal curve. However, in KECK this technique gives an accuracy of around 6 nm [62]. This technique's main disadvantages are the need for specialized hardware, in which each lenslet has to straddle between two inter-segment gap, equally dividing the aperture into two semicircles. This inter-segment pupil registration is crucial in this technique. As the lenslet samples only a small fraction of the segment surface, this technique can only detect and minimize the phase step between the segment edges. This phase step minimization may not reduce the piston error between the segments in a highly aberrated segment surface. Due to all these reasons, we explored the next technique called broadband technique, which use the same optical hardware with a set of Gaussian broadband filters.

4.5 Broadband

The broadband uses a light of wider wavelength band, making it to have a low coherence length by the equation $\lambda^2/2\Delta\lambda$. This will change the total temporal coherence length of light into few microns compared to narrowband. The broadband technique uses Gaussian band-pass filters for its working[66]. When the wavefront phase is with in the filter's coherence length, amplitude and complex phase of different points in the wave-train are in correlation, thereby causing them to sum up coherently at the focus. Whereas once the light's phase difference is out of the filter coherence length, this correlation is damaged. So they sum up incoherently ie, only in intensity. With this difference in the behavior of the generated polychromatic PSF, we can find the piston error in the system. This technique increases the capture range of piston . This is ideal for finding unambiguous piston error with a wider capture range, whereas, in a narrow band, we have to be satisfied by sensing capability limited to small fractions of λ. Different Gaussian band pass filters give different capture ranges in broad band co-phasing.

4.5.1 Mathematical Derivation of Broadband Technique

Broadband can be considered a technique in which the light's temporal coherence is altered using an optical filter, retaining the spatial coherence . Unlike narrowband that considers one wavelength and has a small capture range of the order fraction of λ, a broadband capture range can be extended to few tens of microns. In this, light from the aperture is made to pass to a Gaussian bandpass filter. In a theoretical Gaussian filter considered for derivations, the transmission wings can extend to infinity, but this is not the case in a practical optical filter. In theory, the output intensity for a piston error of δ and k=$2\pi/\lambda$ becomes, [62] [66]

$$I(\vec{\omega}, k\delta) = \int_{-\infty}^{\infty} (\frac{1}{\sqrt{2\pi\sigma k^2}} e^{-\frac{(k-k0)^2}{2\sigma k^2}} [|cos(k\delta)\hat{f}(\vec{\omega}, 0) + sin(k\delta)\hat{f}(\vec{\omega}, \frac{\pi}{2})|]^2 dk) \quad (4.3)$$

The mathematical equation can be stated as output intensity becomes the image of two semicircle apertures as in figure 4.3 with piston difference between them, multiplied by the Gaussian response of the filter and integrated over the entire wavelength band. The system is considered to be diffraction limited. The PSF is the far-field diffraction pattern, which contains information about the piston. This technique is implemented when $\Delta\lambda << \frac{\lambda^2}{2\delta}$ is violated, i.e, the piston error range is extended to few tens of waves [62]. The piston error is large such that it is out of filter coherence length, the complex phase and amplitude of the wavefronts having phase difference that exceeds the filter's coherence length are uncorrelated. In a telescope, the light from the primary with these piston errors is made to pass through a Gaussian band pass filters. As the starlight is coherent, this causes it to loose its temporal coherence. The PSF generated is merely an intensity sum of the beams at that time. If the piston error is well within the coherence length, there will be an amplitude sum, causing distinct change in the patterns of the PSF, which can be used to find the piston error[66]. In Gaussian bandpass filter g(k)=$\frac{1}{\sqrt{2\pi\sigma k^2}}e^{-\frac{(k-k_0)^2}{2\sigma k^2}}$. Also, $e^{-\frac{(\Delta k)/2}{2\sigma k^2}} = 1/2$ and $\sigma k = 1.33/l$. So the output intensity pattern becomes

$$\begin{aligned} I(\vec{\omega}, k\delta) = \frac{1}{2}[1 + e^{-2\sigma k^2\delta^2} cos(2k_0\delta)](\hat{f}(\vec{\omega}, 0)^2) + sin(2k_0\delta)e^{-2\sigma k^2\delta^2} \\ [\hat{f}(\vec{\omega}, 0)\hat{f}(\vec{\omega}, \pi/2)] + \frac{1}{2}[1 - e^{-2\sigma k^2\delta^2} cos(2k_0\delta)](\hat{f}(\vec{\omega}, \pi/2)^2) \end{aligned} \tag{4.4}$$

4.5.2 Generation of Images for Broadband Technique

A Gaussian bandpass filter is used to alter the temporal coherence and generate broad band images. We can do it in two ways. Use the intensity image obtained in narrowband and multiply it with filter response and do a discrete sum of it over a filter bandwidth wavelength. For a practical filter with a definite truncation, this approach suits better. Another way is to go with the simplified mathematical equation of a Gaussian filter in conjunction with the optical system. In this, we use the equation 4.4 to simulate the images.The generated images and contour plots are shown in figures 4.8 and 4.9. The incoherent image's elliptical shape is due to the semicircle diffraction pattern, which is elliptical. In the case of an incoherent image, the summation is happening only in intensity addition, so the shape retained as an ellipse is shown in figure 4.10.

4.5.3 Generation of Broadband Coherence Curve

We select an incoherent image from broadband, then find its centroid using the intensity weighted centroid method. Then we crop every image to one size such that the pixel corresponds to the centroid of the incoherent image is the center of all images. This will keep the centroid pixel of zero piston error image as the center pixel of every image. Then broadband image with unknown piston is correlated with all the narrowband images for piston range of 0 to π in phase, i.e in the

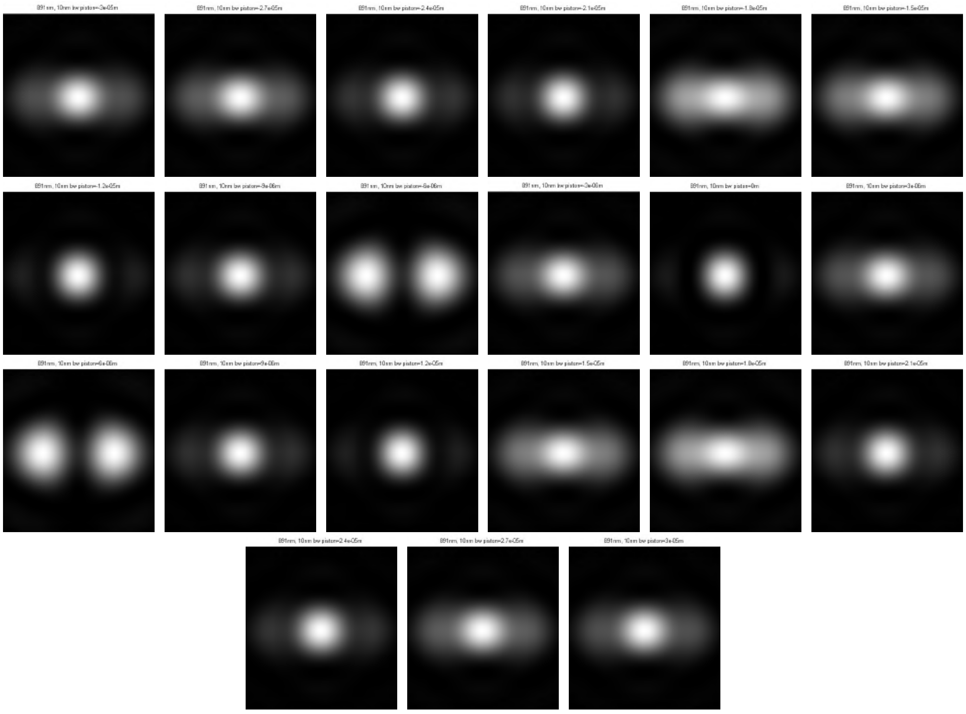

Figure 4.8: Broad band images with a filter coherence length of 40μm with theoretical equation

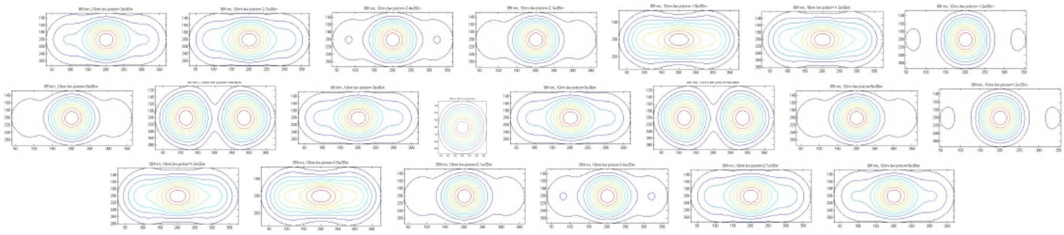

Figure 4.9: Contour plots for broadband images with a filter coherence length of 40μm as per theoretical equation

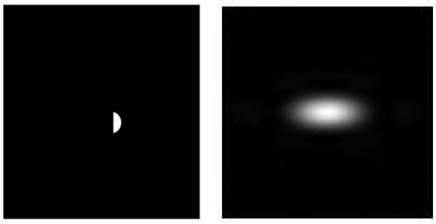

Figure 4.10: semicircle aperture and diffraction pattern

wavelength range of 0 to $\lambda/2$ (this gives a cycle of images in narrowband). We have chosen the Pearson correlation due to its simplicity speed, also due to good correlation values. Keck telescope also uses the same type of correlation. It is better to have the same number of narrowband images as broadband images. It is also advisable to use many images to get a smooth curve. Once the images are correlated, and the correlation coefficient for each broadband image is obtained, we find maximum and minimum values of each image's correlation count. The 'coherence parameter' is this maximum value – minimum value. Then we subtract the value of the incoherent image's coherence parameter from all the images to bring the incoherent image correlation value to zero and obtain the coherence curve.

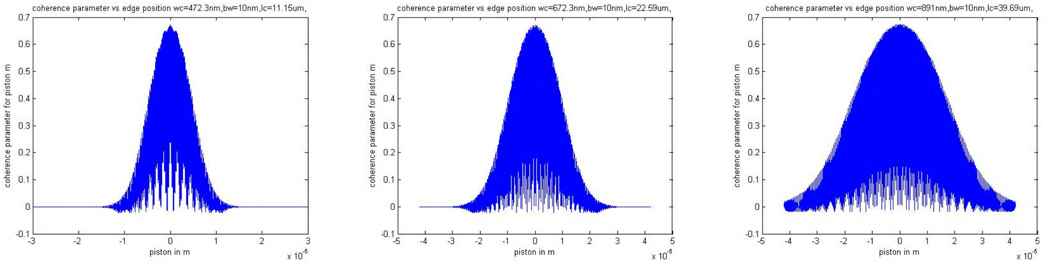

(a) CW:472.3 nm,WB:10 nm, CL:11.15μm

(b) CW:672.3 nm,WB:10 nm, CL:22.59μm

(c) CW:891 nm,WB:10 nm, CL:39.69μm

Figure 4.11: Coherence parameter Vs. piston for different filters simulated with derived theoretical equation considering infinite wing pattern, CW:Central wavelength, WB:Wavelength Band, CL:Coherence length

Images of figure 4.11 are the coherence curves generated with theoretically derived equation 4.4 considering entire wavelength of the spectrum. But when the filter is real, it transmits only the definite wavelength band, similar to the practical case assumed by the Gaussian band pass response. That is the band width at full width half maximum and then the rest of a few more wavelengths. This apporch in selection of filer band width gives the perfect Gaussian curve for coherence parameter as given below in figure 4.12. We decided to continue our study made with a coherence curve made with definite wavelength band Gaussian response as given in figure 4.12.

4.5.4 Co-Phasing of the Segments in Broadband Technique

This section explains the procedure of broad band co-phasing in KECK telescope. Consider the segments are in unphased mode having unknown piston errors. The broad band image for a segment edges are obtained through the APS camera. For the accrued broadband image, the coherence parameter is obtained. This value is considered as a nominal value. That is, this value will be kept at the point of zero piston in the theoretically obtained coherence curve. A known piston

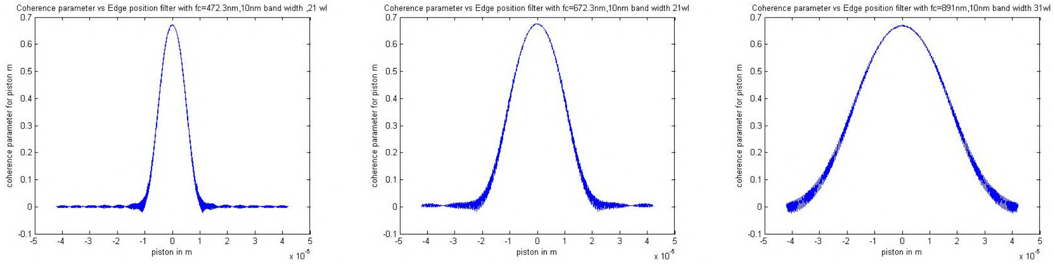

(a) CW:472.3 nm,WB:10 nm, CL:11.15μm

(b) CW:672.3 nm,WB:10 nm, CL:22.59μm

(c) CW:891 nm,WB:10 nm, CL:39.69μm

Figure 4.12: Coherence parameter Vs piston for different filters simulated with definite filter wing cutoff wavelength range (practical), CW:Central wavelength, WB:Wavelength Band, CL:Coherence length

or step height is then introduced into that segment so that we will get another broadband image. This step is introduced in a sequence for complete capture range in a total of n steps. That is, if the capture range is 30 μm, the step size will be 30/(n/2-1)=6 μm for n=11. This is done, first by stepping -30 μm to -6 μm about the nominal position then to the central nominal value then again piston of +6 μm to +30 μm about the nominal position. Where '+' and '-' means a relative shift of one mirror with respect to each other (up and down movement). Then broadband coherence parameters for all these images are obtained and plotted in the respective Y-axis for the given filter. The X-axis will be distributed with respect to the step size. In this graph, a first order Gaussian is fitted through all the coherence parameter points. The piston/edge height corresponding to the peak of this Gaussian is considered as the piston of that segment[72].

4.6 Broadband Phase Retrieval Simulation in MATLAB

In this section, the broadband co-phasing technique used in KECK is simulated in MATLAB. The table 4.1 lists different filters and parameters used in KECK co-phasing system. The number associated with each mode is the repeatably of the mode in nanometers. Step height is the preferred discretization(n) in the total capture range to map out the unknown piston. The capture range is taken between 75% to 85% of the width of a theoretically approximated curve. The magnitude of stars chosen is reduced as we go for larger bandwidth, this to keep the photon count on the detector constant[66].

Table 4.1: Broadband Phasing Parameters of KECK telescope

Mode	Wavelength (nm)	Bandwidth (nm)	Coherence length (nm)	Step size (μm)	Capture range (μm)	Star magnitude
1000	891	10	40	6	± 30	4
300	852	30	12	2	± 10	5
100	870	100	3.8	0.6	± 3	6
30	700	200	1.2	0.2	± 1	7

We randomly take a broadband image that corresponds to a broadband image simulated with a practical filter with a definite cutoff. (The high-frequency structure in the theoretical curve having infinite Gaussian curve is a theoretical noise which can be ignored.) Then giving steps as described in section 4.5.4 we will try to find the piston by fitting a fist order Gaussian through the data. We expect to get the piston value as the X-axis value corresponding to the mean of the Gaussian where the peak occurs. Here in the fitted Gaussians this value is given by parameter 'b1', for the equation f(x) = a1*exp(-((x-b1)/c1)^2).

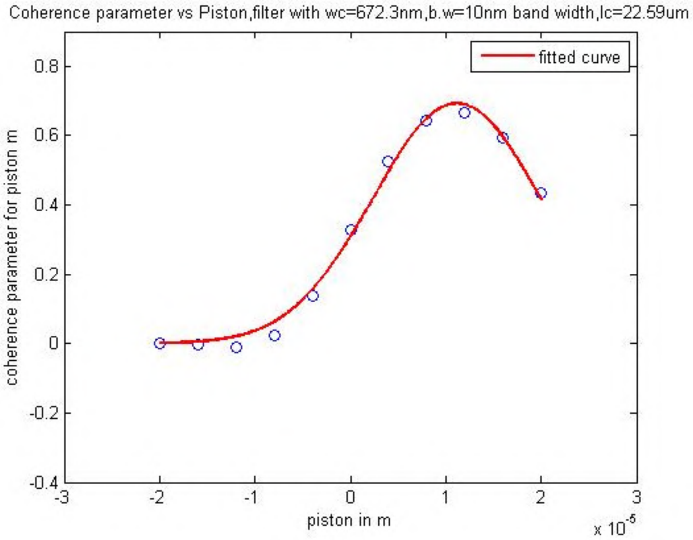

Figure 4.13: Gaussian fitted through piston points , applied piston = 11μm, retrieved piston=11.15 μm

In figure 4.13 and 4.14, the piston is within the coherence length of the filter, and the piston is captured very accurately. However, in figure 4.15, the piston is outside the capture range of the filter. So that piston is not captured properly.

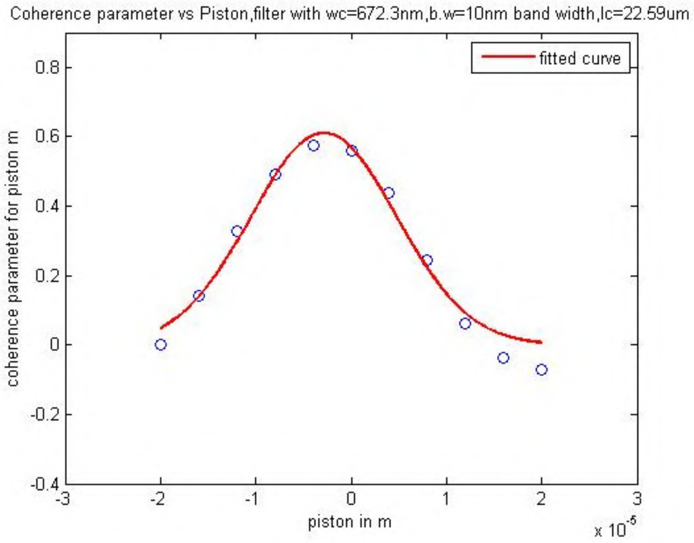

Figure 4.14: Gaussian fitted through piston points, applied piston= - 2.58 μm, retrieved piston=-2.864 μm

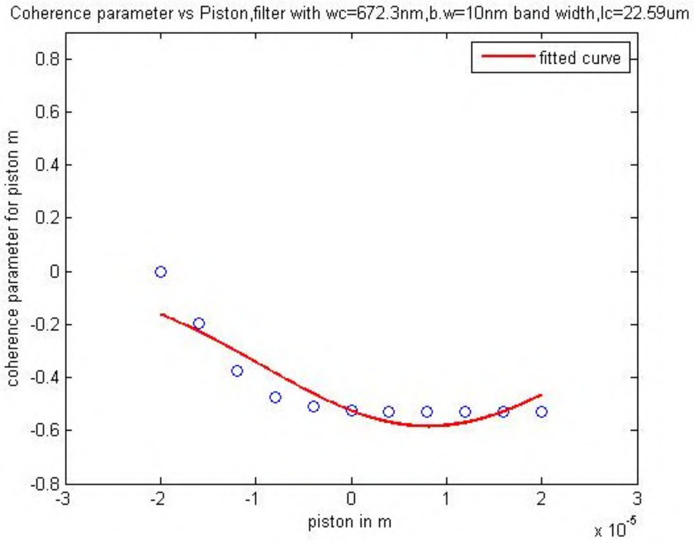

Figure 4.15: Gaussian fitted through piston points, Applied Piston =-26.58μm ,retrieved piston 8.082 μm

This technique will work when the piston is within the order of the coherence length of the Gaussian bandpass filter. From our simulation, we saw that we could retrieve the piston with accuracy within 1%. This technique shares the disadvantages of the requirement of specific optical hardware with narrowband technique. Additionally, the requirement of broadband Gaussian bandpass filters. Like a narrow band technique, this technique can only minimize the phase discontinuity between two segment edges. In a segment with larger surface aberration, this minimization may not achieve the phasing of the segments. Due to the need to introduce piston in steps to trace the coherence curve, this technique is time-consuming. When we try to increase the wavelength band width, the optical system requirement for chromatic correction also increases. The technique's advantage is the large capture range and inherent stability due to the Gaussian fit pattern of the coherence curve. In KECK telescope, full telescope phasing is achieved within 90 minutes, with piston error less than +/- 50 nm RMS [62],[72].

4.7 Experiment on Keck Type Phasing

We experiment to demonstrate the principle of operation of the modified Shack-Hartmann based phasing scheme. We use a narrowband technique to demonstrate the same. Also we intend to validate our MATLAB simulations through this experiment. The preliminary experiment design was done in ZEMAX. The system contains light sources, spatial filtering, collimating setup, and mirror segments to mimic segmented telescope conditions. The light from two edges of phase-shifted mirrors are passed through the circular aperture. Then it is focused on a detector using a good imaging system. The PSF is the far-field diffraction pattern of the aperture. This PSF contains information about the phase difference between the segments. Due to the unavailability of a broadband light source with spatial and temporal coherence in the lab and the broadband Gaussian bandpass filters, we decided to demonstrate the narrowband technique's working principle with laser light as a narrowband source.

4.7.1 Optical Design

When light passes through an aperture and is focused through a well aberration-corrected lens, the PSF is the Fraunhofer diffraction pattern or far-field diffraction pattern of the aperture. Here aperture is two semicircles created by the inter-segment gap of the mirror and the circular mask. The diffraction pattern is sensitive to the piston effect given to the beam; this principle is used in narrowband technique. The optical design of this system is using off-the-shelf components available.

4.7.1.1 Part 1: Source

We use two diode lasers having a wavelength of 532 nm and 650 nm. The lasers have 5 mW Optical power, the spot size of around 4 mm, and are Holmarc made. Two liner polarizes are used to control the intensity.

4.7.1.2 Part 2: Spatial Filtering

The spatial filtering setup consists of a microscope objective and a pinhole. We had three choices in the microscope objective also few pinholes. Out of them, we have chosen New port 20X, 0.4 NA, 9 mm focal length as the microscope objective. Among all the objectives we had (40x, 45x, 20x), this one has the longest focal length. With this objective and 4 mm laser beam, the airy disk diameter will be Da=(2*1.22*650*9/4)x10-9=7.14 μm. The recommended perfect size pinhole diameter will be 1.5 times the size of the airy disk usually. This is to ensure good spatial filtering. By this calculation we can go for a 10.7 μm pinhole for red laser beam. In the same way it should be 8.8 μm for green beam. But among the pin holes we had 12.5 μm as the smallest one. So we use this in the system.

4.7.1.3 Part 3: Collimation

The Collimator used is an achromatic doublet 50 mm clear aperture 150 mm focal length Holmarc made.

4.7.1.4 Part 4: Imaging

After the collimation beam is made into two parts using a 50:50 Holmarc Optics beam splitter of size 50 mm X 50 mm. The reflected beam is made to hit the segmented mirror and reflect. The transmitted beam is not used. The beam is made to pass through the aperture given in figure 4.18a

Then the 10 mm beam which comes out through the system is focused using a 750 mm focal length 50 mm diameter (A.R coated) Aromatic doublet lens. The detector used is Basler made with 7.4 μm pixel size. The diameter of image will be =2x1.22λf/D= 2x(1.22x650x750/10)x10^{-9}=118.95 μm, it will be around 16 pixels for red beam and 13 pixels for green beam. The narrowband simulation images will be double of this size to consider the shape change perfectly. The selection of this imaging lens was a trade-off between availability and set up construction.

4.7.2 Experimental Setup Block Diagram and Images

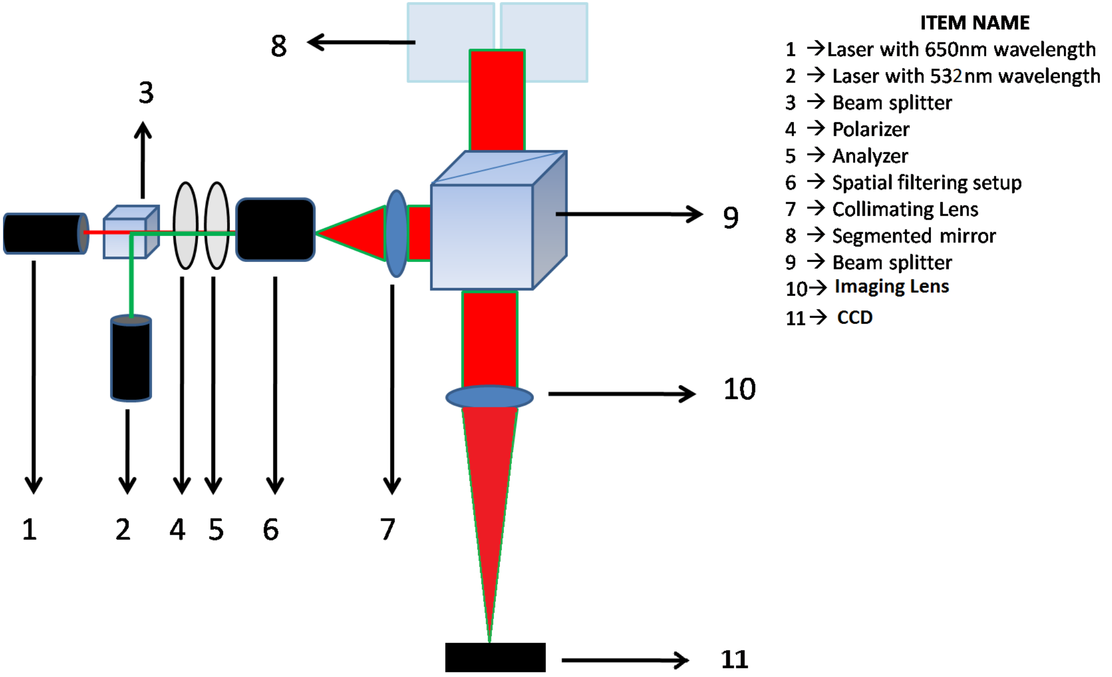

Figure 4.16: Narrowband experimental setup Block Diagram

4.7.3 Procedure

We assemble the experiential setup and leave the system for a few hours to stabilize the mechanical system, see figure 4.16 to see the layout. The room is cooled down, and the setup is allowed to sock in the cooled room temperature thermally. Next, we switch on both lasers and allow some time for them to stabilize. Adjust the lasers and beam splitter so that both beams come through the same path. The beam splitters and lasers are aligned to ensure the beam travels parallel to the optical table without any deviation. Next, we use liner polarizes to cut down the intensity. Both the beams are spatially filtered simultaneously through the same spatial filtering setup. The beam is passed through the collimating lens to collimate the light. Then mirrors are mounted in the kinematic mount with one mirror kept on Throlab's micro-motion stage, capable of moving with a minimum

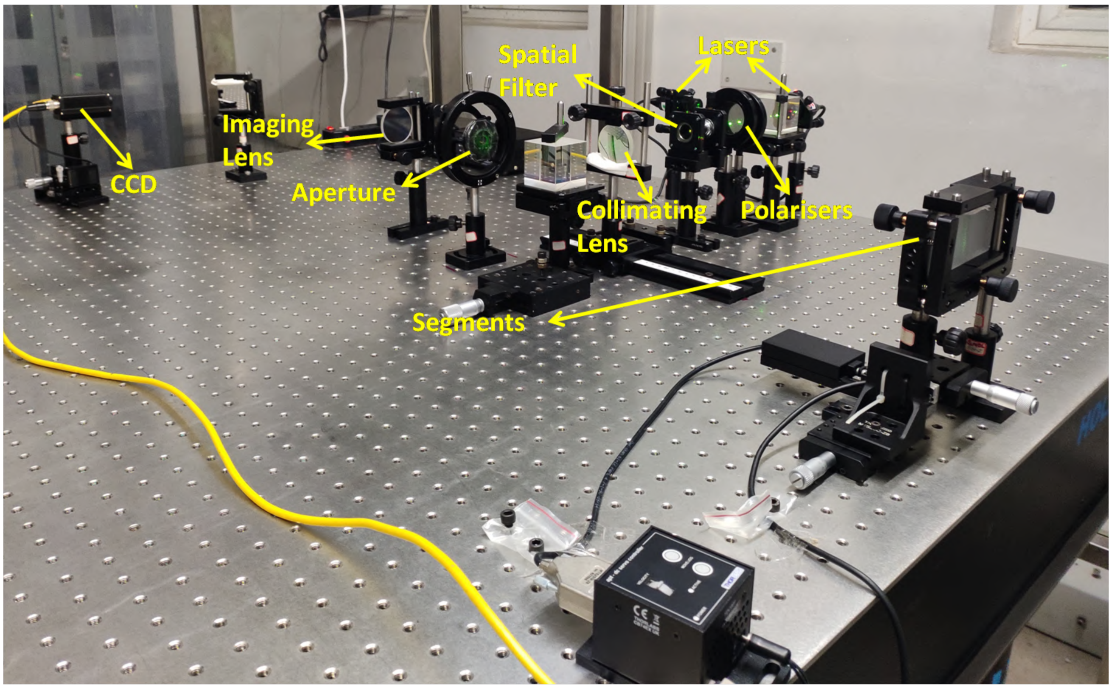

Figure 4.17: Narrowband experimental setup Image

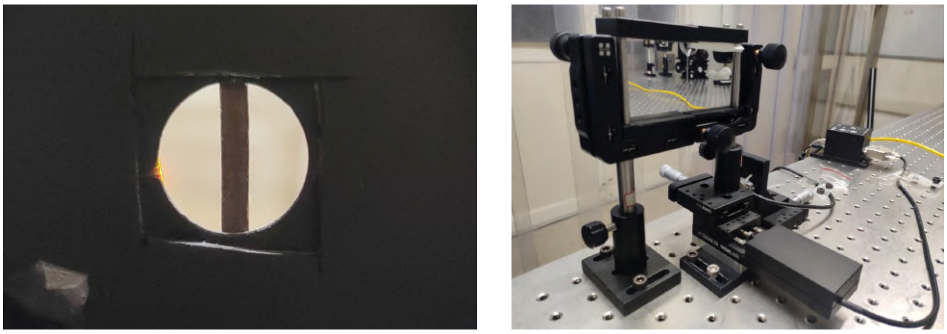

(a) Experimental aperture

(b) Aligned Segments

Figure 4.18: Experimental Image

step of nearly 50 nm. Since the stage used by us is not very precise and for our experimentation, we needed to read the mirror position, which is getting moved with a few nanometer accuracy. Therefore, an external high precision optical encoder from GSI Microsystems, which has got 1.2 nm resolution, has been installed along with the stage. The fixed mirror is considered as the reference mirror. Next, we align the mirrors such that light comes through the circular experiential aperture mask from each respective mirrors. It is shown in figure 4.18a. The aperture is of 10 mm with a 2 mm strip covering its center. This strip is placed to avoid the beveled edges' stray reflections and the gap between the segments. Also, it aids in creating a symmetric diffraction pattern. Care should be taken to minimize this gap between the mirrors to a minimum as it increases the spreading of more energy into the diffraction pattern wings. The tip and tilt between the mirrors are corrected with the help of long-distance alignment, by observing the beam after it traveled around 5 m. Next, we introduce the imaging lens. The imaging lens is the most crucial component in the system. It produces a diffraction limited image of the aperture. To ensure this, we use a long focal length aromatic doublet. By ensuring the beam passes well through the center of this lens, we get diffraction limited PSF. We further align the mirrors such that we get two perfect semi-circles in detector after introducing the imaging lens in the de-focused focal plane. We also avoid stray beams by adjusting the tilt of the mirror. The piston tip and tilt in a segmented aperture are always differential. If we give error to one segment, in a two segment system with in the the spatial coherence range it comes as a cumulative error. So we need to ensure there is no differential tip or tilt between the segments. Errors in the stages movement axis can cause this differential tip or tilt. To avoid this, the stage's axis movement error has to be within 1 pixel, ie around 7.4 microns, this converts to around 2 arcsec maximum tip, tilt cumulative error in the stage axis of movement. To ensure this, we use only the optimum region of the axis, which has this linearity. This region is found by covering the reference mirror, then moving the stage and measuring PSF centroid shifts formed by the moving mirror and choosing the best region of the stage's axis. Then both the mirrors are exposed to the beam, and the beam is well focused through the imaging lens such that they form an interference PSF. To ensure the final alignment, we extract one narrow band PSF image. Then Cover one mirror and extract one image, next extract the next mirror image in the same way. Then we find the centroid of both the images and make sure they are within 1-pixel error. Next, we introduce a known piston in the mirror mounted on the moving stage. Save PSF image for both wavelengths 650 nm and 532 nm one after another by allowing only one laser light to pass through at a time. Next, we do correlation with zero piston simulated image and get the narrow band curve.

4.7.4 Results

Once a set of images (some examples of images are shown in figure 4.19 and 4.20) for a range of piston error is obtained, we correlate the images with Zero piston image generated through simulation. The experimental optical system parameters decide the size of the simulated PSF. The obtained correlation coefficient is plotted Vs the piston value in nm obtained from the linear encoder. The piston applied goes as a differential piston to both the mirrors, the piston plot is expected to show a cyclicity with a frequency of $\lambda/4$. As the applied error at a single mirror position is the same, both the red and green beams should show this cyclicity for the same applied error.

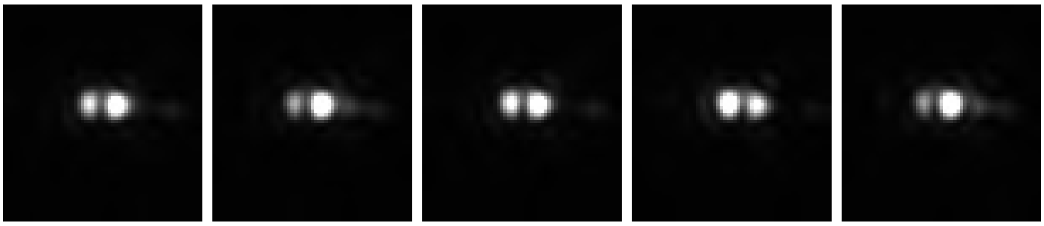

Figure 4.19: Experimental Narrowband PSF's for Green laser of 532 nm

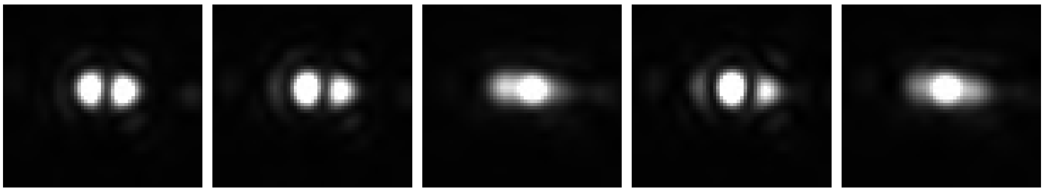

Figure 4.20: Experimental Narrowband PSF's for Red laser of 650 nm

The figure 4.21 gives the experimentally obtained correlation coefficient plot. As the applied piston noted by the encoder is the same, we can see the piston coefficient marked as black dot exactly following the theoretical pattern shown as the sinusoidal curve in figure 4.21a for red and figure 4.21b for green. Which clearly shows the cyclicity as expected. The magnitude of sine curve fitting is between 0.5 to 1. This is in well agreement with the theoretical correlation curve values of 0.4 to 1 obtained for the simulated system. Our piston introducing liner stage has a finer movement of only ± 50 nm due to the minimum piston error we could give around 100 nm. Due to this reason, we could get only a few sets of data points for

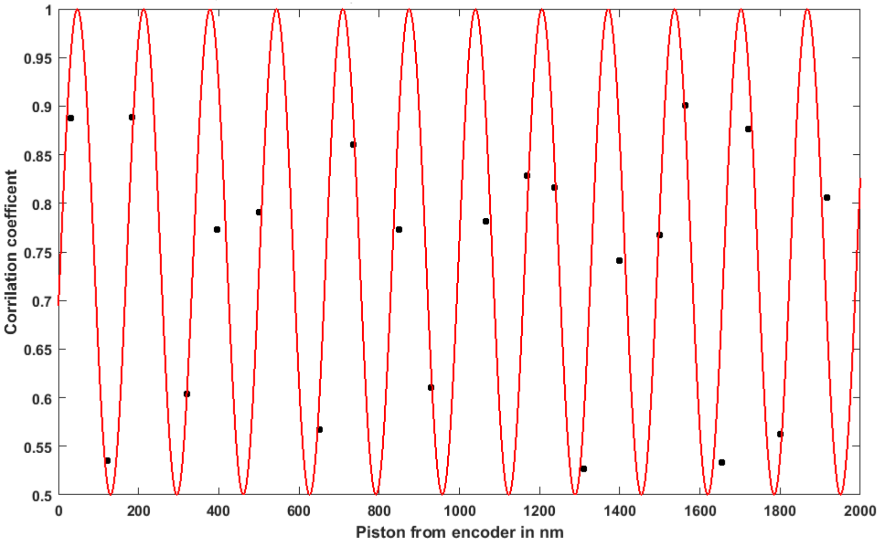

(a) For red laser of 650 nm

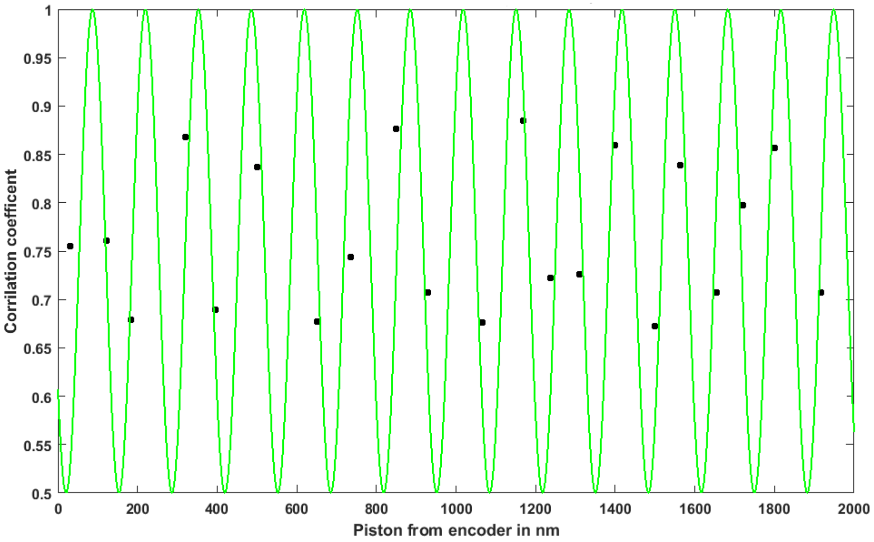

(b) For green laser of 532 nm

Figure 4.21: Experimental Narrowband correlation plots

every cycle. Once we have a linear motion stage with better precision and finer movement, we can solve it and get a more continuous plot. While we generate the correlation curve, the extracted image centroid has to coincide with the center of the image for different piston positions. Since we make sure, the image positions' shift due to other factors like stage axis errors is within one pixel, we chose the centroid of one the image close to zero or 2π piston as the center point and shifted all the other images centroids to this calculated pixel point. Further, we optimize this point by shifting it by one pixel in the +/- X and Y axis and observing the correlation coefficient. The point at which this maximum occurs is taken as the true center pixel. Another point to be taken care to increase the correlation curve's magnitude is the simulated images' template size. We start with a simulated zero piston image template as per the theoretical calculation, i,e, 16 pixels for red laser and 13 pixels for the green beam, and correlate it with the obtained images. This template size is again further optimized to maximize the correlation coefficient variation. In our experiment, due to our stage movement limitation, we expect a repeating correlation coefficient signature in the narrowband images produced. This is one reason for the distribution of points in figure 4.21 within a range. We also observed that there is a drift in the position of the retrieved correlation coefficient. To minimize this, we make sure the random errors present in the system is within ± 5 nm. This drift is checked by taking the encoder reading without applying any piston and monitoring the variations. We observed that we do have a wing effect in the image of PSF in the figures 4.19, 4.20 this was due to the 2 mm gap strip we placed in order to cover our segment edges. Since we have off-the self segments with around 0.5 mm beveling and less than $\lambda/4$ surface accuracy, this size strip was a must. However, irregularities in the strip have made a wing effect to our images. The orientation of the PSF axis depends on the orientation of the mirror axis and the strip. Even with these issues, our experimental images are similar to images in KECK [62]. The KECK telescope can achieve a final phasing error of about better than ± 50 nm RMS with broadband, and the narrowband can give up to 6 nm accuracy. The error with the fitting curve is 20 nm RMS in our laboratory experiment. We plan to further improve the system by introducing a better aperture mask with a strip and a low-stress mirror mounting stage as an alternative to the spring-mounted kinematic system we have now. Along with a better precision stage. Even with all the issues fitting all the data points so accurately for both red and green wavelength for the same applied piston error indicates the correct working of the technique.

Chapter 5

Phasing: Based on Pyramid Sensor

5.1 Introduction

In a segmented telescope, the alignment and phasing is achieved by sensing and correcting the wavefront deviations produced by various errors of the segments. There are several techniques proposed/experimented for wave-front sensing. Among these wavefront sensing techniques, a promising technique appears to be the pyramid based wavefront sensor; primarily, this technique is used in the field of adaptive optics [80] [81] [82]. As a simplified explanation of the pyramid sensor, we can state that it is a modified faucalt's knife-edge test extensively used in optical meteorology. Historically, it was Ragazzoni [74], who proposed this new wavefront sensor for the first time. Since then, the pyramid sensor is gradually becoming more and more popular in astronomy and many other disciplines, where precise measurement of the wavefront profile is required [83] [84]. Unlike Shack-Hartmann sensor, pyramid wavefront sensors are capable of measuring the tilt of segments, piston discontinuity, and other low-order surface distortions in a single observation. Additionally, it has increased sensitivity, adjustable gain, and variable spatial sampling [86],[94]. However, the pyramid sensor suffers from a short operation range, which can be improved with the help of modulation.

Unlike the Shack-Hartmann, the pyramid sensor seems to process both direct and a wavefront slope sensor's behaviors. In this light, the phase sensing mode of the Pyramid wavefront sensor was identified by Verinaud[86]. He showed the behavior of the sensor in the diffractive optics regime. The implementation of the pyramid as a direct phase sensor was showed by Renate [95], further, using a pyramid sensor as a phasing system for segmented mirror telescope was shown by Simone Esposito et al. [76], [75].

In this chapter, we present efforts towards developing a phasing system based on the Pyramid sensor. The pyramid sensor operation is considered in the non-modulated open-loop scheme. We present the basic concepts of the pyramid sensor along with the mathematical methodology for reconstruction. We give details of the MATLAB simulation. We also present the results of our experimentation on pyramid operation.

5.2 Pyramid Based APS the Technique

Pyramid sensor can be equated to a Modified Knife-edge test, which is used extensively in optical metrology. In terms of geometrical optics, the Pyramid-based wavefront sensor's working principle is illustrated in figure 5.1.

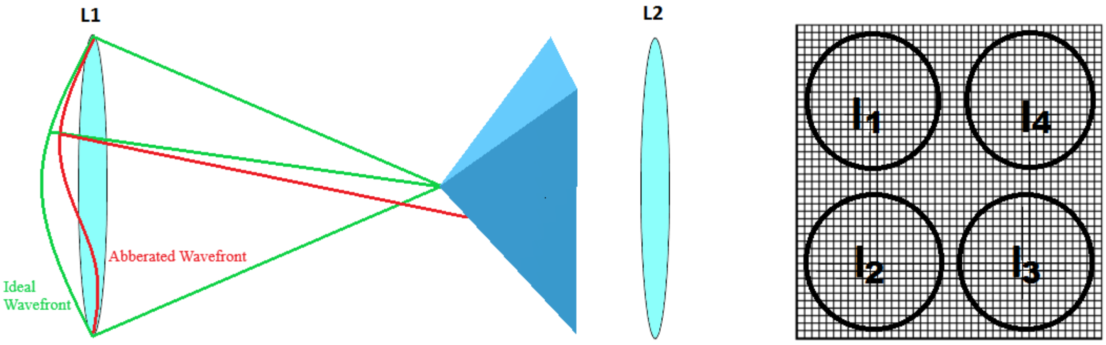

Figure 5.1: Schematic showing working of the Pyramid based wave-front sensor.

As given in figure.5.1, when an ideal spherical wavefront is (shown in the green color) formed by a converging lens, L1, hits the Pyramid tip. Then it gets split into four identical parts, which are reimaged into four identical pupils using a reimaging lens, L2. If there is an aberration in the incoming beam, the converging beam does not hit the Pyramid tip symmetrically due to the change in the ray direction, as shown in the red color light beam. This shift will create variation in the intensity distribution of the pupil images shown as I1 to I4. This phenomenon can be used to identify the aberration present in the system. The change in intensity at a pupil can be related to the change in the wavefront's local slop. From these four intensity images, two signal maps Sx, Sy can be derived as shown in equation 5.1 and 5.2.

$$Sx(x,y) = \frac{(I1(x,y) + I2(x,y)) - (I4(x,y) + I3(x,y))}{Iavg} \tag{5.1}$$

$$Sy(x,y) = \frac{(I1(x,y) + I4(x,y)) - (I2(x,y) + I3(x,y))}{Iavg} \tag{5.2}$$

$$Iavg(x,y) = I1(x,y) + I2(x,y) + I3(x,y) + I4(x,y) \tag{5.3}$$

For a small wavefront aberration of the order of $\lambda/2$, these signals can be linked with the local derivative of the wavefronts given in equation 5.4 and 5.5.

$$Sx \propto \frac{\partial w(x,y)}{\partial x} \tag{5.4}$$

$$Sy \propto \frac{\partial w(x,y)}{\partial y} \tag{5.5}$$

In the geometrical optics regime, both the Pyramid sensor and Shack-Hartmann sensor work on similar principles and provide the wavefront's local derivatives. However, Pyramid has enhanced sensitivity over SH, at least in close loop control. A pyramid sensor's disadvantages are primarily a short operation range, non-linearity, and cyclic ambiguity after capture ranges exceed $\lambda/2$ limit in phase. To understand the ability of a pyramid sensor to find phase error, we need to consider its operation in the wave optics domain. The Pyramid sensor's ability to identify phase discontinuity was numerically verified in [75] and it was experimentally demonstrated as a prototype by the same group in [76]. As per the theory [77] by avoiding modulation and assuming linearity, we can show that

$$Sx(x,y) \propto \int_{-B(y1)}^{+B(y1)} \frac{sin[\phi(x,y1) - \phi(x1,y1)]}{2\pi(x - x1)} \tag{5.6}$$

$$Sy(x,y) \propto \int_{-B(x1)}^{+B(x1)} \frac{sin[\phi(x1,y) - \phi(x1,y1)]}{2\pi(y - y1)} \tag{5.7}$$

The equation 5.6 and 5.7 show that Sx signal for an aberrated wavefront is proportional to the integration of the *sin* of the phase difference between each point on the (circular pupil) chord y = yp (perpendicular to the y coordinate), and Sy is proportional to the integration of the *sin* of the phase difference between each point on the chord x = xp. The B(x1) is the y value of the pupil edge at x=x1 and B(y1) is the x value of the pupil edge at y=y1.

Figure 5.2: Image of a Pyramid wave-front sensor courtesy of INAF - Osservatorio Astrofisico di Arcetri, Italy.

The figure 5.2 shows a pyramid made by INAF-Arcetri. It shows a pyramid having a vertex angle around 30^0 and made of N-SK11. In the Pyramid-based wavefront sensing or phasing approach, the main issue is the Pyramid construction itself. In a real Pyramid based system, an imaging lens focuses the beam into a pyramid tip, and it gets divided into four parts, and we assume that the Pyramid is ideal. But in reality, this is not the case.

In figure 5.4 we show an ideal pyramid designed with a perfect tip with an apex angle of 5^0. However, since it is difficult to manufacture a pyramid with an ideal tip and no edge, we need to consider a real scenario with tip and edge errors. So next, we designed a pyramid with a tip of $30\mu m$ and edge $10\mu m$. This is shown in figure 5.3.

The tip and edge error can cause leakage of the light through these causing error in the reconstruction. We can mitigate this issue by incensing the focal length of the imaging lens system and making the spot size in the tip much larger than these errors. The apex angle X as in figure 5.4 determines the divergence

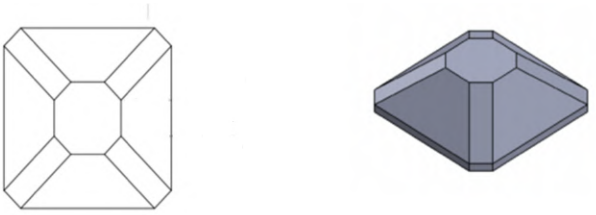

Figure 5.3: An illustration of exaggerated tip and edge of a deformed pyramid

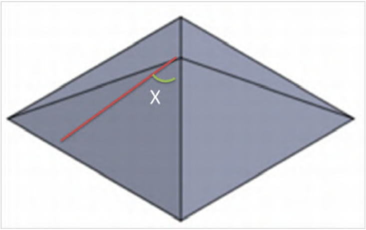

Figure 5.4: Apex angle of pyramid

angle. As per theoretical equation for calculating divergence angle [79],

$$\beta = X(n_{glass} - 1) \tag{5.8}$$

X is the apex angle, and β is the divergence angle n_{glass} is the refractive index of glass. Like the tip and edge error, the apex angle differences across each face can also cause error in the reimaged pupil position. The reimaging lens is usually a standard telecentric lens to take care of differential path length errors in the four pupil positions, if any. Another issue is the dispersion effects and chromatic aberration produced by the Pyramid. To solve this a design with 2 pyramids back to back was suggested by Pinna in 2008 [97]. Here two pyramids made of N-SK11 and N-PSK53 is glued back to back with each other. Nevertheless, with all these methods, the manufacturing of a precise tip and edge and aberration and dispersion correction still stands to make using this sensor extensively. So various groups started exploring ways to work around these problems

In 2006 Jess et al. [96] suggested an alternate approach for emulating a pyramid sensor without using a glass pyramid and modulation, with a lenslet array of 4 units to generate four pupils. However, again making a precise lenslet array consisting of 4 identical lenslets is a challenge. Another approach was by Vyas et al.; in 2013 [98], here a spatial light modulator creates a digital equivalent of pyramid wavefront sensor. There was another try to make a pyramid sensor from two, two-sided prisms [99]. Another method was tried by using four micrometers to emulate four sides of the pyramid [100].In all these methods, various issues still hamper the ease of operation. We intended to use this sensor for mainly metrology purposes in a segmented mirror alignment and phasing. We observed that in a system where static aberrations remain constant, a sequential approach in getting the four pupil images might be acceptable. Due to various disadvantages and difficulties in manufacturing and operation in various techniques we discussed, we came up with an approach where a precise 'L' shaped mask with only few micron edge error is used along with a precision rotating stage to generate the four pupil images sequentially. This new approach can be considered a modified knife-edge test, keeping in line with the pyramid operation principle. With this, we developed our simulation approach, as discussed in section 5.2.1.

5.2.1 MATLAB Simulation Tool for Generation of Pupil Images

The MATLAB Fourier transform tool, along with Zemax, simulate the images as one can expect from an ideal pyramid. The MATLAB simulation scheme is given in figure 5.5.

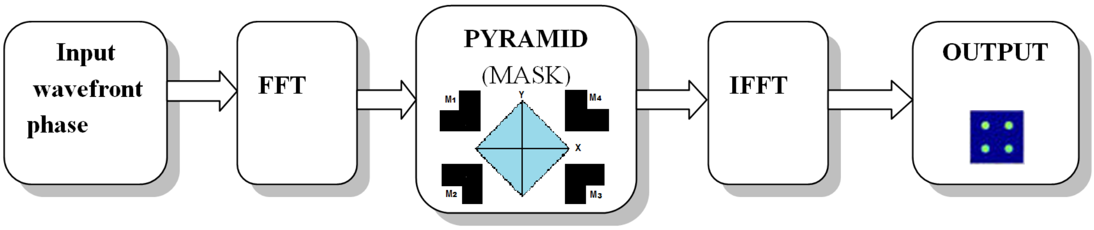

Figure 5.5: Block diagram showing the steps involved in the MATLAB Simulation

The incoming phase ϕ, in the orders of wave, is converted into a wavefront taking $\exp^{(i\phi)}$. The pupil plane field is generated by taking Fourier transform. We have considered an odd number of data points for obtaining an unambiguous center 'zero' point. Subsequently, the pupil plane field is multiplied with the four masks M1 to M4, as shown in figure 5.5. The mathematical representation of the masks are given in equations 5.9 to 5.12. The alignment of the center of the mask with the pupil plane field's center is an essential requirement . Conversely, a pixel misalignment could cause a shear / high order tilt error, introduced into the reconstructed wavefront, as observed in figure 5.6 .In our simulation, we came across the effects of misalignment of the mask (4 masks) as given in equation 5.9 to 5.12 . As the mask is misaligned, pyramid understands this incoming wavefront as a sheared wavefront because the pyramid tilt, tip, and piston of the wavefront are differential. This effect is described by Yong Liu [85]. Thus it is essential to have the centroid of the PSF coinciding with the center of the mask. As in figure.5.6, the lack of this alignment can cause a higher order tilt error in the reconstructed wavefront. Since we have an odd number of points in the incoming wavefront, care should be taken while simulating mask in MATLAB to create center point as ((No of pixels in X)/2+1), ((No of pixels in Y)/2+1).

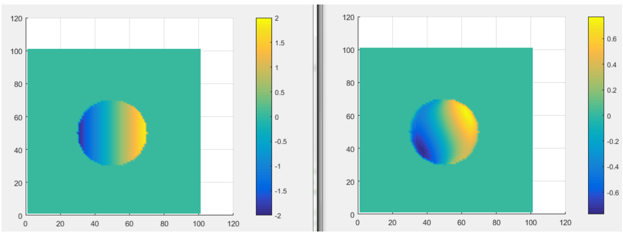

Figure 5.6: higher order tilt error in the reconstructed wavefront due to 1 pixel misalignment in the mask (Left) Incoming wavefront , (Right)Reconstructed wavefront)

$$M1(x,y) = \begin{cases} 1, & \text{if } x \leq 0, y \geq 0 \\ 0, & \text{otherwise} \end{cases} \tag{5.9}$$

$$M2(x,y) = \begin{cases} 1, & \text{if } x \geq 0, y \geq 0 \\ 0, & \text{otherwise} \end{cases} \tag{5.10}$$

$$M3(x,y) = \begin{cases} 1, & \text{if } x \geq 0, y \leq 0 \\ 0, & \text{otherwise} \end{cases} \tag{5.11}$$

$$M4(x,y) = \begin{cases} 1, & \text{if } x \leq 0, y \leq 0 \\ 0, & \text{otherwise} \end{cases} \tag{5.12}$$

Once the pupil plane field is obtained, the same is multiplied with the mask;

upon taking inverse Fourier transform of the same, it produces four pupil images I1 to I4 in that order. In these simulations, a case of an ideal pyramid is considered. i.e., no flat top and edges as well as no effect of dispersion. Though the technique is developed for the PSMT(Prototype segmented mirror telescope), which is made of seven hexagonal segmented mirrors, here first we present simulation results on one mirror system to clearly state why we adopted our reconstruction procedure and the different parameters to be considered, this is done to decide the choices for PSMT simulation.

5.3 Methodology for Wavefront Reconstruction

In section 5.2.1, we described the methodology used to generate pupil plane images and the technique to obtain Sx and Sy signal maps. In this section, we explain the algorithms used to reconstruct the wavefront. These algorithms were then used to generate the reconstruction code using the MATLAB platform. Once pupil images and signal maps are generated from the experimentation/optical simulation, the next challenge is to reconstruct the wavefront. There are different approaches explored in this area but most of these techniques are developed, keeping adaptive optics into consideration, where reconstruction is required for the continuous wavefront. Whereas, the work done by Pinna [78], deal with the segmented wavefront. Our focus is to retrieve piston, tilt, and defocus linked to the segmented mirror telescope using a pyramid sensor. As described earlier, the intensity signals obtained from pyramid pupil images are used to reconstruct the wavefront. From these intensity images, two synthetic images will be generated using equations 5.1 and 5.2. The wavefront reconstruction techniques use Sx and Sy signals for their operation.

Two approaches have been explored to reconstruct the wavefront from the data obtained by the pyramid sensor.In the first approach ,equations 5.4 and 5.5 are used . These equations and approaches describe the nature of the measurements made by the pyramid sensor [86]. Hereby creating equations for the distribution of electromagnetic field upon its interaction with the pyramid avoiding modulation and the interference effects happening inside the pyramid, we deduce a set of relations between the slop of the phase distribution at each point to the intensity variation across the Sx and Sy signal images. The intensity to phase relation at each point is the cumulative effect of all the points in the X and Y cord of the aperture passing through the point under consideration. This relation is obtained by deriving the distribution of electromagnetic field considering the pyramid as a modified knife-edge consisting of two perpendicular knifes. The phase is then represented as a set of discrete tilts obtained by matrix equations. This approach does not require a calibration matrix. This can be equated to a zonal reconstruction approach.

In the second approach assuming linearity, we formulate a relation for the phase to intensity variation inside an aperture. Here we represent this as a combination of a set of known push-pull errors. Here we need to generate a pre-calibrated interaction -control matrix to train the system to identify the corresponding error. This approach is equivalent to a model reconstruction approach.

5.3.1 Approach-I

This approch works as per the theory, given by [77]. as per equations 5.6 and 5.7, avoiding modulation and assuming linearity. In a symmetric pupil when considering low order aberrations, the X and Y slop of wavefront on each pixel is given with the approximation of $sin\,\theta = \theta$. So we tried to derive a matrix equation approach for each pixel, given as in equations 5.22 and 5.23 the derivation of which is given as:

$$\phi(x,y) = \sum_{m=1}^{N} amZm(x,y) \tag{5.13}$$

where 'a_m' is the Zernike coefficients and '$Zm(x,y)$' are the Zernike polynomials. The Sx and Sy are proportional to change in phase as given in equation 5.6 and 5.7. The equation can be written assuming linearity as

$$Sx(x,y) = C \sum_{m=1}^{N} a_m \int_{-B(y)}^{+B(y)} \frac{[Zm(x',y) - Zm(x,y)]}{(x'-x)} dx' \tag{5.14}$$

$$Sy(x,y) = C \sum_{m=1}^{N} a_m \int_{-B(x)}^{+B(x)} \frac{[Zm(x,y') - Zm(x,y)]}{(y'-y)} dy' \tag{5.15}$$

For low order aberrations we can consider a wavefront as a combination of X and Y tilts in each pixel. Considering all the multiplication factors outside the term,

$$Gxm = \int_{-B(y)}^{+B(y)} \frac{[Zm(x',y) - Zm(x,y)]}{(x'-x)} dx' \tag{5.16}$$

$$Gym = \int_{-B(x)}^{+B(x)} \frac{[Zm(x,y') - Zm(x,y)]}{(y'-y)} dy' \tag{5.17}$$

where 'C' is the scaling factor. Upon writing this equation in matrix form we get S=GA, where S is the signal obtained form synthetic images and A is the coefficient matrix. here G=[Gxm' Gym'] and S=[Sx' Sy'].

Upon taking pseudo-inverse of G using SVD, we get A=G^{+}S. Forming a matrix for x and y slop of each pixel considering linearity and low scale aberration approximation, we calculate the Gxm and Gym matrix for the X tilt and Y tilt by considering Zernike in Cartesian coordinates Let m=1 (inclination in y-direction) then Z1 (x,y)=y. By substituting this in the sensor signal equations Sx and Sy we get:

$$Gx1 = C * a1 \int_{-B(y)}^{+B(y)} \frac{[y-y]}{(x-x')} dx' = C * a1 * 0 \tag{5.18}$$

$$Gy1 = C * a1 \int_{-B(x)}^{+B(x)} \frac{[y-y']}{(y-y')} dy' = C * a1 * 2B(x) \tag{5.19}$$

Let m=2 (inclination in x direction) then Z2 (x,y)=x. Substituting this in the sensor signal equations Sx and Sy we get:

$$Gx2 = C * a2 \int_{-B(y)}^{+B(y)} \frac{[x-x']}{(x-x')} dx' = C * a2 * 2B(y) \tag{5.20}$$

$$Gy2 = C * a2 \int_{-B(x)}^{+B(x)} \frac{[x-x]}{(y-y')} dy' = C * a2 * 0 \tag{5.21}$$

From equations 5.18 ,5.19,5.20 and 5.21 we get

$$Sx = C(a1 * 0 + a2 * 2B(y)) \tag{5.22}$$

$$Sy = C(a1 * 2B(x) + a2 * 0) \tag{5.23}$$

where B(x) and B(y) are the pupil boundaries in x and y of the point considered (note that symmetry is assumed). With these equations, a matrix form of X and Y tilts of the wave-front have been obtained per pixel. The results of the simulation are given in section 5.4.1.

5.3.2 Approach-II

This approach works on the principle that in pyramid, for the low magnitude aberration (order of $\lambda/2$ in phase) and considering linear sensor response, the signals Sx and Sy represented by 'S', can be written as a sum of static aberration signal 'So'(i.e the aberrations inherently present in the ideal system) and rate of change of signal with respect the some aberration, characterized by Zernike polynomial [83] (see equation 5.24 and equation 5.25).

$$S_i + = So + ai\frac{\partial S}{\partial \alpha i} \tag{5.24}$$

$$S_i - = So - ai\frac{\partial S}{\partial \alpha i} \tag{5.25}$$

where a_i and α_i are multiplier for zernike coefficient and related polynomial term. From these two equations (equ5.24 & equ. 5.25) we can derive, S_o and the derivatives as follows:

$$So = ((S_i +) + (S_i -))/2 \tag{5.26}$$

$$\frac{\partial S}{\partial \alpha i} = ((S_i +) - (S_i -))/2ai \tag{5.27}$$

From theory the S_o should be same for all the aberrations. The experimental signal map can be represented with the matrix S_e, the following matrix equation can be formulated:

$$S_e = So - \begin{pmatrix} \frac{\partial S_1}{\partial \alpha 1} & - & - & - & \frac{\partial S_1}{\partial \alpha n} \\ - & - & - & - & - \\ \frac{\partial S_m}{\partial \alpha 1} & - & - & - & \frac{\partial S_m}{\partial \alpha n} \end{pmatrix} \begin{pmatrix} a1 \\ - \\ an \end{pmatrix} \tag{5.28}$$

Where the matrix $\begin{pmatrix} \frac{\partial S_1}{\partial \alpha 1} & - & - & - & \frac{\partial S_1}{\partial \alpha n} \\ - & - & - & - & - \\ \frac{\partial S_m}{\partial \alpha 1} & - & - & - & \frac{\partial S_m}{\partial \alpha n} \end{pmatrix}$, is an equivalent to interaction matrix and may be represented as $\mathbf{M}$.

Finally, the signals S_e, generated from experimental/simulated error data's pupil images, carrying information related to aberration in the incoming wavefront can be decomposed to Zernike polynomial as follows:

$$\begin{pmatrix} a1 \\ - \\ an \end{pmatrix} = \mathbf{M}^{+}[\mathbf{S_e} - \mathbf{So}] \tag{5.29}$$

Where the inverse of the matrix $\mathbf{M}$ is obtained by using SVD technique. In order to make use of the outlined methodology, the task is to generate $\mathbf{M}$ i.e control matrix and also estimate $\mathbf{S_o}$ as given in the equation.5.26. To obtain this, the following approach is chosen. The aberrated wavefront was generated by ZEMAX ray-tracing software and passed through a MATLAB based pyramid simulation tool. The simulation tool generates four pupil intensity images. From which we generate Signal matrix [$\mathbf{S}$] composed of Sx and Sy, by using equations 5.1 and 5.2. Next using equation 5.27, $\mathbf{M}$ - matrix is populated. The number of rows in the $\mathbf{M}$ matrix is dependent on the size of the signal map, whereas, the number of columns is related to the number of aberration present (probed) in the wavefront. In the simulation approach its better to set the calibration wavefront for reference segment piston, tip and tit and defocus to ideal system wavefront. This is due to the differential wavefront behavior of the pyramid. These aberrations are estimated as a differential value with respect to reference segment. In our approach, we do the open-loop operation of the pyramid in the diffraction limited region. We do not consider any atmospheric turbulence effects or dispersion effects due to the pyramid.

5.4 Single Aperture Simulations

This section will discuss the results of the wavefront reconstruction technique. We explored two wavefront reconstruction procedures. Approach-II in section 5.3.2 was explored after we observed the issues associated with Approach-I in section 5.3.1. The various considerations and observations we had in different scenarios are presented in this section.

5.4.1 Reconstruction with Approach-I

In this approach, we convert the Sx and Sy signals to the wavefront using the equations 5.22 and 5.23, The orientation of the mask and the corresponding I1 to I4 images are very important in this mode of the reconstruction as the equations depend on the coordinate system. The incoming and reconstructed wavefronts and I1 to I4 images for a few standard Zernike polynomial aberration are listed here. Some of them are defocus, astigmatism at 0 degrees and astigmatism at 45 degrees given by Zernike notations Z^{0}_{-2} (or Z4), Z^{2}_{-2} (or Z5), Z^{2}_{2} (or Z6).

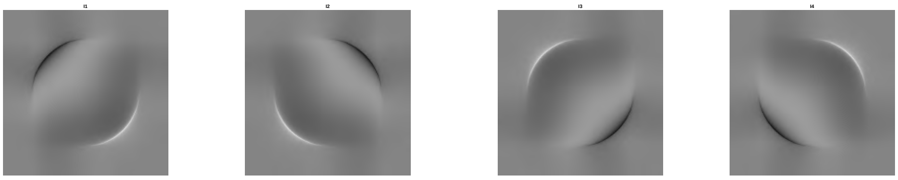

(a) I1 of Z5 **(b)** I2 of Z5 **(c)** I3 of Z5 **(d)** I4 of Z5

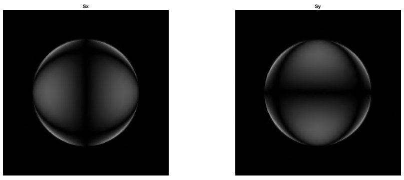

(e) Sx of Z5 **(f)** Sy of Z5

Figure 5.7: Z5 Pupil images and Sx and Sy signals

In the figure 5.7, we have presented the I1 to I4 pupil images and the Sx and Sy signals for Z5. The wave-front is reconstructed using the matrix equations 5.22 and 5.23 as described earlier and SVD techniques. The incoming, reconstructed and residual wavefront for Z5 standard Zernike coefficients by this approach is given in figure 5.8.

As we have observed in the in figure 5.8c, showing the residual wavefront, indicates that the reconstructed wavefront suffers from the error in the reconstruction at the boundary of the aperture. This reconstruction error is because Pyramid works as a modified knife-edge test. In the wave optics domain, we can consider pyramid as a type of spatial filter. Whenever a wavefront encounters any obstruction, there a diffraction effect that takes place. In the re-imaged pupil plane, the edge effect manifests the high-intensity patterns towards the areas where the

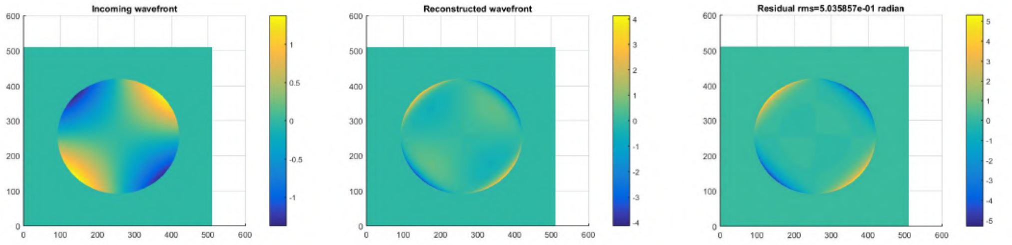

(a) Incoming **(b)** Reconstructed **(c)** Residual

Figure 5.8: Wavefront of Z5

wavefront experience sudden changes. As an example, for each point in the wavefront's field represented by a local tip & tilt with a certain magnitude, when this complex field is passed through the pyramid, it manifests as the intensity variation in the four pupil images. If a wavefront encounters an edge, it acts like an infinite tilt that causes strong intensity variation in the re-imaged pupil. As a result of this intensity variation, the signal mask generated i.e., Sx and Sy, show strong signal variation over these areas of sudden phase variations. In this reconstruction approach as explained in section (5.3.1), the equation uses these intensities and their corresponding pixel position in the pupil images to reconstruct the wavefront. Wherever there is this sudden variation, the approximation for continuous wavefront does not hold. So it generates errors in the reconstructed wavefront. Also gain of the slop variation of tip, tilt approximation has different values for different aberrations patterns making a unified multiplication factor 'C' as per equation 5.22 and 5.23 difficult.

This method suffers from edge noise from the reconstructed wavefront. This model is best suited for continuous wavefront. There is the scope of modifying this approach for a segmented telescope, but with complication of need for pre-calculated mathematical equations. Nevertheless, this technique's main advantage is the non-requirement of an interaction-control matrix of the system. In the experimentation, this method can be used to evaluate the axis of the system,optimum size of of re-imaged pupil, and alignment issues of the pupil image.

We also present few images of the same incoming wavefront with reconstruction is performed only inside a selected circular region, where the approximation for the continuous wavefront can be held with better accuracy.

The reconstruction inside the circular region produces better results compared

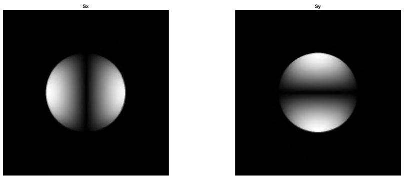

(a) Sx **(b)** Sy

Figure 5.9: Modified Sx and Sy of Z5 inside a circular region

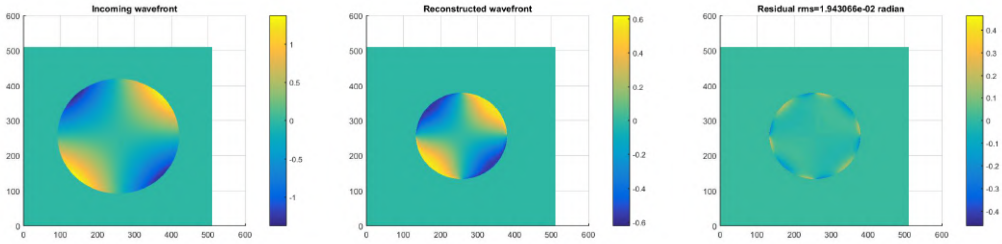

(a) Incoming **(b)** Reconstructed **(c)** Residual

Figure 5.10: Z5 modified wavefronts

to the full aperture. The residual RMS errors can be seen to reduce for Z4 from 1.57 rad to 0.116 rad, around 14 times as we cut the aperture. For Z5 as per figure 5.8c 0.5035 rad to 0.0194 rad as per figure 5.10c, around 25 times. In the case of Z6 we observed an improvement of 0.5146 rad to 0.06407, by almost 10 times. This approach works in the geometrical optics domain. So we propose to use this approach as a qualitative reconstruction method. The disabilities of this approach can be overcome by the next approach, as given in section 5.3.2.

5.4.2 Reconstruction with Approach-II

The first approach suffers from errors at reconstruction, predominantly at the edges. Approach-II was developed to solve the issues with Approach-I. This is an interaction-control matrix based approach. The mathematics is explained in section 5.3.2. The interaction matrix as explained, gives the relation between the change of intensity signals Sx and Sy with the aberration present in the system. Ideally, the interaction matrix needs to be generated for all the aberrations aimed at exploration in this method. By using the SVD matrix inversion method, the reconstructed wave-front can be generated. The images obtained using this approach, have been shown in the figures 5.11 and 5.12.

This approach shows less residual RMS error compared to Approach-I. How-

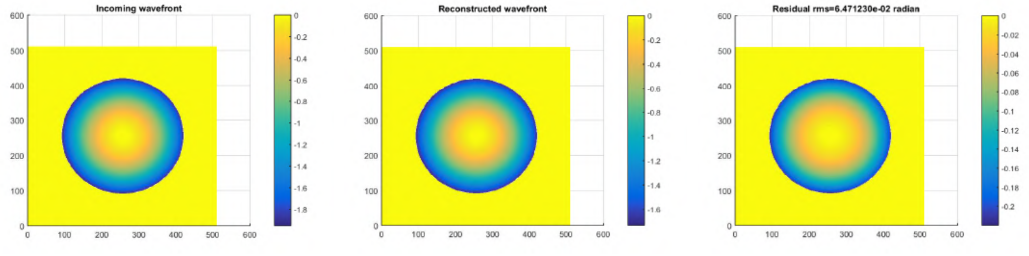

(a) Incoming **(b)** Reconstructed **(c)** Residual

Figure 5.11: Wavefront of Z4 with Approach II

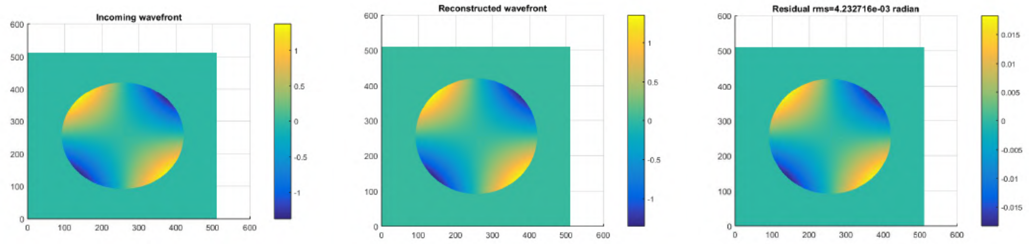

(a) Incoming **(b)** Reconstructed **(c)** Residual

Figure 5.12: Wavefront of Z5 With Approach II

ever, in this Approach-II, we can find a very systematic residual for all the aberrations. The retrieved coefficients always show around 10% error in the reconstructed value. This is mainly due to the leakage into the other calibrated but non-present aberration coefficients. As Approach-I do not follow this kind of a calibrated interaction - control matrix approach, so it is not subjected to leakage to other aberrations. But in overall, accuracy of the Approach-II is far better than Approach-I, especially in segmented apertures. Residual error is 0.0647 rad as per figure 5.11c for Z4. Figure5.12c for Z5 has 0.0043 rad error and for Z6 it is 0.0049 rad. This technique improves the reconstruction by another factor of 10 compared to Approach-I. The drawback of this method is the leaked coefficients and miss interpreted coefficients to other calibrated aberrations. If the Interaction matrix 'M' is not adequately populated with aberration we try to explore, there will be an error in the retrieved coefficient. In this method, we get back the multiplier of the corresponding calibration coefficient, which we supplied to generate the interaction Matrix. The under-calibrated matrix will miss an un-calibrated aberration for another aberration present in the calibration matrix. However, this reconstruction is very sensitive. It can be used for a segmented approach, and it works very well for the wave optics domain. So we selected this technique as an approach for segmented mirror wave-front reconstruction and as our preferred reconstruction method for further studies.

5.5 PSMT: Segmented Aperture Simulations

PSMT is primarily an R&D effort to get acquainted with segmented mirror technology needed for the realization of National Large Optical Telescope (NLOT). PSMT is described in Chapter 2 and NLOT is described in Chapter 3. The pyramid sensor was seen as a potential candidate for the alignment and phasing system of PSMT. We developed the methodology and did an experimentation as given in Section 5.7 to validate our selected approach as in Section 5.3.2. As the next step, we applied our tool in a ZEMAX based simulation platform for PSMT. In the following sections, we will be explaining our methods. PSMT will have two phases of operation. Phase-I is the laboratory demonstration using only primary Spherical segments and a ROC (Radius of curvature) test beam. Phase-II is a full telescope integrated with primary and secondary(see figure 5.13). In phase one, the primary is considered ideal, i.e., no static aberrations is present in the system, making it work like a diffraction limited system. However, PSMT fully-integrated telescope has inherent aberrations present in the system. We studied the effect of both approaches, and we will be discussing both. The numbering scheme of the segments is given in figure 5.14.

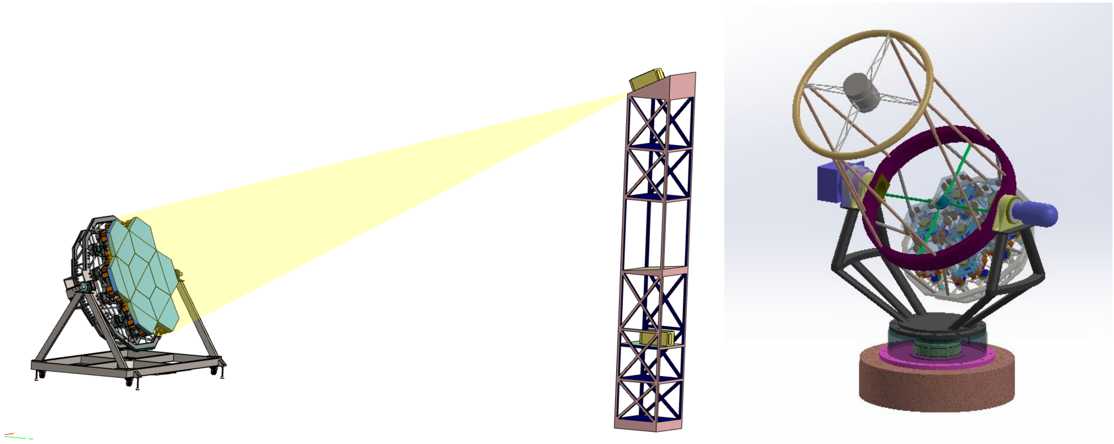

Figure 5.13: 3D model of the PSMT phase-I which is a laboratory test-bed (left) and the PSMT phase-II, a full-fledged segmented mirror telescope (right).

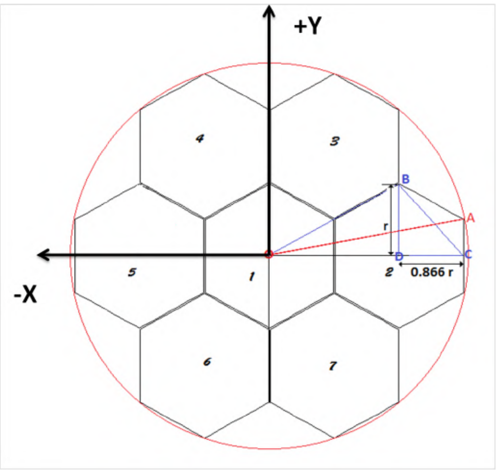

Figure 5.14: The numbering style of 7 segments

5.5.0.1 Ideal Segmented aperture- Retrieval of Multiple Aberrations

In this case, we intend to study the system's ability to operate in an ideal segmented aperture without any static aberration within the high sensitivity linear range of operation in the presence of multiple aberrations. The ideal system is diffraction-limited and over which the aberrations are injected. We mainly intend to sense piston, tip, tilt, and defocus as these are the four main aberrations in a segmented telescope. Active optics can correct these aberrations. However, defocus is an aberration that is usually difficult to correct with warping harness, which is a tool that is extensively used in active optics. As PSMT has spherical segments, this defocus can be corrected by placing the segments onto a new global ROC as required by the defocus error, using a piston, tip, and tilt of segments. But this will create piston error in the system. For a set of Z1-Z4 aberrations simultaneously applied in the system, the simulated incoming wavefront, reconstructed wavefront and the difference in wavefront are given in the figure 5.15 and Zernike coefficients in mm are given in Table 5.2.

The system shows an excellent reconstruction with an error of less than or equal to 10%. One reason for the difference is the leakage of dominant aberration signal intensities to other segments and vice verse. Another reason for these leakage coefficients is the intensity fluctuation in one segment affecting the next one. We observed that the cause of this error is the similarity in the Sx and Sy signal patterns of different aberrations, causing wrong calculation of the aberration

Seg .NO	Input Zernike (Z1)	Input Zernike (Z2)	Input Zernike (Z3)	Input Zernike (Z4)	Output Zernike (Z1)	Output Zernike (Z2)	Output Zernike (Z3)	Output Zernike (Z4)
1	0	0	0	0	0	0	0	0
2	0	2E-6	0	5E-6	0	2.11E-6	0	5.12E-6
3	2E-6	0	1E-6	0	2.11E-6	0	1.14E-6	0
4	5E-6	0	0	2E-6	4.95E-6	0	0	2.02E-6
5	3E-6	-2E-6	0	1E-6	2.67E-6	-1.39E-6	0	1.29E-6
6	0	0	0	0	0	0	0	0
7	2.5E-6	0	2.5E-6	3E-6	2.53E-6	0	2.11E-6	2.91E-6

Table 5.1: 7 mirror system with random piston tilt and defocus coefficients in mm, retrived coefficients less than 10% of the maximum aberration coefficent are shown as zero

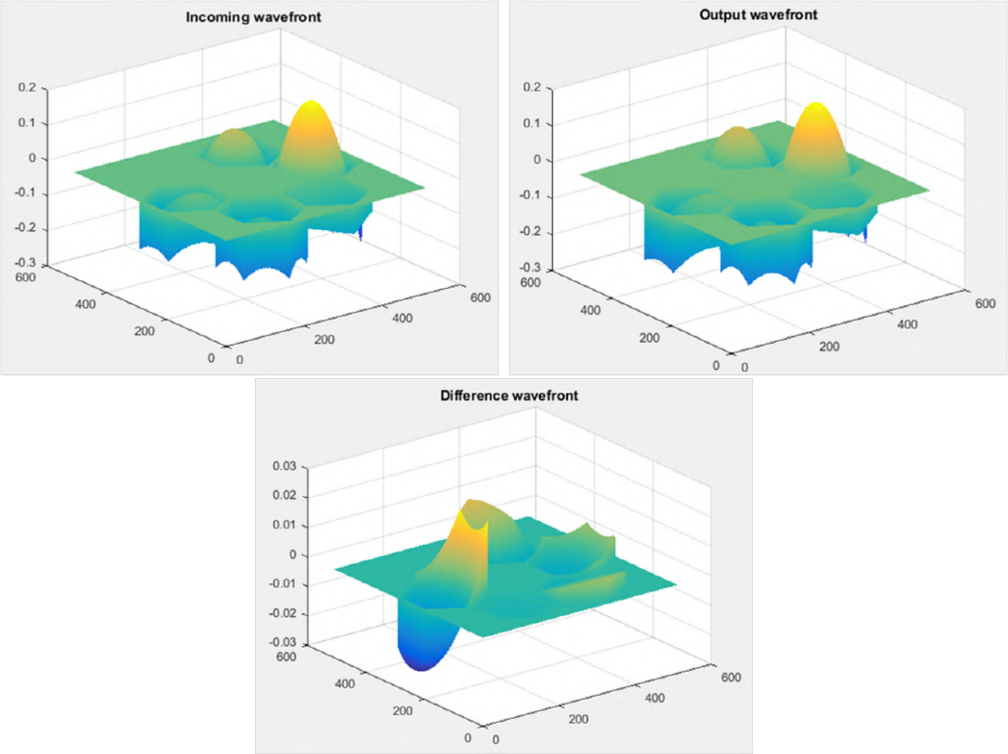
Incoming wavefront

Output wavefront

Difference wavefront

Figure 5.15: 7 mirror system wavefronts with all segments given random piston tilt and defocus aberration.(top left)Incoming, (top right)Output, (bottom) residual.

coefficients. This can be observed in Table 5.2, where given piston (Z1) causes dominant variation in defocus (Z4) and spherical aberration (Z11). We made an optical system calibrated with Z1 to Z15 standard Zernike (Noll) and injected with piston, tip, and tilt and defocus error (Z1-Z4) to study these. We observed that by reducing the number of aberrations probed, we could reduce this leakage, but this may not be an acceptable approach, as in real optics where many aberrations do come to existence. We also studied how different changes in PSF affect the retrieved coefficients. An overview of this is given in section 5.5.0.2.

One other issue we faced in this reconstruction approach is the very short capture range of aberrations. Modulation is usually considered an interesting technique in improving the sensitivity of the pyramid to capture large magnitudes. Modulation technique, based on different approaches, has been explored in detail in multiple studies [86],[74],[73]. However, our studies were conducted without using conventional modulation techniques.

5.5.0.2 Simulation on PSF Modification

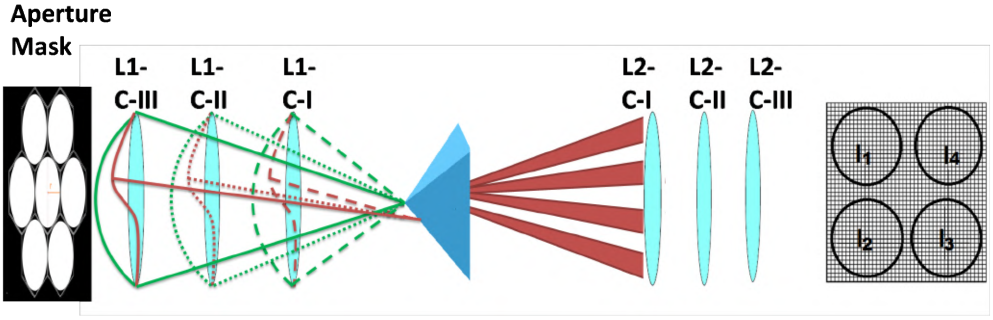

Figure 5.16: 'L1' is the imaging lens, 'L2' is the re-imaging lens, and 'C' indicates one simulation condition iteration, indicating the variation in lens positions. Aperture cutting mask is kept at the pupil

We did three simulation cases. All rooted in the same principle of PSF modification. Unlike a real optical system, in the software-based digitized simulation, the pixel size Pix_{psf} in the focal plane of the simulated PSF which will be falling at the tip of the pyramid can be given by,

$$Pix_{psf} = \frac{\lambda F_{no} D}{N \Delta p} \tag{5.30}$$

where N is the total number of pixels in Fourier transform matrix of size N × N, and F_{no} is the F-number of the system. $\Delta\, p$ is the pixel size in the pupil plane, D is the diameter of the aperture, and λ is the wavelength, all in units of length.

Case-I Case-I is done by enlarging the PSF. As given in figure 5.16, 'L' stands for the lens and 'C' stands for simulation condition. 'L1' is the imaging lens, 'L2' is the re-imaging lens 'C-n' indicates one simulation condition, showing the variation in lens positions. In this case, L1 and L2 simultaneously change for all iterations in the optical system. An iteration is equivalent to a combination of L1-Cn with L2-Cn, for n=I, II, III, along with a fixed aperture mask of seven apertures, each of full segment radius. This simulation is equivalent to simultaneously increasing the focal length of the lens system (L1) for imaging to the pyramid's tip, along with the re-imaging lens (L2), to make sure the re-imaged pupil sampling is constant. This operation results in the size enlargement of the PSF falling at the pyramid's tip without changing the imaging system's angular resolution.

As per equation 5.30, this analysis is equivalent to reducing the pixel size in the PSF plane or analogously increasing the PSF size by keeping the re-imaging pupil sampling same. The aberration magnitude and PSF Strehl ratios are kept same. The results are presented in Section 5.5.1.1 and Section 5.5.2.

Case-II Case-II simulation can be considered analogous to an optical system (see Figure 5.16) which has focal length of the imaging lens (L1) increased while keeping the focal length of the re-imaging lens same. 'L1' is the imaging lens, 'L2' is the re-imaging lens, and 'C' indicates one simulation condition, showing the variation in lens position. Here, L2 remains in the same position for all iterations. So each iteration is equivalent to a combination of L1-Cn with L2-CI, for n=I, II, III, along with a fixed aperture mask of seven apertures, each of full segment radius. In this simulation, as per equation 5.30, as the PSF is cropped to a reduced size, the number of pixels over which the pupil is re-imaged is reduced. This results in a reduction in the re-imaged pupil size with an increase in the size of the PSF.

This iteration can also be considered analogous to a system where the re-imaged pupil plane detector system with an increased pixel size, consecutively reduced the total sampling pixels for Sx, Sy signals. The results are presented in Section 5.5.1.2 and Section 5.5.2.

Case-III Case-III is the reduction of the pupil's clear aperture over each segment by varying the mask radius, ie., vary the aperture used to generate the PSF. See figure 5.17. So as per figure 5.16 each iteration is equivalent to a fixed combination of L1-CI with L2-CI, along with changing the aperture mask of radius size over each segment.

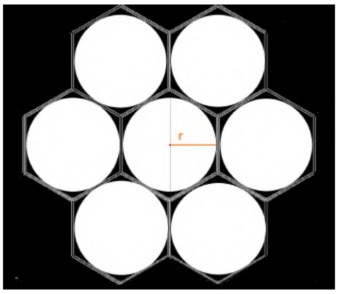

Figure 5.17: Image of the circular mask with radius 'r' covering 7 segments

The pixel radius is the radius of the circle created to cut down the aperture as in figure 5.17. The total pixel radius considered in each case will be($\sqrt{3}/2\times$(side length of hexagon in number of pixels)), because the segments are hexagon in shape. A simulated optical system generates the segmented wavefronts required for calibration and simulation of the analysis in our approach. The results are presented in Section 5.5.1.3 and Section 5.5.2.

5.5.1 PSMT-Phase I

In this simulation approach, the telescope is considered ideal, ie., there is no static aberration present in the system. This study is significant when considering the pyramid sensor as a high-level correction sensor with high sensitivity and a short operation range. We observed that the pyramid sensor has the ability to sense multiple aberrations at one time. This ability makes it useful in sensing and correcting multiple aberrations simultaneously. We explored up to 15 standard Zernike aberration (Noll) coefficients staring from Piston. As it is a segmented pupil, we use the approach as in Section 5.3.2 to reconstruct the wavefront by finding the individual aberration coefficients of each of the segments. In the coming sections, different pyramid sensor properties in the case of a segmented mirror telescope and the fine-tuning of our aberration sensing technique are explored.

5.5.1.1 Case-I

Since the system is analogous to increasing the focal length of the imaging and re-imaging lenses simultaneously without changing the aperture size, we call the ideal System F_{no} to be 'X'. The different observations are given in the figure 5.18 to figure 5.20.

Zernike No	(Z4)F	(Z4)F/3.35	(Z1)F	(Z1)F/3.35
Z1	-0.253159	-0.253040	1	1
Z2	-0.014100	-0.014109	0.000974	0.000619
Z3	0.00E+00	-3.54E-15	1.87E-15	5.10E-16
Z4	1	1	-0.002042	-0.002540
Z5	-6.39E-16	-2.14E-15	2.97E-16	1.68E-15
Z6	9.88E-05	1.05E-04	-0.006547	-0.006472
Z7	1.61E-15	6.43E-16	-6.12E-16	2.72E-16
Z8	0.0022105	0.002204	0.006662	0.006641
Z9	-7.03E-16	-1.41E-15	1.30E-15	2.45E-15
Z10	-7.40E-05	-7.34E-05	1.56E-03	1.70E-03
Z11	-0.000487	-0.000355	-0.008113	-0.008324
Z12	2.97E-06	4.24E-06	-0.003352	-0.003322
Z13	-1.90E-16	2.84E-15	1.21E-16	-4.09E-15
Z14	0.000540	0.000534	-0.004523	-0.004769
Z15	-1.69E-16	2.66E-16	-1.00E-16	6.93E-17

Table 5.2: 7 mirror system with second segment given normalized defocus (Z4) or Piston (Z1)of 1 unit. Table shows the leakage coefficient to other calibrated aberrations of the same segment for the imaging lens and re-imaging lens combination, each of focal length F and 3.35 F.

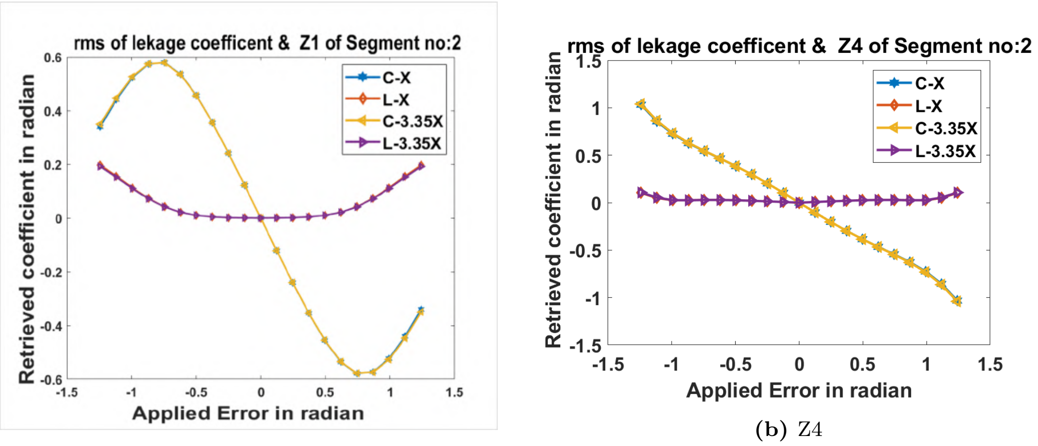

(a) Z1

(b) Z4

Figure 5.18: RMS of leakage coefficients and retrieved coefficient v/s the applied error for segment 2, imaging and re-imaging lens focal lengths F and 3.5 F. 'C' denotes coefficient and 'L' denotes leakage.

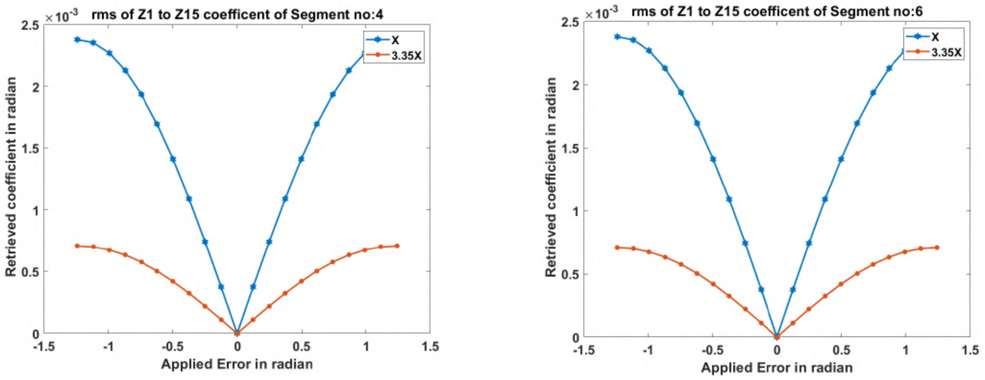

(a) Applied Z1 in S2 v/s cross-talk in S4

(b) Applied Z1 in S2 v/s cross-talk in S6

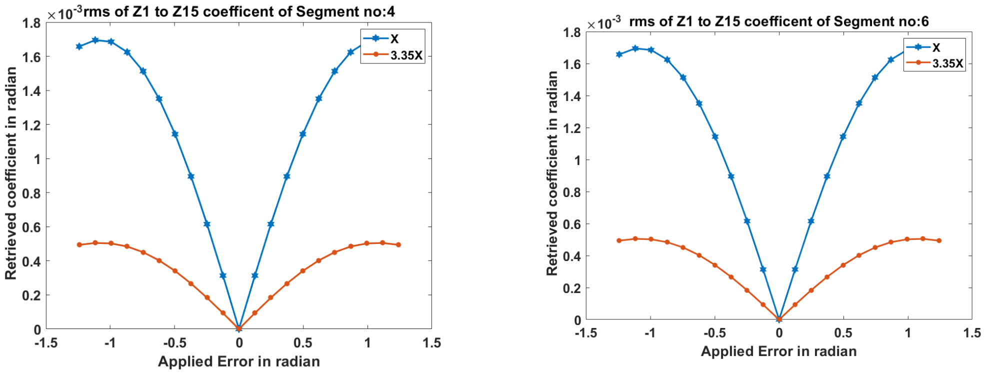

(c) Applied Z4 in S2 v/s cross-talk in S4

(d) Applied Z4 in segment 2, cross-talk in S6

Figure 5.19: RMS of retrieved cross-talk coefficients Z1 to Z15 in segments 4 and 6 with applied error in Segment 2

We observed a slight improvement in the coefficient properties with focal length improvement of the imaging system(see Table 5.2). In the simulation with MATLAB Fourier transform, this focal length improvement is achieved through zero padding. It's advisable to do a zero padding of at least twice the aperture size. If the PSF is smooth and broad, the corresponding OTF (Optical transfer function) is narrow and smooth, making the re-imaged pupil intensity variations better. If the zero padding is not done, the resultant PSF will behave like a jagged PSF; see the coefficient plot with final $F_{no} = 1 \times initialF_{no}$,(X) in the figure 5.20. The effect of the jagged PSF as a result of no zero padding can be seen in the non-linear region of coefficients. Without zero padding the telescope aperture is a 511×511 pixel matrix.

In figure 5.18, we observe that if the focal length of L1 and L2, as in Figure 5.16 is increased, the linear capture range remain the same. However, a closer examination of the leakage coefficients in the other segments (figure 5.19) indi-

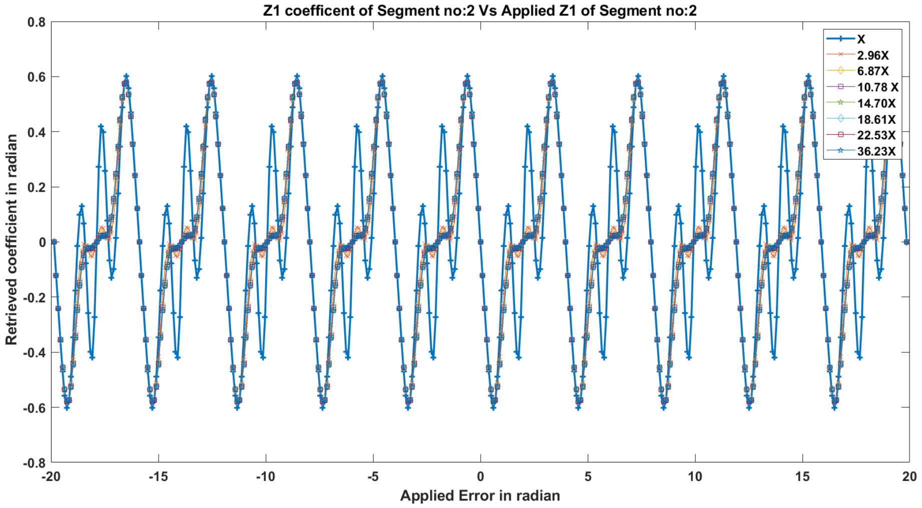

Figure 5.20: Z1 retrieved coefficient for applied Z1, of segment 2 for various imaging system F_{no}(X)

cates a reduction in the leakage coefficients. This can be directly related to the improvement in PSF smoothing. The fact that the linear range is sustained indicates that the Strehl ratio improvement helps in improving the sensor's linear range sensitivity. Our primary interest lies with the pyramid's piston coefficient. The sinusoidal cyclic nature considered in most approximations in the pyramid coefficient becomes more prominent with the PSF's enlargement. For simulated Piston, this is shown in the figure 5.20.

We observed that as the total P.V (Peak to valley) error increases in other aberrations in the Zernike standard aberration system, there are strong non-linearities introduced into the simulated Sx and Sy signals. Simply put, we can state that this is due to a drop in the Strehl ratio. From this analysis, we concluded that improving the PSF sampling without actually improving the Strehl ratio, ie., changing the PSF profile form jagged to smooth, will result in a smoother variation in the intensity in the re-imaged pupil images. This PSF smoothening will reduce the jump in non-linear regions of the aberration coefficients, mildly reducing the leakage to other calibrated aberration coefficients of the same segment, and reduce the cross-talk between the segment edges. This can be seen in figure 5.19. Nevertheless, this will not improve the linear range of the sensor.

5.5.1.2 Case-II

In this case, from the focal plane complex field, we select a part equivalent to the ideal wavefront size in the number of pixels, i.e., 511×511. This selection reduces the re-imaged pupil sampling upon taking inverse Fourier transform of the PSF. This system is analogous to increasing the re-imaged plane pixel size/ reducing the re-imaged pupil size/ binning the re-imaged pupil.

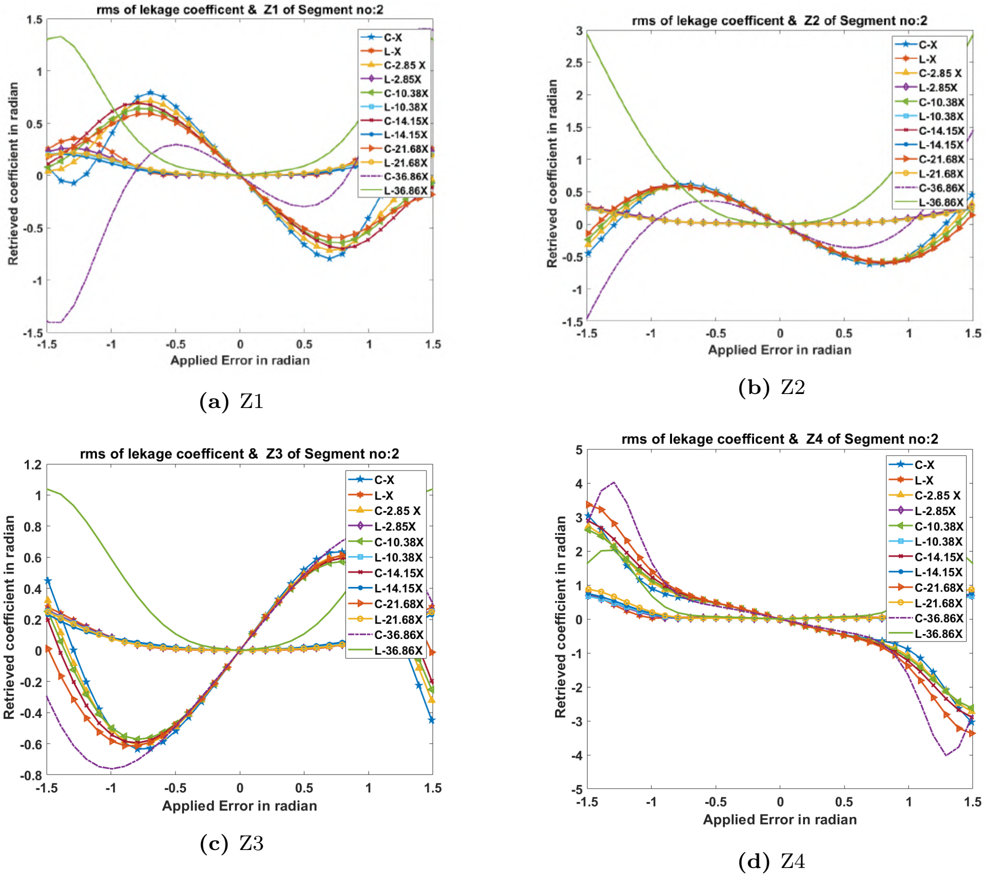

(a) Z1

(b) Z2

(c) Z3

(d) Z4

Figure 5.21: RMS leakage and Retrieved coefficient v/s Applied coefficient for detector pixel size variation from ≈X to 37X. 'C' - coefficient, 'L' - RMS of leakage into other calibrated coefficients.

Figure 5.21 shows that as the re-imaged pupil pixel size increase (or re-imaged pupil sampling reduces) as a consequence of the PSF enlargement, the retrieved coefficient dynamic range varies. The reduction is more or less linear till the pixel size reaches ≈22 times the initial value. However, there is a higher reduction of dynamic range for Z1, Z2, and Z4 as the pixel size reaches ≈37 times. This behavior is due to the reduction in the total number of pixels available for matrix inversion, especially from the edges. However, in the case of Z3 or Y-tilt, as the pixel size reach ≈37 times, the dynamic range of the retrieved coefficient seems to improve. Due to the axis alignment of the hexagonal segment with the pyramid, Z3 appears corner to corner or with Y-axis alignment in a segment(see figure 5.14). When we introduce a circular mask to make the Hexagon aperture to a circle, the wavefront's PV variation is reduced. The increase in the pixel size causes a binning effect in this case. The signal intensities from the edges and corners add up to give a better linear response in the signal patterns, slightly improving the dynamic range. The variation in the retrieved coefficient's dynamic range due to wavefront PV reduction through aperture reduction is explained in section 5.5.1.3. When we consider the leakage into other calibrated coefficients in the same segment as in 'L' of figure 5.21, within the linear range of the applied error, the leakage is minimum, with a slight reduction in the leakage as we increase the pixel size. This is due to the binning effect introduced by this simulation approach.

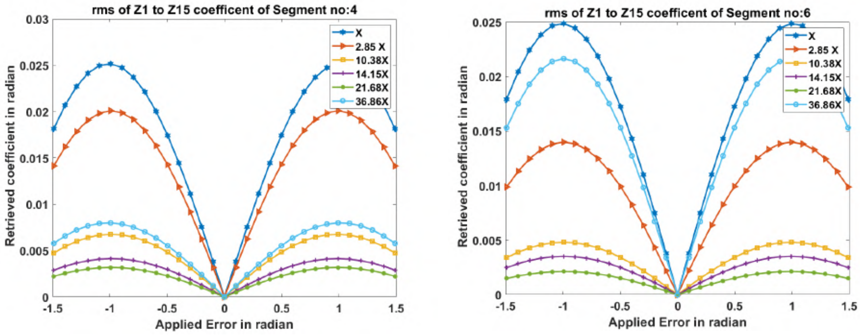

(a) S4 **(b)** S6

Figure 5.22: RMS of retrieved cross-talk coefficients on Segment(S) 4 and 6, for applied Z1 in S2

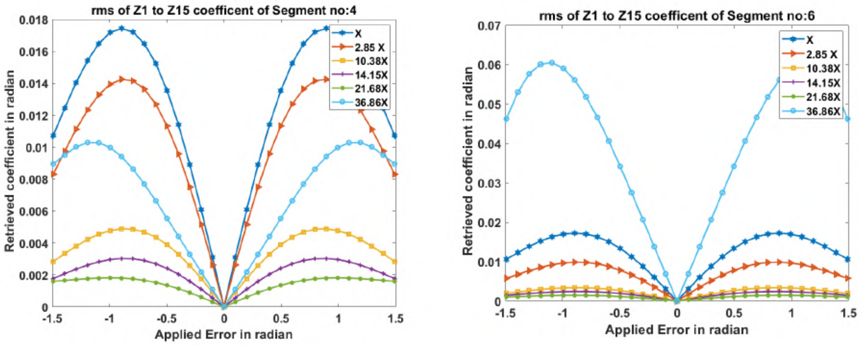

(a) S4 **(b)** S6

Figure 5.23: RMS of retrieved cross-talk coefficients on Segment(S) 4 and 6, for applied Z4 in S2

When we consider leakage into other segments as in figure 5.23 till the pixel size reaches ≈22 times the initial value, the leakage seems to reduce linearly then as the the pixel size reaches ≈37 times it increases again. As explained earlier this is due to reduction in the number of pixels with signals for matrix inversion.

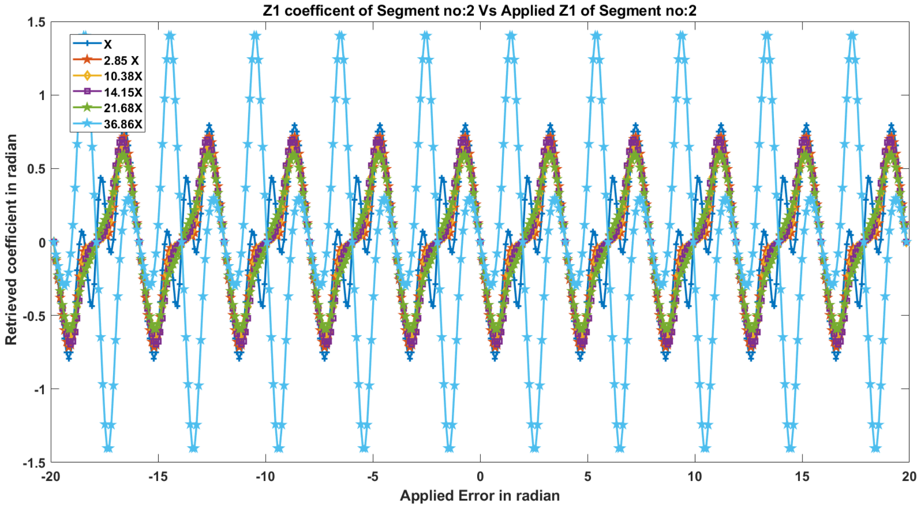

(a) Z1

Figure 5.24: Retrieved Z1 coefficient v/s Applied Z1 coefficient for zero padded aperture, resulting in detector system pixel size variation from ≈X to 37X .'C' is for the coefficient and 'L' is for the leakage into other calibrated coefficients,in S2

From the figure 5.24 for piston we can see that smoothing of the non-linear region with the improvement of the cyclicity till pixel size is increased up to 22 times the initial value. This is showing the binning effect of this simulation. However, suppose we increase the pixel size further. In that case, the total number of pixels is reduced; the non-linear range's intensity variation is interpreted as a high magnitude variation in the signal value. This causes the non-linear region to peak up again, as seen in pixel size is about 37 times of initial value.

In this simulation, we observed that the coefficient's linear range does not improve much. However, we observed that this kind of reduction in the re-imaged pupil sampling could not be chosen arbitrarily. It has an improving effect by diminishing the cross-talk to other segments, as seen in figure 5.23 for segment numbers four and six. This re-imaged pupil sampling first also improves cyclicity by smoothing and linearizing the nonlinear jump regions of the coefficient plot, mainly in the case of piston, see Figure 5.24. In PSMT, starting with a PSF pixel size of around 7 μm in the ideal case, we can go up to 150 μm (22 times) in the maximum pixel size as per equation 5.30. We consider the PSMT aperture size of 1.3 m, with 511×511 pixels at the F/11 system and 632.8 nm wavelength.

5.5.1.3 Case-III

Once we observed the improvement in the re-imaging plane due to the PSF sampling, we wanted to know the effect of reducing the aperture, analogously, reducing the Peak to valley aberrations present in the system. The injected aberrations remain the same; the study aims to see the effect of reducing the clear aperture over each hexagonal segment in the real-time scenario, so as to improve the sensitivity of the pyramid to large aberrations. The pyramid's sensitivity relates to the Strehl ratio, especially when you consider the non modulated case. Also, in the real system, we intend to use aperture masks to cut down the aberration in sensing, but extrapolated aberration will be used in the total correction system.

Different aberrations will have different sensitivity profiles, but our interest mainly lies with four aberrations from Z1 to Z4 (Piston to defocus standard Zernike (Noll) coefficients). As Z2 and Z3, namely tip and tilt, behave in the same manner, we will be discussing one of them.

In figure 5.25, we have plotted the behavior of Zernike aberrations Z1 to Z4 under various mask radii, in a zoomed range.

Tip/tilt, as in figure 5.25b shows improvement in the linear range as the aperture is cut down. In figure 5.25a and figure 5.25c, we can see that in the case of Piston and defocus, the approach of reducing the aperture had an effect in the improvement of sensitivity of the system by eroding the low magnitude aberrations. This eroding is, in turn, the behavior of pyramid signal as, f(x)=Sin(x)-x given in the paper by Costa, et.al. in 2003[87]. This gives an insight into this kind of behavior of the sensor. The large aberration has an eroding effect on the small aberrations when the aperture is cut down for the pyramid. This approach improves the system's sensitivity in the case of aberrations, mainly like Piston and defocus. At the same time, if we observe Figure 5.26, we can see that as the mask radius is reduced, the aberrations whose intensity patterns are similar to the probed aberration gets larger coefficients. This is a disadvantage. We propose this approach with proper calibration in conditions where varying the dynamic range

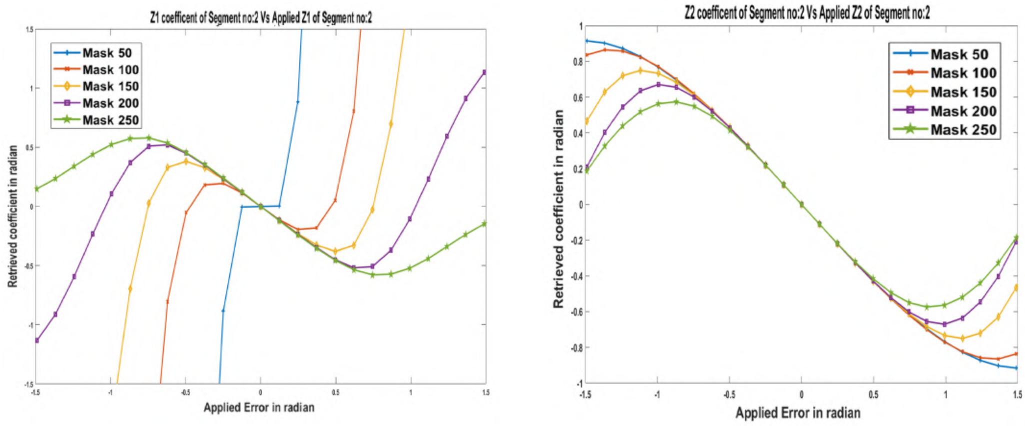

(a) Z1 Retrieved coefficient v/s Z1 Applied coefficient for various aperture mask sizes

(b) Z2 Retrieved coefficient v/s Z2 Applied coefficient for various aperture mask sizes

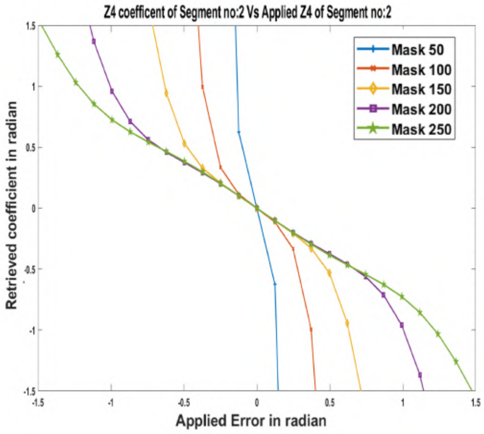

(c) Z4 Retrieved coefficient v/s Z4 Applied coefficient for various aperture mask sizes

Figure 5.25: Applied error ±1.5 radian, Zoomed image, for segment 2

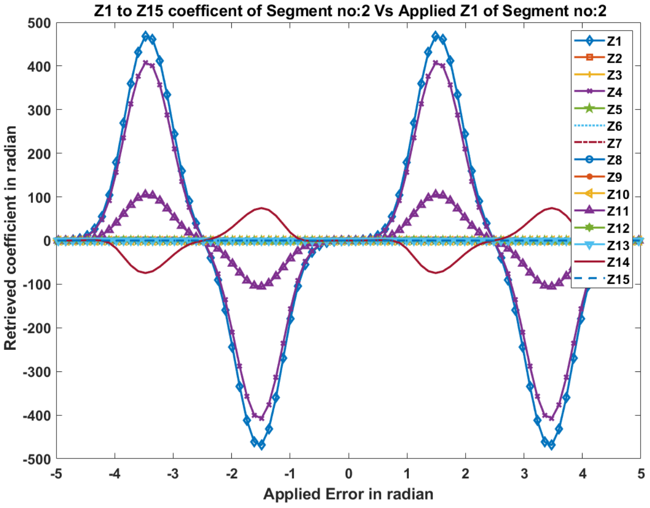

(a) Z1

Figure 5.26: Retrieved coefficient v/s Applied coefficient along with leakage coefficients for segment 2, mask radius of 50 pixel

and sensor sensitivity are required. This technique can modify the linear range. As expected, this is due to the change in Strehl ratio as the total aberrations are reduced.

5.5.2 PSMT-Phase II

Pyramid sensor is mainly a high-level sensor, working best in the diffraction-limited or near diffraction systems where static aberrations are significantly less. PSMT, in its fully integrated telescope form, is having inherent aberrations on the system (see Table 5.3). These inherent aberrations cause changes in reconstruction behavior. We did studies to understand this. We generated the wavefront of the fully integrated telescope with the ZEMAX software. Then, as in the case of a system without static aberrations, we studied increasing the PSF size with and without changing the re-imaging lens system and reducing aperture radius.

Table 5.3: Values of decomposed Zernike coefficients in the wave unit for the segment 2 of PSMT fully integrated telescope of Phase-II, at 632.8 nm wavelength

Zernike-Term	Coefficient	Zernike Equation	Related aberration
Z 1	-0.04804998	1	Piston
Z 2	-0.00983817	$4^{\frac{1}{2}}(p)\cos(A)$	X-tilt
Z 3	0.0	$4^{\frac{1}{2}}(p)\sin(A)$	Y-Tilt
Z 4	-0.01772813	$3^{\frac{1}{2}}(2p^2-1)$	Defocus
Z 5	0.0	$6^{\frac{1}{2}}(p^2)\sin(2A)$	Oblique astigmatism
Z 6	-0.00690247	$6^{\frac{1}{2}}(p^2)\cos(2A)$	Vertical Astigmatism
Z 7	0.0	$8^{\frac{1}{2}}(3p^3-2p)\sin(A)$	Vertical Coma
Z 8	0.02258552	$8^{\frac{1}{2}}(3p^3-2p)\cos(A)$	Horizontal Coma
Z 9	0.0	$8^{\frac{1}{2}}(p^3)\sin(3A)$	Vertical Trefoil
Z 10	0.02647413	$8^{\frac{1}{2}}(p^3)\cos(3A)$	Horizontal Trefoil
Z 11	0.00785729	$5^{\frac{1}{2}}(6p^4-6p^2+1)$	Primary Spherical
Z 12	0.00876303	$10^{\frac{1}{2}}(4p^4-3p^2)\cos(2A)$	Vertical Sec-Astigmatism
Z 13	0.0	$10^{\frac{1}{2}}(4p^4-3p^2\sin(2A)$	Oblique Sec-Astigmatism
Z 14	0.00000705	$10^{\frac{1}{2}}(p^4)\cos(4A)$	Vertical Quadrafoil
Z 15	0.0	$10^{\frac{1}{2}}(p^4)\sin(4A)$	Oblique Quadrafoil

In our analysis with the Case-I approach with static aberration, we noticed a DC shift in the retrieved coefficient and a shift in the non-liner region's position.

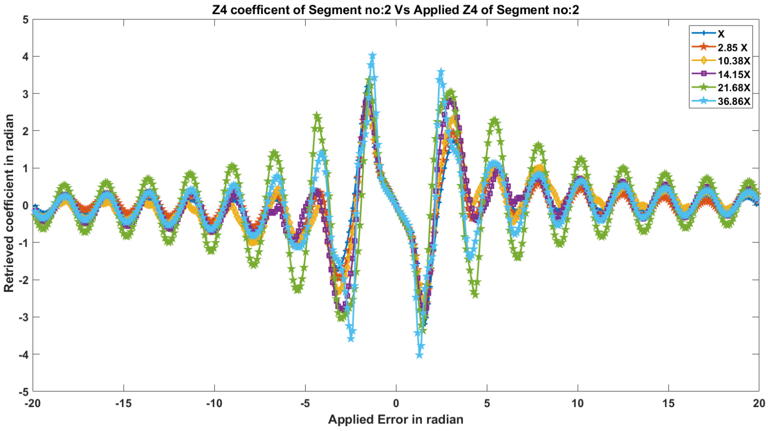

(a) Z4 Phase-I

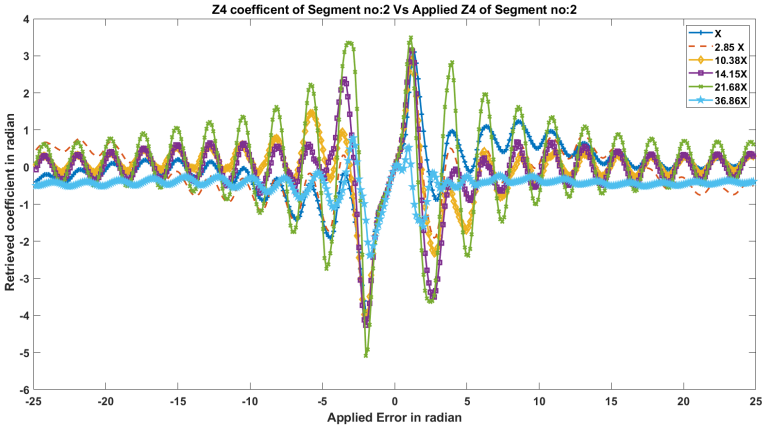

(b) Z4 Phase-II

Figure 5.27: (Case-II)Retrieved coefficient v/s Applied coefficient for detector system pixel size variation from ≈ X to 37 X.

In the same way, the figure 5.27 gives two plots (a)Phase-I, and (b)Phase-II. For the Case-II , the coefficient retrieved is DC shifted to the plot's bottom regions compared to the Phase-I image. This is due to the nominal telescope errors. When we consider the signals Sx and Sy, the null signals Sxo and Syo are the average of all the aberrations Sxo and Syo used for calibration. So even though the static aberrations are taken care of in theory, effects created by these are retained in the system in practice. The polarity difference in the coefficient axis is due to two mirrors present in the system. Along with this, the static aberrations present in the system cause a DC shift in the retrieved coefficient values. We observed that upon subtracting the nominal system aberration coefficients from the unknown aberration coefficients, the DC shift to the sinusoidal curve could be avoided. However, the shift in the position of the non-linear range is not avoidable. This is due to a shift in the saturation range due to inherent aberrations. Nevertheless, we present the result without the subtraction of nominal aberration. It is not easy in a real system to separate nominal pre-existing aberrations from the newly introduced unknown aberrations to the full extend. The figure 5.27b, is for the Case-II when we have an inherent static aberration in the system, our system's linear operation range is limited. The coefficients obtained through matrix inversion depend on the intensity patterns; the non-linear region can produce an error in the magnitude of coefficients compared to the linear region when we reduce the pupil sampling. This emphasizes our suggestion that re-imaged pupil sampling should not be chosen arbitrarily but with proper optimization as per the user requirement.

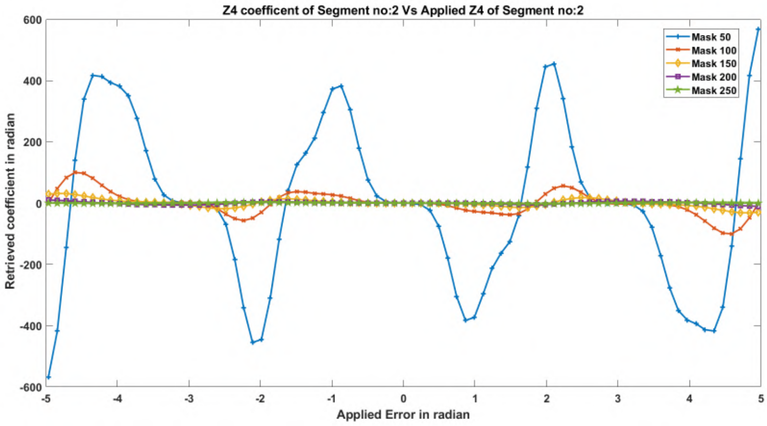

(a) Z4 Phase-I

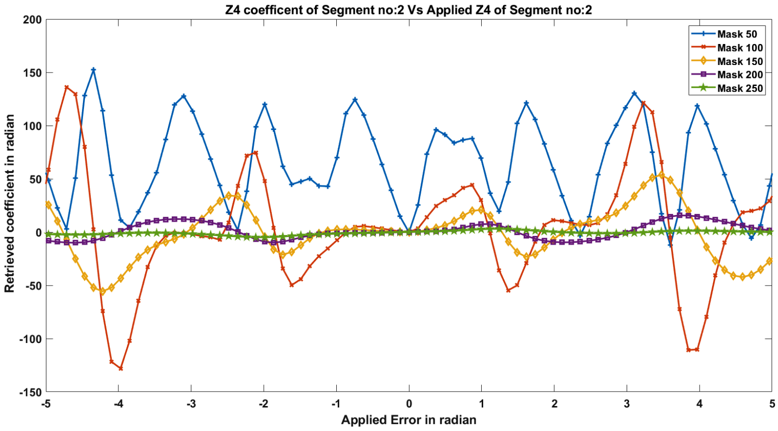

(b) Z4 Phase-II

Figure 5.28: Retrieved coefficient v/s Applied coefficient for various aperture mask sizes, Case-III

In the case-III, as in figure 5.28b, plot with static aberration is shown. We have observed that the DC shift and non-linearity region shift in the coefficients are present due to static aberrations. The polarity of the retrieved coefficients is inverted due to multiple mirrors in the system. The system follows the same linearization behavior for large coefficients as in figure 5.28a without static aberration. But the linearization also shows a DC shift. However, when we cut down the aperture in a system where static aberrations are nominally present, due to similarity in aberration patterns, there will be an issue with false identification of an aberration as another aberration probed. This can reduce the retrieved magnitude of the aberration probed, as in figure 5.28b. So, a proper prior calibration is essential with varying aperture radius for implementing this technique in a real system.

5.6 Increasing Piston Detection Range with Broadband Technique

In all our simulations, as in section 5.5.0.2, we observed that we still struggle with the cyclicity and short dynamic linear range, which is an inherent problem for the pyramid sensor. We observed in the KECK broadband technique [66] that by varying the system's temporal coherence length, we can create a signal modulation in the PSF patterns. Also, in Simone Esposito et al. in 2003 [76] we see that the pyramids signal has a sinusoidal dependency on the piston error present in the system. So we tried to improve the capture range of piston by introducing broadband technique into the pyramid. In all the analyses we have done, till now, we consider only monochromatic wavelength. This causes cyclicity in the frequency of $\lambda/4$ in the PSF, which in turn makes the capture length in piston only of $\lambda/4$ in surface sag variation. As per temporal coherence length equation $\lambda^2/(2\ \Delta\ \lambda)$, the monochromatic wavelength has infinite coherence length. So this PSF cyclicity will exist for infinity, causing a tiny capture range within $\lambda/4$ on the surface. Broadband uses a band of wavelength, which makes it have a low coherence length by the coherence length equation. This will give it a capture range of few microns. This is ideal for finding unambiguous piston error, whereas in a narrowband or ideally speaking monochromatic wavelength case, we have to be satisfied by fractions of $\lambda/4$. The broadband technique uses Gaussian bandpass filters for its working. For a phase error within the filter's coherence length, the amplitude and phase correlation of the wavefronts are not altered, thereby causing them to sum up coherently at the focus. Whereas once the wavefront deformation is out of the filter coherence length, they will sum up incoherently only in intensity. With this difference in the behavior of PSF, we can find the piston error in the system. In the pyramid case, when you have a wavelength band, we can simulate this effect by the basic pyramid behavior, as given below.

In the simulation, we create the wavefront with a particular piston error in the segment under consideration. The focal plane field generated with both real and complex part intact is multiplied with the filter transmission function and co-added for multiple wavelengths. The final focal plane field obtained like that is used to create the re-imaged pupil. The signal intensities [S]=[Sx Sy] obtained by this method for the segment under study can be given as

$$S = 4\pi\delta \int_{\frac{4\pi\delta}{\lambda_1}}^{\frac{4\pi\delta}{\lambda_2}} [\frac{sin[t]}{t^2}]dt \tag{5.31}$$

$$S = 4\pi\delta[C_i[t] - \frac{sin[t]}{t}]_{\frac{4\pi\delta}{\lambda_2}}^{\frac{4\pi\delta}{\lambda_1}} \tag{5.32}$$

Upon integration we can write this equation as

$$S = \frac{1}{4\pi\delta}[\lambda_2 sin\frac{4\pi\delta}{\lambda_2} - \lambda_1 sin\frac{4\pi\delta}{\lambda_1}] + ln\frac{\lambda_2}{\lambda_1} + \sum_{k=1}^{\infty} \frac{-1^k 4\pi\delta^{2k}[\frac{\lambda_2^{2k}}{\lambda_1^{2k}}]}{2k(2k!)} \tag{5.33}$$

Whereλ_1 and λ_2 are the extreme wavelengths used in the Gaussian transmission filter and δ is the piston error.

Retrieved coefficients are expected to follow an amplitude modulation,as the same effect is seen in the Sx and Sy signals.

In figure 5.29, we give how the retired coefficient modulates the retrieved piston coefficient with the variation of coherence length with a Gaussian broadband filter. We can see that the cyclicity is still present in the system. Then, we plotted the leakage into the other calibrated Z1 to Z15 coefficients in the figure 5.30. We can see modulation is not only for piston but also for the entire calibrated aberration coefficients. This indicates that just by changing the system's temporal coherence length, we can achieve a signal modulation of all the aberration coefficients. This helps in the overall minimization of the wavefront error. By varying

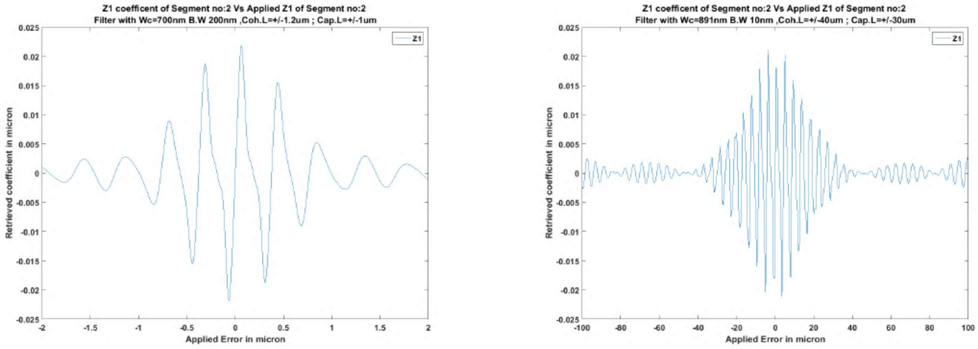

(a) Filter with capture length of ±1 micron and coherence length of ±1.2 micron

(b) Filter with capture length of ±30 micron and coherence length of ±40 micron

Figure 5.29: Retrieved Z1 coefficient v/s applied Z1 coefficient of segment:2, PSMT-Phase-I, in micron

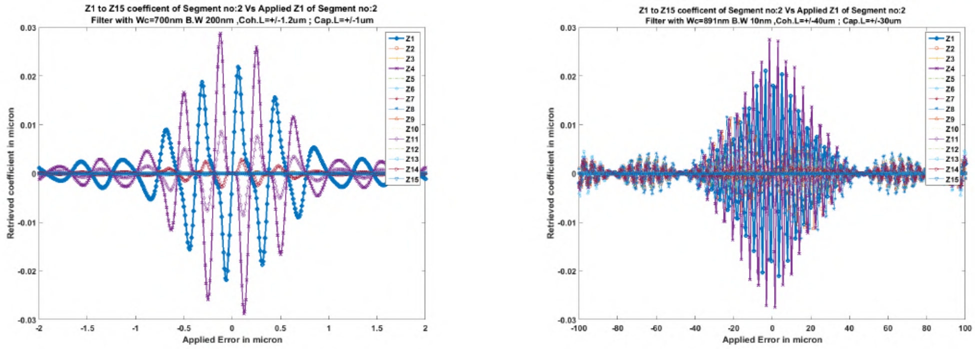

(a) Filter with capture length of ±1 micron and coherence length of ±1.2 micron

(b) Filter with capture length of ±30 micron and coherence length of ±40 micron

Figure 5.30: Retrieved Z1-Z15 coefficient v/s applied Z1 coefficient of segment:2, PSMT-Phase-I, in micron

different Gaussian bandpass filters, we can have different maximum aberration sensing range. This is a promising approach for phasing of the system.

Now we explain how we can retrieve an unknown piston from the system. First, the current telescope segment state is assumed as the zero value or nominal piston value. The segments are piston up and down in steps of ±25 numbers to the nominal value. These unknown absolute piston values are known only as a differential value to the nominal value. In a simulation, the wavefronts created by optical software for the required number of steps are given to the pyramid simulation system. Next, we obtain the coefficients for the given range of piston values, (outside coherence length of filter, the signal modulation will not be present, causing an ambiguous finding of the piston error impossible). From the retrieved aberration coefficient matrix, obtain the coefficient matrix corresponding to the piston (Z1). After DC subtraction, we find the absolute of the peaks of the Z1 coefficient matrix. Then the peaks are smoothed. This final value is chosen as the Y value, and the corresponding X values are chosen as the differential X values, about the nominal mirror position value taken as Zero piston.

Then a first-order Gaussian is fitted into this X and Y values and the

General model Gauss1: $f(x) = a1 * exp(-((x - b1)/c1)^2)$ the b1 coefficient gives the approximate value of the actual piston error . In the figure 5.31 we can see the curve fitted with this approch and its values. Y axis values are arbitrary.

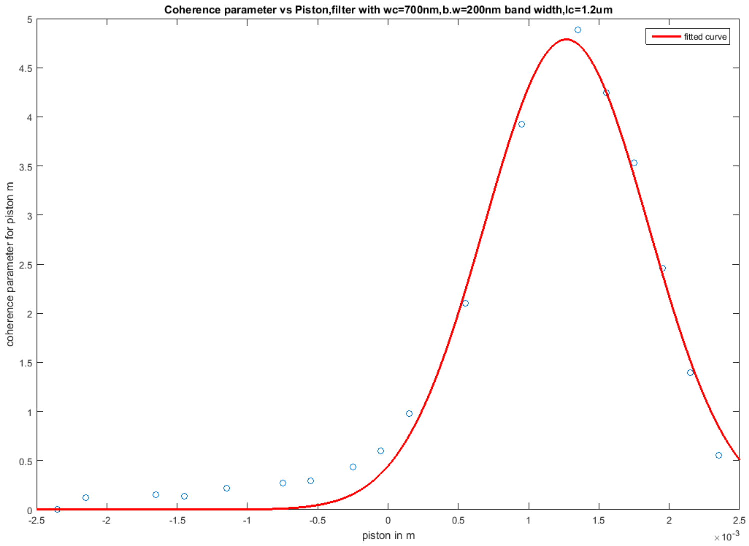

Figure 5.31: Broad band fitted curve with found piston of 1.268μm given piston of 1.2μm

Once we find the approximate piston in this way, we can use the equation 5.33 to finally fine-tune the piston value to the exact value

In the figure 5.32 we can see the curve fitted with this approach and its values. This approach is more time consuming but more accurate as the fitting is done for more number of data points.We propose this technique is well suited for the segmented mirror telescopes to minimize the overall wavefront error. However, the requirement of many piston points to trace and fit the coherence coefficient plot can make this technique time-consuming. As aberration signals in pyramid are mainly localized, to solve this demand on time requirement, we propose to piston all the segments from the nominal value by the required number of steps in one continuous stepped motion. Then solving the matrix equations and finding the

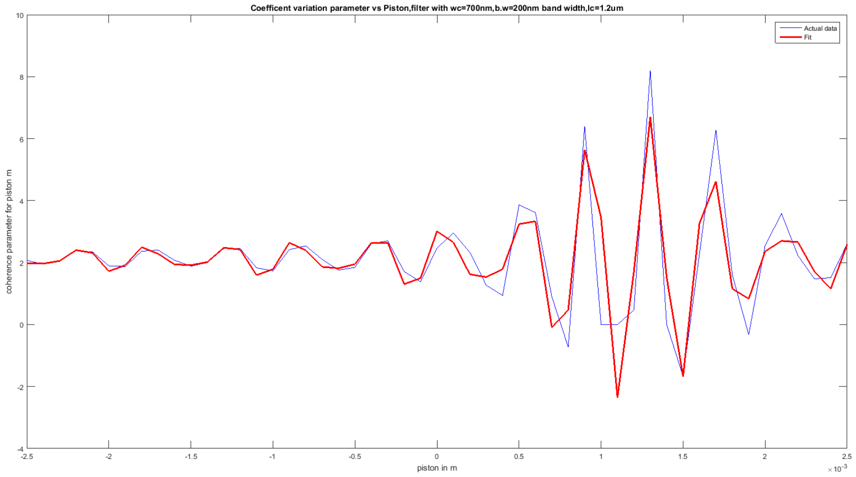

Figure 5.32: Broad band fitted curve with found piston of 1.26μm given piston of 1.2 μm

corresponding piston error for all the segments simultaneously.

5.7 Experimentation of Pyramid Based Phasing Scheme

After the successful completion of the simulation, we decided to set up an experiment. This experiment's primary objective is to get hands-on a pyramid-based wavefront sensor and verify the simulation results. We have not used the actual Pyramid in our experimentation. Instead, we have utilized a rotating mask, which allows one quadrant of the PSF to pass at a time. This way, in a sequence, we created four pupil images, which otherwise would have been done by a pyramid. We have carried out our experimentation in the non-modulated scheme of the pyramid sensor. Our aim is to demonstrate the principle of operation of Pyramid based phasing scheme.

5.7.1 Optical Design

The system contains light sources; Spatial filtering and collimating setup also mirror segments to mimic segmented telescope. The light from two edges of phase-shifted mirrors are passed through two circular apertures. The beam focused on the center of an 'L' shaped mask using a long focal length imaging lens. The PSF contains information about the phase difference between the segments and other aberrations. The PSF is cut into four quadrants sequentially. Correspondingly four reimaged pupils are formed with a reimaging lens. The experiment layout is given in figure 5.33 The intensity variation in the pupil image sensitive to the piston error given to the beam. The optical design of this system is done using off-the-shelf components available.

5.7.1.1 Part 1: Source

We use two diode lasers having wavelength of 532 nm and 650 nm. The lasers have 5 mW Optical power, spot size of around 4 mm. lasers are Holmarc made. Two linear polarizes are used to control the intensity.

5.7.1.2 Part 2: Spatial Filtering

The spatial filtering setup consists of a microscope objective and a pinhole. We had three choices in the microscope objective also a few no of pinholes Out of them, we have chosen New port 20X, 0.4NA, 9 mm focal length as the microscope objective. As among all the objectives we had (40x, 45x, 20x), this one has the longest focal length. With this objective and 4mm laser beam, the airy disk diameter will be Da=(2*1.22*650*9/4)x10-9=7.14 μm The recommended perfect size pinhole diameter will be 1.5 times the size of the airy disk usually. This is to ensure good spatial filtering. We can go for a 10.7 μm pinhole for red laser beam by this calculation. In the same way, it will be 8.8 μm for green wavelength. Nevertheless, among the pinholes, we had 12.5 μm is the smallest one.So we use this in the system.

5.7.1.3 Part 3: Collimation

The Collimator used is an achromatic doublet 50 mm clear aperture 150 mm focal length Holmarc made.

5.7.1.4 Part 4: Focusing

After the collimation beam is made into two parts using a 50:50. Holmarc Optics 50 mm X 50 mm beam splitter. The reflected beam is allowed to fall onto two plane mirrors mounted on a kinematic mount. The reflected light is collected through two circular apertures of 10 mm each. The transmitted beam is not used. The aperture is given in figure 5.35a. Then the two 10 mm beams, each coming out through the system is focused using a long focal length telephoto lens made of a converging lens of 750 mm and a diverging lens of -150 mm focal length respectively, together they create a 6000 mm focal length. Then two PSF's each of the order of about 950 microns for the red laser light at 650 nm and 780 microns at 532 nm green laser light are created using this telephoto lens.

5.7.1.5 Part 5: Rotating Mask

A closer look at the PSF grabbed at the imaging lens's focal plane improves the optical setup's alignment. The tilt and tip of the segmented mirrors are adjusted to displace all the stray PSF's from the main mirror PSF. A field stop helps to avoid all the stray light. Then a rotating 'L' shaped mask is introduced into the focal plane. The mask is precisely positioned such that it cuts the PSF of the reference mirror (the one at the center of the optical axis). PSF is cut into four parts. This mask mimics the effects of a pyramid without any dispersion effects.

5.7.1.6 Part 6: Re-imaging

Once the PSF is cut perfectly into 4 parts a 400 mm focal length 50mm diameter (A.R coated) achromatic doublet lens is used to form 4 pupils sequentially with each quadrant of PSF generated with a mask rotation. The re-imaging lens's position and focal length decide the pupil image's size and pupil sampling. The Detector used is Basler made with 7.4 μm pixel size. This re-imaging lens selection was due to availability as an off the shelf component and the maximum CCD chip size.

5.7.2 Experimental Setup Block Diagram and Images

The figure 5.33 gives the layout of the experiment and figure5.34 gives the image of the actual experimental set up . The experiment was set up in a 1.5 m X 2 m vibration isolated optical table in a controlled environment. Once the experimental setup is assembled, the setup is left to cool down and get socked into the cooled room temperature for few hours. The entire setup set under a PVC curtained thermally stable area in the room to ensure the system's stability.

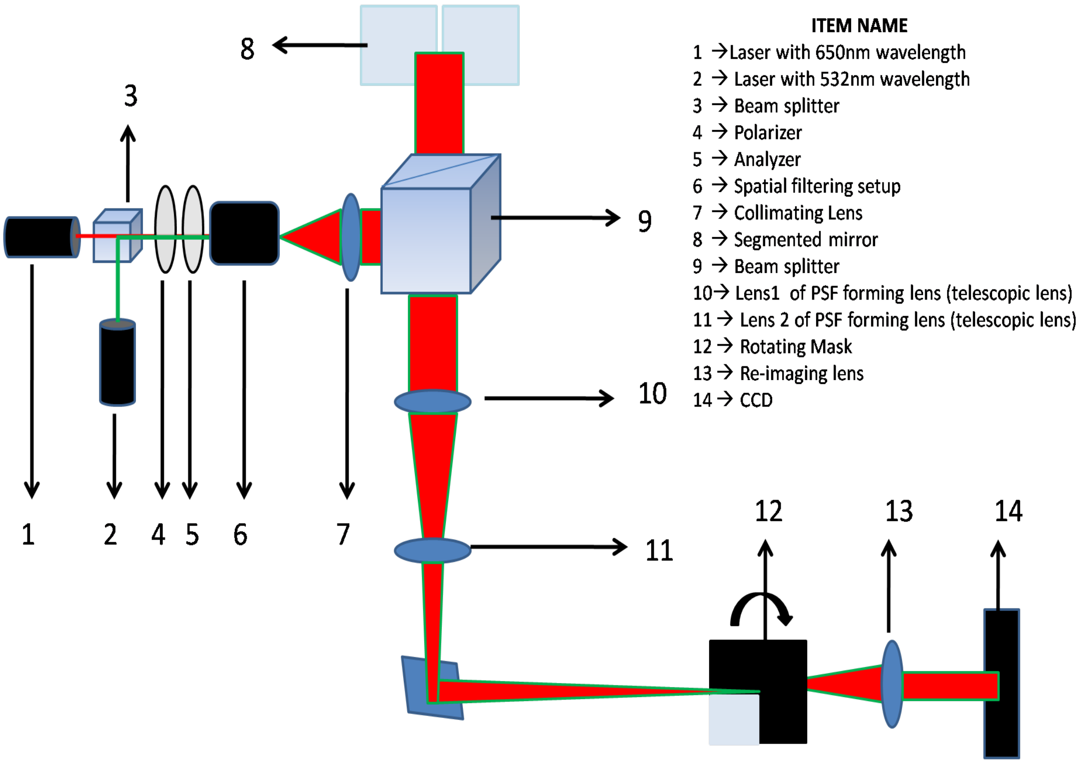

Figure 5.33: Layout of Experiment

5.7.3 Procedure

We assemble the experiential setup and leave the system for a few hours to stabilize the mechanical system. The room is cooled down, and the setup is allowed to sock in the cooled room temperature thermally. Switch on both lasers and allow some time for them to stabilize. Adjust the lasers and first beam splitter so that both beams come through the same path. The beam splitters and lasers are aligned to ensure the beam travels parallel to the optical table without any deviation. Next, we use a linear polarizer to cut down the intensity. Both the beams are spatially filtered simultaneously through the same spatial filtering setup. The beam is passed through the collimating lens to collimate the light. Then mirrors are mounted in the kinematic mount with one mirror kept on Throlab's micro-motion stage, which is capable of moving with a minimum step of nearly 50 nm. Since the stage used by us is not very precise and for our experimentation, we

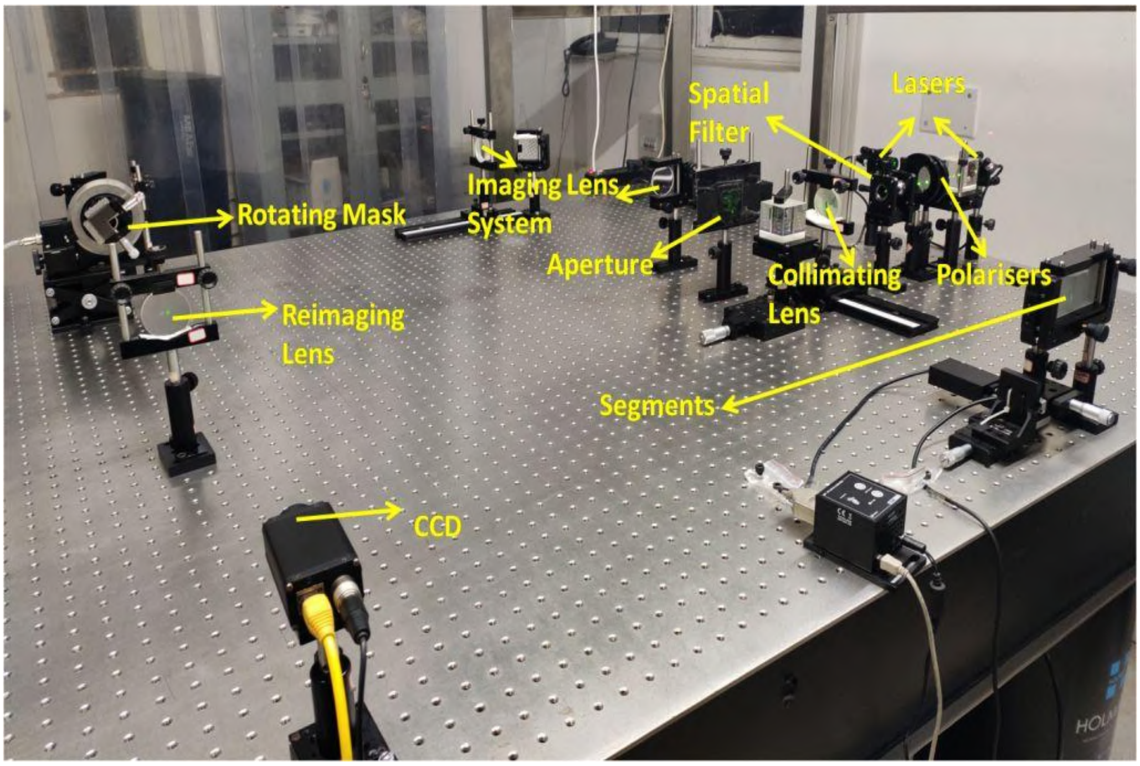

Figure 5.34: Image of Experimental setup

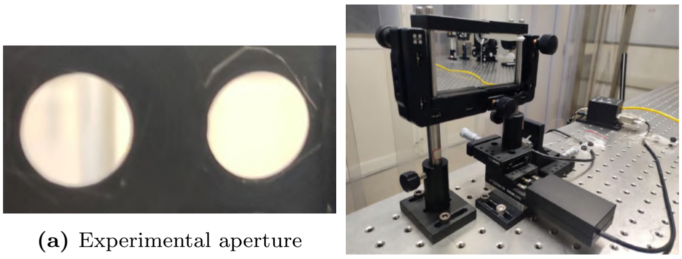

(a) Experimental aperture

(b) Aligned Segments

Figure 5.35: Experimental Image

needed atleast to read the position of the mirror which is getting moved with a few nanometer accuracy. Therefore, an external high precision optical encoder from GSI Microsystems, which has got 1.2 nm resolution, has been installed along with the stage.

Next, we align the mirrors such that light comes through two circular apertures from each respective mirrors. The tip and tilt between the mirrors are corrected with the help of long-distance alignment. The main beam is aligned such that it gets separated from ghost reflections and stray beams. Cover the mirror mounted on the moving platform and allow the light from the next mirror to pass. This fixed mirror is considered a reference mirror. Place the Detector at the focal plane adjust the Detector's position to get focused PSF of the reference mirror at the center of the Detector. Introduce field stop to avoid stray beam PSFs. Then the light from two mirrors is focused to create a total system PSF. By pushing the Detector away from focus by a known amount and introducing a rotating 'L' shaped mask precisely in its position, we cut PSF into quadrants. Then we introduce and align the reimaging lens to create a pupil image in the required sampling in the Detector placed at the reimaged pupil plane. By rotating the mask, which is mounted on a high precision rotating stage, we get the four pupil images. The 'L' shaped mask's alignment is the most crucial thing in this experiment and should be done with great care. The mask's initial alignment is done with a small aperture collimated beam centered on the reference mirror's center. We learned from our rigorous optical alignment exercise that the error in the mask's alignment to an incoming wavefront is seen as shear in the reconstructed wavefront. We use that technique to center the mask to high accuracy.

As we stated, Once the mask is centered correctly, then the reimaging lens is used to form the pupil. Rotate the mask in intervals of 90^0 to save four pupil image for both wavelengths 650 nm and 532 nm one after another. Since a laser with large coherence length has been used as a source, we expect a cyclic behavior in signal over a sufficiently large piston range. We obtained a set of pupil images by applying known displacement to one of the mirrors. For the same applied piston error, the pupil images are generated first for red laser at 650 nm then for green laser at 532 nm. After getting a required number of images, we use the reconstruction approach in section 5.3.2 and retrieve the piston coefficient for each mirror.

5.7.4 Results

A simulated example signal maps generated for the piston of $\lambda/8$ is given in figure 5.36. As we can see, the phase signal variation is high at the edge of the segment. Also, proper calibration of the shape of the aperture is important. Once the pupil images are obtained, we remove the rotating mask and take an image of the two apertures in the reimaged pupil plane without the mask in place with the laser intensity adjusted to get a clear image of the two apertures. This image is used as the aperture mask for making the interaction-control matrix. ZEMAX generates a wavefront for a set of push-pull aberrations as per Zernike calibration coefficients given. The wavefront gets multiplied with the aperture shape mask obtained through the experiment. This modified wavefront is used to make the interaction-control matrix. One of the important aspects of the experimental reconstruction is registering the pupil boundary. We use the aperture mask as a starting point and increase or decrease the boundary radius by one pixel such that we get the maximum amplitude in the retrieved coefficients. This is done for both red and green wavelength pupil images. Intensity variation within the pupil boundary of both apertures are only considered for calculation of errors. This is because we observed that the intensity variations due to differential piston are localized during our simulation studies.This intensity variation will be seen inside the segment and the nearby segment under this differential piston's influence. Also, the magnitude of these variations is equal and opposite as per image 5.36. As we are only interested in the piston, all other aberrations retrieved are discarded, and the variation of the retrieved coefficient for the moving segment is plotted.

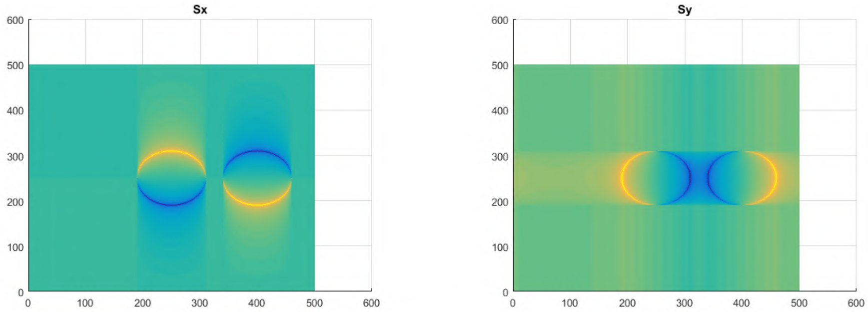

Figure 5.36: The Sx and Sy signal maps for the two mirror system, in which one mirror is subjected to the piston error.

The experimental figures are given in figure 5.37 and 5.38. These pupil images are analyzed using the method outlined in section 5.3.2. The the plot of the derived piston value against encoder reading is shown in the figure 5.38. From the plot, it is clear that as expected the derived piston value is modulating as a sinusoidal with a period of $\lambda/4$. This period is because the applied piston gets distributed to both segments as a differential piston. We can see the red and green laser wavelength's retrieved piston following the expected cyclical pattern

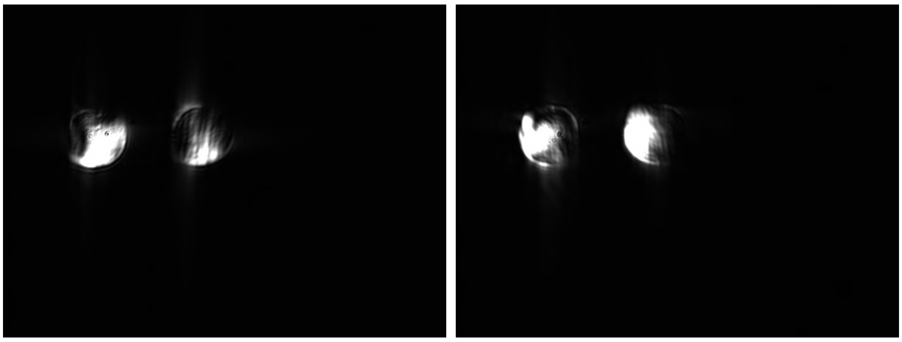

(a) Pupil 1 **(b)** Pupil 2

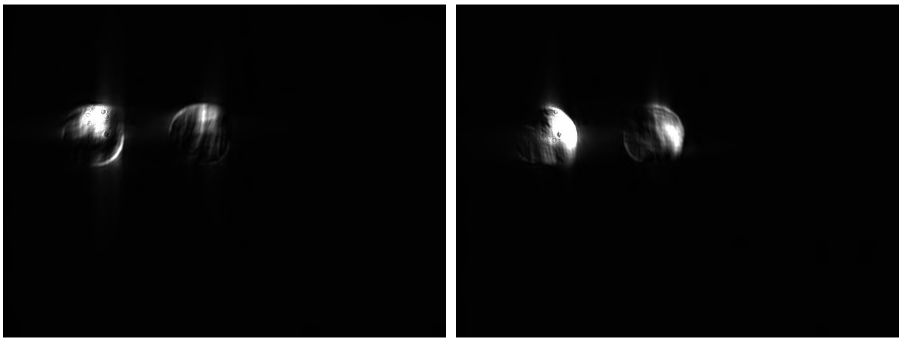

(c) Pupil 3 **(d)** Pupil 4

Figure 5.37: Data for Green laser

for each applied encoder value. During the experiment, we observed that there is drift coming into the retrieved coefficient after some time due to cumulative errors in the system over the experiment's coarse. To minimize this, we make sure the random errors present in the system is within ±5 nm. This is done by taking the encoder reading without applying any piston and monitoring the variations. We got the fit error in curve to be around 20 nm RMS. The curve reflects a precise working of our experimentation as well as opted wavefront reconstruction methodology. The beauty is that we could very successfully and precisely recover the applied piston by using a very inexpensive optical setup and without using a real pyramid.

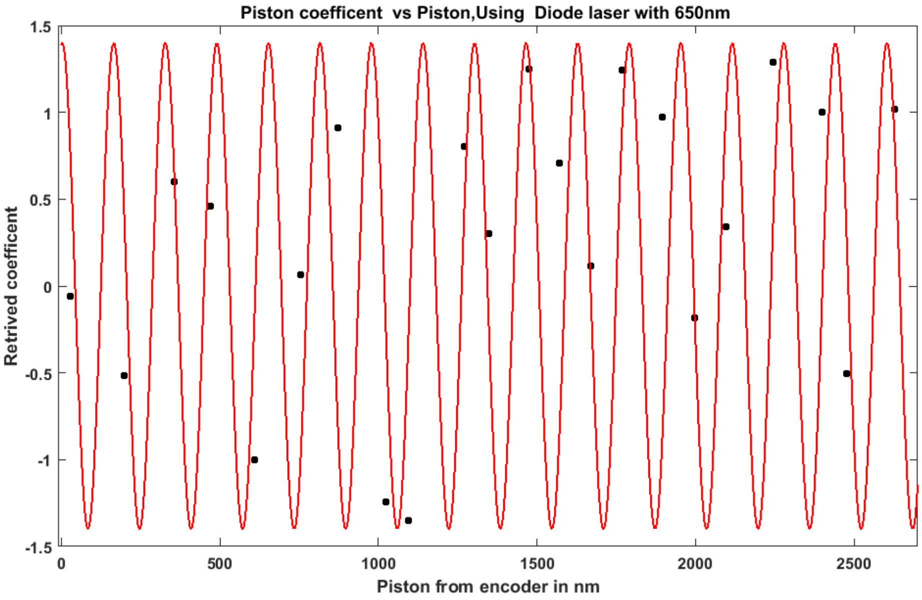

(a) For red beam 650nm

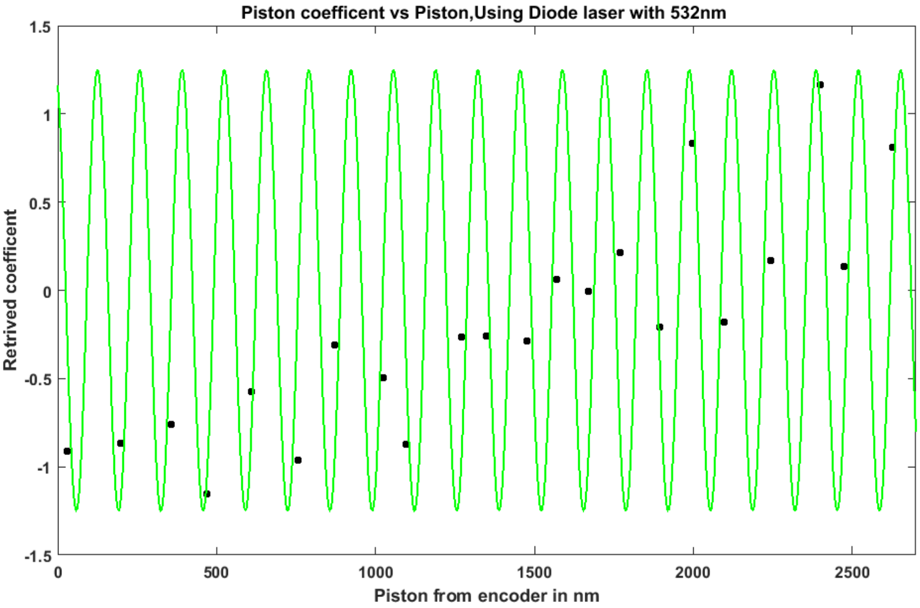

(b) For green beam 532nm

Figure 5.38: Exprimental Pyramid Retrieved piston plots

Chapter 6

Summary and Future Work

As astronomy progress to new frontiers, it requires finer resolving power as well as enhanced light detection sensitivity. Therefore, it demands to build larger and larger size telescopes in every wavelength regime of the electromagnetic spectrum, starting from radio to gamma rays. For the optical and NIR observations, the segmented mirror technology seems to be only viable solution to build large telescopes of more than 8-10 m diameter in aperture. In addition to being partner to the TMT project which is going to be worlds second largest optical telescope and having 3.6 m DOT telescope, Indian astronomical community requires a 10 m class general purpose telescope. The project to install 10 m class telescope named NLOT has all ready been initiated. Surveying suitable sites, as well as designing its optics and subsystems have been undertaken. Building a 10 m class telescope not only requires huge amount of money and a big workforce, but many technological challenges need to be also handled. The task becomes even more difficult when telescope has to be developed using segmented primary mirror which is not yet very standardized technology. Once segments are aligned and phased in any segmented mirror telescope, then after keeping the alignment intact over weeks and months, using a precision actuator, edge sensor, and primary mirror controller in variable gravity and environment condition is a big challenge. Except the twin Keck telescopes, all other segmented telescopes developed so far, such as HET, SALT, GTC, and LAMOST, have gravely suffered over the years after their commissioning to deliver intended performances. Therefore, before embarking to build large telescope made of segmented mirror, it is always safer to get acquainted with the technology by conducting experimentation using either a prototype system or some realistic laboratory based simulator. There are two primary objectives of this thesis work. The first objective is to provide optimum optics design for two different size segmented mirror telescopes having very different requirements. Whereas, the second motivation is to develop technology needed to align and phase the telescopes made of the segmented mirrors. In this last concluding chapter, we briefly summarize the work already done under this thesis along with the activities which can be further undertaken in the near future.

6.0.1 Design of the PSMT optics

The PSMT is a small prototype segmented mirror telescope which will be used primarily to demonstrate the segmented mirror technology. The entire development activities of the PSMT is divided into two phases. In the first phase, a seven segments laboratory test-bed will be developed. Whereas, in the second phase, the full-edged telescope will be realized. The PSMT primary is decided to be made of seven segments each of 500 mm corner-corner in size. To reduce the developmental cost of the PSMT, it has been decided to make use of spherical primary mirror. Since the telescope with spherical primary mirror is subjected to large spherical aberration therefore, we explored many design options in which primary can made of spherical rather widely used parabola or hyperbola. However, after extensive exploration and analysis, of many existing designs, we have come up with a new two-mirror design which uses an oblate ellipsoidal secondary. The importance of our this design is that it is a two mirror design which provides close to diffraction limited performances for the on-axis and then after image quality degrades rapidly. The detailed design optimization has been carried out considering the primary mirror as monolithic as well as segmented. We observed a noticeable improvement in the telescope's performance when primary is segmented instead of the monolithic. We attribute this to the reduction of the marginal rays as well as reshaping of the segmented primary by providing additional tilt and the piston. In the next step we have carried out a detailed sensitivity, tolerance and error budget analysis. During the analysis we found that segment figure error is the most dominant factor to decide the telescope performance and hence we investigated it thoroughly. The two mirror optics provide acceptable image quality up to only one arc-minute then after presence of sever aberration makes off-axis field unusable. The two mirror optics is good enough to use the PSMT telescope as a technology demonstrator on the segmented mirror as well as to carry out few scientific research with the narrow field. However, to use PSMT as general purpose research grade telescope, its off-axis image quality need to be improved. We could achieve this by designing corrective optics within the a faint object spectrograph and camera (FOSC) system. This unit one hand correct the off-axis aberration and hence act like aberration corrector which provide decent image quality up to 10 arc-minutes FOV. Whereas, on the other hand it works like very useful science instrument which not only be used for the imaging but can also work as a spectrograph.

The PSMT project is still under development phase, we plan to further improve the design of the PSMT wide filed corrector cum FOSC. The current design uses only air-spaced singlet to minimize the cost of manufacturing. However, it introduces severe chromatic observations, which can be eliminated by changing the collimator and camera lenses to doublets. We may also like to experiment with aspheric refractive optics which is readily available nowadays. We also plan to do a detailed tolerance and error budget analysis of the FOSC and finally we like to realize it so the it can be used in the PSMT telescope.

6.0.2 Design of the NLOT Optics

Another optics design and analysis work which we have carried as a part of this thesis is designing the NLOT optics. After exploring many potential design options for the proposed 10 m class telescope, we finally ended up with a Ritchey-Chretien(RC) type design. Likewise the PSMT, NLOT optics is designed around segmented primary mirror. For a diffraction limited large telescope, various errors linked with the segmentation plays very critical role to decide the performance of the telescope. Therefore, to study the segmentation effects, we developed a python-based tool that can be used along with ZEMAX ray-tracing software. In the great detail, we have studied the effect of the segment piston, tip and tilt, clocking, the radius of curvature, the shear, the segment size, inter-segment gap as well as figuring error on the telescope performances. We have also carried tolerance and sensitivity analysis so that most sensitive opt-mechanical parameters affecting the telescope performances can be identified. Once realistic tolerances are derived then after we have generated the error budget for the NLOT. Since manufacturing off-axis aspheric mirrors segments is a complex and expensive task, therefore, an attempt has been also made by us to mimicking an aspheric primary by using spherical mirror segments. From our this study, we have shown that by introducing asphericity into spherical segments through a warping harness, it may be possible to use a spherical mirror segment in place of an aspheric one.

All the analyses in this chapter have been carried out with the telescope primary facing toward the zenith direction. However, in a real telescope system, there is a need to analyze the system's segmentation effects while the telescope is pointed at different directions in the elevation. This requires mechanical design and analysis of the telescope structure to be completed. In the near future, once the mechanical analysis is over, we plan to continue our study and explore the effect of gravity and temperature-induced problems in the telescope performances. The segmentation analysis code which we have developed is a general-purpose tool that will be a robust aid to conduct such analyses. We also plan to undertake further studies into a warping harness as a potential asphericity-inducing system for converting spherical segments to aspheric.

6.0.3 Alignment and Phasing of Segmented Mirror

Any large telescope made of a segmented primary mirror can not performed as one can expect from a equivalent size monolith mirror, unless all mirror segments are co-aligned, co-focused and co-phased. In terms of technique, co-aligning and co-focusing are far less complex tasks than co-phasing and it is usually done with a classical Shack-Hartmann based device. Whereas, phasing of mirror segment requires a specialized device which works on the physical optics domain. The second half of the thesis is dedicated to exploring and developing technology required to phase the mirror segments. We have explored two potential phasing schemes, which can be used in the PSMT and NLOT telescopes. The first phasing techniques which was initially developed for the Keck telescope uses Shack-Hartmann kind of device working on the principle of physical optics. Whereas, the second technique is based on the pyramid wave-front sensor. First the physical basis of both the phasing schemes have been explored then after through extensive simulation, we have studied their performances. Finally, laboratory experiments have been setup on the both phasing techniques and experiments are conducted. Through our experimentation, we could demonstrate that even by making use of simple and crude experimental setup one can measure the phase error between two mirror segment with an accuracy of 20 nm. The pyramid based system is expected to give much more precise phase measurement but it has got a small operation range, which can be improved by using a broadband light source. We have also developed a robust code which can make use of conventional Shack-Hartmann images and provides optical aberration present in the mirror segment. By making use of warping harness these aberration can be corrected and hence telescope performance can be further improved.

We have used relatively less precise inexpensive optics to conduct experiment on phasing techniques. These optics suffers from aberration and hence affect the phasing related measurements. In the future experiment we like to use the best quality optics and more accurate measurements is expected. Another limitation of our experiments is not having very precise actuator which can be used to create small displacement of the order of just few nano-meter. We also like to conduct experiments with a broadband light source, which will improve the capture range of the piston measurement by many folds.

Finally the novel aspects of the thesis is enumerated below:

1. We have developed a scalable general-purpose code which can be used to analyse segmentation related effect in the segmented telescopes of any size and the optical configuration.

2. We have come up with an unique optical design of 1.3 m Prototype Segmented Mirror Telescope which uses a spherical primary mirror.

3. We have not only designed the optics of proposed 10 m class NLOT telescope but have carried out very extensive analysis to understand the effect of the

segmentation on the telescope performance.

4. A detailed study on the possibility of using spherical mirror segments to mimic an aspheric primary have been conducted.
5. We have carried out extensive simulation and experimentation on Keck type and pyramid based wave-front sensor to precisely measure segment phase error.
6. Experimentation on pyramid based phasing scheme using a rotating mask, which emulates the actual pyramid sensor is some thing unique in approach.

Bibliography

---

[1] J. R. Fienup, ”Phase retrieval algorithms: a comparison”, Appl. Opt. 21, 2758-2769, (1982)

[2] Carmen J. Carrano, Scot S. Olivier, James M. Braseet.al, ”Phase retrieval techniques for adaptive optics”, Proc. SPIE 3353, Adaptive Optical System Technologies, (1998);

[3] Marshall D. Perrin, Rémi Soummer, Élodie Choquet,et.al ”James Webb Space Telescope Optical Simulation Testbed I: overview and first results”, Proc. SPIE 9143, Space Telescopes and Instrumentation 2014: Optical, Infrared, and Millimeter Wave, 914309, (2014)

[4] J.-N. Aubrun,K.R. Lorell ”The development of an integrated experiment to study the controls/structures interaction problem in large optical systems”, Automatic Control in Aerospace 1989, Elsevier, (1990)

[5] François Roddier, ”Curvature sensing and compensation: a new concept in adaptive optics”, Appl. Opt. 27, 1223-1225, (1988)

[6] Marsha J. Wolf, Povilas Palunas, John A. Booth, et.al ”Mirror alignment recovery system (MARS) on the Hobby-Eberly Telescope”, Proc. SPIE 4837, Large Ground-based Telescopes, (2003)

[7] Luzma Montoya Martinez, Natalia Yaitskova, Philippe Dierickx, Kjetil Dohlen, ”Mach-Zehnder wavefront sensor for phasing of segmented telescopes”, Proc. SPIE 4840, Future Giant Telescopes, (2003)

[8] Aden B.Meinel and Marjorie P.Meinel, ”Wind Deflection Compensated, Zero-Coma Telescope Truss Geometries”, Proc. SPIE 0628, (1986).

[9] Mehdi Bahrami and Alexander V. Goncharov, ”All-spherical catadioptric telescope design for wide-field imaging”, Appl.Opt.49.5705-12, (2010)

[10] Andrew Rakich, ”Four-mirror anastigmats, part 1: a complete solution set for all-spherical telescopic systems”, Opt. Eng. 46(10) 103001, (2007)

[11] R.N.Wilson and B.Delabre, ”New optical solutions for very large telescopes using a spherical primary”, Astron.Astrophysics. 294. 322-338, (1995)

[12] Jerry Nelson, Terry Mast, G.Chanan , ”Segmented Mirror Telescopes,In: Planets, Stars and Stellar Systems”, pp-105-109 Oswalt, Terry McLean, Ian S.(Ed.) Springer, (2013)

[13] Horn D'Arturo G, ”Horn D'Arturo G. 1955”, Publications of the University Astronomical Observatory of Bologna, VI, 6, (1955)

[14] Jean-Pierre Chevillard, Pierre Connes, Maximilien Cuisenier, Jean Friteau, and Claude Marlot, ”Near infrared astronomical light collector”, Appl. Opt. 16, 1817-1833, (1977)

[15] Theodore W. J. Unti, ”Best-Fit Sphere Approximation to a General Aspheric Surface,” Appl.Opt.5, 319-321, (1966)

[16] Yesudasan Sumith, ”Fast Geometric Fit Algorithm for Sphere Using Exact Solution”, abs/1506.02776,ArXiv, (2015)

[17] J. M. Beckers, B. L. Ulich, J. T. Williams, ”Performance Of The Multiple Mirror Telescope (MMT) I. MMT-The First Of The Advanced Technology Telescopes”, Proc. SPIE 0332, (1982)

[18] Nelson Jerry E.,Mast Terry S. and Faber Sandra M, ”The Design of the Keck Observatory and Telescope”, Keck Observatory Report, 90,1:6,4:2-29, 5:41-5:71, (1985)

[19] Scott Roberts, John Rogers, Hugh Thompson, et.al, ”Systems engineering of the Thirty Meter Telescope for the construction phase”, Proc. SPIE 9150, 91500V, (2014)

[20] A. Omar, R. K. S. Yadav, V. Shukla, S. Mondal, J. Pant, ”Design of FOSC for 360-cm Devasthal Optical Telescope”, Proc. SPIE 8446, 844614, (2012)

[21] Nobunari Kashikawa, Motoko Inata, Masanori Iye,et.al, ”FOCAS: faint object camera and spectrograph for the Subaru Telescope”, Proc. SPIE 4008,(2000)

[22] Buzzoni Bernard, Delabre B, Dekker Hans, et.al, ”The ESO Faint Object Spectrograph and Camera (EFOSC)”,The Messenger, dec,38,9-13, (1984)

[23] Delabre B, ”Optical design for an adaptive anastigmatic five-mirror extremely large telescope”, Astronomy and Astrophysics, 487(1), (2008)

[24] Ma Donglin, ”Recommended conceptual optical system design for China's Large Optical-infrared Telescope (LOT)”,Optics Express, 26,108-119, (2018)

[25] Xiangqun Cui, Yongtian Zhu, Ming Liang,et.al, ”Introduction on Chinese 12m optical/infrared telescope (LOT)”, Proc. SPIE 10700, Ground-based and Airborne Telescopes VII, 107001P, (2018)

[26] Feenix Y. Pan, James H. Burge, Rene Zehnder, and Yanqui Wang, ”Fabrication and Alignment Issues for Segmented Mirror Telescopes”, Appl. Opt, 43,2632-2642,(2004)

[27] Thirty Meter Telescope (TMT), http://www.tmt.org

[28] Gary Chanan and Mitchell Troy, ”Strehl ratio and modulation transfer function for segmented mirror telescopes as functions of segment phase error”, Appl. Opt. 38, 6642-6647, (1999)

[29] Jerry E. Nelson, Terry S. Mast, ”Construction of the Keck Observatory”, Proceedings of a ESO Conference on Very Large Telescopes and their Instrumentation, 30, 7-15, (1988)

[30] Jacob Lubliner and Jerry E. Nelson, ”Stressed mirror polishing. 1: A technique for producing nonaxisymmetric mirrors,” Appl. Opt. 19, 2332-2340, (1980)

[31] C. Gray, I. Baker, G. Davies, R. Evans,et.al, ”Fast manufacturing of E-ELT mirror segments using CNC polishing”, Proc. SPIE 8838, 88380K, (2013)

[32] Hugot Emmanuel, Bernard Anaïs, Laslandes Marie, et.al, ”Stress polishing demonstrator for ELT Ml segments and industrialization”, Proc. SPIE, 9145,914539, pp 11,(2014)

[33] Ulrich Müller, Jay Daniel, ”Tinsley proves stress mirror polishing for giant segmented telescopes”, Proc. SPIE 8450, 845025, (2012)

[34] Darragh O’Donoghue,Arek Swat,”Spherical aberration corrector of the Southern African Large Telescope (SALT)”,Proc. SPIE, 4411, (2002)

[35] Arek Swat, Darragh O’Donoghue, Jian Swiegers, Leon Nel, David A. H. Buckley, ”Optical design of the Southern African Large Telescope”, Proc. SPIE 4837, (2003)

[36] David A. H. Buckley, Jacobus G. Meiring, Jian Swiegers, Gerhard Pieter Swart, ”Many segments and few dollars: SALT solutions for ELTs?”, SPIE 5382, (2004)

[37] Jim H. Burge, J. Roger P. Angel, ”Wide-field telescope using spherical mirrors”, Proc. SPIE, 5174, 83-92, (2003)

[38] Mette Owner-Petersen, ”Optical design and performance analysis of a 25-m class telescope with a segmented spherical primary”, Proc. SPIE 2871, (1997)

[39] Raymond N. Wilson, Bernard Delabre, Francis Franza, ”New 4-mirror optical concept for very large telescopes with spherical primary and secondary mirrors, giving excellent field and obstruction characteristics”, Proc. SPIE 2199, (1994)

[40] Eric Ponslet, Dan Blanco, Myung Cho, et.al, ”Development of the primary mirror segment support assemblies for the Thirty Meter Telescope”, Proc. SPIE 6273,627319, (2006)

[41] Eric C. Williams, Curtis Baffes, Terry Mast, et.al, "Advancement of the segment support system for the Thirty Meter Telescope primary mirror", Proc. SPIE 7018,701810, (2008)

[42] Lluis Cavaller, Juan Marrero, Javier Castro, et.al, "Design of the primary mirror segment support system for the E-ELT", Proc. SPIE 7012, 70121F, (2008)

[43] Wilson R.N, F. Franza and L. Noethe "Active optics I. A system for optimizing the optical quality and reducing the costs of large telescopes", Journal of Modern Optics,34:4, 485-509, (1987).

[44] Wilson R.N,"Reflecting Telescope Optics I", Springer, Edition 1. Pages:56-324, (1996)

[45] Wilson R.N, "The History and Development of the ESO active Optics System", ESO Messenger,113, (2003)

[46] Hubert M. Martin, Shawn P. Callahan, Brian Cuerden, et.al, "Active supports and force optimization for the MMT primary mirror," Proc. SPIE 3352, (1998)

[47] Byoung-Joon Seo, Carl Nissly, George Angeli, et.al, "Investigation of primary mirror segment's residual errors for the Thirty Meter Telescope", Proc. SPIE 7427,74270F, (2009)

[48] Xiang-Qun Cui, Yong-Heng Zhao, Yao-Quan Chu et.al.," The Large Sky Area Multi-Object Fiber Spectroscopic Telescope (LAMOST)", Research in Astronomy and Astrophysics 12,9, 1197-1242, (2012)

[49] Stephen F. Sporer, "TMT: stressed mirror polishing fixture study", Proc. SPIE 6267, 62672R, (2006)

[50] Yong Zhang and Xiang-Qun Cui "Calculations for the Pre-Calibration of LAMOST Active Optics", Chinese Journal of Astronomy and Astrophysics, 5, 3, 302, (2005)

[51] Gary Chanan "Principles of Wavefront Sensing and Reconstruction", ASP Conference Series, (2004)

[52] J. W. Hardy, "Active optics: A new technology for the control of light", in Proceedings of the IEEE, 66,6, pp. 651-697, (1978)

[53] K. L. Baker and M. M. Moallem, "Iteratively weighted centroiding for Shack-Hartmann wave-front sensors", Opt. Express 15, 5147-5159, (2007)

[54] J.M. Geary. "Introduction to Wavefront Sensors", SPIE tutorial texts. SPIE Optical Engineering Press,(1995)

[55] R. G. Lane and M. Tallon, "Wave-front reconstruction using a Shack–Hartmann sensor", Appl. Opt. 31, 6902-6908, (1992)

[56] Jan Herrmann, "Least-squares wave front errors of minimum norm", J. Opt. Soc. Am. 70, 28-35, (1980).

[57] Russell B. Makidon, Anand Sivaramakrishnan, Marshall D. Perrin, et.al, "An analysis of fundamental waffle mode in early aeos adaptive optics images", Astronomical Society of the Pacific, 117:831-846, (2005).

[58] Francois Roddier, "Adaptive optics in astronomy", Cambridge university press, (1999)

[59] W.H. Southwell. "Wave-front estimation from wave-front slope measurements", J. Opt. Soc. Am. 70(8):998-1006, (1980).

[60] Virendra N Mahajan. "Zernike polynomials and optical aberrations", Applied optics, 34(34):8060-8062, (1995)

[61] Robert J. Noll, "Zernike polynomials and atmospheric turbulence", J. Opt. Soc. Am. 66, 207-211, (1976)

[62] Gary A. Chanan, Mitchell Troy, Catherine Mayumi Ohara, "Phasing the primary mirror segments of the Keck telescopes: a comparison of different techniques", Proc. SPIE 4003, 188–202, (2000)

[63] Bely Pierre,"The design and construction of large optical telescopes", Springer,pp.333-334, (2003)

[64] Natalia Yaitskova, Kjetil Dohlen, Philippe Dierickx, ”Diffraction in OWL: effects of segmentation and segments edge misfigure”, Proc. SPIE 4840,171–182, (2003)

[65] Natalia Yaitskova, Kjetil Dohlen, and Philippe Dierickx, ”Analytical study of diffraction effects in extremely large segmented telescopes”, J. Opt. Soc. Am. A 20, 1563-1575, (2003)

[66] Gary Chanan, Mitchell Troy, Frank Dekens, et.al, ”Phasing the mirror segments of the Keck telescopes: the broadband phasing algorithm”, Appl. Opt. 37, 140-155, (1998)

[67] Gary A. Chanan, ”Design Of The Keck Observatory Alignment Camera”, Proc. SPIE, 1036,59,(1989)

[68] Gary A. Chanan, Jerry E. Nelson, Terry S. Mast, et.al, ”W.M. Keck Telescope phasing camera system”, Proc. SPIE 2198,1139-1150,(1994)

[69] Surdej Isabelle,”Co-phasing segmented mirrors: theory, laboratory experiments and measurements on sky”, PhD thesis, lmu,(2011)

[70] Gary Chanan, Catherine Ohara, and Mitchell Troy, ”Phasing the mirror segments of the Keck telescopes II: the narrow-band phasing algorithm”, Appl. Opt. 39, 4706-4714, (2000)

[71] Mats G. Lofdahl, Henrik Eriksson, ”Algorithm for resolving 2pi ambiguities in interferometric measurements by use of multiple wavelengths”, Opt. Eng. 40(6), 984-990, (2001)

[72] Gary A. Chanan, Terry S. Mast, Jerry E. Nelson, et.al, ”Phasing the mirror segments of the W.M. Keck Telescope”, Proc. SPIE 2199,622-632, (1994).

[73] Ragazzoni Roberto, Diolaiti Emiliano , Vernet Elise, ”A pyramid wavefront sensor with no dynamic modulation”, Optics Communications. 208. 51-60, (2002).

[74] Ragazzoni Roberto, ”Pupil plane wavefront sensing with an oscillating prism”, Journal of Modern Optics, 43, 2, 289-293, (1996)

[75] Esposito Simone, Devaney Nicholas, ”Segmented telescopes co-phasing using Pyramid Sensor”, ESOC,58, 161, (2002)

[76] Simone Esposito, Enrico Pinna, Andrea Tozzi, et.al ”Cophasing of segmented mirrors using the pyramid sensor,” Proc. SPIE 5169, (2003)

[77] Simone Esposito, Orla Feeney, Armando Riccardi ,”Laboratory test of a pyramid wavefront sensor” ,Proc.SPIE,4007, (2000)

[78] E. Pinna, S. Esposito, A. Puglisi, et.al, ”Phase ambiguity solution with the Pyramid Phasing Sensor”, Proc. SPIE 6267, 62672Y, (2006)

[79] Arcidiacono Carmelo, ”Beam divergence and vertex angle measurements for refractive pyramids”,Optics Communications - OPT COMMUN, 252,239-246, (2005)

[80] Roberto Ragazzoni, Simone Esposito, Adriano Ghedina, et.al, ”Pyramid wavefront sensor aboard AdOpt@TNG and beyond: a status report”, Proc. SPIE 4494, (2002)

[81] Katie M. Morzinski,Laird M Close, Jared R. Males et.al ,”MagAO: Status and on-sky performance of the Magellan adaptive optics system”, Proc.SPIE,9148,914804,13, (2014)

[82] Currie Thayne, Guyon Olivier, Martinache Frantz et.al, ”SCExAO: First Results and On-Sky Performance”, Proceedings of the International Astronomical Union, 8 ,34–35, (2013)

[83] Carmelo Arcidiacono,Xinyang Chen,Zhaojun Yan et.al, ”Sparse aperture differential piston measurements using the pyramid wave-front sensor”, Proc.SPIE,9909, 99096K, (2016)

[84] Elizabeth M. Daly, Christopher J. Dainty, ”Measuring Phase Aberrations using a Pyramid Wavefront Sensor”, Proc. SPIE 7726, 77260W, (2010)

[85] Yong Liu, Quanquan Mu, Zhaoliang Cao et.al, ”Precise calibration of pupil images in pyramid wavefront sensor”, Appl. Opt.,OSA, 12,3281-3286 ,56, (2017)

[86] Vérinaud, C., ”On the nature of the measurements provided by a pyramid wave-front sensor”, Optics Communications, 233, 27-38, (2004)

[87] Joana Buechler Costa, Roberto Ragazzoni, Adriano Ghedina, et.al ,”Is there need of any modulation in the pyramid wavefront sensor?”, Proc. SPIE 4839, 288-298, (2003)

[88] Kochhar Rajesh , Narlikar Jayant. ”Astronomy in India : a perspective”, New Delhi:Indian National Science Academy, c1995 -1, (1995)

[89] HIROT Team, ”Recent astronomical site survey at Hanle, Ladakh”, Bulletin of the Astronomical Society of India,24,859, (1996)

[90] Sanders Gary, ”The Thirty Meter Telescope (TMT): An International Observatory”, Journal of Astrophysics and Astronomy, 34, 81-86,(2013)

[91] Curtis Baffes, Terry Mast, Jerry Nelson, Eric Ponslet, Vince Stephens, Larry Stepp, Eric C. Williams, ”Primary mirror segmentation studies for the Thirty Meter Telescope”, Proc. SPIE 7018, 70180S, (2008)

[92] Burgarella D., Dohlen K., Ferrari M., et.al, ”Large petal telescope for the next-generation Canada-France-Hawaii Telescope, in Future Giant Telescopes”, ed. J. R. P. Angel R. Gilmozzi (Bellingham: SPIE). Proc. SPIE, 4840, 93–103, (2002)

[93] Gelys Trancho, Christophe Dumas, Robert Anderson ,”TMT.SEN.DRD.05.002.CCR37 :OBSERVATORY ARCHITECTURE DOCUMENT”,P.48,January 8, (2020)

[94] Chew Theam, Clare Richard, Lane Richard, ” A comparison of the Shack–Hartmann and pyramid wavefront sensors”, Optics Communications, 268. 189-195, (2006)

[95] Renate Kupke, Don Gavel, Jess Johnson, Marc Reinig, ”Implementation of the pyramid wavefront sensor as a direct phase detector for large amplitude aberrations”, Proc. SPIE 7015, 70155H, (2008)

[96] Jess A. Johnson, Renate Kupke, Donald Gavel, Brian Bauman, ”Pyramid wavefront sensing: theory and component technology development at LAO”, Proc. SPIE 6272, 62724R, (2006)

[97] E. Pinna, F. Quirós-Pacheco, S. Esposito, A. Puglisi, P. Stefanini, ”The Pyramid Phasing Sensor (PYPS)”, Proc. SPIE 7012, 70123D, (2008)

[98] Vyas Akondi, Sara Castillo, and Brian Vohnsen, ”Digital pyramid wavefront sensor with tunable modulation”, Opt. Express 21, 18261-18272, (2013)

[99] Jianxin Wang, Fuzhong Bai, Yu Ning, et.al, ”Comparison between nonmodulation four-sided and two-sided pyramid wavefront sensor,” Opt. Express 18, 27534-27549, (2010)

[100] Kainan Yao, Jianli Wang, Xinyue Liu, et.al, ”Pyramid wavefront sensor using a sequential operation method”, Appl. Opt. 54, 3894-3901, (2015)

[101] Allan Wirth, Tom Gonsiorowski, Jennifer Roberts, et.al, ”Developing and testing an optical alignment system for SALT’s segmented primary mirror,” Proc. SPIE 5489, (2004)

[102] Eric Williams, Jerry Nelson, and Larry Stepp ”TMT Segment Polishing Principles”, TMT.OPT.TEC.10.052.REL03, (2010).

[103] Ben Gallagher,Bill Tyler, Gelys Trancho, Fengchuan Liu, Gary Sanders, ”Specification for finished 1.44-meter primary Mirror segments”, TMT.OPT.SPE.07.002.CCR06, P-11-12, (2019)

[104] George Z. Angeli, Byoung-Joon Seo, Carl Nissly, Mitchell Troy, ”A convenient telescope performance metric for imaging through turbulence”, Proc. SPIE 8127, 812709, (2011)

Appendix A

Segmentation

A.1 A segmentation tool

In a highly segmented telescope design, user has to input and optimize parameters for many segments, making manual handling of these operations difficult even with a optical design software like ZEMAX. We developed a python based generic hexagonal segmentation code that generates different data required for segmentation in the format required by ZEMAX optical design software. This tool was used with the ZEMAX-python dynamic exchange platform to do segmentation and corresponding studies. The tool has provision to create segmented primary and calculate the segment elongation. It also has the option to calculate and input various design requirements for various analyses like clocking, mimicking aspheric primary with the spherical segments, surface figure, generating and importing Grid sag surface, Zernike de-composition, etc.

A.1.1 Tool for Creating segmented primary mirror

The mirror segments are considered regular hexagons on projection to the primary with a uniform gap between them. Only the side length characterizes the regular hexagon. These hexagons fill the entire aperture by forming multiple rings, except any aperture positions that have to be avoided. The tool provides hexagonal aperture files required by ZEMAX, called as user-defined aperture (UDA) file, required for creating segmented primary. UDA files are apertures considered by ZEMAX as a surface projected from the aperture's vertex tangent plane into the optical base surface. The code takes the inter-segment gap, the number of rings/outer diameter, ROC, conic constant, and aspheric coefficients values for various calculations. The code computes each hexagon's center coordinate and coordinates all six corners with equations of the law of cosines; these are available in both the polar and Cartesian coordinate systems. Some of the results are shown in figure A.1. The tool can also give a master sector to carry out segmentation related studies, as shown in figure A.1c.

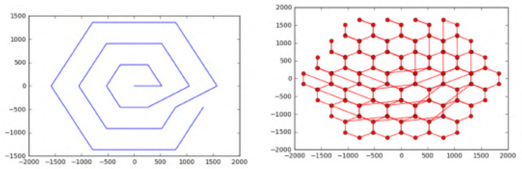

(a) Center coordinates in anti-clockwise counting

(b) Six corner coordinates in anti-clockwise counting

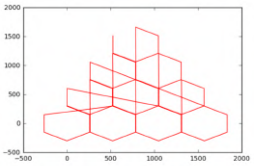

(c) Master sector

Figure A.1: 300 mm side length , 3 ring segmented primary

The code has an inbuilt option to calculate the sag value at any point on the surface described by the optical system's X-Y coordinate (rectangular/ hexagonal grid) and design parameters. With this sag calculation option's help, the code provides a 'Grid sag surface file' used with ZEMAX for creating surface deformations. As per requirement, the sag can be decomposed using the matrix inversion technique to find Zernike coefficients. The code creates a UDA (user-defined aperture) file for each segment as a regular or elongated hexagon(see section A.1.2). UDA files can be created in Local (Same aperture file for the segments) or Global (Unique aperture files for the segments) coordinate system, see figure A.6. If the UDA files are designed in a Global coordinate system user has to input surface parameters like ROC, conic constant, and aspheric coefficients to each segment.

Suppose it is in the local coordinate system, along with these parameters, the segment position and additional asphericity (as Zernike coefficients) to correct for the surface sag errors have to be entered into the ZEMAX design. The global ordinate system UDA is the preferred method for aspheric primary design.

A.1.2 Computation of irregular hexagon

In a segmented telescope, Segment support assembly (SSA), along with a segment position control system consisting of an actuator and edge sensor and the control software, maintains the segmented mirror's global profile. The edge sensor, which detects the local misalignment between two segments, is mounted between the segment edges. To accurately determine the edge movements, a uniform inter-segment gap must be maintained across all the segments. Such that on the projection from the top, all hexagons look regular with a uniform gap. As the optical surfaces are curved, the hexagons that look regular on projection are, in reality, elongated irregular hexagons. Usually the method to calculate this elongation is finding the radial elongation as per angle θ and further optimization(see figure A.2)[91]. We developed an alternative approach by Taking the 3D x,y,z coordinates of each segment and then converting them to 2D X, Y elongated coordinates by solving distance equations, assuming all the segments will be convex hexagons.

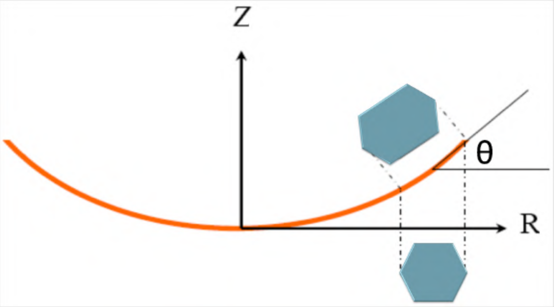

Figure A.2: Radial elongation approach, R:Radius, Z:Sag

As given in figure A.3asegments in projection looks as a regular hexagon ABCDEF. With each corner defined by its x,y,z coordinates. The 2D irregular hexagon defined by its X,Y coordinates is given as A'B'C'D'E'F'. The relationship between the 3D regular hexagon and 2D irregular hexagon projection is given

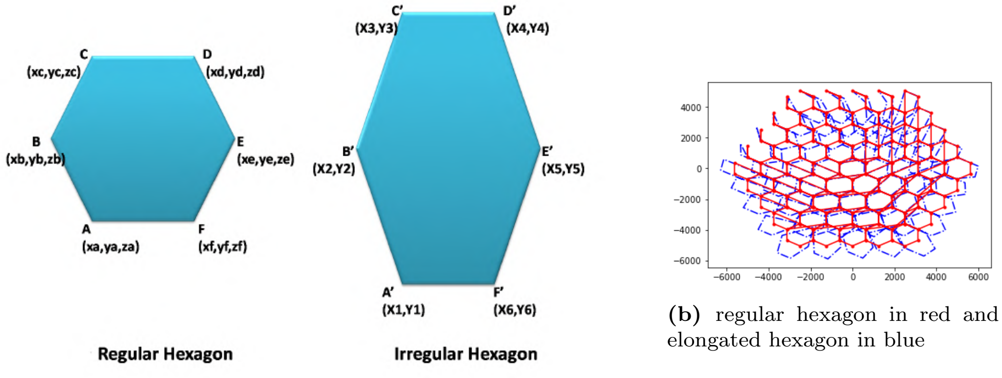

(a) Regular and elongated irregular hexagon

(b) regular hexagon in red and elongated hexagon in blue

Figure A.3: Elongated Hexagon

by equations A.2 to A.7.

$$\alpha_1 = \angle BAF, \alpha_2 = \angle ABC \tag{A.1}$$

$$[X1],[Y1] = [0],[0] \tag{A.2}$$

$$[X2],[Y2] = [AB],[0] \tag{A.3}$$

$$[X3],[Y3] = [\sqrt{|(AC^2 - (BCsin\alpha_2)^2)|}]$$

$$,[-|(BCsin(\alpha_2))|] \tag{A.4}$$

$$[X4],[Y4] = [((AD^2 - BD^2 + AB^2)/(2AB))],$$

$$[-(\sqrt{|(AD^2 - ((AD^2 - BD^2 + AB^2)/(2AB))^2)|}] \tag{A.5}$$

$$[X5],[Y5] = [((AE^2 - BE^2 + AB^2)/(2AB))],$$

$$[-\sqrt{|(AE^2 - ((AE^2 - BE^2 + AB^2)/(2AB))^2)|}] \tag{A.6}$$

$$[X6],[Y6] = [-\sqrt{|(AF^2 - (AFsin\alpha_1)^2)|}],$$

$$[-|(AFsin\alpha_1)|] \tag{A.7}$$

The X, Y coordinates obtained from input local x,y,z of each regular hexagon is called local elongation of each segment. Later, by 2D rotation of the local elongation points by 30^0 in the anticlockwise fashion and decentering the center of each elongated hexagon to make them coincide with the center coordinates of a regular hexagon, we get coordinates corresponding to each irregular segment's orientation in the telescope axis. See figure A.3b to see the plot of a regular hexagon and elongated hexagon in a segmented primary.

A.1.3 Local Radius of Curvature

In astronomical telescopes making aspheric primaries made of off-axis mirror segment is a challenge. We have conducted a study in which we explored the possibility of mimicking an aspheric hyperbolic primary mirror using smaller spherical mirror segments. One method we explored to calculate this equivalent spherical radius of curvature(ROC) of the aspheric primary segment is using its Local ROC(R_l) (see the Figure A.4) or the ROC given by a spherometer, commonly used in meteorological purposes. The R_l of spherical hexagonal mirror segments is chosen in such a way that it fits local sag at the center of the aspheric mirror segments with a local sphere.

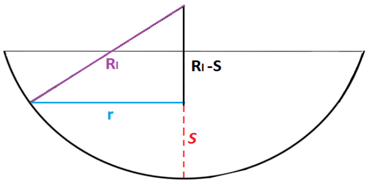

Figure A.4: Calculation of Local radius of curvature (R_l). 'S' is the sag of the aspheric segment with ideal vertex radius of curvature R_a

In a telescope optical system using aspheric mirrors, the equation of any aspheric surface can be given by:

$$S = \frac{r^2}{R_a * \left(1 + \sqrt{1 - (1+K) * \frac{r^2}{R_a^2}}\right)} + \sum_{i=1}^{n} A_{2i} * r^{2i} \tag{A.8}$$

where R_a is the vertex radius of curvature of aspheric, 'r' is the radial coordinate, 'K' is the conic constant. A_{2i} is the higher-order aspheric coefficient, which is not required while designing an RC kind of optics. We can equate the sag 'S' at the center of an aspheric to a local radius of curvature R_l as in Fig.A.4 corresponding to a local spherical surface .R_l is given by equation A.9.

$$2R_l = \frac{r^2}{S} + S \tag{A.9}$$

where R_l is the local ROC corresponding to aspheric sag 'S' at the center of each segment. This ROC can be fed into each segment of the primary mirror system using ZEMAX Python dynamic data exchange platform.

A.1.4 Best-fit radius of curvature

Another way to find a custom ROC for each aspheric segment is to find the best fit sphere to fit aspheric mirror segments. In optical manufacturing, this is done to find out the best fit sphere so that the volume of the material removed from the aspheric is minimum. This method involves the fitting of the parameters either through the least square or by geometric approach [15]. Both of these iterative methods are time-consuming. Instead, we use the approach of the fitting sphere through a set of 3D (x,y,z) data points to find the best fit sphere ROC [16].

The code calculates a set of x,y,z coordinates inside each aspheric hexagon segment, with user-defined sampling. Using the matrix inverse equations,we find the local center of curvature xc,yc,zc for the each segment. Once the center of curvature is known, then the best fit radius is obtained using equation A.15. We check the accuracy using the fit quality coefficient and iterate if needed to get the best solution.

$$S = \sqrt{(R_b^2 - (x - x_c)^2 - (y - y_c)^2)} + z_c \tag{A.10}$$

where x_c, y_c, z_c are the coordinates of the center of the sphere, and R_b is the radius of the best fit sphere. We can form following matrix equations as

$$A = 2 \begin{bmatrix} \sum_{i=1}^{n} \frac{x_i(x_i-\overline{x})}{n} & \sum_{i=1}^{n} \frac{x_i(y_i-\overline{y})}{n} & \sum_{i=1}^{n} \frac{x_i(z_i-\overline{z})}{n} \\ \sum_{i=1}^{n} \frac{y_i(x_i-\overline{x})}{n} & \sum_{i=1}^{n} \frac{y_i(y_i-\overline{y})}{n} & \sum_{i=1}^{n} \frac{y_i(z_i-\overline{z})}{n} \\ \sum_{i=1}^{n} \frac{z_i(x_i-\overline{x})}{n} & \sum_{i=1}^{n} \frac{z_i(y_i-\overline{y})}{n} & \sum_{i=1}^{n} \frac{z_i(z_i-\overline{z})}{n} \end{bmatrix} \tag{A.11}$$

$$B = \begin{bmatrix} \sum_{i=1}^{n} \frac{({x_i}^2+{y_i}^2+{z_i}^2).(x_i-\overline{x})}{n} \\ \sum_{i=1}^{n} \frac{({x_i}^2+{y_i}^2+{z_i}^2).(y_i-\overline{y})}{n} \\ \sum_{i=1}^{n} \frac{({x_i}^2+{y_i}^2+{z_i}^2).(z_i-\overline{z})}{n} \end{bmatrix} \tag{A.12}$$

Where, x_i, y_i, z_i are the data points on the aspheric surface and

$$\overline{x} = \frac{1}{n}\sum_{i=1}^{n} x_i, \qquad \overline{y} = \frac{1}{n}\sum_{i=1}^{n} y_i, \qquad \overline{z} = \frac{1}{n}\sum_{i=1}^{n} z_i \tag{A.13}$$

Therefore, the solution for the center of the best fit sphere can be obtained by matrix inversion as follows

$$\begin{bmatrix} x_c \\ y_c \\ z_c \end{bmatrix} = (A^T.A)^{-1}.A^T.B \tag{A.14}$$

Once the center of the best fit sphere is known, then the best fit radius of curvature R_b can be derived.

$$R_b = \sqrt{\frac{\sum_{i=1}^{n}((x_i - x_c)^2 + (y_i - y_c)^2 + (z_i - z_c)^2)}{n}} \tag{A.15}$$

A.1.5 Clocking Analysis

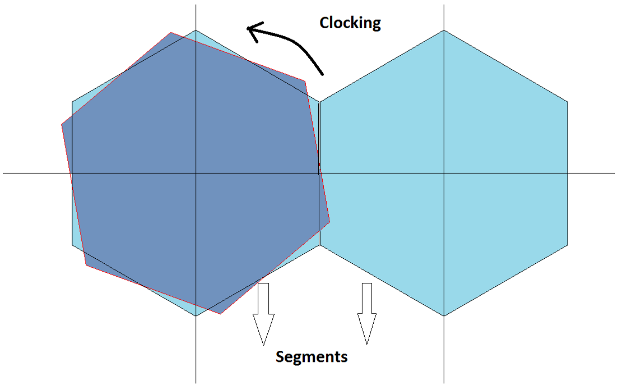

Figure A.5: Illustration of clocking

Clocking is the in-plane rotation of a segment about its center with segment origin fixed as in figure A.5. As per the theory, we can state the error due to clocking after correction of piston, tip and tilt as $\Delta W_i = (ka^2{b_i}^2/R^3)(\rho^2 sin2\theta)(\Delta\theta_i)$ where ΔW_i is the wavefront error of the ith segment for rotational error of $\Delta\theta_i$ in radian. In our analysis, we introduce the system's clocking error as tilt about Z-axis(Sag-Axis) in ZEMAX, such that ± X arcsec clocking the error is given into the system as a normal distribution with zero mean and standard deviation as ±X/2. For the given tilt about Z-axis, the segment rotates about its local segment center also about the global telescope center due to the UDA aperture file created with the telescope's global axis points. Using 3D rotational matrix techniques, we find the change in each segment's center coordinate in the X and Y-axis. By applying the opposite polarity of this value as correction, we bring the center coordinate of each segment to its ideal position. We call this called fixing of the local axis. Then we correct the piston, tip, and tilt (PTT) error associated with this transformation through Optimization, thereby correcting the segment position displacement errors other than clocking. In a working telescope, a major portion of these in-plane errors is correctable with Segment control systems.

A.2 Segmented Design

The segmented design was done exclusively with the help of ZEMAX ray-tracing software. In this, the primary is segmented with a uniform inter-segment gap, keeping all other telescope design parameters the same as monolithic design. This design was done in two ways, one using a Sequential- Non-Sequential 'mixed-mode' system and another using a Pure Sequential mode system, both with user-defined aperture. In mixed mode, the segmented primary is considered a non-sequential entity, and all other optical elements are placed in sequential space. A sequential system, a ray can produce only one ray, with each optical element in the system addressed sequentially. The non-sequential system design is more like a real physical optical system. Each element is defined with its own independent parameters, where a ray can go anywhere depending on the position and parameters of optical elements present in the system. In a segmented telescope, segments are entities that are having individual control, but they need to work together as a single equivalent optical surface. So the sequential mode design approach will present with a complicated design if we want to avail control in all the six degrees of freedom(X, Y, Z rotation and displacement) of individual segments. Whereas in the mixed-mode approach, the primary designed by individuality controlled segments in the non-sequential space, we consequently have this opportunity, this aids in the ease of analysis of the segmentation effects and further optimization of telescope performance.

A.2.1 Segmentation design using Sequential mode system

For this analysis, a single UDA file with all the segment positions is invoked on top of the monolithic primary. This approach is equivalent to an ideal segmentation in which projections of all the segments are regular hexagons, and they all have a uniform gap. The optimized wavefront is equivalent to the monolithic wavefront with ideal segmentation incorporated into the system, and we do not have control over individual segments.

A.2.2 Segmentation design using Mixed mode system

In sequential- Non-sequential mixed-mode system, the segmented primary is defined in a non-sequential space, with an entrance pupil and exit pupil, and other optics are kept in a sequential space. We followed ZEMAX non-sequential mode design principles to create the segmented primary. In this design approach, user has control over individual segments six degrees of freedom and its optical parameters.

If the telescope has a spherical primary, it does not have a unique optical axis; also, there are no off-axis aspheric segments. Because of this, we can develop the segmented primary with segment apertures made of a single UDA file in local segment coordinates defined about the center of the segment(See figureA.6). Segments are placed at their respective position in the total telescope aperture by pre-calculated X, Y, Z position, and tilt about X, Y, Z-axis. Tilt about Z-axis or clocking is an important parameter in an aspherical segment, but it is not of much consequence in spherical segments. The maximum aperture of each hexagon is set as its side length. The required tilt about the axis for each hexagon can be found with 3D rotational matrices. X Y position is the center coordinate of each segment. The Z position of the segments is the relative sag difference of the segments with respect to the center segment. Next, set the radius of curvature to

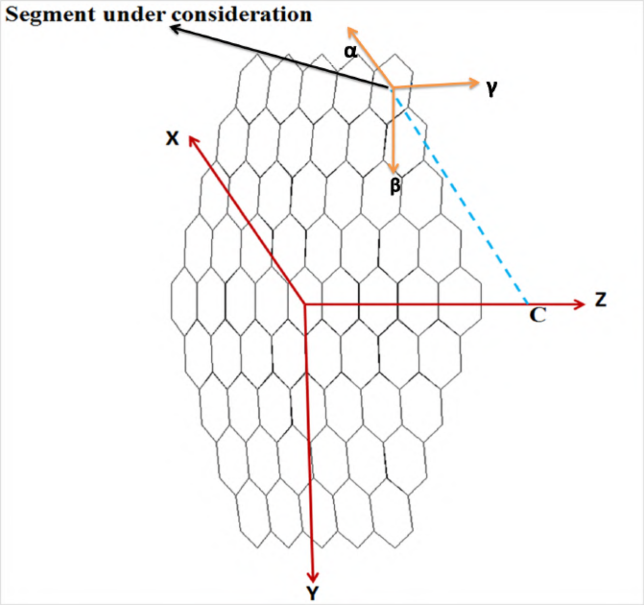

Figure A.6: Global coordinate system of 'X,Y,Z' and local coordinate system of 'α, β, γ'

the desired value, the conic as zero for a spherical mirror. The segmentation code provides all these parameters into the ZEMAX file for the ease of design. In the case of an aspheric primary, this design method will not be ideal due to the need to provide asphericities to each segment, preferably through Zernike coefficients.

In the case of aspheric primaries, the use of aperture files defined in the global coordinate system about the center segment's vertex is the ideal design approach. Here as UDA files are aperture files in the global coordinate system (see figureA.6), the user does not have to take efforts into calculating the X, Y, Z position, and tilt of individual segments. Given the radius of curvature, conic, higher-order aspheric coefficients, and other monolithic equivalent parameters to each segment, the UDA file will create the segments with proper elongation and orientation and place them at the required position. The segmentation code helps in providing all the required parameters into the ZEMAX non-sequential data editor.

Appendix B

Shack-Hartman wavefront sensor MATLAB code (SWSMC) for co-focusing

The light coming out of a telescope depart from its ideal performance as it undergoes what is known as wavefront aberration. This degradation could be due to existing aberrations on the incoming wavefront or aberrations induced by telescope optics. The Shack-Hartman test is used to find these aberrations. This test uses an array of small lenslets arranged in a regular manner spreading across the entire telescope re-imaged pupil [52]. A collimated mirror beam is made to fall into a detector through the lenslet array. If the telescope optics is perfect, then the resulting array of spots on the detector will also be perfect and well arranged. Any imperfection will shift the spots from their ideal position. For accurate measurement of the wavefront, the optics will be chosen such that each spot will be falling in a specific pixel area (PSD) assigned to it in the detector (See figure B.1) The spot displacement can be related directly to the gradient of the incoming wavefront [55],[54]. Thus they provide information about the telescope optics aberrations.[52]. We use a reference beam to calibrate and avoid static aberrations present in the lenslet array and imaging system. To retrieve the wavefront aberration from the spots, we need to calculate the mirror and reference beam spot's centroids. Next, we map each beam spot corresponding to each nominal reference spot. Using a grid geometry that defines the relationship between the X, Y gradient of local phase point, and the shift in the mirror spot position with respect to the ideal reference spot location, we retrieve the wavefront as an array of XY tilts [51]. Once the wavefront error is obtained, we do a Zernike decomposition to find corresponding aberration coefficients. In the coming sections, we explain important steps in our code.

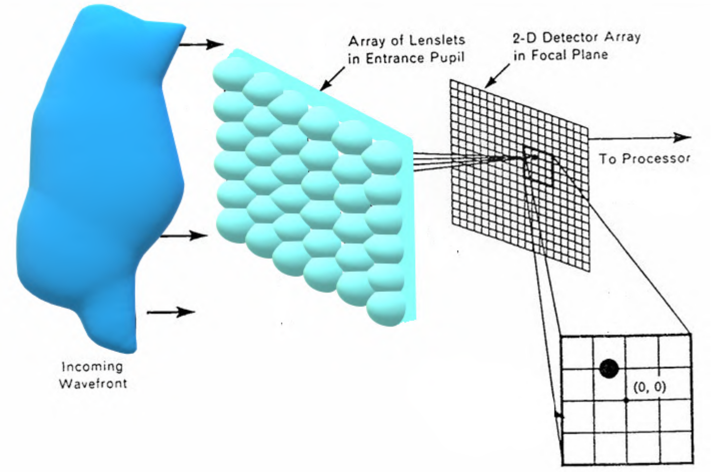

Figure B.1: A diagram containing the incoming wavefront, SH lenslets array and the CCD array. A PSD is shown as Zoomed image

B.1 Centroiding and shift calculation

One import task in finding wavefront error from a spot pattern is finding accurate centroids of the spots. We use Gaussian bivariate function weighted centroiding for this.[53]. The program requires the location of reference and the mirror image. Users can choose the dynamic range, which is the number of pixels assigned to each sub-apertures (PSD) which depends on the total size of array and number of spots in the image. Code numbers all the PSD in ascending order. Subsequently, code identifies sub-apertures or PSDs where the spot is present. To perform this identification,we threshold the intensity of spot images. Spatial filtering is then applied to each spot such that each spot is blurred out into the entire PSD assigned for each spot. As a result, each PSD containing spot gets connected to each other.

Using a MATLAB in a build function called "bwlabel()", all the pixels connected are labeled as one group, thereby effectively achieving the aperture through which the Shack-Hartman sensor receives the light. We call this a BLUR matrix. Our code is unique in its ability to do wavefront sensing in segmented or irregular apertures through this approach. Next, improve the image contrast of the spot image. Then the center x_o, y_o coordinates, and extend of each spot are found iteratively. For the Spot Profiling, the spot model used was a bivariate Gaussian function as given in equation B.1

$$P(x,y) = \frac{N_{ph}}{2\pi{\sigma_{spot}}^2} exp\frac{[-(x-x_0)^2+(y-y_0)^2]}{2{\sigma_{spot}}^2} \tag{B.1}$$

Here, (x_o, y_o) is the position of the center coordinate of the spot. The FWHM $(H_{x,y})$of such a spot is given by equation $H_{x,y} = 2.3548\sigma_{spot}$. Once we know the extent of the spot which was found iteratively as $H_{x,y}$, we can get the σ_{spot} by the same equation. The Gaussian spots are chosen as they are convenient for analytical analysis. The other spot model that can be used is the aperture distorted by atmospheric turbulence. In this case,profile P(x, y) becomes a random function, and its parameters, like $H_{x,y}$, can be defined only in a statistical sense [58].Here, σ_{spot} is the root-mean-squared deviation (RMS) from the mean. In this expression x, x_0, y, y_0 and σ_{spot} are real values. For centroiding various position moments up to the second order are given in equations B.2 to B.6.

$$S_w = \sum_{x,y} I(x,y)(F_w)_{x,y} \tag{B.2}$$

$$S_x = \sum_{x,y} xI(x,y)(F_w)_{x,y} \tag{B.3}$$

$$S_y = \sum_{x,y} yI(x,y)(F_w)_{x,y} \tag{B.4}$$

$$S_{xx} = \sum_{x,y} x^2I(x,y)(F_w)_{x,y} \tag{B.5}$$

$$S_{yy} = \sum_{x,y} y^2 I(x,y)(F_w)_{x,y} \tag{B.6}$$

Where $F_w(x,y)$ is the function given as in equation B.1. The location of the centroid is given in equation B.7.

$$\vec{X_c} = \frac{S_x}{S_w}, \vec{Y_c} = \frac{S_y}{S_w} \tag{B.7}$$

For a Gaussian spot, the rms deviation of position can be calculated as:

$$\sigma = \frac{1}{S_w}\sqrt{S_{xx}S_w - {S_x}^2 + S_{yy}S_w - {S_y}^2} \tag{B.8}$$

Centroiding is done for both Reference and Mirror image. Before finding the centroid of the reference image spots, the reference image is multiplied by a BLUR matrix. The reason to do so is, reference image, in general, has more spots than the mirror image. By this, we can reduce the computation requirement. Next we need to calculate the shift of the mirror spots from the corresponding reference spot. For this, a sub-aperture of rXc PSD's is assigned around the reference spot, keeping the reference spot at the center.

The reference spot is in the sub-aperture S, whereas Q, W, E, A, D, Z, X, C are the other sub-apertures surrounding the reference spot (Qwerty Keyboard geometry). The algorithm checks for a Mirror spot near the reference spot in E. All the mirror spots with the surrounding eight PSDs, whose distance is less than half of the dynamic range, are considered. The one with the smallest distance is assigned as a pair to the reference spot and the reference spot is removed from further comparisons.

Once a mirror spot is assigned to a reference spot, the distance between their centroids is calculated by subtracting their centers $X_{(difference)} = (X_{(ref)} – X_{(mir)})$ and $Y_{(difference)} = (Y_{(ref)} – Y_{(mir)})$. These values are saved in a slope matrix for each PSD as $S_{PSD} = \begin{bmatrix} Y_{(difference)} \\ X_{(difference)} \end{bmatrix}$ This process is iterated until all the required reference spot is connected to the relative mirror spots.

B.2 Wavefront Reconstruction and Decomposition

A variety of approaches have been proposed to accomplish phase reconstruction. Each estimation approach may be categorized as either zonal or modal, depending on whether the estimate is a phase value in a local zone or as a coefficient of an aperture function. In either case, the least-squares estimation is used for the phase reconstruction. One of the most critical factor is the selection of geometry of relationship of gradient to wavefront points , considering, geometry of the slope measurements given by the wavefront sensor,Numerical complexity, convergence problems, storage, computation speed,Error Propagation and the effect of noise. However, as we are not introducing any noise in our system, we ignore the Error Propagation and the effect of noise.

The Reconstruction geometry used here is ”Fried Geometry.”

We also consider waffle[57] in our reconstruction. The reconstruction geometry matrix or ’A’ matrix is formed by the relationship between the slop matrix. S= $\begin{bmatrix} Sy \\ Sx \end{bmatrix}$ and the local phase difference ϕ.Such as $S = A\phi$,[59]. For each adjacent phase points this relation can be given as in equations B.9 and B.10

$$S_{ij}x = \frac{[(\phi_{i+1,j} + \phi_{i+1,j+1}) - (\phi_{i,j} + \phi_{i,j+1})]}{2h} \tag{B.9}$$

$$S_{ij}y = \frac{[(\phi_{i,j+1} + \phi_{i+1,j+1}) - (\phi_{i,j} + \phi_{i+1,j})]}{2h} \tag{B.10}$$

Here (i j) represents the cell, and in our case, the PSD, and ’h’ represents the distance between centers two adjacent phase points.

To convert the retrieved coefficients to nanometer (nm) or millimeter (mm), we need to multiply this A matrix with a scaling factor (SF),[51] given as B.11

$$ScalingFactor(SF) = \frac{F_t F_l \lambda}{F_c 2hCCD_{pixel} 2\pi} \tag{B.11}$$

here, Ft = focal length of telescope; Fl= focal length of lens-let ; Fc=focal length of collimator; h= sub aperture length; CCD_{pixel} = CCD Pixel size; λ = Wavelength. The unit of SF depends upon the values provided . The standard equation is:

$$S = SF * A * \phi \tag{B.12}$$

If we consider A = SF*A

$$S = A\phi \tag{B.13}$$

$$\phi = A^{+} * S \tag{B.14}$$

Here, S = Slope matrix. A^{+} = pseudo inverse matrix of A (using Single Value Decomposition technique. ϕ = Reconstructed wavefront. The ϕ obtained as a 1D matrix, it is made to a 2D matrix, and plotted. The reconstructed wavefront is again multiplied with the BLUR MATRIX to get a wavefront called the final wavefront.BLUR matrix acts as a mask, and we get the wavefront in the aperture.

Once the wavefront is obtained,we use the Zernike coefficient to represent the decomposed wavefront obtained through Singular value decomposition (SVD)[60].

$$\phi = A * Z \tag{B.15}$$

A is the Coefficient matrix Z is the Zernike matrix ϕ is the psi matrix
(reconstructed wavefront)

$$A = Z^{+}\phi \tag{B.16}$$

Z^{+} Is the pseudo inverse matrix of Z.

The main advantages of Zernike polynomial is their orthogonality over the unite circle, rotational in-variance, and direct relationship of expansion coefficients with known aberrations of the optical system[61]. Each Zernike term is a product of three components: a normalization factor, a radial part, and an azimuthal part of type cos mϕ or sin mϕ. The Zernike decomposition is done as in equationB.15.The Zernike matrix is generated using the Zernike polynomials. To find the coefficient matrix 'A', we use the equation B.16.

Once the tool was developed, to calibrate the code , it is run against a known synthetic aberration based spot diagram. Another aberrated spot data are created through ZEMAX using 'physical optics propagation' and this data is processed with the code.

The parameters considered in generating the data are

CCD pixel size : 5 micron

lenslet focal length : 5.2 mm

lenslet pitch : 150 micron.

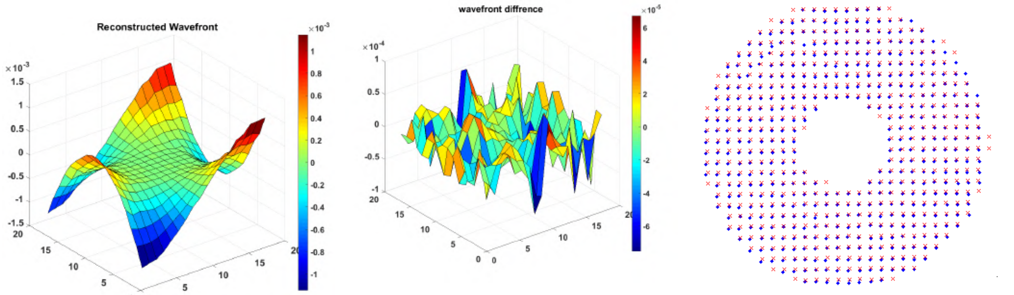

(a) Reconstructed Wavefront for synthetic data

(b) Difference between Final wavefront and Wavefront generated from Zernike for synthetic data

(c) The vector plot of centroid point differences between reference and mirror spots for Hanle Data

Figure B.2: SWSMC results

The data generated consists of 17 spots, and the dynamic range of movement is 30 X 30 pixels for each spot.For the applied error of Z10 (trefoil) the reconstructed wavefront is shown in figure B.2a. The applied error is 'Z10' coefficient of RMS -6.328E-4mm. The retried wavefront is decomposed and the Zernike Coefficients are obtained, the Z10 aberration value is close to the value expected, as -6.25E-4mm. From the figure B.2b, we can see that the residual wavefront errors are less than 10% for the one time open-loop operation. Once the code's calibration was successfully carried out, we used data provided by the Shack-Hartmann sensor existing in the 2m class HCT telescope in Hanle. A vector plot is plotted between the centers of both referee and mirror spots . The red "x" represents the reference and the blue "dot" represents the image; it is shown in figure B.2c. With the addition of a GUI and with more work on calibration, this tool can be used to do the fine alignment and find figure errors of the segmented telescope segments.